Shining light on T6SS Mode of Action and Function within Single Cells and Bacterial Communities

Inauguraldissertation

zur

Erlangung der Würde

eines Doktors der Philosophie

vorgelegt der Philosophisch-Naturwissenschaftlichen Fakultät

der Universität Basel

von

Andrea Vettiger

aus Basel-Stadt, Schweiz

2019

Genehmigt von der Philosophisch-Naturwissenschaftlichen Fakultät auf Antrag von

Prof. Dr. Marek Basler und Prof. Dr. Urs Jenal

Basel, den 25.06.2019

Prof. Dr. Martin Spiess

Dekan

'It is very easy to answer many fundamental biological questions; you just look at the thing!'

Richard Feynman (1918-1988)

To Paula and Noah

Because without you none of this would make any sense, I love you both!

STATEMENT TO MY THESIS

The work included in this thesis has been carried out in the research group of Prof. Marek Basler in the Focal Area Infection Biology at the Department Biozentrum, University of Basel Switzerland.

My PhD thesis committee includes:

Prof. Dr. Marek Basler, Biozentrum, University of Basel, Switzerland

Prof. Dr. Urs Jenal, Biozentrum, University of Basel, Switzerland

Prof. Dr. Martin Ackermann, ETH-Zürich, Switzerland

This thesis is written as a cumulative dissertation and starts with a general introduction on microbial interference competition and the recent advances in the T6SS field. The result section consists of two previously published research articles and two manuscripts which are currently submitted or in preparation for publication, respectively. The structure of the result section follows the sequence of T6SS biogenesis, starting with a chapter on the mechanism of sheath assembly, followed by studies on identifying the signal initiating its contraction. The following two chapters focus on the consequence of T6SS substrate delivery into sister cells as well as by-standing prey cells. Supplementary information to each research article is provided in the appendixes as well as in the electronic document of this thesis. To conclude, I provide a general discussion of the results obtained during the course of my thesis and give an outlook for future directions of these projects.

SUMMARY

Bacteria are ubiquitously found in the environment and form the basis for all known ecosystems on our planet. Most bacterial cells reside in complex multi-species bacterial communities, which are often associated with a host, such as the human microbiota. These bacterial communities are shaped by cooperative and competitive interactions amongst their members. Like higher animals, bacteria also compete with their conspecifics for nutrients and space. This evolutionary arms race resulted in a diverse set of strategies for microbial competition. In particular, bacteria residing on solid surfaces can compete with their neighbors through the use of specialized nanomachines, called secretion systems, enabling the direct delivery of toxic effector molecules into by-standing target cells. The most commonly used weapon for contact-dependent antagonism is the bacterial Type VI secretion system (T6SS).

The T6SS belongs to the family of contractile injection systems (CISs). All CISs are structurally and functionally related to contractile bacteriophages (e.g. phage T4) and translocate proteins into target cells by means of physical force, which is generated by rapid sheath contraction. This results in the ejection of the inner tube associated with a sharp tip and effector proteins at its end. Effector translocation leads ultimately to target cell death. Importantly, the T6SS is capable translocating effectors across broad ranges of biological membranes making it a powerful weapon in microbial warfare as well as potent virulence mechanism towards eukaryotic host cells.

Our current understanding of T6SS mode of action is primarily based on the combination of structural biology and fluorescence live-cell microscopy studies. While in particular cryo-electron microscopy (cryo-EM) revealed the detailed architecture of the T6SS *in situ* and of isolated subassemblies, fluorescence live-cell microscopy uncovered the remarkable dynamics of T6SS biogenesis. However, a complete understanding of T6SS dynamics is hampered in standard fluorescent microscopy due to: (i) the spatial and temporal resolution limit, (ii) the inability to efficiently label secreted components of the machinery, (iii) the weak signals due to low protein abundance and rapid photobleaching, (iv) the difficulty to perform long-term co-incubation experiments as well as (v) the inability to precisely control

spatial and chemical environment. My doctoral thesis aimed to overcome these limitations to allow novel insights into dynamics of the T6SSs of *Vibrio cholerae, Pseudomonas aeruginosa* and *Acinetobacter baylyi*. Specifically sheath assembly, initiation of sheath contraction, T6SS mediated protein translocation in to sister cells as well as strategies for prey cell inhibition were studied in this thesis.

First, I studied sheath assembly in ampicillin induced *V. cholerae* spheroplasts. These enlarged cells assemble T6SS sheaths which are up to 10x longer as compared to rod shaped cells. This allowed us to photobleach an assembling sheath structure and demonstrate that new sheath subunits are added to the growing sheath polymer at the distal end opposite the baseplate. Importantly, this was the first direct observation made for any contractile machines studied to date. Moreover, I showed that unlike for all other CISs, T6SS sheath length is not regulated and correlates with cell size.

In order to monitor protein translocation into target cells, we developed a T6SS dependent interbacterial protein complementation assay, enabling the indirect detection of translocated T6SS components into the cytosol of recipient cells. This allowed us to demonstrate that secreted T6SS components are exchanged among by-standing sister cells within minutes upon initial cell contact. Importantly, these results were the first experimental indication that T6SS is capable of translocating its components into the cytosol of Gram-negative target cells. Furthermore, we showed that the amount and the composition of the secreted tip influences the number of T6SS assemblies per cell, whereas different concentration of the tube protein influenced sheath length. We also provided evidence that precise aiming of T6SS assemblies through posttranslational regulation in *P. aeruginosa* increases the efficiency of substrate delivery.

In addition, together with two Nanoscience master students we have also been implementing microfluidics in the Basler laboratory. This powerful technology enabled us to control the spatial arrangements of aggressor and prey populations and to follow these populations at single-cell level over time scales of several hours. In collaboration with Prof. Kevin Forster, University of Oxford, we demonstrated that the rate of target cell lysis heavily influences the outcome of contact-dependent T6SS killing and thus drives evolution of lytic effectors.

Moreover, microfluidics allows for the dynamic change of the chemical microenvironment during imaging experiments. By following the T6SS dynamics in response to hyperosmotic shocks resulting in a rapid cell volume reduction, we found that physical pressure from the collapsing cell envelope could trigger sheath contraction. This led us to propose a model for sheath contraction under steady-state conditions where continued sheath polymerization against membrane contact site leads to a gradual increase in pressure applied to the assembled sheath. We propose that this could be potentially sensed by the baseplate, which in turn would trigger sheath contraction.

ACKNOWLEDGEMENTS

I would like to take a moment and acknowledge the many people inside and outside academia who supported me throughout my PhD thesis.

First and foremost, I would like to thank my doctoral supervisor Prof. Marek Basler for his constant support and willingness to discuss any scientific and non-scientific projects. His open-door policy and direct attitude for problem solving is unprecedented. I also would like to express my deepest gratitude for the great career support Prof. Basler gave me throughout my thesis. He encouraged me attend multiple high-level international conference and present my research in front of dedicated experts in the field of microbiology. Also, his input for finding a postdoctoral position was always highly appreciated. Last, I would like to thank Prof. Basler for being always fully supportive of my family reconciliations, no matter how often Noah was sick or unable to attend daycare.

I am also grateful to my PhD committee members, Prof. Urs Jenal and Prof. Martin Ackermann, who have always provided me with outstanding scientific and career input. Also, I would like to thank them for providing me with several reference letters for postdoctoral fellowship applications and positions. I will remember my PhD committee meetings warmly.

Importantly, I would like to thank all previous and current lab members of the Basler research group making this such a wonderful place to carryout research as well as for their scientific input in countless discussions. I am certain that I will miss our fun lunch conversations at my next position. In particular, I would to acknowledge my peers Dr. Max Backmann, who introduced me to most laboratory techniques when I joined the lab, as well as Dr. Peter Ringel and Maj Brodmann sharing the PhD experience with me. I am also highly grateful to Julius Winter, Till Ryser and Andreas Keppler, whose master thesis I had the pleasure of supervising. I would also like to express my gratitude to Dr. Mihai Ionescu for always keeping the lab running smoothly and taking care of ordering my supplies.

In addition, I would like to thank all members of the infection biology department for a great working atmosphere and support with ideas and reagents. In particular, I would like to point

CONTENTS

LIST OF ABBREVIATIONS

AAA	ATPase associated with diverse cellular activities
ADP	Adenosine diphosphate
AFM	Atomic force microscopy
ATP	Adenosine Triphosphate
CDI	Contact-dependent growth inhibition
CFU	Colony forming unit
CPRG	Chlorophenol red-β-D-galactopyranoside
cryo-EM	Cryo-electron microscopy
cryo-ET	Cryo-electron tomography
CTX	Cholera toxin
DMSO	Dimethyl sulfoxide
DNA	Deoxyribonucleic acid
Ecc	ESX conserved component
EM	Electron microscopy
ESX	ESAT six
FHA	Forkhead-associated domain
FIB	Focused ion beam
FRAP	Fluorescence recovery after photobleaching
FRET	Förster resonance energy transfer
HEK	Human embryonic kidney cells
HGT	Horizontal gene transfer
IAHP	IcmF associated homologous proteins
IBM	Individual based modelling
IM	Inner membrane
IPTG	Isopropyl-β-D-thiogalactopyranoside

kDa	Kilodalton
LPS	Lipopolysaccharide
MDa	Megadalton
MW	Molecular weight
NAD	Nicotinamide adenine dinucleotide
OD	Optical density
OM	Outer membrane
PAGE	Polyacrylamide gel electrophoresis
PBS	Phosphate buffered saline
PCR	Polymerase chain reaction
PG	Peptidoglycan
PTX	Pertussis toxin
QS	Quorum sensing
RHS	Recombination hotspot
RNA	Ribonucleic acid
SIM	Structured illumination microscopy
Sec	General secretory pathway
T2SS	Type II secretion system
T3SS	Type III secretion system
T4SS	Type IV secretion system
T5SS	Type V secretion system
T6SS	Type VI secretion system
T7SS	Type VII secretion system
Tag	Type six secretion system associated gene
Tat	Twin-arginine pathway
TCA	Trichloroacetic acid
Tse	Type six secretion system effector
Tsi	Type six secretion system immunity protein
Tss	Type six secretion system component

CHAPTER 1

Introduction

1.1   The implications of compartmentalization through biological membranes

All cells are surrounded by at least one biological membrane creating a confined space commonly referred to as cytosol. This compartmentalization from the extracellular environment is crucial and allows biochemical reactions to take place under controllable conditions. Moreover, maintaining membrane integrity is essential for cell survival.

Prokaryotic cells are typically surrounded by at least one membrane (monoderm) (Gupta, 1998) and in most organisms by an additional layer of peptidoglycan (PG) mesh-like heteropolymer made up of N-acetyl-glucosamine and N-acetyl-muramic acids, forming the cell wall (Typas et al., 2011). Diderm bacteria possess a second outer membrane (OM) creating an additional cellular compartment, the periplasmic space (Gupta, 1998). These membranes form a strong diffusion barrier, and thus forced bacteria to evolve a plethora of membrane channels and pores in order to import nutrients (Nikaido, 2003), as well as complex export machines, in order and secrete macromolecules. Currently, we know of nine different classes of secretion systems (Costa et al., 2015; Lasica et al., 2017). These complex nanomachines allow bacterial cells to interact with their surroundings and manipulate their microenvironment. Microbes secrete for example soluble effector molecules across their cell envelope into the environment in order to interfere with other organisms during microbial competition across large distances. However, often effectors can also be injected directly into neighboring cells, thereby breaching target cell membrane (Ghoul and Mitri, 2016). To date, only three secretion systems are known to translocate their substrates directly across target cell membranes, namely the non-flagellar type III secretion system (T3SS) (Wagner et al., 2018), the type IV secretion system (T4SS) (Christie, 2016) and the type VI secretion system (T6SS) (Cianfanelli et al., 2016). Importantly, the T3SS exclusively translocates its substrates into eukaryotic target cells and is an important virulence factor of many human pathogens (Deng et al., 2017). However, this thesis focuses on strategies employed by bacteria for microbial interference competition and will therefore not discuss the T3SS further. Instead, I will give a broad overview how bacteria compete against one another using soluble effector molecules and then particularly focus on the strategies used for contact-

dependent antagonism. These include the T4SS, the type V secretion system (T5SS), in particular two-partner secretion systems more often also referred to as contact-dependent growth inhibition (CDI) (Ruhe et al., 2013), the T6SS and the ESX type VII secretion system (T7SS) (Unnikrishnan et al., 2017).

1.2 Strategies for microbial interference competitions using soluble effector molecules

Microbes compete with each other for essential resources such as space and nutrients. Thus, the ability to interfere with other members of the bacterial community is critical for its success. Microbial interference competition is described as a process of competition among bacterial cells through the use of toxic molecules. It is distinct in that sense from exploitive competition, where an organism consumes the resources required by another cell (Ghoul and Mitri, 2016). Here after, I am solely going to focus on strategies for microbial interference competition.

1.4.5 Low-molecular-weight bacteriocins

Bacteria produce a diverse range of soluble toxins, referred to as bacteriocins. These are in contrast to non-ribosomally synthesized small molecule antibiotics, such as streptomycin, of proteinaceous nature. Typically, bacteriocins display only narrow antibacterial activity, mostly against closely related strains due to the requirements of a designated surface receptor for uptake by the target cell. Bacteriocins encompass various small peptide effectors, such as microcins which consist of small peptides (MW < 10 kDa), as well as large macromolecules such as colicins and pyocins and are effective against sessile and planktonic target cells (García-Bayona and Comstock, 2018).

Recently, microcins produced by *Escherichia coli* Nissle 1917 were shown to prevent the growth of other commensal or pathogenic *E. coli* strains as well as *Salmonella enterica* serovar Typhimurium (Sassone-Corsi et al., 2016). Microcins often display a 'trojan horse' mode of action, for example by containing a siderophore moiety at their C-terminus, thereby intoxicating non-immunocompetent bacteria taking up iron through catecholate siderophores by inhibition of DNA replication, transcription, or protein synthesis (Destoumieux-Garzón et al., 2002; Patzer et al., 2003). Thus, microcin producing *E. coli* Nissle 1917 only displays antibacterial activity under iron-limited conditions, a hall mark of the inflamed gastrointestinal track, and could therefore be used as a probiotic during dysbiosis characterized by an enterobacterial bloom (Sassone-Corsi et al., 2016).

Another common example of low-molecular-weight bacteriocins is the lantibiotic nisin, which forms part of class I bacteriocins. This broad-spectrum peptide antibiotic (MW < 5 kDa) is produced by monoderm bacteria and interferes with target cells through pore-forming activity. Additionally, it was shown that nisin also interacts with the PG precursor

Lipid II, indicating that cell wall biogenesis might also be a targeted. Posttranslational peptide modifications such as the formation of lanthionine rings by the producing cell are critical for the antibacterial activity (Breukink and de Kruijff, 1999). Nisin is routinely used as a food preservative (E-234) and its target spectrum can be extended to diderm bacteria if co-administered with ion chelator EDTA (Aymerich et al., 2011).

1.4.8 High-molecular-weight bacteriocins

In contrast to low-molecular-weight bacteriocins which are commonly not larger than 10 kDa, high-molecular-weight bacteriocins encompass large multi-subunit proteins, which in some cases may oligomerize to multi-molecular assemblies (García-Bayona and Comstock, 2018). All high-molecular-weight bacteriocins have been reported to be highly potent, where a single particle may be sufficient to kill a target cell (Jacob et al., 1952; Scholl, 2017). The two most prominent examples of high-molecular-weight bacteriocins are colicins and pyocins produced by *E. coli* and *P. aeruginosa*, respectively. Both colicins and pyocins production are regulated by the SOS response induced upon DNA damage (Michel, 2005). While the colicin operon is encoded on a colicinogenic plasmid, pCol, which is widespread among many natural *E. coli* isolates, pyocins are chromosomally encoded (Cascales et al., 2007; Michel-Briand and Baysse, 2002). A common operon consists of SOS response specific promoter followed by the bacteriocin encoding gene, an independent internal promoter for constitutive immunity protein transcription, the immunity gene itself and an autolysin ensuring particle release by mediating cell lysis of the producing cell (Riley, 1993). Structurally and functionally colicins and S-type pyocins are highly similar and consist of three distinct modular domains: The receptor binding domain (i), the translocation domain (ii) and the activity domain (iii) (Cascales et al., 2007). For example, colicin Ia attaches to target cells via the OM protein Cir and is then translocated across the periplasmic space by the help of TonB and accessory IM proteins ExbB and ExbD. Ultimately, the activity domain forms an ion-leaking pore into the inner membrane (IM) resulting in target cell death (Fig. 1) (Wiener et al., 1997).

Figure 1: Mechanism of colicin attachment and translocation. OM (cir) and IM (TonB) target cell receptors are indicated. Colicin Ia is represented as a ribbon diagram. Receptor binding domain is represented in green, translocation domain in blue and pore-forming activity domain in red. *Source: Wiener et al., 1997*
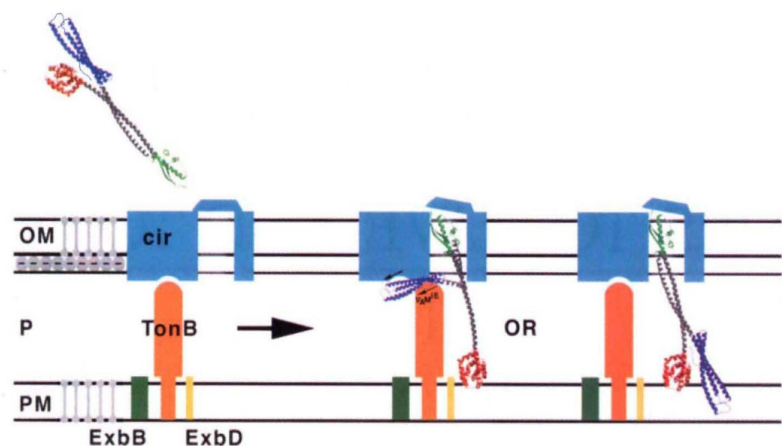
All known S-type pyocins and colicins mediate cell death through pore-forming or nuclease activity, except in few cases Lipid II is targeted (e.g. colicin M, pyocin M1) and thus interferes with cell wall biogenesis (Cascales et al., 2007; Michel-Briand and Baysse, 2002).

In contrast to S-type pyocins, F- and R-type pyocins form complex multi-protein assemblies and belong to the class of tailocins, which share functional and structural homology to bacteriophage tails (Scholl, 2017). While flexible F-type pyocins are closely related to non-contractile phage λ, rigid R-type pyocins belong the family of contractile injection systems (CISs) and are related to *Myoviridae* bacteriophages (Nakayama et al., 2000). In particular, R-type pyocins consist of a contractile sheath which is wrapped around a stable inner tube with a sharp tip at its distal end, which is linked via the baseplate to the tail fibers (Ge et al., 2015). Binding of target cell lipopolysaccharide (LPS) O-antigen by tail fibers triggers sheath contraction, thereby expelling the inner tube across the target cell envelope, resulting in cell death (Fig. 4) (Buth et al., 2018). Importantly, both R- and F-type pyocins kill target cells through pore-forming mechanism (Scholl, 2017).

The structural and functional aspects of contractile nanomachines will be discussed further in sections 1.3.3 and 1.4.1.

1.3   Strategies for contact-dependent interference antagonism

While transmission and dissemination into new ecological niches occurs through motile planktonic cells, the vast majority of bacterial cells resides in surface associated communities, referred to as biofilms (Watnick and Kolter, 2000). Living in bacterial communities is commonly associated with several beneficial traits, such as enhanced resilience to changing environmental conditions (e.g. aridity, antimicrobials etc.). However, it also brings several disadvantages, such as limited access to nutrients and spatial constraints (Flemming et al., 2016; Stoodley et al., 2002). Thus, in order to maximize their fitness, bacteria utilize a broad range of nanomachines to translocate toxic effector molecules into neighboring competitors. While some of these systems are very flexible allowing bacteria to compete with a wide range of target cells (e.g. T4SS, T6SS), others are highly specific and rely on target cell surface receptors for protein translocation (e.g. CDI, T7SS). Importantly, unlike soluble bacteriocins, these systems are only active across short ranges and require physical contact between the aggressor and the victim cell (García-Bayona and Comstock, 2018).

1.3.1 The type IV secretion system

The bacterial T4SSs encompass a wide range of highly flexible secretion systems which are capable translocating protein and protein associated DNA substrates likewise. Moreover, T4SSs are capable of translocating their substrate into both pro- and eukaryotic cells (Alvarez-Martinez and Christie, 2009). These versatile multiprotein nanomachines are found

in Gram-positive and Gram-negative bacteria, as well as some archaea and are the most widespread secretion system in nature (Costa et al., 2015).

T4SSs can be either chromosomally encoded or located on a plasmid. The architecture of both protein and conjugative T4SSs is generally conserved, however differ in some aspects (e.g. pilus length) (Alvarez-Martinez and Christie, 2009). Here, I will give a brief outline of the general architecture of conjugative T4SSs in Gram-negative bacteria, which are the best characterized systems. These cell envelope spanning nanomachines are made up of 12 components (VirB1-11 and VirD4) (Ilangovan et al., 2015). Briefly, the machine is divided into three components. The pilus (i) consists of VirB2 subunits forming five-start helical filaments with stoichiometric protein-phospholipid interactions containing a cap protein (VirB5) at its distal end (Fig. 2A) (Costa et al., 2016). Type 4 pili can form several micrometer long cellular appendages (Babic et al., 2008). In order to translocate DNA across such large distances, it is believed that lipid coating of the pilus facilitates transport of negatively charged molecules such as nucleic acids (Costa et al., 2016). VirB5 was described to mediate target cell recognition and be involved in incorporation of new VirB2 subunits (Aly and Baron, 2007; Moore et al., 1993). Pilus biogenesis depends on the action of the lytic transglycosylase VirB1 (Zupan et al., 2007). The translocation apparatus (ii) consist of VirB3, VirB6, VirB7, VirB8, VirB9 and VirB10 which form a cell envelope spanning scaffold. VirB7, VirB9 and VirB10 form the core complex which is incorporated into the OM following 14-fold symmetry (Sgro et al., 2018). Accordingly, the inner membrane complex (IMC) is made up of VirB3, VirB6, VirB8 following a 12-fold symmetry and is connected through the OM complex via the N-terminal IM-inserting segments of VirB10 as well as a central stalk, presumably formed by VirB2 (Low et al., 2014). Last, three distinct
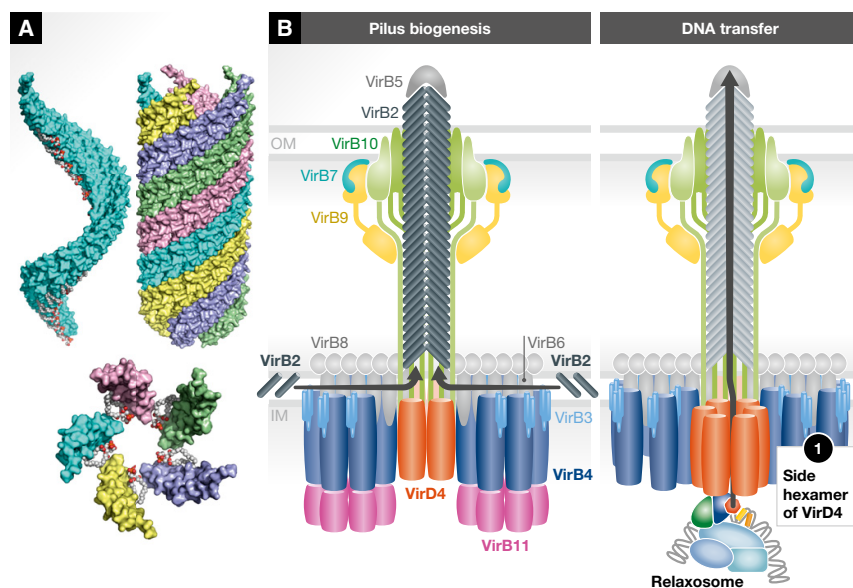
Figure 2: Overview of the conjugative T4SS. **(A)** Atomic structure of F-pilus. Five-fold helical symmetry of individually colored VirB2 subunits is indicated. **(B)** Pilus biogenesis and DNA translocation are being energized by different sets of ATPases (VirB4, VirD4 and VirB11). *Adapted from: Waksman, 2019*

ATPases (iii), VirB4, VirB11 and VirD4 respectively, localize at the inner leaflet of the IMC (Low et al., 2014; Redzej et al., 2017). An attractive hypothesis suggests how different functions of the T4SS may be carried out. Association of VirB4 and VirB11 at the IMC mediates pilus biogenesis, which precedes until the pilus cap protein VirB5 established target cell contact. This would then result in a conformational switch at the IM where VirB11 is replaced by VirD4, which then allows for relaxosome bound substrate translocation (Fig. 2B) (Costa et al., 2015; Waksman, 2019).

T4SSs are most known for their conjugation machinery mediating relaxase bound single stranded DNA (ssDNA) translocation into target cells (Ilangovan et al., 2015; Lederberg and Tatum, 1946). This enables the rapid spread of mobile genetic elements as well as integrative and conjugative elements in bacterial populations and thus contributes to dissemination of antimicrobial resistance and pathogenicity islands (Juhas, 2015). Importantly, conjugation is a widely used method in biotechnology in order to genetically modify plants, bacteria or yeast and paved the way for molecular biology and genetics (Griffiths et al., 2000; Heinemann and Sprague, 1989; Pitzschke and Hirt, 2010). Besides DNA transfer into target cells, there are also T4SSs which function in DNA uptake and release from the environment, which have been found in *Neisseria gonorrhoeae* and *Helicobacter pylori* (Lederberg and Tatum, 1953).

Importantly, T4SS also secrete proteinaceous substrates form both cytoplasm and periplasmic space. While, for secretion of cytosolic substrates a Type 4 Coupling Protein (T4CP) is essential, periplasmic substrate are translocated across the IM by the Sec pathway (Cascales and Christie, 2003; Costa et al., 2015). Currently, there is only a single periplasmic substrate known to be secreted by the T4SS, namely the pertussis toxin (PTX) from *Bordetella pertussis* (Covacci and Rappuoli, 1993). PTX is secreted into the extracellular space where it oligomerizes to a heterohexamer and is then internalized by host cells via receptor-mediated endocytosis and retrograde transport, where it ultimately catalyzes ADP-ribosylation of G proteins interfering with cellular physiology (Locht et al., 2011). T4SSs are also used as a virulence factor by several additional human pathogens, such as *H. pylori* or *Legionella pneumophilla*. While, *H. pylori* secretes only a single effector, the immunomodulatory and oncogenic CagA (Backert et al., 2015), *L. pneumophilla* encodes up to 300 different T4SS substrates in order to manipulate their eukaryotic host cells (Burstein et al., 2016).

Recently, a new role of T4SSs in microbial competition of the phytopathogen *Xanthomonas citri* was described. This T4SS mediates the capacity to kill Gram-negative bacteria in a contact-dependent manner through the use of effector proteins targeting PG and phospholipids mediating efficient prey cell lysis (Sgro et al., 2018; Souza et al., 2015). Protein translocation into Gram-negative target cells by other T4SS has been shown

previously using Cre-recombination based assays (Luo and Isberg, 2004), however Souza et al., were the first in demonstrating that T4SSs can be involved in bacterial antagonism. How widespread this feature of the T4SS is, remains to be elucidated.

1.3.2 The type V secretion system

The T5SS belongs to the class of two-step secretion systems, meaning that substrate transport across the IM and OM is carried out by different translocation systems. T5SS substrates contain an N-terminal Sec secretion system signal sequence mediating transport across the IM into the periplasmic space (Desvaux et al., 2004). A so-called passenger domain is responsible for exerting its biological function and is linked to a β-domain, forming a hydrophobic β-barrel in the OM, allowing substrates translocation to the cell surface (Gawarzewski et al., 2013). Due to the capability to mediate their own secretion across the OM, T5SS are also referred to as autoinducers. The biological function of distinct passenger domains varies and was first described to mediate self-aggregation and biofilm formation (Garcia et al., 2016; Kajava et al., 2001; Relman et al., 1989; Rojas et al., 2002). Today five different classes of T5SSs (Va-e) have been described in various diderm organisms such as *E. coli*, *B. pertussis*, *P. aeruginosa* or *Yersinia spp*. (Leo et al., 2012).
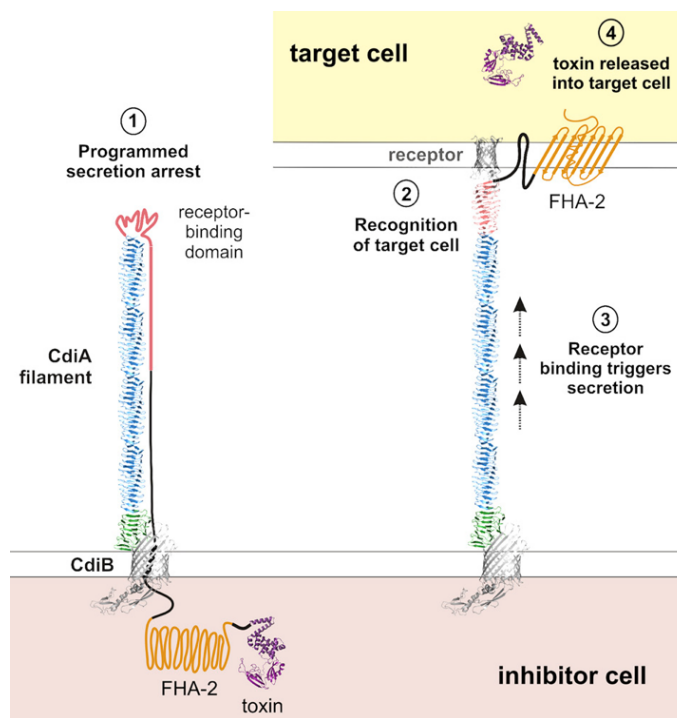
Figure 3: CDI architecture and mechanism for substrate translocation. Numbers indicate steps of CdiA secretion and translocation across target cells. CdiB froms the OM secretion channel for CdiA translocation. CdiA encodes a C-terminal pore-forming toxin domain inserting into IM of target cells, which is neutralized by the immunity protein CdiI in the inhibitor cell (not depicted). *Source: Ruhe et al., 2018*

Importantly, later it was also discovered that specialized two-partner T5SSs (Vb) also contribute to microbial competition through a process referred to as contact-dependent growth inhibition (Aoki et al., 2005). CDI was the first identified mechanism for contact-dependent interference competition among bacteria. Importantly, although CDI needs cell-cell contacts in order to display its toxicity, it remains functional in liquid medium, indicative of a strong aggressor-prey association (Aoki et al., 2011). This is in stark contrast to T4SS

and T6SS, which exclusively mediate prey cell killing on solid surfaces (Hood et al., 2010; Souza et al., 2015). The two-partner secretion system (TPS) of *E. coli* EC93 consists of CdiB, an OM pore, mediating secretion of CdiA, a large (320 kDa) multi domain protein containing the toxic effector domain. In order to prevent self-intoxication, the producing cell additionally expresses the immunity protein CdiI (Ruhe et al., 2013). CDI was often referred to as 'toxin-on-a-stick' (Aoki et al., 2011). However, recent insight by electron cryotomography (cryo-ET) revealed a much more complicated architecture and mode of action for CDI systems (Fig. 3) (Ruhe et al., 2018). Secretion of CdiA across the OM by CdiB is a two-step procedure. First the N-terminal domain of CdiA translocates into the extracellular space and where it forms 33nm long filaments displaying the target cell receptor binding site on their surface. At this stage the C-terminal domain of CdiA containing the effector domain resides still in the periplasmic space (Ruhe et al., 2018). Binding of target cell surface receptor OmpC or Tsx, then results in the secretion of the C-terminal part of CdiA (Aoki et al., 2008; Ruhe et al., 2017). It is believed that the C-terminal domain FHA-2 then forms a pore in the OM of the target cell mediating effector translocation. The effector domain is then cleaved and imported to the cytosol (e.g. nucleases) or inserted into the IM (e.g. pore-forming toxins) depending on effector function (Hayes et al., 2014).

1.3.3 The type VI secretion system

T6SSs are found in 25% of sequenced Gram-negative bacteria (Bingle et al., 2008) and is structurally and functionally related to an inverted contractile bacteriophage tail (Ho et al., 2014). Briefly, the T6SS consists of a long cytosolic sheath which is warped around a tube containing a toxin decorated tip at its end. The sheath is connected to a cell envelope spanning complex via a baseplate. As for all CISs, sheath contraction mediates the energy for substrate translocation into the extracellular space or across target cell membranes (Fig. 4) (Brackmann et al., 2017; Silverman et al., 2012).

Even though first identified in a virulence screen against eukaryotic cells (Pukatzki et al., 2006), it became later clear that the T6SS is primarily utilized to inject effectors into by-standing prokaryotic target cells during contact-dependent microbial competition on solid surfaces (Cianfanelli et al., 2016; Russell et al., 2011).

A detailed description of T6SS architecture, mode of protein translocation, effector repertoire and function within bacterial communities will be outlined in section 1.4.
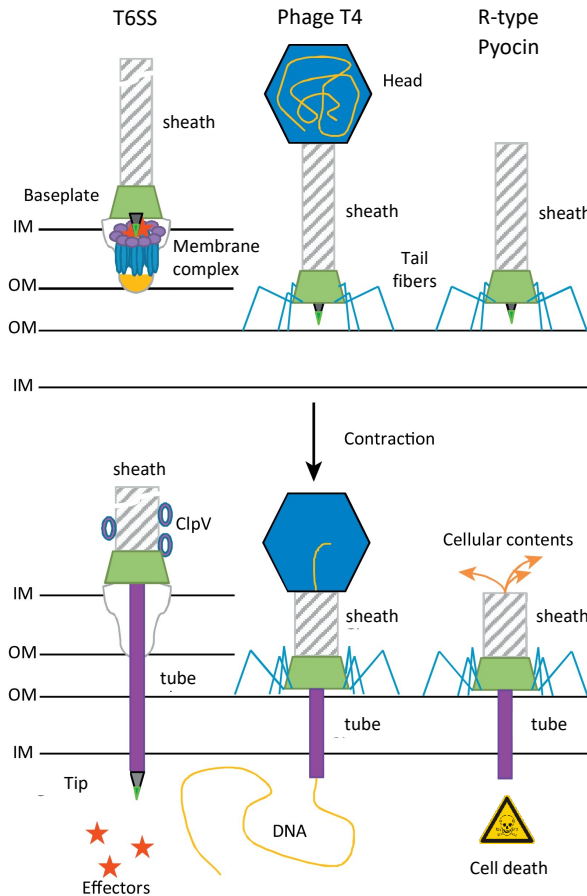
Figure 4: Structural and functional comparison between different CISs. Three common examples of CISs are displayed: Intercellular T6SSs, soluble *Myoviridae* phage T4 and R-type pyocins produced by *P. aeruginosa*. These nanomachines are composed of a sharp tip attached to an inner tube which is surrounded by a contractile sheath. Translocation of large hydrophobic macromolecules across cellular membranes is powered by sheath contraction transition from a high energy state to a low energy state. While surface receptor binding through tail fibers of extracellular CISs induces sheath contraction, the molecular mechanism for intracellular T6SSs is not understood. R-type pyocins generate stable holes into the cell envelope of target cells, thereby provoking cell death. T6SSs translocate effectors bound either to the tip or tube into target cells leading to their inhibition and lysis, while protein translocation in phages creates a channel enabling DNA translocation. *Adapted from: Brackmann et al., 2017*

1.3.4 The type VII secretion system

Generally, monoderm bacteria possess fewer and simpler secretion systems as compared to their diderm counterparts due to the absence of an OM (Unnikrishnan et al., 2017). Nevertheless, also monoderm bacteria utilize designated secretion systems for virulence towards eukaryotic host cells as well as competing bacteria. One of these specialized secretion systems is the T7SS, first identified in *Mycobacterium tuberculosis* (Hsu et al., 2003). Five copies (Esx 1-5) of the T7SS are encoded on the genome of *M. tuberculosis* and serve as crucial virulence factor for macrophage infection and intracellular survival (Houben et al., 2014; Stanley et al., 2003). Currently, only few structural data on the architecture of T7SS are available. However, a negative stain electron microscopy (EM) structure of the Esx-5 of *M. xenopi* was recently revealed. It was found that four proteins (EccB, EccC, EccD, EccE) insert with six-fold symmetry into the IM forming 1.8 MDa secretion complex (Beckham et al., 2017). The ATPase EccC contains long C-terminal protrusions into the cytosol and has been proposed to be involved in substrate recognition and may also mediate the energy for protein translocation (Beckham et al., 2017; Rosenberg et al., 2015). However, route of assembly, mechanism of substrate recognition, mechanism and state (folded or unfolded) of translocated substrates as well as transport across the OM remain currently unclear.

Importantly, T7SSs are not restricted to diderm mycobacteria but are also found in many monoderm bacteria such as *Staphylococcus aureus*, *Bacillus subtilis* or *Listeria monocytogenes* and are associated with diverse function such as virulence, DNA transfer, nutrient uptake and metal scavenging or sporulation (Bitter et al., 2009; Unnikrishnan et al., 2017). *S. aureus* utilizes its T7SS to compete with non-isogenic strains through a nuclease, EsaD (Cao et al., 2016). The cytotoxic activity of EsaD is neutralized by the immunity protein EsaG and is presumably stripped off during secretion. EsaD is guided to the T7SS by the chaperon EsaE and translocated by the ATPase EssC (Cao et al., 2016). If EsaD is simply secreted in the medium or remains attached at the cell surface and how it is then internalized by target cells remains to be elucidated. In general, a similar mechanism as for CDI is envisioned, where toxin translocation is dependent of a target cell receptor. In support for this, EsaD mediated toxicity was found to be active liquid culture.

1.4 The antibacterial type VI secretion system

Today we know of three injection system found in Gram-negative bacteria, namely T3SS, T4SS and the most recently discovered T6SS (Costa et al., 2015). In 2006, Pukatzki *et al.*, identified in a transposon screen for novel virulence factors in non-pandemic (O1/O139) *V. cholerae* V52 strain, a series of secreted proteins mediating toxicity against *Dictyostelium* amoebae and mammalian J774 macrophages in a contact-dependent manner (Pukatzki et al., 2006). Importantly, these proteins all lacked a N-terminal signal sequence for secretion via the Sec pathway, which was already previously realized by Williams and colleagues for hemolysin-coregulated protein (Hcp) (Williams et al., 1996). Moreover, genome sequencing revealed that *V. cholerae* V52 does not encode a T3SS or T4SS. Thus, it was proposed that a novel secretion apparatus is responsible for secreting these virulence factors into target cells (Pukatzki et al., 2006). Interestingly, many transposon insertion mapped to a locus previously known as the IcmF associated homologous proteins (IAHP), which resembles in part to the icmF/dotU T4SS in *L. pneumophilla* (Das and Chaudhuri, 2003). IAHPs were found to be widely distributed among pathogenic and commensal Gram-negative bacteria such as *S. enterica*, *E. coli* O157, *Francisella tularensis*, *P. aeruginosa*, *Rhizobium leguminosarum*, *Agrobacterium tumefaciens* or *Edwardsiella ictalurid* (Bladergroen et al., 2003; Das and Chaudhuri, 2003; Das et al., 2000; Folkesson et al., 2002; Nano et al., 2004; Parsons and Heffron, 2005; Rao et al., 2004; Roest et al., 1997). Thus, previously identified mutations in the IAHP locus mediating decreased in virulence in various *in vivo* and *in vitro* infection models could thereafter be associated to loss-of-function mutations of the T6SS.

Canonical T6SS clusters consist of 13 conserved structural components (type six secretion [Tss$_{A-M}$] components) and a variable number of accessory proteins (tss-associated gene [Tag] components) as well as effector proteins (Alcoforado Diniz et al., 2015; Boyer et al., 2009; Cianfanelli et al., 2016). Such gene clusters have been identified in > 25 % in Gram-negative

(Bingle et al., 2008), with a high prevalence among proteobacteria, which can be divided into six subclusters (Barret et al., 2013; Boyer et al., 2009). In addition, three non-canonical T6SSs have been identified in *Francisella* (de Bruin et al., 2007), *Bacteroides* (Russell et al., 2014a) and *Amoebophilus asiaticus* (Böck et al., 2017). Interestingly, multiple T6SS clusters may be encoded on the same genome, which are thought to carry out distinct functions during the bacterial life cycle and are often regulated differentially. For example, up to six different T6SS clusters are found in *Burkholderia pseudomallei* or *Y. pestis* (Boyer et al., 2009), each of which can have distinct roles in virulence (anti pro- or eukaryotic) (Schwarz et al., 2010) or manganese scavenging (Si et al., 2017).

Although at first T6SS clusters were identified as anti-eukaryotic virulence factors in serval human pathogens (de Bruin et al., 2007; Dudley et al., 2006; Mougous et al., 2006; Pukatzki et al., 2006, 2007; Shalom et al., 2007), it was soon realized that these gene clusters were also widely distributed among environmental bacteria implicating a more general role for T6SSs (Bingle et al., 2008; Persson et al., 2009). Its role in targeting prokaryotic cells was discovered investigating a T6SS specific toxin-immunity pair (Tse2, Tsi2) in *P. aeruginosa* (Hood et al., 2010). The authors demonstrated that an isogenic *P. aeruginosa* strain lacking the toxin-immunity pair is killed by the parental strain in a T6SS dependent manner on solid surfaces. In a subsequent publication that same year the Mougous laboratory also demonstrated that T6SS targets its antimicrobial activity to broad spectrum of different Gram-negative bacterial species (Schwarz et al., 2010). These findings paved the way for studying the T6SS in the context of microbial competition, which is nowadays believed to be its paramount function (Russell et al., 2014b). Still, T6SS mediated anti-eukaryotic virulence is an important feature of the secretion system (Hachani et al., 2016). Additionally, some organisms, such as *Francisella spp.*, exclusively utilize their T6SS for phagosomal escape in macrophages and do not target any prokaryotic cells (Brodmann et al., 2017). Additional reports involving T6SSs in metal scavenging currently remain the exception (Chen et al., 2016; Lin et al., 2017; Si et al., 2017) and whether the systems could be used for contact-dependent signaling among sister cells remains to be elucidated (Gallique et al., 2017).

1.4.1 T6SS mode of action

The T6SS shares structural and functional homology to extracellular CISs, such as *Myoviridae* bacteriophages (Leiman and Shneider, 2012), R-type pyocins of *P. aeruginosa* (Scholl, 2017), metamorphosis-associated contractile (MAC) structures expressed by *Pseudoalteromonas luteoviolacea* (Shikuma et al., 2016), antifeeding prophages (Afp) of *Serratia entomophila* (Heymann et al., 2013; Hurst et al., 2007) or photorhabdus virulence cassettes (PVC) encoded by various insect pathogens (Jiang et al., 2019; Yang et al., 2006). The T6SS was first visualized in 2012 using Cryo-ET in intact *V. cholerae* cells revealing
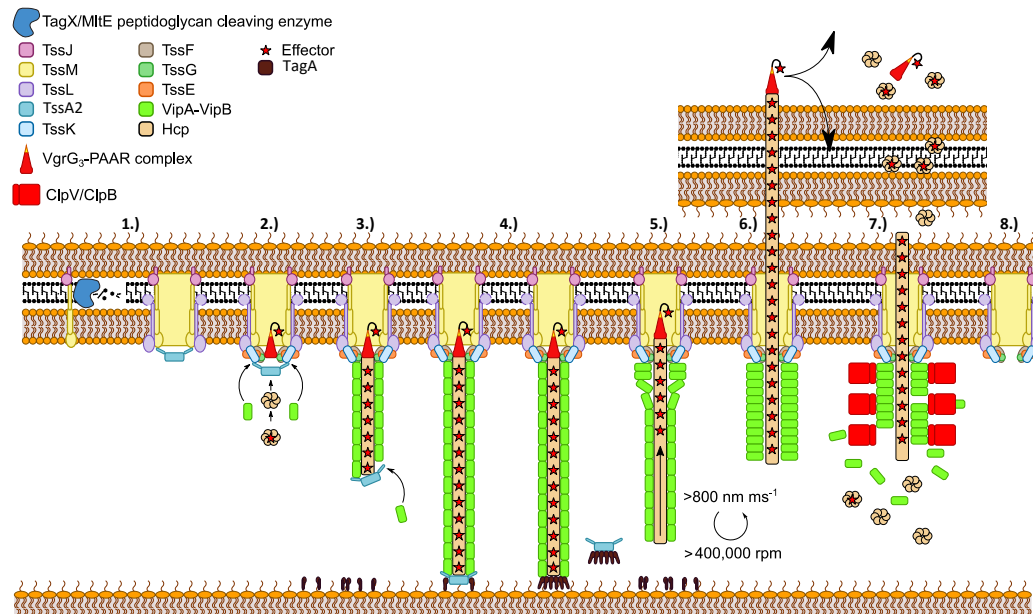
Figure 5: Overview of T6SS biogenesis. 1.) Insertion of the membrane complex (TssJ,L,M) may require local cleavage of cell wall and serves as a scaffold for baseplate (TssA2,E,F,G,K, VgrG-PAAR, effectors) assembly **2.)**. Sheath polymerizes onto the baseplate through addition of Hcp and VipA-B subunits at its distal end **3.)** which in some organisms is mediated by the cap protein TssA2. **4.)** Upon membrane contact sheath polymerization ceases and may remain stalled in some organisms though stabilization of TagA. T6SS contraction **5.)** is initiated through conformational changes of the baseplate triggering a progressive sheath contraction wave towards the distal end thereby propelling the Hcp tube with associated tip and effectors into target cells **6.)**. Contracted sheath is disassembled by an unfoldase under ATP consumption **7.)**. Whether membrane complex and baseplate are reused for next round of assembly or disassemble similar to sheath remains unknown **8.)**. Legend of distinct T6SS components is provided in the figure. Individual step in of the assembly are denoted with numbers. For more detailed description please refer to corresponding chapters. *Adapted from: Schneider et al., accepted*

its overall architecture and mode of secretion (Basler et al., 2012). In contrast to beforementioned CISs, the T6SS is an intracellular organelle. The assembly is tethered to the cell envelope via a membrane-baseplate complex from which a long spring-like sheath extends into the cytosol (Fig. 5 + 6.). Fluorescent live-cell imaging revealed that these sheaths undergo dynamic assembly, contraction and disassembly cycles, suggesting that sheath contraction mediates the energy for protein translocation (Fig. 5) (Basler et al., 2012). Sheath contraction occurs within less than 2 ms and releases an energy equivalent estimated to correspond to the conversion of 1000 molecules of ATP to ADP (Vettiger et al., 2017; Wang et al., 2017). This mode of protein secretion allows to breach target cell envelope by means of physical force without the need of a designated target cell surface receptor (Brackmann et al., 2017). This allows the T6SS to translocate its substrates across a broad range of eukaryotic and fungal cell membranes, as well as Gram-negative cell envelopes (Alcoforado Diniz et al., 2015; Hachani et al., 2016; Trunk et al., 2018). This flexibility in target cell spectrum makes the T6SS a highly versatile and powerful tool for microbial competition and virulence.

1.4.2   The membrane complex

The T6SS membrane complex (MC) consists of TssJ, TssL and TssM forming an overall five-fold symmetric dome-shaped assembly spanning across the entire Gram-negative cell envelope (Fig. 6d) (Durand et al., 2015; Rapisarda et al., 2019; Yin et al., 2019). Based on sequence similarity, TssM and TssL have been identified in early studies of the T6SS as homologues of the T4SS proteins IcmF and DotU respectively (Cianfanelli et al., 2016; Das and Chaudhuri, 2003).

Fluorescence microscopy identified MC assembly as the first step in T6SS biogenesis starting with the association of a single subunit of the OM lipoprotein TssJ with the IM protein TssM, subsequently inserting into the cell envelope (Brunet et al., 2015; Durand et al., 2015; Gerc et al., 2015). While TssM proteins in some species such as *A. tumefaciens, P. aeruginosa, V. cholerae or E. tarda* may contain a Walker A and B motive (Ma et al., 2012), however ATP hydrolysis seems often not to be a prerequisite for MC assembly (Zheng and Leung, 2007). Importantly, the PG mesh size is too small to accommodate the entire 1.7 MDa MC requiring local cell wall hydrolysis. Recently, the housekeeping lytic transglycosylase MltE or the membrane bound L-alanyl-D-glutamic acid carboxypeptidase TagX were described to carry out this function in *E. coli* (Santin and Cascales, 2016) or *Acinetobacter baylyi* (Weber et al., 2016) respectively. However, most T6SS cluster do not encode their own PG hydrolases, thus future investigation will clarify which enzymes are responsible for this process in other T6SS positive organisms.

This TssJM complex was shown to then recruit the IM protein TssL as well as the T6SS assembly chaperon, TssA (Aschtgen et al., 2010a, 2010b, 2012; Durand et al., 2012, 2015; Ma et al., 2009b; Zheng and Leung, 2007; Zoued et al., 2016). The MC may be anchored to the cell wall via PG binding domains of TssL (Ma et al., 2009b) or by accessory proteins such as TagL or TagN (Aschtgen et al., 2010a, 2010b). Interestingly, PG anchoring of the MC does not seem to be essential for T6SS function. Several organisms, such a *V. cholerae* or *E. tarda* do not encode PG interacting domains on any of their T6SS core or accessory components (Aschtgen et al., 2010a).

It is likely that in addition to the sheath and the baseplate, the MC also undergoes a conformational change upon secretion. In a recent cryo-EM structure a TssM loop was found protruding into the central lumen of the channel, presumably representing the closed state of the MC (Rapisarda et al., 2019; Yin et al., 2019). Whether this TssM loop is simply pushed aside or indeed is displaced by a conformational change during contraction remains to be seen.

Figure 6: Architecture of the T6SS. (a) General overview of T6SS components are indicated with their names. (b) Additional density was found at the distal sheath (olive) end of *V. cholerae* and *E. coli*, most certainly corresponding to TssA2 (red, orange). (c) Close up view of the baseplate (red) containing the spike (purple) and MC connecting TssK trimers (pink). (d) Closeup view of the MC (blue/green/yellow). Structural data for the connection to baseplate (pink) is absent. *Image modified from: Nazarov et al. 2018 and Rapisarda et al, 2019*

1.4.3 The baseplate

The baseplate assembles subsequently through the interactions with TssA onto the MC (Brunet et al., 2015; Zoued et al., 2016). Overall, the T6SS baseplate shares close structural homology to the baseplate of T4 bacteriophage. Phage homologues of the corresponding T6SS components are given in brackets. The baseplate consists of a hub surrounded by six wedges (Nazarov et al., 2018; Nguyen et al., 2018; Park et al., 2018; Taylor et al., 2018). The hub is made up of three copies of VgrG (gp27 and gp5) and is further sharpened by the addition of a single PAAR protein (gp5.4) (Kanamaru et al., 2002; Pukatzki et al., 2007; Shneider et al., 2013). Importantly, VgrG and PAAR proteins serve as scaffolds for effectors forming a needle-like poisoned tip (Brooks et al., 2013; Hachani et al., 2011, 2014; Quentin et al., 2018). The base of the VgrG structure has a similar fold as a Hcp dimer. Therefore, VgrG trimer provides a platform onto which the Hcp tube can polymerize (Renault et al., 2018).

The T6SS baseplate wedge consists of TssE, TssF, TssG and TssK at 1:2:1:6 stoichiometry (Fig. 6a + c) (Cherrak et al., 2018; Nazarov et al., 2018). TssE (gp25) is a highly conserved phage homologue and found in all CISs (Leiman et al., 2009). Its function is to connect the sheath polymer to the baseplate through the handshake domain (Basler et al., 2012; Kudryashev et al., 2015; Nazarov et al., 2018). TssE also interacts with two molecules of TssF (gp6), which in turn bind to a single copy of TssG (gp7) (Cherrak et al., 2018; Nazarov et al., 2018; Park et al., 2018). These two proteins form the core wedge complex, which is also broadly conserved and thought to be critical for initiating the contraction of the system. In contrast to the T4 baseplate, the T6SSs lack a homologue of gp53, a LysM containing inter-wedge clamp that joints the wedges into the baseplate (Arisaka et al., 2016). While gp53 homologues are conserved among single use extracellular CISs, the T6SS displays a highly dynamic nature and needs to efficiently disassemble its components after contraction for a next round of assembly. TssG contains two loops for binding two timers of TssK via

hydrophobic interactions (Cherrak et al., 2018; Nguyen et al., 2017). Unlike other baseplate components, TssK does not share homology to T4 phage, but resembles closely the receptor binding protein (RPB) of non-contractile *Siphoviridae* (Nguyen et al., 2017, 2018). The major difference between these RPBs lies in their binding specificity. While phage RBPs evolved to bind surface structures of Gram-positive cell envelopes (e.g. lipoteichoic acids) (Sciara et al., 2010), the TssK binds the cytosolic domains of TssL and TssM, thereby docking the baseplate to the MC (Nguyen et al., 2017; Zoued et al., 2013). It should be noted that in contrast to the MC, baseplate, sheath and tube components follow a six-fold symmetry, resulting in a symmetry mismatch. How this problem is resolved remains to be elucidated.

Mechanism for inducing sheath contraction is conserved among all extracellular CISs (Kudryashev et al., 2015; Wang et al., 2017). Conformational changes in the baseplate upon surface receptor binding triggers progressive sheath contraction towards the distal end (Leiman and Shneider, 2012; Taylor et al., 2016). What triggers sheath contraction in T6SSs is currently not understood. Based on recent cryo-EM data, it has been postulated, that the interaction of TssK with the central wedge is flexible (Park et al., 2018). This might give hints towards which signal are being sensed by the baseplate. TssK may either respond to extracellular signals, which could be propagated through conformational changes in MC, or cytosolic signals, which might alter the confirmations of TssK-MC and/or TssK-baseplate wedge interactions, respectively. Chapter 3 of this thesis aims at elucidating the potential signal for initiation of T6SS contraction.

Of special interest to T6SS biogenesis are TssA proteins. As a common feature, these proteins possess a conserved N-terminal ImpA domain assembling into a compact anti-parallel α-helix, while in contrast displaying highly variable C-terminal regions, dividing members of TssA into separate classes with different functions and localization (Dix et al., 2018). While TssA1 proteins of *P. aeruginosa* and *B. cenocepacia* exclusively localize and stabilize the baseplate (Dix et al., 2018; Planamente et al., 2016), TssA2 of *E. coli* was shown to also prime and participate in T6SS assembly in each step (Zoued et al., 2016, 2017). Based on co-immunoprecipitations and bacterial two hybrid screens, TssA2 was shown to interact with the TssJ and TssM of the MC complex; TssE, TssK, VgrG of the baseplate; as well as with the Hcp tube and sheath component VipB (Zoued et al., 2016). While TssA2 is necessary for T6SS function, deletion of TssA1 does not abolish T6SS activity completely (Planamente et al., 2016; Zoued et al., 2016). TssA2 forms a homo-dodecameric assembly following 6-fold symmetry and consists of a central pore from which six highly flexible arms extend, overall resembling a snowflake structure (Zoued et al., 2016, 2017).

1.4.4   The contractile tail

After MC and baseplate assembly, the contractile tail is polymerized onto this scaffold (Fig. 5 + 6). Structural information is available from various organisms and is overall conserved (Clemens et al., 2015; Kudryashev et al., 2015; Salih et al., 2018a). The contractile T6SS tail displays helical C6 symmetry and consists of the tube protein, Hcp, being surrounded by a sheath (Fig. 7) (Wang et al., 2017). While Hcp shares homology to tube proteins of non-contractile phage λ gpV and gp19 of phage T4 respectively (Leiman et al., 2009; Mougous et al., 2006), T6SS sheaths differ significantly from their phage counterparts. In phage T4, sheath subunits are made up of a single gp18 molecules (Aksyuk et al., 2009), whereas T6SS sheath subunits consists of two molecules: VipA (TssB) and VipB (TssC) (Bönemann et al., 2009; Clemens et al., 2015; Kudryashev et al., 2015; Leiman et al., 2009). These fold into three domains: Domain 1 and 2 are structurally conserved among other CISs linking sheath subunits VipA to VipB through the handshake domain and mediate stabilizing interaction with the Hcp tube, while domain 3 is specific to T6SSs (Clemens et al., 2015; Kudryashev et al., 2015; Salih et al., 2018b; Wang et al., 2017). Importance of domain 3 will be outlined below. While isolating the contracted sheath from cells was relatively straight forward, it was for long time not possible to extract the system in its extended state due its inherent instability. Thus, a non-contractile sheath was generated by the insertion of 3 amino acids into the N-terminal linker region of VipA resulting in an aberrant linkage of sheath protomers (Brackmann et al., 2018). It was found that this sheath mutant contains in addition to several baseplate components also the Hcp tube, which was absent in contracted structures (Brackmann et al., 2018; Kudryashev et al., 2015; Nazarov et al., 2018; Wang et al., 2017). This revealed that the Hcp hexamer follows the helical symmetry of the surrounding extended sheath (Wang et al., 2017), a feature which was overlooked in previous crystal structures (Brunet et al., 2014; Mougous et al., 2006). Unlike tube proteins from phage of R-type pyocins, Hcp is highly instable in absence of sheath, which could explain why it is not possible to isolate an intact T6SS tube thus far and account for its rapid disassembly after secretion (Ge et al., 2015; Wang et al., 2017).
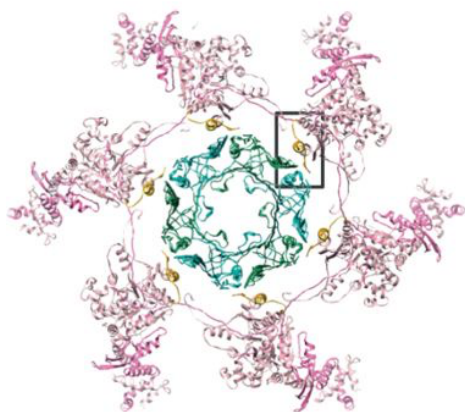
Figure 7: Atomic model of T6SS sheath and tube. Non-contractile *vipA3AA* sheath mutant was isolated from *V. cholerae* and resolved by cryo-EM to a resolution of 3.5 - 8 Å. Top view displays a single sheath ring (pink), surrounding the Hcp tube (green). The black rectangle marks the attachment helix of VipB (yellow) with the Hcp tube. *Modified from: Wang et al., 2017*

During assembly, sheath subunits polymerize in a meta-stable extended state together with Hcp subunits forming the cytosolic contractile tail (Basler et al., 2012; Zoued et al., 2016). While live-cell imaging suggested that polymerization proceeds in a linear fashion (Basler et al., 2012; Brunet et al., 2013; Gerc et al., 2015), its underlying mechanism was not clear. Work described in this thesis (Chapter 2) demonstrated that new sheath subunits are added exclusively at the distal end opposite the baseplate (Vettiger et al., 2017). Interestingly, TssA2 was also shown in enteroaggregative *E. coli* to be present at this site during sheath assembly (Fig 8.) and known to interact with Hcp and VipB (Zoued et al., 2016). Based on this, it is currently hypothesized that TssA2 mediates the sheath polymerization process by inserting new Hcp subunits through its central pore, while simultaneously adding new sheath subunits via its arms (Zoued et al., 2016, 2017). However, it should be mentioned that sheath polymerization does also take place in absence of a TssA2 homologue as exemplified by the H1-T6SS of *P. aeruginosa* (Planamente et al., 2016). Also Unlike other CISs, the T6SSs do not encode a homologue of a tape measure protein (gp29) (Leiman et al., 2010). Thus, the assembly of the contractile T6SS tail proceeds across the entire cell body until the opposite membrane to the baseplate is reached (Fig. 8 + 10) (Basler et al., 2012; Brunet et al., 2013; Gerc et al., 2015). Recently, a third TssA family protein, named TagA, was described to localize to the distal sheath end upon membrane contact resulting in termination of the polymerization process (Santin et al., 2018). Fluorescence microscopy revealed that T6SS may be stalled in this confirmation for several minutes prior to contraction (Santin et al., 2018; Szwedziak and Pilhofer, 2019). However, what then triggers sheath contraction still remains elusive. It should be noted, that TagA is absent from many T6SS clusters. Interestingly, these organisms also do not display any stalled assemblies (Brodmann et al., 2017; Ringel et al., 2017). Thus, polymerizing sheaths contract immediately upon membrane contact. In chapter 3 we aim at elucidating the mechanism inducing T6SS contraction. We provide evidence that the force generated by sheath polymerization against the cell envelope according to a Brownian ratchet (Peskin et al., 1993) could trigger the contraction of the T6SS.
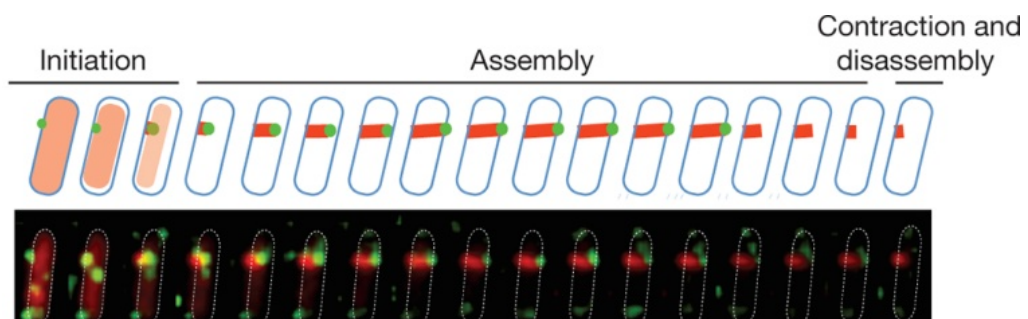
Figure 8: TssA2 mediates sheath polymerization in enteroaggregative *E. coli*. Different steps of T6SS biogenesis are indicated. VipA-mCherry (red) and TssA2-sfGFP (green) were followed by fluorescence microscopy at a acquisition frame rate of 30 s. *Modified from: Zoued et al., 2016*
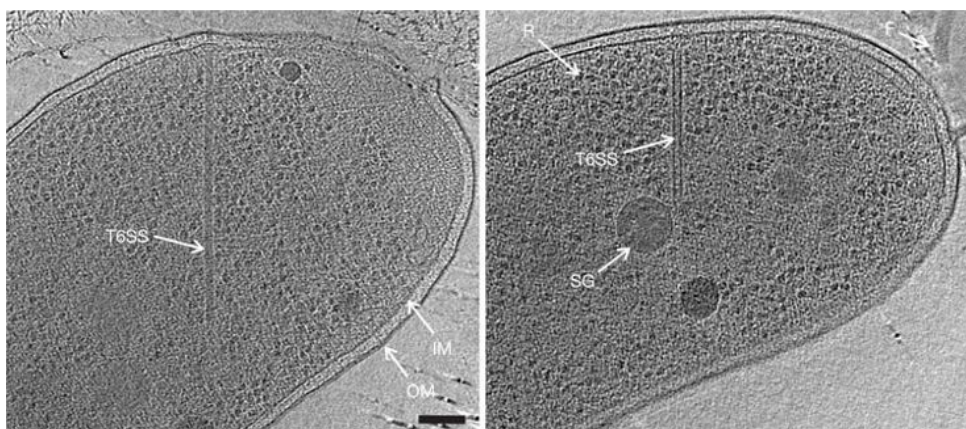
Figure 9: *In situ* structure of T6SS in *V. cholerae*. Extended filled (left) and hollow contracted (right) T6SS assemblies are shown. SG = storage granule, Scale bar = 100 nm. Image source: Basler et al., 2012

Comparison between the extended (narrow, filled) and contracted sheath (wide, empty) revealed the mechanism for T6SS substrate translocation according to the inverted phage tail model (Fig. 9 + 10) (Basler et al., 2012; Chang et al., 2017). Upon contraction, the sheath expands its diameter while reducing its length by approximately 50 % within less than 2 ms, thereby propelling the Hcp tube across the cell envelope at a rotational speed of 477'000 rpm assuming the contraction of a 1 μm long sheath (Wang et al., 2017). Thus, T6SSs may function rather as a powerful drill, than a harpoon, crossbow, syringe or similar commonly used analogies. Mechanism of sheath contraction is conserved among all CISs through inter-strand and inter-ring linkers, which propagate the contraction in a ring to ring fashion along the sheath polymer (Brackmann et al., 2018; Ge et al., 2015; Wang et al., 2017). Hcp interacts with sheath via α-helix of VipB as reported for R-type pyocins (Fig. 7) (Ge et al., 2015; Wang et al., 2017). Thus, sheath contraction abrogates these interactions, releasing the Hcp tube along the contracting wave, while still being held by yet uncontracted sheath subunits (Wang et al., 2017). This therefore results in a directed forward motion of the Hcp tube with associated spike and effectors.
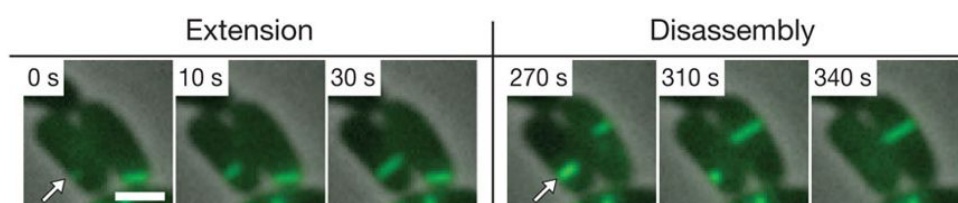
Figure 10: T6SS sheath dynamics in *V. cholerae* by fluorescence microscopy. Arrow marks a VipA-sfGFP labelled sheath undergoing extension and disassembly. Note the stalling time (4 min) in-between terminated extension (30 s) and first frame after contraction (270 s). Scale bar = 1 μm. *Modified from Basler et al. 2012*

1.4.5 Recycling and reuse of T6SS components

Importantly, sheath contraction also results in a conformational change of VipB unfolding its domain 3, which is buried in the extended state. Thus, now surface exposed domain 3 becomes accessible to the AAA+ ATPase ClpV (Pietrosiuk et al., 2011; Wang et al., 2017).

Hexameric ClpV pulls via N-terminus of VipB on contracted sheath subunits and restores under ATP consumption the high energy state conformation of sheath protomers (Fig 11) (Basler and Mekalanos, 2012; Bönemann et al., 2009; Douzi et al., 2018; Kapitein et al., 2013; Pietrosiuk et al., 2011). The exact mechanism of this process remains currently unknown. ClpV recycling of contracted sheath subunits also replenishes the pool for subsequent rounds of T6SS assemblies. Recently, it was shown that in *F*. *novicida* where a canonical ClpV protein is missing, the contracted sheath of T6SS is dissembled by the general purpose unfoldase ClpB (Brodmann et al., 2017). In some organisms an accessory protein, TagJ, might also be involved in sheath disassembly through interactions with VipA and ClpV (Förster et al., 2014; Lossi et al., 2012). However, the importance of this remains unknown, as deletion of this protein does not have any measurable phenotype under laboratory conditions. More generally, deletion of ClpV greatly reduces T6SS killing efficiency but does not completely abolish it, highlighting the importance of multiple firing events and the dynamics of the system (Basler et al., 2012; Zheng et al., 2011). This also clearly supports the current inverted phage tail mechanism for protein secretion over of a pumping mechanism for substrate translocation energized through ATP hydrolysis similar to the T3SSs or T4SSs as envisioned in early studies on the T6SS (Corbitt et al., 2018; Filloux et al., 2008; Mougous et al., 2006).
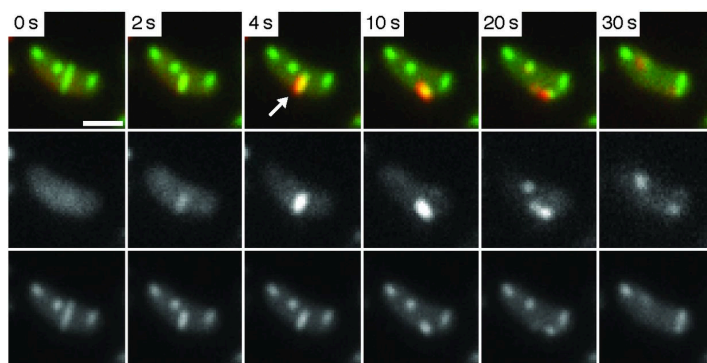
Figure 11: Dynamics of sheath disassembly by ClpV in *V. cholerae*. A merge of ClpV-mCherry2 and VipA-sfGFP channels are displayed at indicated time points (top row). In addition, mCherry2 (middle row) and sfGFP (bottom row) channels are displayed individually as grey scale images. Scale bar = 1 μm. *Modified form Basler and Mekalanos*

Rate of secretion depends on the number of assemblies per cell as well as their turnover time. Measuring ClpV dynamics by fluorescent microscopy results in a secretion rate of approximately 1 contraction min^{-1} $cell^{-1}$ (Basler and Mekalanos, 2012; Basler et al., 2013; Ringel et al., 2017). Thus, costs of the disassembly of the contraction of 1 μm long sheath (approx. 1500 VipA/B subuntis) could be as high as 45'000'000 molecules of ATP h^{-1} assuming same parameter as for ClpXP (Basler, 2015; Kenniston et al., 2003). In addition, over 42'000 Hcp molecules are secreted into the supernatant and would need to be replenished (Basler, 2015). In chapter 4, we provide evidence that secreted T6SS substrates can be reused by neighboring sister cells, which could lower the overall costs of an active T6SS.

1.4.6   T6SS regulation

Due to the associated costs, tight regulation of the T6SS activity is crucial. Thus, the majority of organisms represses their T6SS on the transcriptional and posttranscriptional level in absence of appropriated environmental cues (Bernard et al., 2010; Joshi et al., 2017; Leung et al., 2011). Transcriptional regulation is exemplified for *Vibrio cholerae*, which has been studied most extensively (Joshi et al., 2017). Pandemic *V. cholerae* strains (O1/O139) express their T6SS in their natural aquatic environmental niche in response to quorum sensing (QS) (Ishikawa et al., 2009; Watve et al., 2015; Zheng et al., 2010), growth on chitinous surfaces (Borgeaud et al., 2015; Lo Scrudato et al., 2014), catabolite repression (Ishikawa et al., 2009; Liang et al., 2007) and nucleoside scavenging (Watve et al., 2015). Interestingly, growth on chitinous surfaces also induces genes of the natural competence machinery (Meibom et al., 2005), which is often coregulated with T6SS (Borgeaud et al., 2015; Lo Scrudato et al., 2014; Ringel et al., 2017). Thus, a prevailing hypothesis states, that T6SS mediated prey cell killing is fostered for horizontal gene transfer (HGT) allowing for efficient niche adaptation of aggressor strains (Le Roux and Blokesch, 2018; Veening and Blokesch, 2017). Moreover, one of the major reasons why the T6SS was discovered only relatively late was that under standard laboratory conditions, these cues are absent. T6SS transcription is also regulated by the second messenger cyclic di-GMP through the response regulators TfoX and TfoY (Metzger et al., 2016, 2019). In addition, T6SS is influenced by several host factors, such as temperature, mucin and bile salts (Bachmann et al., 2015; Ishikawa et al., 2012; Townsley et al., 2016). This allows *V. cholerae* to displace members of the resident microbiota (Zhao et al., 2018). Furthermore, T6SS transcription is self-regulated by VasH in combination with RpoN (Dong and Mekalanos, 2012; Pukatzki et al., 2006). However once expressed, T6SS assembles from at seemingly random sites within bacterial cells firing at a continuous rate (Basler and Mekalanos, 2012; Basler et al., 2012).

In contrast to *V. cholerae*, fluorescent microscopy revealed more complex localization patterns for other organisms. For example, *P. aeruginosa* was shown to assemble its H1-T6SS in response to membrane damage (Basler et al., 2013; Ho et al., 2013; Wilton et al., 2016). This allows *P. aeruginosa* to retaliate T6SS attacks from competing species within few seconds upon inflicted damage at the same subcellular localization (Basler and Mekalanos, 2012; Basler et al., 2013). This is dependent on the threonine phosphorylation pathway (TPP) regulating the initiation and positioning of the T6SS on the posttranscriptional level in several organisms (Basler et al., 2013; Fritsch et al., 2013; Mougous et al., 2007; Ostrowski et al., 2018). The best studied TPP of *P. aeruginosa* is outlined here. TPP consist of a sensor module formed by cell envelope associated TagQ/R/S/T (Casabona et al., 2013; Mougous et al., 2007), the serine/threonine kinase PpkA (Hsu et al., 2009), and the phosphatase PppA (Basler et al., 2013). While PpkA and PppA are found also in other organisms, the TagQ/R/S/T pathway is unique to *P. aeruginosa*. The

lipoprotein TagQ is localized to the inner leaflet of the OM where it sequesters periplasmic TagR (Casabona et al., 2013). Membrane damage is supposed to alter the localization of TagR, allowing to bind the periplasmic domain of IM localized kinase PpkA (Hsu et al., 2009). This then triggers PpkA dimerization, autophosphorylation and subsequent phosphorylation of Fha, resulting in T6SS assembly (Hsu et al., 2009; Lin et al., 2014). T6SS firing ceases upon dephosphorylation of Fha by PppA (Basler et al., 2013; Ostrowski et al., 2018). T6SS activity was also shown to be repressed independent of TTP through TagF preventing phosphorylation of Fha (Lin et al., 2018). Even though *V. cholerae* lacks TPP, it still requires presence of Fha for T6SS activity suggesting that Fha is an important mediator for protein for assembly of other structural T6SS components (Zheng et al., 2011). However, it should be noted that currently the molecular mechanisms of posttranslational regulation of T6SSs remain poorly understood. Besides being essential for T6SS activity, the role of Fha is unknown. Moreover, signal sensing and transduction mechanism of the TagQ/R/S/T-PpkA pathway remain largely unclear. In particular, the role of TagST remains elusive.

In addition, anti-eukaryotic T6SSs of *F. novicida* or *B. thailandiesis* were shown be exclusively localized to bacterial poles (Brodmann et al., 2017; Lennings et al., 2019; Schwarz et al., 2014), a feature which was also observed for T4SS of *L. pneumophila* (Jeong et al., 2017). However, importance and mechanism of polar localization are currently not understood.

1.4.7 T6SS effectors

Here, T6SS effectors are defined as proteinaceous substrates eliciting a cytotoxic effect in target cells. The T6SS effector repertoire is highly diverse and targets both a wide range of eukaryotic and prokaryotic cells. Thus, effectors may be classified according their target specificity as anti-eukaryotic (e.g. actin cross-linkers) or anti-prokaryotic (e.g. PG hydrolases). Effectors targeting both eukaryotic and prokaryotic cells are referred to as trans-kingdom effectors (e.g. nucleases, lipases, pore-forming toxins, etc.) (Alcoforado Diniz et al., 2015). T6SS effectors may either be encoded as a dedicated domain of a structural T6SS component (effector and structural domain form one polypeptide), referred to as evolved effector (Shneider et al., 2013), or alternatively may be non-covalently fused to a structural component, then referred to as a cargo effector (Fig. 12) (Liang et al., 2015; Unterweger et al., 2015). Cargo effector are loaded on their designated secreted T6SS component (Hcp, VgrG, PAAR) through chaperon proteins (T6SS effector chaperones (TEC)) or adaptor proteins (T6SS adaptor protein (Tap)) (Cianfanelli et al., 2016; Liang et al., 2015; Unterweger et al., 2015). It should be noted that most effectors localize to the VgrG/PAAR spike, probably due to higher degree of spatial flexibility as compared to the tight lumen (40 Å in diameter) of the Hcp tube (Shneider et al., 2013; Silverman et al., 2013; Zheng and Leung, 2007). The central baseplate hub is formed by three copies of VgrG and a single copy

of PAAR, each of which may be associated with a designated effector (Shneider et al., 2013). Based on structural data, it was estimated the baseplate may accommodate up to 450 kDa space for effectors (Nazarov et al., 2018). Importantly, this inflicts that during one secretion event only few effector molecules will be translocated into target cells, thus making effector synergy crucial for attacking target cells simultaneously at multiple points thereby lowering chances of resistance development and ensuring efficient killing (LaCourse et al., 2018).

Figure 12: Multiple T6SS effector translocation model. Sites of possible effector domains are indicated with numbers. Evolved effectors are often found as part of C-terminal domains of VgrG **(1)** or PAAR **(2)** proteins. Cargo effectors bind non-covalently to secreted components of the T6SS (**3-6**). Spatial constraints of the Hcp tube restrict effector binding, thus most T6SS effectors localize to the spike. According to this model, a single T6SS secretion event results in translocation of only a handful of different effector molecules into target cells, illustrating the strong cytotoxic potency of these molecules. *Adapted from: Ho et al., 2014*
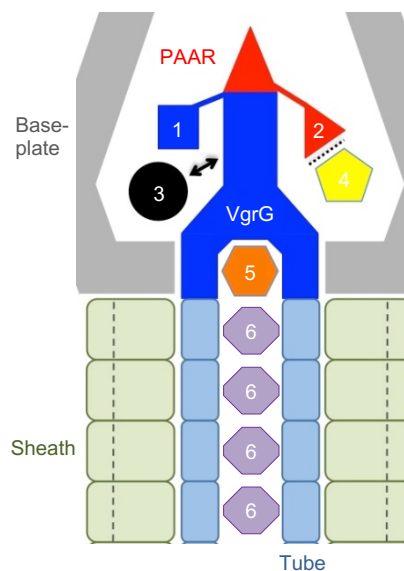
T6SS effectors can either be encoded within the main cluster or be scattered over the genome (Alcoforado Diniz et al., 2015; Dong et al., 2013; Ringel et al., 2017). Usually, effectors are encoded in a single operon together with their designated structural component and a designated immunity protein, which may be absent for anti-eukaryotic effectors (Alcoforado Diniz et al., 2015; Kirchberger et al., 2017; Russell et al., 2014b). Importantly, immunity proteins expression was shown to be independent of active T6SS transcription, thus mediating constant protection against sister cell directed T6SS attacks (Miyata et al., 2013). In case of cargo effector, the designated adaptor or chaperon protein is also encoded within the operon (Liang et al., 2015; Unterweger et al., 2015). Nomenclature of T6SS effectors is based either on their enzymatic activity (e.g. Tae: Type six amidase effector; TseL: Type six effector lipase) or if activity is unknown as Type Six Effector X (TseX), each denoted with a number dependent on the respective copy number of the effector class encoded on the genome. Accordingly, immunity proteins are named Type Six Immunity protein X (TsiX) (Hood et al., 2010; Shalom et al., 2007). Here, I outline a short overview of each effector class and provide examples. However, this summary is by no means complete as new effectors are discovered continuously.

Anti-eukaryotic effectors target commonly cytoskeletal elements such as actin and tubulin (Ma et al., 2009a; Pukatzki et al., 2007). In addition, also host cell singling cascades are targeted mediating immune evasion (Hachani et al., 2016). For example, *B. cenocepacia*

secretes TecA inactivating RhoA and Rac1 GTPases, thus inducing caspase-1 inflammasome activation (Aubert et al., 2016). On the other hand, *E. tarda* was shown to downregulate NLRP3 inflammasome through its T6SS effector EvpP, inhibiting ASC SPECK oligomerization (Chen et al., 2017). Furthermore, it was shown that VgrG-5 secreted by *Burkholderia* spp. induces membrane fusions leading to the characteristic multinucleated giant cells (MNGC) phenotype (Lennings et al., 2019; Schwarz et al., 2014).

Trans-kingdom effectors target conserved elements found in both bacteria and eukaryotic cells such as phospholipid membranes, nucleases or glycohydrolases (Jiang et al., 2014; Ma et al., 2014; Russell et al., 2013, 2014b; Whitney et al., 2015). Lipases are enzymes carrying a characteristic GXSXG or HXKXXXXD catalytic motif, disintegrating biological membranes and are a very commonly found T6SS effector class (Russell et al., 2013). Pore-forming toxins are characterized by their ability to insert firmly into biological membranes through their hydrophobic domains and subsequently oligomerize to form a stable pore. This results in uncoupling of the ion gradient and thus disrupts rapidly all biochemical processes within the cell (Peraro and van der Goot, 2016). The lipase TseL and the pore-forming toxin VasX of *V. cholerae* are typical trans-kingdom effectors, displaying both antimicrobial activity as well as mediating protection against *Dictyostelium* predation (Dong et al., 2013; Miyata et al., 2011, 2013). Nucleases commonly carry an HNH domain and are also often associated to Rhs domains. Such domains are found on Hcp of *E. coli* or VgrG of *Dickeya dadantii* (Koskiniemi et al., 2013; Ma et al., 2017). Glycohydrolases are less commonly found in the T6SS repertoire as compared to phospholipases or pore-forming toxins. However, PAAR fused Tse6 of *P. aeruginosa* cleaves the nicotinamide moiety of NAD(P)$^+$, inducing growth arrest in target cells (Quentin et al., 2018; Whitney et al., 2015).

Anti-prokaryotic T6SS effectors primarily consist of different PG hydrolases and amidases (Alcoforado Diniz et al., 2015; Russell et al., 2012). The Gram-negative cell wall consists of long β-1,4 linked N-acetyl-glucosamine and N-acetyl-muramic-acid glycan strands, which are crosslinked through either 3,4 or 3,3 peptide bonds (Typas et al., 2011). Accordingly, the sacculus may be targeted at distinct sites, e.g. the T6SS amidase Tae1 of *P. aeruginosa* catalyses the cleavage in the peptide crosslink between D-Glu and m-DAP at position 2 and 3 respectively (Chou et al., 2012; Hood et al., 2010; Russell et al., 2011), while the glycoside hydrolases Tge1 mediates the cleavage of the glycan backbone (Russell et al., 2011; Whitney et al., 2013). Interestingly, despite carrying several PG targeting effectors, Gram-positive bacteria have been so far reported to be completely immune to T6SS mediated antagonism (Schwarz et al., 2010). Whether this is due to the inability of T6SS to breach the thick cell wall of Gram-positive bacteria or due to a more complex resistance mechanism remains to be seen.

One emerging question in the T6SS field focused at elucidating into which subcellular compartments T6SS effectors are translocated during microbial competition, since different effectors target structures localized specifically to the periplasmic space (e.g. PG) or cytosol (DNA). In chapter 4, we demonstrate that T6SS effectors can be translocated directly into the cytosol of target cells. Interestingly, some antibacterial effectors, in particular VgrG3 and TseL of *V. cholerae* were shown to carry a non-canonical internal Tat secretion signal enabling these effectors to reach their target site (periplasmic space) independent of the compartment they have been deployed (Ho et al., 2017). Another interesting question centres on the underlying mechanism of distinct effectors inducing cell death as being bacteriostatic or bacteriolytic. Due to the strict contact dependence for T6SS killing one could predict that in order to maximize killing efficiency, rapid target cell lysis must be induced. In chapter 5, we provide evidence that indeed target cell lysis rate determines T6SS killing efficiency and further show that bacteriolytic effectors are overrepresented in the effector repertoire.

1.4.8 Importance of T6SS in bacterial communities

Examples for T6SS mediated bacterial competition can be found in aquatic, terrestrial or host-associated microbial communities (García-Bayona and Comstock, 2018; Ghoul and Mitri, 2016; Kostiuk et al., 2017). T6SS competition may be carried out at the intrastrain level, mediating self from non-self discrimination, or at the interspecies level, mediating antagonism against different bacterial species. On the intrastrain level, T6SS susceptibility is determined by the presence of different sets of effector/immunity proteins as shown for *V. fisheri* (Speare et al., 2018), *V. cholerae* (Borgeaud et al., 2015; Thomas et al., 2017; Unterweger et al., 2014), *B. fragilis* (Chatzidaki-Livanis et al., 2016; Hecht et al., 2016; Russell et al., 2014a; Wexler et al., 2016) or *Proteus mirabilis* (Alteri et al., 2013; Wenren et al., 2013) in both *in vitro* and *in vivo* studies. It was recently shown that different strains of bioluminescent *V. fisheri* compete with each other in a T6SS dependent manner for the colonization of the light organ of *Euprymna scolopes* squids (Fig. 13) (Speare et al., 2018). Moreover, different strains of *P. mirabilis* were known for a long time to form distinct intrastrain boundaries during swarming, resulting in Dienes lines at the strain interface
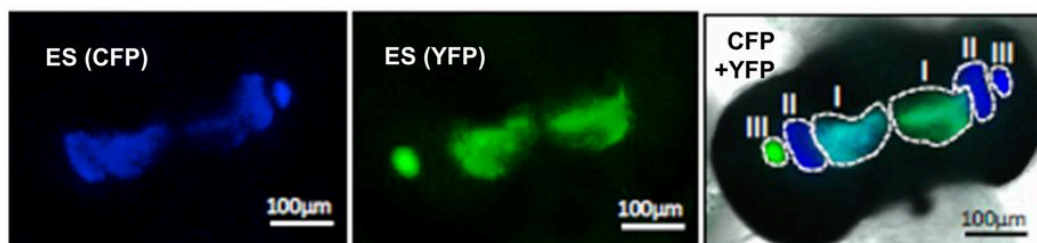
Figure 13: T6SS mediated competition between *V. fisheri* strains for the colonization of the light organ of *Euprymna scolopes*. Crypt (I-III) colonization after 44 h post inoculation of strains expressing different fluorophores is shown. Crypts III (left) and crypts II (both) and III (right) appear to be mono-colonized by either YFP or CFP expressing strains respectively, while for both crypts I competition is ongoing. *Modified from: Speare et al., 2018*

(Dienes, 1946). This process was later found to be a T6SS dependent competition phenotype of strains carrying distinct effector/immunity pairs (Alteri et al., 2013).

Importantly, several recent studies also described T6SS mediated competition in members of the human microbiota as well as pathogenic species. Commensal *B. fragilis* strains were shown to compete with each other as well as with *B. thetaiotaomicron* in a mouse model and through metagenomic analyses in the human gut (Chatzidaki-Livanis et al., 2016; Russell et al., 2014a; Wexler et al., 2016). A first step towards functionalizing T6SS was made recently by demonstrating that symbiotic nontoxigenic *B. fragilis* strains were able to outcompete toxigenic strains in a mouse model (Hecht et al., 2016). Further it was shown that *V. cholerae*, *Shigella sonnei* and *S. enterica* utilizes their T6SS to displace members of the host microbiota, which is thought to be critical for niche colonization of the gut epithelium and driving virulence (Anderson et al., 2017; Sana et al., 2016; Zhao et al., 2018).

In vitro competition experiments are primarily carried out to compare killing efficiency of different T6SS mutants in order to comprehend the molecular mechanism of type six secretion and its effects on bacterial communities under controlled environmental conditions. Commonly used T6SS model organisms such as *V. cholerae* or *A. baylyi*, reliably reduce prey cell (e.g. *E. coli*) survival by 99.99 % after 3h of co-incubation as compared to isogenic T6SS negative mutants (Basler et al., 2012, 2013; Hachani et al., 2013; Ringel et al., 2017). However, it should be noted that due to its contact-dependency and short range, the overall T6SS killing efficiency depends strongly on the degree of cell mixing as well as starting inoculum concentrations (Borenstein et al., 2015). *In silico* competition modelling in combination with experimental data has indeed previously shown, that T6SS killing leads to phase separation between competing strains (McNally et al., 2017), a process similar to oil droplet formation in water. Since killing will exclusively occur at the inter-strain boundary, prey cells may still display net growth in case of a lower surface killing rate as compared to colony growth rate (Fig. 14) (Borenstein et al., 2015; Wong et al., 2016). This
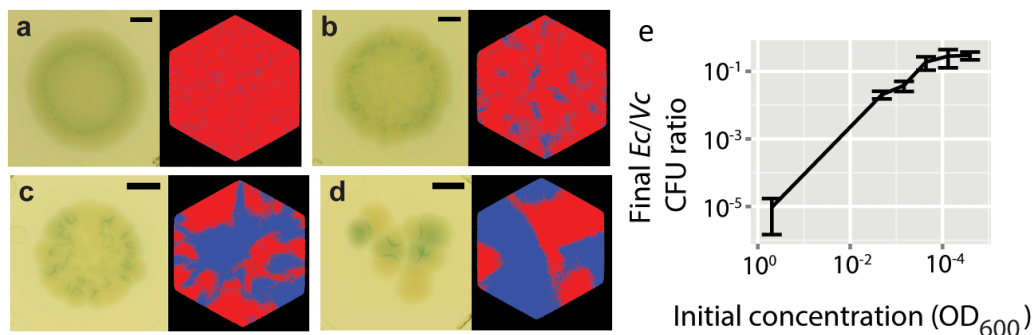
Figure 14: T6SS killing efficiency depends on the starting cell density. Equal amounts of T6SS positive *V. cholerae* cells were competed against susceptible *lacZ+ E. coli* (appearing blueish) overnight on agar plates containing X-Gal starting from different cell densities (**a-d** = High-low). Corresponding computational simulation are shown on the right (Blue = E. coli; Red = *V. cholerae*). **(e)** Final ratio after competition between *E. coli* prey cells and *V. cholerae* aggressors as a function of inoculum concentration. *Modified from: Borenstein et al., 2015*

process depends further on target cell lysis rate as outlined in chapter 5. T6SS mediated phase separation was also shown to promote the evolution of public goods, since a producer will be likely surrounded by its kin cells (McNally et al., 2017). While, this could result in cheaters, not contributing to active T6SS expression and public good production, it was recently shown that immunity protein expression in *B. thailandensis* was coupled to QS. Thus, cheaters not engaging in QS become susceptible to T6SS attacks from their sister cells and are therefore efficiently eliminated (Majerczyk et al., 2016). However, this mechanism for cheater prevention is not conserved, as *V. cholerae* strain express their immunity constantly even in absence of active type six secretion (Miyata et al., 2013).

1.4.9 T6SS model organisms

I have used three distinct T6SS model organism throughout my PhD, namely *V. cholerae* 2740-80, *A. baylyi* ADP1 and *P. aeruginosa* PAO1. Each of these organisms offers its own unique strengths to study different aspects of the T6SS.

Vibrio spp. are a broad genus of facultative anaerobic Gram-negative marine and aquatic bacteria encoding their genome on two chromosomes (Baker-Austin et al., 2018). *V. cholerae*, the etiological agent of cholera, is the most prominent member of this family. Infections with *V. cholerae* occur via the fecal-oral route after exposure to contaminated brackish water in combination with insufficient hygiene precautions (Baker-Austin et al., 2018). Critical virulence factors for *V. cholerae* are cholera toxin (CT), which was acquired through HGT from phage CTX , utilizing toxin coregulated pili (TCP) as its surface receptor for infection (Waldor and Mekalanos, 1996). CT is a heterohexameric AB_5-toxin secreted by T2SS, consisting of five B subunit oligomerizing with one A subunit (Hirst et al., 1984; Streatfield et al., 1992; Tauschek et al., 2002). B subunits mediate translocation of the A subunit across intestinal epithelial cell membranes resulting in ADP-ribosylation of a G-protein (Bobak et al., 1990; Gill and Meren, 1978). This then leads to elevated cAMP levels inducing the expression of CFTR receptor resulting in high levels of ion efflux into the intestinal lumen provoking watery diarrhea, the typical symptom of cholerae disease (Baker-Austin et al., 2018; Wolf et al., 1998). Despite encoding anti-eukaryotic and trans-kingdom effectors, in pandemic *V. cholerae* strains, T6SS is thought to contribute indirectly to virulence in the host by competing with members of the resident microbiota (Fu et al., 2018; Zheng et al., 2018), while in the environment mediating intrastrain competition with other isolates growing on planktonic crustaceans and protection against amoeba predation (Le Roux and Blokesch, 2018; Metzger et al., 2016, 2019; Unterweger et al., 2014). However, in a zebrafish infection model, it was recently shown that anti-eukaryotic effector, VgrG1 containing an actin crosslinking domain, also contributes to displacement of the microbiota by enhancing host intestinal movements independent of anti-microbial T6SS activity (Logan et al., 2018). Different *V. cholerae* strains were found to express highly variable

effector/immunity proteins, indicative of strong intrastrain competition and HGT in nature (Borgeaud et al., 2015; Kirchberger et al., 2017; Unterweger et al., 2014). While pandemic *V. cholerae* strains repress their T6SS under laboratory conditions, environmental strain rarely associated with disease, express a highly active secretion system characterized by a high number of assemblies per cell making *V. cholerae* a particularly useful for fluorescent microscopy studies (Basler et al., 2012; Pukatzki et al., 2006).

A. baylyi is an aerobic non-flagellated Gram-negative soil bacterium closely related to the emerging opportunistic pathogen *Acinetobacter baumanii* (Juni and Janik, 1969; Lee et al., 2017). *A. baylyi* encodes a single constitutively active anti-prokaryotic T6SS cluster and is similarly to *V. cholerae* naturally competent (de Berardinis et al., 2008; Ringel et al., 2017; Shneider et al., 2013; Weber et al., 2013, 2016). Research in our lab has shown that T6SS mediated killing can be fostered for HGT if target cells are lysed efficiently (Ringel et al., 2017). While *A. baylyi* displays high T6SS *in vitro*, *A. baumanii* strains were found to repress Hcp secretion on the posttranslational level (Repizo et al., 2015; Weber et al., 2013, 2016). However, the mechanism for this repression is currently not understood. Another interesting aspect of the *A. baylyi* T6SS is the lack of the lipoprotein TssJ, which is normally an integral part of the membrane complex. In contrast to *V. cholerae*, *A. baylyi* commonly only assembles a single T6SS per cell at a time, however its turnover is much more dynamic, since assembled sheaths contract right away upon membrane contact of the distal end (Ringel et al., 2017). Another critical aspect of *A. baylyi* is the fact that one can delete all of its known effectors, without losing secretion activity, thus enabling the construction of single effector strains (Ringel et al., 2017).

P. aeruginosa is a generalist environmental Gram-negative bacterium found in soil, water and may also be associated to the human microbiota (Griffith et al., 1989; Moradali et al., 2017). Due to its ability to proliferate in such diverse habitats, *P. aeruginosa* encodes a series of soluble and contact-dependent anti eu- and prokaryotic virulence factors. Most famous examples are the soluble antibiotic pyocyanin (Baron and Rowe, 1981), the broad range of R-, F- and S-type pyocins (Scholl, 2017) as well as T3SS and T6SSs (Moscoso et al., 2011). *P. aeruginosa* encodes three T6SS clusters (H1-H3) which are regulated through the Two-Component Signal Transduction systems (TCST) GacS/GacA (H1) (Brencic and Lory, 2009; Moscoso et al., 2011) as well as QS (H2-H3) (Lesic et al., 2009). Activation of the GacS/GacA signalling cascade results in transcription of the small RNAs (sRNA) rsmY/Z sequestering RsmA, thereby abolishing the transcriptional repression of the H1-T6SS clusters (Brencic and Lory, 2009; Chen et al., 2015; Moscoso et al., 2011). The GacS/GacA signaling cascade can be artificially activated by the deletion of the retS (Goodman et al., 2004). Thus, in order to study the H1-T6SS most experiments are carried out in a *retS* deletion mutant. In addition to the transcriptional regulation, *P. aeruginosa* also regulates the assembly of its H1-T6SS on the posttranslational level through the TPP (Basler et al.,

2013; Casabona et al., 2013). Thus, in contrast to *V. cholerae* and *A. baylyi*, *P. aeruginosa* utilizes its H1-T6SS in a defensive way, only triggering assemblies in response to membrane damage. This behavior is thought to have major biological implications, as it allows other organisms to co-exist with *P. aeruginosa* as long as they do not impose any harm (Basler et al., 2013). The T6SS attack retaliation was also shown to confer immunity to T4SS mediated HGT (Ho et al., 2013).

1.5   Aims of this thesis

Despite only being discovered in 2006, tremendous advances were made elucidating T6SS mode of action and regulation over the past 13 years. Moreover, T6SS strarts to be recognized as one of the major players for microbial antagonism in natural microbial communities, including the human microbiota. Cryo-EM revealed the detailed architecture of isolated subassemblies as well as the whole T6SS *in situ*. In addition, fluorescence live-cell microscopy uncovered the remarkable dynamics of T6SS biogenesis. However, T6SS assembly, initiation of sheath contraction, substrate translocation as well as T6SS importance for competition in microbial communities remain still poorly understood. Fluorescent microscopy approaches to observe the T6SS inside bacterial cells face several challenges such as: (i) the spatial and temporal resolution limit of optical microscopy, (ii) the inability to efficiently label secreted components of the machinery, (iii) the weak signals due to low protein abundance and rapid photobleaching, (iv) the difficulty to perform long-term co-incubation experiments as well as (v) the inability to precisely control spatial and chemical environment during the experiment.

This doctoral thesis aims to overcome these challenges and limitations to facilitate novel insights into dynamics of the T6SSs of *V. cholerae, P. aeruginosa* and *A. baylyi*. We specifically aim at uncovering aspects of sheath assembly and initiation of T6SS contraction in *V. cholerae,* since sheath dynamics can be reliably visualized in these cells. In particular, we aim to elucidate at which site the sheath polymer undergoes polymerization. Is it at the baseplate or the distal end of the sheath? To address this question, we will use *V. cholerae* grown in the presence of cell wall inhibitors, resulting in formation of large spheroplasts, which assemble longer sheaths than rod shaped cells. This will allow us to use photobleaching techniques to study sheath assembly. To get insights into mechanisms of sheath contraction initiation, microfluidic devices allowing rapid exchange of growth medium will be used to test if increased pressure due to hyperosmotic shocks could trigger sheath contractions in *V. cholerae*. Furthermore, we aim at elucidating the fate of translocated T6SS components with the focus on establishing to what subcellular compartment of diderm bacteria effectors and structural T6SS components are translocated. To answer this question, we will test if the lack of secreted structural components required for sheath assembly (tip and tube) can be complemented by translocation of these proteins

from neighboring cells. Since, T6SS biogenesis starts in the cell cytosol, this will serve as an indirect readout for cytosolic delivery of T6SS substrates. Last, we aim at further understanding T6SS specific strategies for prey cell inhibition during microbial competition. In particular, we will investigate if prey cell lysis rate limits T6SS-mediated killing. We plan to use variants of *A. baylyi* encoding single lytic or non-lytic effectors and compare outcomes of microbial competitions *in silico* as well as *in vitro* in custom made microfluidic devices that allow prolonged observation times and single cell analyses.

1.6 References

Aksyuk, A.A., Leiman, P.G., Kurochkina, L.P., Shneider, M.M., Kostyuchenko, V.A., Mesyanzhinov, V.V., and Rossmann, M.G. (2009). The tail sheath structure of bacteriophage T4: a molecular machine for infecting bacteria. EMBO J. *28*, 821–829.

Alcoforado Diniz, J., Liu, Y., and Coulthurst, S.J. (2015). Molecular weaponry: diverse effectors delivered by the Type VI secretion system. Cell. Microbiol. *17*, 1742–1751.

Alteri, C.J., Himpsl, S.D., Pickens, S.R., Lindner, J.R., Zora, J.S., Miller, J.E., Arno, P.D., Straight, S.W., and Mobley, H.L.T. (2013). Multicellular Bacteria Deploy the Type VI Secretion System to Preemptively Strike Neighboring Cells. PLoS Pathog. *9*.

Alvarez-Martinez, C.E., and Christie, P.J. (2009). Biological diversity of prokaryotic type IV secretion systems. Microbiol. Mol. Biol. Rev. MMBR *73*, 775–808.

Aly, K.A., and Baron, C. (2007). The VirB5 protein localizes to the T-pilus tips in Agrobacterium tumefaciens. Microbiol. Read. Engl. *153*, 3766–3775.

Anderson, M.C., Vonaesch, P., Saffarian, A., Marteyn, B.S., and Sansonetti, P.J. (2017). Shigella sonnei Encodes a Functional T6SS Used for Interbacterial Competition and Niche Occupancy. Cell Host Microbe *21*, 769-776.e3.

Aoki, S.K., Pamma, R., Hernday, A.D., Bickham, J.E., Braaten, B.A., and Low, D.A. (2005). Contact-dependent inhibition of growth in Escherichia coli. Science *309*, 1245–1248.

Aoki, S.K., Malinverni, J.C., Jacoby, K., Thomas, B., Pamma, R., Trinh, B.N., Remers, S., Webb, J., Braaten, B.A., Silhavy, T.J., et al. (2008). Contact-dependent growth inhibition requires the essential outer membrane protein BamA (YaeT) as the receptor and the inner membrane transport protein AcrB. Mol. Microbiol. *70*, 323–340.

Aoki, S.K., Poole, S.J., Hayes, C.S., and Low, D.A. (2011). Toxin on a stick. Virulence *2*, 356–359.

Arisaka, F., Yap, M.L., Kanamaru, S., and Rossmann, M.G. (2016). Molecular assembly and structure of the bacteriophage T4 tail. Biophys. Rev. *8*, 385–396.

Aschtgen, M.-S., Thomas, M.S., and Cascales, E. (2010a). Anchoring the type VI secretion system to the peptidoglycan: TssL, TagL, TagP... what else? Virulence *1*, 535–540.

Aschtgen, M.-S., Gavioli, M., Dessen, A., Lloubès, R., and Cascales, E. (2010b). The SciZ protein anchors the enteroaggregative Escherichia coli Type VI secretion system to the cell wall. Mol. Microbiol. *75*, 886–899.

Aschtgen, M.-S., Zoued, A., Lloubès, R., Journet, L., and Cascales, E. (2012). The C-tail anchored TssL subunit, an essential protein of the enteroaggregative Escherichia coli Sci-1 Type VI secretion system, is inserted by YidC. MicrobiologyOpen *1*, 71–82.

Aubert, D.F., Xu, H., Yang, J., Shi, X., Gao, W., Li, L., Bisaro, F., Chen, S., Valvano, M.A., and Shao, F. (2016). A Burkholderia Type VI Effector Deamidates Rho GTPases to Activate the Pyrin Inflammasome and Trigger Inflammation. Cell Host Microbe *19*, 664–674.

Aymerich, T., Garriga, M., and Monfort, J. (2011). 12 - Applications of protective cultures, bacteriocins and bacteriophages in fermented meat products. In Protective Cultures, Antimicrobial Metabolites and Bacteriophages for Food and Beverage Biopreservation, C. Lacroix, ed. (Woodhead Publishing), pp. 297–323.

Babic, A., Lindner, A.B., Vulic, M., Stewart, E.J., and Radman, M. (2008). Direct visualization of horizontal gene transfer. Science *319*, 1533–1536.

Bachmann, V., Kostiuk, B., Unterweger, D., Diaz-Satizabal, L., Ogg, S., and Pukatzki, S. (2015). Bile Salts Modulate the Mucin-Activated Type VI Secretion System of Pandemic Vibrio cholerae. PLoS Negl. Trop. Dis. *9*, e0004031.

Backert, S., Tegtmeyer, N., and Fischer, W. (2015). Composition, structure and function of the Helicobacter pylori cag pathogenicity island encoded type IV secretion system. Future Microbiol. *10*, 955–965.

Baker-Austin, C., Oliver, J.D., Alam, M., Ali, A., Waldor, M.K., Qadri, F., and Martinez-Urtaza, J. (2018). Vibrio spp. infections. Nat. Rev. Dis. Primer *4*, 8.

Baron, S.S., and Rowe, J.J. (1981). Antibiotic action of pyocyanin. Antimicrob. Agents Chemother. *20*, 814–820.

Barret, M., Egan, F., and O'Gara, F. (2013). Distribution and diversity of bacterial secretion systems across metagenomic datasets. Environ. Microbiol. Rep. *5*, 117–126.

Basler, M. (2015). Type VI secretion system: secretion by a contractile nanomachine. Phil Trans R Soc B *370*, 20150021.

Basler, M., and Mekalanos, J.J. (2012). Type 6 secretion dynamics within and between bacterial cells. Science *337*, 815.

Basler, M., Pilhofer, M., Henderson, G.P., Jensen, G.J., and Mekalanos, J.J. (2012). Type VI secretion requires a dynamic contractile phage tail-like structure. Nature *483*, 182–186.

Basler, M., Ho, B.T., and Mekalanos, J.J. (2013). Tit-for-tat: Type VI secretion system counterattack during bacterial cell-cell interactions. Cell *152*, 884–894.

Beckham, K.S.H., Ciccarelli, L., Bunduc, C.M., Mertens, H.D.T., Ummels, R., Lugmayr, W., Mayr, J., Rettel, M., Savitski, M.M., Svergun, D.I., et al. (2017). Structure of the mycobacterial ESX-5 type VII secretion system membrane complex by single-particle analysis. Nat. Microbiol. *2*, 17047.

de Berardinis, V., Vallenet, D., Castelli, V., Besnard, M., Pinet, A., Cruaud, C., Samair, S., Lechaplais, C., Gyapay, G., Richez, C., et al. (2008). A complete collection of single-gene deletion mutants of Acinetobacter baylyi ADP1. Mol. Syst. Biol. *4*, 174.

Bernard, C.S., Brunet, Y.R., Gueguen, E., and Cascales, E. (2010). Nooks and Crannies in Type VI Secretion Regulation. J. Bacteriol. *192*, 3850–3860.

Bingle, L.E., Bailey, C.M., and Pallen, M.J. (2008). Type VI secretion: a beginner's guide. Curr. Opin. Microbiol. *11*, 3–8.

Bitter, W., Houben, E.N.G., Bottai, D., Brodin, P., Brown, E.J., Cox, J.S., Derbyshire, K., Fortune, S.M., Gao, L.-Y., Liu, J., et al. (2009). Systematic Genetic Nomenclature for Type VII Secretion Systems. PLOS Pathog. *5*, e1000507.

Bladergroen, M.R., Badelt, K., and Spaink, H.P. (2003). Infection-blocking genes of a symbiotic Rhizobium leguminosarum strain that are involved in temperature-dependent protein secretion. Mol. Plant-Microbe Interact. MPMI *16*, 53–64.

Bobak, D.A., Bliziotes, M.M., Noda, M., Tsai, S.C., Adamik, R., and Moss, J. (1990). Mechanism of activation of cholera toxin by ADP-ribosylation factor (ARF): both low- and high-affinity interactions of ARF with guanine nucleotides promote toxin activation. Biochemistry *29*, 855–861.

Böck, D., Medeiros, J.M., Tsao, H.-F., Penz, T., Weiss, G.L., Aistleitner, K., Horn, M., and Pilhofer, M. (2017). In situ architecture, function, and evolution of a contractile injection system. Science *357*, 713–717.

Bönemann, G., Pietrosiuk, A., Diemand, A., Zentgraf, H., and Mogk, A. (2009). Remodelling of VipA/VipB tubules by ClpV-mediated threading is crucial for type VI protein secretion. EMBO J. *28*, 315–325.

Borenstein, D.B., Ringel, P., Basler, M., and Wingreen, N.S. (2015). Established Microbial Colonies Can Survive Type VI Secretion Assault. PLoS Comput Biol *11*, e1004520.

Borgeaud, S., Metzger, L.C., Scrignari, T., and Blokesch, M. (2015). The type VI secretion system of Vibrio cholerae fosters horizontal gene transfer. Science *347*, 63–67.

Boyer, F., Fichant, G., Berthod, J., Vandenbrouck, Y., and Attree, I. (2009). Dissecting the bacterial type VI secretion system by a genome wide in silico analysis: what can be learned from available microbial genomic resources? BMC Genomics *10*, 104.

Brackmann, M., Nazarov, S., Wang, J., and Basler, M. (2017). Using Force to Punch Holes: Mechanics of Contractile Nanomachines. Trends Cell Biol. *27*, 623–632.

Brackmann, M., Wang, J., and Basler, M. (2018). Type VI secretion system sheath inter-subunit interactions modulate its contraction. EMBO Rep. *19*, 225–233.

Brencic, A., and Lory, S. (2009). Determination of the regulon and identification of novel mRNA targets of Pseudomonas aeruginosa RsmA. Mol. Microbiol. *72*, 612–632.

Breukink, E., and de Kruijff, B. (1999). The lantibiotic nisin, a special case or not? Biochim. Biophys. Acta *1462*, 223–234.

Brodmann, M., Dreier, R.F., Broz, P., and Basler, M. (2017). Francisella requires dynamic type VI secretion system and ClpB to deliver effectors for phagosomal escape. Nat. Commun. *8*, 15853.

Brooks, T.M., Unterweger, D., Bachmann, V., Kostiuk, B., and Pukatzki, S. (2013). Lytic Activity of the Vibrio cholerae Type VI Secretion Toxin VgrG-3 Is Inhibited by the Antitoxin TsaB. J. Biol. Chem. *288*, 7618–7625.

de Bruin, O.M., Ludu, J.S., and Nano, F.E. (2007). The Francisella pathogenicity island protein IglA localizes to the bacterial cytoplasm and is needed for intracellular growth. BMC Microbiol. *7*, 1.

Brunet, Y.R., Espinosa, L., Harchouni, S., Mignot, T., and Cascales, E. (2013). Imaging type VI secretion-mediated bacterial killing. Cell Rep. *3*, 36–41.

Brunet, Y.R., Hénin, J., Celia, H., and Cascales, E. (2014). Type VI secretion and bacteriophage tail tubes share a common assembly pathway. EMBO Rep. *15*, 315–321.

Brunet, Y.R., Zoued, A., Boyer, F., Douzi, B., and Cascales, E. (2015). The Type VI Secretion TssEFGK-VgrG Phage-Like Baseplate Is

Recruited to the TssJLM Membrane Complex via Multiple Contacts and Serves As Assembly Platform for Tail Tube/Sheath Polymerization. PLOS Genet. *11*, e1005545.

Burstein, D., Amaro, F., Zusman, T., Lifshitz, Z., Cohen, O., Gilbert, J.A., Pupko, T., Shuman, H.A., and Segal, G. (2016). Genomic analysis of 38 *Legionella* species identifies large and diverse effector repertoires. Nat. Genet. *48*, 167–175.

Buth, S.A., Shneider, M.M., Scholl, D., and Leiman, P.G. (2018). Structure and Analysis of R1 and R2 Pyocin Receptor-Binding Fibers. Viruses *10*, 427.

Cao, Z., Casabona, M.G., Kneuper, H., Chalmers, J.D., and Palmer, T. (2016). The type VII secretion system of Staphylococcus aureus secretes a nuclease toxin that targets competitor bacteria. Nat. Microbiol. *2*, 16183.

Casabona, M.G., Silverman, J.M., Sall, K.M., Boyer, F., Couté, Y., Poirel, J., Grunwald, D., Mougous, J.D., Elsen, S., and Attree, I. (2013). An ABC transporter and an outer membrane lipoprotein participate in posttranslational activation of type VI secretion in Pseudomonas aeruginosa. Environ. Microbiol. *15*, 471–486.

Cascales, E., and Christie, P.J. (2003). The versatile bacterial type IV secretion systems. Nat. Rev. Microbiol. *1*, 137–149.

Cascales, E., Buchanan, S.K., Duché, D., Kleanthous, C., Lloubès, R., Postle, K., Riley, M., Slatin, S., and Cavard, D. (2007). Colicin biology. Microbiol. Mol. Biol. Rev. MMBR *71*, 158–229.

Chang, Y., Rettberg, L.A., Ortega, D.R., and Jensen, G.J. (2017). In vivo structures of an intact type VI secretion system revealed by electron cryotomography. EMBO Rep. *18*, 1090–1099.

Chatzidaki-Livanis, M., Geva-Zatorsky, N., and Comstock, L.E. (2016). Bacteroides fragilis type VI secretion systems use novel effector and immunity proteins to antagonize human gut Bacteroidales species. Proc. Natl. Acad. Sci. *113*, 3627–3632.

Chen, H., Yang, D., Han, F., Tan, J., Zhang, L., Xiao, J., Zhang, Y., and Liu, Q. (2017). The Bacterial T6SS Effector EvpP Prevents NLRP3 Inflammasome Activation by Inhibiting the Ca2+-Dependent MAPK-Jnk Pathway. Cell Host Microbe *21*, 47–58.

Chen, L., Zou, Y., She, P., and Wu, Y. (2015). Composition, function, and regulation of T6SS in Pseudomonas aeruginosa. Microbiol. Res. *172*, 19–25.

Chen, W.-J., Kuo, T.-Y., Hsieh, F.-C., Chen, P.-Y., Wang, C.-S., Shih, Y.-L., Lai, Y.-M., Liu, J.-R., Yang, Y.-L., and Shih, M.-C. (2016). Involvement of type VI secretion system in secretion of iron chelator pyoverdine in *Pseudomonas taiwanensis*. Sci. Rep. *6*, 32950.

Cherrak, Y., Rapisarda, C., Pellarin, R., Bouvier, G., Bardiaux, B., Allain, F., Malosse, C., Rey, M., Chamot-Rooke, J., Cascales, E., et al. (2018). Biogenesis and structure of a type VI secretion baseplate. Nat. Microbiol. 1.

Chou, S., Bui, N.K., Russell, A.B., Lexa, K.W., Gardiner, T.E., LeRoux, M., Vollmer, W., and Mougous, J.D. (2012). Structure of a peptidoglycan amidase effector targeted to Gram-negative bacteria by the type VI secretion system. Cell Rep. *1*, 656–664.

Christie, P.J. (2016). The Mosaic Type IV Secretion Systems. EcoSal Plus *7*.

Cianfanelli, F.R., Monlezun, L., and Coulthurst, S.J. (2016). Aim, Load, Fire: The Type VI Secretion System, a Bacterial Nanoweapon. Trends Microbiol. *24*, 51–62.

Clemens, D.L., Ge, P., Lee, B.-Y., Horwitz, M.A., and Zhou, Z.H. (2015). Atomic Structure and Mutagenesis of T6SS Reveals Interlaced Array Essential to Function. Cell *160*, 940–951.

Corbitt, J., Yeo, J.S., Davis, C.I., LeRoux, M., and Wiggins, P.A. (2018). T6SS dynamics reveals a novel secretion mechanism in Pseudomonas aeruginosa. J. Bacteriol.

Costa, T.R.D., Felisberto-Rodrigues, C., Meir, A., Prevost, M.S., Redzej, A., Trokter, M., and Waksman, G. (2015). Secretion systems in Gram-negative bacteria: structural and mechanistic insights. Nat. Rev. Microbiol. *13*, 343–359.

Costa, T.R.D., Ilangovan, A., Ukleja, M., Redzej, A., Santini, J.M., Smith, T.K., Egelman, E.H., and Waksman, G. (2016). Structure of the Bacterial Sex F Pilus Reveals an Assembly of a Stoichiometric Protein-Phospholipid Complex. Cell *166*, 1436-1444.e10.

Covacci, A., and Rappuoli, R. (1993). Pertussis toxin export requires accessory genes located downstream from the pertussis toxin operon. Mol. Microbiol. *8*, 429–434.

Das, S., and Chaudhuri, K. (2003). Identification of a unique IAHP (IcmF associated homologous proteins) cluster in Vibrio cholerae and other proteobacteria through in silico analysis. In Silico Biol. *3*, 287–300.

Das, S., Chakrabortty, A., Banerjee, R., Roychoudhury, S., and Chaudhuri, K. (2000). Comparison of global transcription

responses allows identification of Vibrio cholerae genes differentially expressed following infection. FEMS Microbiol. Lett. *190*, 87–91.

Deng, W., Marshall, N.C., Rowland, J.L., McCoy, J.M., Worrall, L.J., Santos, A.S., Strynadka, N.C.J., and Finlay, B.B. (2017). Assembly, structure, function and regulation of type III secretion systems. Nat. Rev. Microbiol. *15*, 323–337.

Destoumieux-Garzón, D., Peduzzi, J., and Rebuffat, S. (2002). Focus on modified microcins: structural features and mechanisms of action. Biochimie *84*, 511–519.

Desvaux, M., Parham, N.J., and Henderson, I.R. (2004). Type V protein secretion: simplicity gone awry? Curr. Issues Mol. Biol. *6*, 111–124.

Dienes, L. (1946). Reproductive Processes in Proteus Cultures. Proc. Soc. Exp. Biol. Med. *63*, 265–270.

Dix, S.R., Owen, H.J., Sun, R., Ahmad, A., Shastri, S., Spiewak, H.L., Mosby, D.J., Harris, M.J., Batters, S.L., Brooker, T.A., et al. (2018). Structural insights into the function of type VI secretion system TssA subunits. Nat. Commun. *9*, 4765.

Dong, T.G., and Mekalanos, J.J. (2012). Characterization of the RpoN regulon reveals differential regulation of T6SS and new flagellar operons in Vibrio cholerae O37 strain V52. Nucleic Acids Res. *40*, 7766–7775.

Dong, T.G., Ho, B.T., Yoder-Himes, D.R., and Mekalanos, J.J. (2013). Identification of T6SS-dependent effector and immunity proteins by Tn-seq in Vibrio cholerae. Proc. Natl. Acad. Sci. *110*, 2623–2628.

Dörr, T., Davis, B.M., and Waldor, M.K. (2015). Endopeptidase-mediated beta lactam tolerance. PLoS Pathog. *11*, e1004850.

Dörr, T., Alvarez, L., Delgado, F., Davis, B.M., Cava, F., and Waldor, M.K. (2016). A cell wall damage response mediated by a sensor kinase/response regulator pair enables beta-lactam tolerance. Proc. Natl. Acad. Sci. U. S. A. *113*, 404–409.

Douzi, B., Logger, L., Spinelli, S., Blangy, S., Cambillau, C., and Cascales, E. (2018). Structure-Function Analysis of the C-Terminal Domain of the Type VI Secretion TssB Tail Sheath Subunit. J. Mol. Biol. *430*, 297–309.

Dudley, E.G., Thomson, N.R., Parkhill, J., Morin, N.P., and Nataro, J.P. (2006). Proteomic and microarray characterization of the AggR regulon identifies a pheU pathogenicity island in enteroaggregative Escherichia coli. Mol. Microbiol. *61*, 1267–1282.

Durand, E., Zoued, A., Spinelli, S., Watson, P.J.H., Aschtgen, M.-S., Journet, L., Cambillau, C., and Cascales, E. (2012). Structural characterization and oligomerization of the TssL protein, a component shared by bacterial type VI and type IVb secretion systems. J. Biol. Chem. *287*, 14157–14168.

Durand, E., Nguyen, V.S., Zoued, A., Logger, L., Péhau-Arnaudet, G., Aschtgen, M.-S., Spinelli, S., Desmyter, A., Bardiaux, B., Dujeancourt, A., et al. (2015). Biogenesis and structure of a type VI secretion membrane core complex. Nature *523*, 555–560.

Filloux, A., Hachani, A., and Bleves, S. (2008). The bacterial type VI secretion machine: yet another player for protein transport across membranes. Microbiology *154*, 1570–1583.

Flemming, H.-C., Wingender, J., Szewzyk, U., Steinberg, P., Rice, S.A., and Kjelleberg, S. (2016). Biofilms: an emergent form of bacterial life. Nat. Rev. Microbiol. *14*, 563–575.

Folkesson, A., Löfdahl, S., and Normark, S. (2002). The Salmonella enterica subspecies I specific centisome 7 genomic island encodes novel protein families present in bacteria living in close contact with eukaryotic cells. Res. Microbiol. *153*, 537–545.

Förster, A., Planamente, S., Manoli, E., Lossi, N.S., Freemont, P.S., and Filloux, A. (2014). Coevolution of the ATPase ClpV, the sheath proteins TssB and TssC, and the accessory protein TagJ/HsiE1 distinguishes type VI secretion classes. J. Biol. Chem. *289*, 33032–33043.

Fritsch, M.J., Trunk, K., Diniz, J.A., Guo, M., Trost, M., and Coulthurst, S.J. (2013). Proteomic Identification of Novel Secreted Antibacterial Toxins of the Serratia marcescens Type VI Secretion System. Mol. Cell. Proteomics MCP *12*, 2735–2749.

Fu, Y., Ho, B.T., and Mekalanos, J.J. (2018). Tracking Vibrio cholerae Cell-Cell Interactions during Infection Reveals Bacterial Population Dynamics within Intestinal Microenvironments. Cell Host Microbe *23*, 274-281.e2.

Gallique, M., Bouteiller, M., and Merieau, A. (2017). The Type VI Secretion System: A Dynamic System for Bacterial Communication? Front. Microbiol. *8*.

Garcia, E.C., Perault, A.I., Marlatt, S.A., and Cotter, P.A. (2016). Interbacterial signaling via Burkholderia contact-dependent growth

inhibition system proteins. Proc. Natl. Acad. Sci. U. S. A. *113*, 8296–8301.

García-Bayona, L., and Comstock, L.E. (2018). Bacterial antagonism in host-associated microbial communities. Science *361*.

Gawarzewski, I., Smits, S.H.J., Schmitt, L., and Jose, J. (2013). Structural comparison of the transport units of type V secretion systems. Biol. Chem. *394*, 1385–1398.

Ge, P., Scholl, D., Leiman, P.G., Yu, X., Miller, J.F., and Zhou, Z.H. (2015). Atomic structures of a bactericidal contractile nanotube in its pre- and postcontraction states. Nat. Struct. Mol. Biol. *22*, 377–382.

Gerc, A.J., Diepold, A., Trunk, K., Porter, M., Rickman, C., Armitage, J.P., Stanley-Wall, N.R., and Coulthurst, S.J. (2015). Visualization of the Serratia Type VI Secretion System Reveals Unprovoked Attacks and Dynamic Assembly. Cell Rep. *12*, 2131–2142.

Ghoul, M., and Mitri, S. (2016). The Ecology and Evolution of Microbial Competition. Trends Microbiol. *24*, 833–845.

Gill, D.M., and Meren, R. (1978). ADP-ribosylation of membrane proteins catalyzed by cholera toxin: basis of the activation of adenylate cyclase. Proc. Natl. Acad. Sci. U. S. A. *75*, 3050–3054.

Goodman, A.L., Kulasekara, B., Rietsch, A., Boyd, D., Smith, R.S., and Lory, S. (2004). A signaling network reciprocally regulates genes associated with acute infection and chronic persistence in Pseudomonas aeruginosa. Dev. Cell *7*, 745–754.

Griffith, S.J., Nathan, C., Selander, R.K., Chamberlin, W., Gordon, S., Kabins, S., and Weinstein, R.A. (1989). The epidemiology of Pseudomonas aeruginosa in oncology patients in a general hospital. J. Infect. Dis. *160*, 1030–1036.

Griffiths, A.J., Miller, J.H., Suzuki, D.T., Lewontin, R.C., and Gelbart, W.M. (2000). Bacterial conjugation. Introd. Genet. Anal. 7th Ed.

Gupta, R.S. (1998). What are archaebacteria: life's third domain or monoderm prokaryotes related to gram-positive bacteria? A new proposal for the classification of prokaryotic organisms. Mol. Microbiol. *29*, 695–707.

Hachani, A., Lossi, N.S., Hamilton, A., Jones, C., Bleves, S., Albesa-Jové, D., and Filloux, A. (2011). Type VI Secretion System in Pseudomonas aeruginosa SECRETION AND MULTIMERIZATION OF VgrG PROTEINS. J. Biol. Chem. *286*, 12317–12327.

Hachani, A., Lossi, N.S., and Filloux, A. (2013). A visual assay to monitor T6SS-mediated bacterial competition. J. Vis. Exp. JoVE e50103.

Hachani, A., Allsopp, L.P., Oduko, Y., and Filloux, A. (2014). The VgrG Proteins Are "à la Carte" Delivery Systems for Bacterial Type VI Effectors. J. Biol. Chem. *289*, 17872–17884.

Hachani, A., Wood, T.E., and Filloux, A. (2016). Type VI secretion and anti-host effectors. Curr. Opin. Microbiol. *29*, 81–93.

Hayes, C.S., Koskiniemi, S., Ruhe, Z.C., Poole, S.J., and Low, D.A. (2014). Mechanisms and Biological Roles of Contact-Dependent Growth Inhibition Systems. Cold Spring Harb. Perspect. Med. *4*.

Hecht, A.L., Casterline, B.W., Earley, Z.M., Goo, Y.A., Goodlett, D.R., and Bubeck Wardenburg, J. (2016). Strain competition restricts colonization of an enteric pathogen and prevents colitis. EMBO Rep. *17*, 1281–1291.

Heinemann, J.A., and Sprague, G.F. (1989). Bacterial conjugative plasmids mobilize DNA transfer between bacteria and yeast. Nature *340*, 205–209.

Heymann, J.B., Bartho, J.D., Rybakova, D., Venugopal, H.P., Winkler, D.C., Sen, A., Hurst, M.R.H., and Mitra, A.K. (2013). Three-dimensional structure of the toxin-delivery particle antifeeding prophage of Serratia entomophila. J. Biol. Chem. *288*, 25276–25284.

Hirst, T.R., Sanchez, J., Kaper, J.B., Hardy, S.J., and Holmgren, J. (1984). Mechanism of toxin secretion by Vibrio cholerae investigated in strains harboring plasmids that encode heat-labile enterotoxins of Escherichia coli. Proc. Natl. Acad. Sci. U. S. A. *81*, 7752–7756.

Ho, B.T., Basler, M., and Mekalanos, J.J. (2013). Type 6 secretion system-mediated immunity to type 4 secretion system-mediated gene transfer. Science *342*, 250–253.

Ho, B.T., Dong, T.G., and Mekalanos, J.J. (2014). A View to a Kill: The Bacterial Type VI Secretion System. Cell Host Microbe *15*, 9–21.

Ho, B.T., Fu, Y., Dong, T.G., and Mekalanos, J.J. (2017). Vibrio cholerae type 6 secretion system effector trafficking in target bacterial cells. Proc. Natl. Acad. Sci. 201711219.

Hood, R.D., Singh, P., Hsu, F., Güvener, T., Carl, M.A., Trinidad, R.R.S., Silverman, J.M., Ohlson, B.B., Hicks, K.G., Plemel, R.L., et al. (2010). A Type VI Secretion System of

Pseudomonas aeruginosa Targets a Toxin to Bacteria. Cell Host Microbe *7*, 25–37.

Houben, E.N.G., Korotkov, K.V., and Bitter, W. (2014). Take five - Type VII secretion systems of Mycobacteria. Biochim. Biophys. Acta - Mol. Cell Res. *1843*, 1707–1716.

Hsu, F., Schwarz, S., and Mougous, J.D. (2009). TagR promotes PpkA-catalysed type VI secretion activation in Pseudomonas aeruginosa. Mol. Microbiol. *72*, 1111–1125.

Hsu, T., Hingley-Wilson, S.M., Chen, B., Chen, M., Dai, A.Z., Morin, P.M., Marks, C.B., Padiyar, J., Goulding, C., Gingery, M., et al. (2003). The primary mechanism of attenuation of bacillus Calmette–Guérin is a loss of secreted lytic function required for invasion of lung interstitial tissue. Proc. Natl. Acad. Sci. *100*, 12420–12425.

Hurst, M.R.H., Beard, S.S., Jackson, T.A., and Jones, S.M. (2007). Isolation and characterization of the Serratia entomophila antifeeding prophage. FEMS Microbiol. Lett. *270*, 42–48.

Ilangovan, A., Connery, S., and Waksman, G. (2015). Structural biology of the Gram-negative bacterial conjugation systems. Trends Microbiol. *23*, 301–310.

Ishikawa, T., Rompikuntal, P.K., Lindmark, B., Milton, D.L., and Wai, S.N. (2009). Quorum sensing regulation of the two hcp alleles in Vibrio cholerae O1 strains. PloS One *4*, e6734.

Ishikawa, T., Sabharwal, D., Bröms, J., Milton, D.L., Sjöstedt, A., Uhlin, B.E., and Wai, S.N. (2012). Pathoadaptive conditional regulation of the type VI secretion system in Vibrio cholerae O1 strains. Infect. Immun. *80*, 575–584.

Jacob, F., Siminovitch, L., and Wollman, E. (1952). [Biosynthesis of a colicin and its mode of action]. Ann. Inst. Pasteur *83*, 295–315.

Jeong, K.C., Ghosal, D., Chang, Y.-W., Jensen, G.J., and Vogel, J.P. (2017). Polar delivery of Legionella type IV secretion system substrates is essential for virulence. Proc. Natl. Acad. Sci. *114*, 8077–8082.

Jiang, F., Waterfield, N.R., Yang, J., Yang, G., and Jin, Q. (2014). A Pseudomonas aeruginosa type VI secretion phospholipase D effector targets both prokaryotic and eukaryotic cells. Cell Host Microbe *15*, 600–610.

Jiang, F., Li, N., Wang, X., Cheng, J., Huang, Y., Yang, Y., Yang, J., Cai, B., Wang, Y.-P., Jin, Q., et al. (2019). Cryo-EM Structure and Assembly of an Extracellular Contractile Injection System. Cell *177*, 370-383.e15.

Joshi, A., Kostiuk, B., Rogers, A., Teschler, J., Pukatzki, S., and Yildiz, F.H. (2017). Rules of Engagement: The Type VI Secretion System in Vibrio cholerae. Trends Microbiol. *25*, 267–279.

Juhas, M. (2015). Horizontal gene transfer in human pathogens. Crit. Rev. Microbiol. *41*, 101–108.

Juni, E., and Janik, A. (1969). Transformation of Acinetobacter calco-aceticus (Bacterium anitratum). J. Bacteriol. *98*, 281–288.

Kajava, A.V., Cheng, N., Cleaver, R., Kessel, M., Simon, M.N., Willery, E., Jacob-Dubuisson, F., Locht, C., and Steven, A.C. (2001). Beta-helix model for the filamentous haemagglutinin adhesin of Bordetella pertussis and related bacterial secretory proteins. Mol. Microbiol. *42*, 279–292.

Kanamaru, S., Leiman, P.G., Kostyuchenko, V.A., Chipman, P.R., Mesyanzhinov, V.V., Arisaka, F., and Rossmann, M.G. (2002). Structure of the cell-puncturing device of bacteriophage T4. Nature *415*, 553–557.

Kapitein, N., Bönemann, G., Pietrosiuk, A., Seyffer, F., Hausser, I., Locker, J.K., and Mogk, A. (2013). ClpV recycles VipA/VipB tubules and prevents non-productive tubule formation to ensure efficient type VI protein secretion. Mol. Microbiol. *87*, 1013–1028.

Kenniston, J.A., Baker, T.A., Fernandez, J.M., and Sauer, R.T. (2003). Linkage between ATP consumption and mechanical unfolding during the protein processing reactions of an AAA+ degradation machine. Cell *114*, 511–520.

Kirchberger, P.C., Unterweger, D., Provenzano, D., Pukatzki, S., and Boucher, Y. (2017). Sequential displacement of Type VI Secretion System effector genes leads to evolution of diverse immunity gene arrays in Vibrio cholerae. Sci. Rep. *7*, 45133.

Koskiniemi, S., Lamoureux, J.G., Nikolakakis, K.C., Roodenbeke, C. t'Kint de, Kaplan, M.D., Low, D.A., and Hayes, C.S. (2013). Rhs proteins from diverse bacteria mediate intercellular competition. Proc. Natl. Acad. Sci. *110*, 7032–7037.

Kostiuk, B., Unterweger, D., Provenzano, D., and Pukatzki, S. (2017). T6SS intraspecific competition orchestrates Vibrio cholerae genotypic diversity. Int. Microbiol. Off. J. Span. Soc. Microbiol. *20*, 130–137.

Kudryashev, M., Wang, R.Y.-R., Brackmann, M., Scherer, S., Maier, T., Baker, D., DiMaio, F., Stahlberg, H., Egelman, E.H., and Basler, M. (2015). Structure of the Type VI Secretion System Contractile Sheath. Cell *160*, 952–962.

LaCourse, K.D., Peterson, S.B., Kulasekara, H.D., Radey, M.C., Kim, J., and Mougous, J.D. (2018). Conditional toxicity and synergy drive diversity among antibacterial effectors. Nat. Microbiol. 1.

Lasica, A.M., Ksiazek, M., Madej, M., and Potempa, J. (2017). The Type IX Secretion System (T9SS): Highlights and Recent Insights into Its Structure and Function. Front. Cell. Infect. Microbiol. 7, 215.

Le Roux, F., and Blokesch, M. (2018). Eco-evolutionary Dynamics Linked to Horizontal Gene Transfer in Vibrios. Annu. Rev. Microbiol. 72, 89–110.

Lederberg, J., and Tatum, E.L. (1946). Gene Recombination in Escherichia Coli. Nature 158, 558.

Lederberg, J., and Tatum, E.L. (1953). Sex in bacteria; genetic studies, 1945-1952. Science 118, 169–175.

Lee, C.-R., Lee, J.H., Park, M., Park, K.S., Bae, I.K., Kim, Y.B., Cha, C.-J., Jeong, B.C., and Lee, S.H. (2017). Biology of Acinetobacter baumannii: Pathogenesis, Antibiotic Resistance Mechanisms, and Prospective Treatment Options. Front. Cell. Infect. Microbiol. 7.

Leiman, P.G., and Shneider, M.M. (2012). Contractile tail machines of bacteriophages. Adv. Exp. Med. Biol. 726, 93–114.

Leiman, P.G., Basler, M., Ramagopal, U.A., Bonanno, J.B., Sauder, J.M., Pukatzki, S., Burley, S.K., Almo, S.C., and Mekalanos, J.J. (2009). Type VI secretion apparatus and phage tail-associated protein complexes share a common evolutionary origin. Proc. Natl. Acad. Sci. U. S. A. 106, 4154–4159.

Leiman, P.G., Arisaka, F., Raaij, M.J. van, Kostyuchenko, V.A., Aksyuk, A.A., Kanamaru, S., and Rossmann, M.G. (2010). Morphogenesis of the T4 tail and tail fibers. Virol. J. 7, 355.

Lennings, J., Mayer, C., Makhlouf, M., Brötz-Oesterhelt, H., and Schwarz, S. (2019). Polar localization of the ATPase ClpV-5 occurs independent of type VI secretion system apparatus proteins in Burkholderia thailandensis. BMC Res. Notes 12, 109.

Leo, J.C., Grin, I., and Linke, D. (2012). Type V secretion: mechanism(s) of autotransport through the bacterial outer membrane. Philos. Trans. R. Soc. Lond. B. Biol. Sci. 367, 1088–1101.

Lesic, B., Starkey, M., He, J., Hazan, R., and Rahme, L.G. (2009). Quorum sensing differentially regulates Pseudomonas aeruginosa type VI secretion locus I and homologous loci II and III, which are required for pathogenesis. Microbiol. Read. Engl. 155, 2845–2855.

Leung, K.Y., Siame, B.A., Snowball, H., and Mok, Y.-K. (2011). Type VI secretion regulation: crosstalk and intracellular communication. Host–Microbe Interact. 14, 9–15.

Liang, W., Pascual-Montano, A., Silva, A.J., and Benitez, J.A. (2007). The cyclic AMP receptor protein modulates quorum sensing, motility and multiple genes that affect intestinal colonization in Vibrio cholerae. Microbiol. Read. Engl. 153, 2964–2975.

Liang, X., Moore, R., Wilton, M., Wong, M.J.Q., Lam, L., and Dong, T.G. (2015). Identification of divergent type VI secretion effectors using a conserved chaperone domain. Proc. Natl. Acad. Sci. U. S. A. 112, 9106–9111.

Lin, J., Zhang, W., Cheng, J., Yang, X., Zhu, K., Wang, Y., Wei, G., Qian, P.-Y., Luo, Z.-Q., and Shen, X. (2017). A Pseudomonas T6SS effector recruits PQS-containing outer membrane vesicles for iron acquisition. Nat. Commun. 8, 14888.

Lin, J.-S., Wu, H.-H., Hsu, P.-H., Ma, L.-S., Pang, Y.-Y., Tsai, M.-D., and Lai, E.-M. (2014). Fha interaction with phosphothreonine of TssL activates type VI secretion in Agrobacterium tumefaciens. PLoS Pathog. 10, e1003991.

Lin, J.-S., Pissaridou, P., Wu, H.-H., Tsai, M.-D., Filloux, A., and Lai, E.-M. (2018). TagF-mediated repression of bacterial type VI secretion systems involves a direct interaction with the cytoplasmic protein Fha. J. Biol. Chem. 293, 8829–8842.

Lo Scrudato, M., Borgeaud, S., and Blokesch, M. (2014). Regulatory elements involved in the expression of competence genes in naturally transformable Vibrio cholerae. BMC Microbiol. 14, 327.

Locht, C., Coutte, L., and Mielcarek, N. (2011). The ins and outs of pertussis toxin. FEBS J. 278, 4668–4682.

Logan, S.L., Thomas, J., Yan, J., Baker, R.P., Shields, D.S., Xavier, J.B., Hammer, B.K., and Parthasarathy, R. (2018). The Vibrio cholerae type VI secretion system can modulate host intestinal mechanics to displace gut bacterial symbionts. Proc. Natl. Acad. Sci. U. S. A. 115, E3779–E3787.

Lossi, N.S., Manoli, E., Simpson, P., Jones, C., Hui, K., Dajani, R., Coulthurst, S.J., Freemont, P., and Filloux, A. (2012). The archetype Pseudomonas aeruginosa proteins TssB and TagJ form a novel subcomplex in

the bacterial type VI secretion system. Mol. Microbiol. *86*, 437–456.

Low, H.H., Gubellini, F., Rivera-Calzada, A., Braun, N., Connery, S., Dujeancourt, A., Lu, F., Redzej, A., Fronzes, R., Orlova, E.V., et al. (2014). Structure of a type IV secretion system. Nature *508*, 550–553.

Luo, Z.-Q., and Isberg, R.R. (2004). Multiple substrates of the Legionella pneumophila Dot/Icm system identified by interbacterial protein transfer. Proc. Natl. Acad. Sci. *101*, 841–846.

Ma, A.T., McAuley, S., Pukatzki, S., and Mekalanos, J.J. (2009a). Translocation of a Vibrio cholerae Type VI Secretion Effector Requires Bacterial Endocytosis by Host Cells. Cell Host Microbe *5*, 234–243.

Ma, J., Pan, Z., Huang, J., Sun, M., Lu, C., and Yao, H. (2017). The Hcp proteins fused with diverse extended-toxin domains represent a novel pattern of antibacterial effectors in type VI secretion systems. Virulence *8*, 1189–1202.

Ma, L.-S., Lin, J.-S., and Lai, E.-M. (2009b). An IcmF family protein, ImpLM, is an integral inner membrane protein interacting with ImpKL, and its walker a motif is required for type VI secretion system-mediated Hcp secretion in Agrobacterium tumefaciens. J. Bacteriol. *191*, 4316–4329.

Ma, L.-S., Narberhaus, F., and Lai, E.-M. (2012). IcmF family protein TssM exhibits ATPase activity and energizes type VI secretion. J. Biol. Chem. *287*, 15610–15621.

Ma, L.-S., Hachani, A., Lin, J.-S., Filloux, A., and Lai, E.-M. (2014). Agrobacterium tumefaciens Deploys a Superfamily of Type VI Secretion DNase Effectors as Weapons for Interbacterial Competition In Planta. Cell Host Microbe *16*, 94–104.

Majerczyk, C., Schneider, E., and Greenberg, E.P. (2016). Quorum sensing control of Type VI secretion factors restricts the proliferation of quorum-sensing mutants. ELife *5*, e14712.

McNally, L., Bernardy, E., Thomas, J., Kalziqi, A., Pentz, J., Brown, S.P., Hammer, B.K., Yunker, P.J., and Ratcliff, W.C. (2017). Killing by Type VI secretion drives genetic phase separation and correlates with increased cooperation. Nat. Commun. *8*, 14371.

Meibom, K.L., Blokesch, M., Dolganov, N.A., Wu, C.-Y., and Schoolnik, G.K. (2005). Chitin induces natural competence in Vibrio cholerae. Science *310*, 1824–1827.

Metzger, L.C., Stutzmann, S., Scrignari, T., Van der Henst, C., Matthey, N., and Blokesch, M. (2016). Independent Regulation of Type VI Secretion in Vibrio cholerae by TfoX and TfoY. Cell Rep. *15*, 951–958.

Metzger, L.C., Matthey, N., Stoudmann, C., Collas, E.J., and Blokesch, M. (2019). Ecological implications of gene regulation by TfoX and TfoY among diverse Vibrio species. Environ. Microbiol.

Michel, B. (2005). After 30 Years of Study, the Bacterial SOS Response Still Surprises Us. PLoS Biol. *3*.

Michel-Briand, Y., and Baysse, C. (2002). The pyocins of Pseudomonas aeruginosa. Biochimie *84*, 499–510.

Miyata, S.T., Kitaoka, M., Brooks, T.M., McAuley, S.B., and Pukatzki, S. (2011). Vibrio cholerae Requires the Type VI Secretion System Virulence Factor VasX To Kill Dictyostelium discoideum. Infect. Immun. *79*, 2941–2949.

Miyata, S.T., Unterweger, D., Rudko, S.P., and Pukatzki, S. (2013). Dual Expression Profile of Type VI Secretion System Immunity Genes Protects Pandemic Vibrio cholerae. PLOS Pathog *9*, e1003752.

Moore, D., Hamilton, C.M., Maneewannakul, K., Mintz, Y., Frost, L.S., and Ippen-Ihler, K. (1993). The Escherichia coli K-12 F plasmid gene traX is required for acetylation of F pilin. J. Bacteriol. *175*, 1375–1383.

Moradali, M.F., Ghods, S., and Rehm, B.H.A. (2017). Pseudomonas aeruginosa Lifestyle: A Paradigm for Adaptation, Survival, and Persistence. Front. Cell. Infect. Microbiol. *7*.

Moscoso, J.A., Mikkelsen, H., Heeb, S., Williams, P., and Filloux, A. (2011). The Pseudomonas aeruginosa sensor RetS switches type III and type VI secretion via c-di-GMP signalling. Environ. Microbiol. *13*, 3128–3138.

Mougous, J.D., Cuff, M.E., Raunser, S., Shen, A., Zhou, M., Gifford, C.A., Goodman, A.L., Joachimiak, G., Ordoñez, C.L., Lory, S., et al. (2006). A Virulence Locus of Pseudomonas aeruginosa Encodes a Protein Secretion Apparatus. Science *312*, 1526–1530.

Mougous, J.D., Gifford, C.A., Ramsdell, T.L., and Mekalanos, J.J. (2007). Threonine phosphorylation post-translationally regulates protein secretion in Pseudomonas aeruginosa. Nat. Cell Biol. *9*, 797–803.

Nakayama, K., Takashima, K., Ishihara, H., Shinomiya, T., Kageyama, M., Kanaya, S., Ohnishi, M., Murata, T., Mori, H., and Hayashi, T. (2000). The R-type pyocin of Pseudomonas aeruginosa is related to P2 phage, and the F-type is related to lambda phage. Mol. Microbiol. *38*, 213–231.

Nano, F.E., Zhang, N., Cowley, S.C., Klose, K.E., Cheung, K.K.M., Roberts, M.J., Ludu, J.S., Letendre, G.W., Meierovics, A.I., Stephens, G., et al. (2004). A Francisella tularensis pathogenicity island required for intramacrophage growth. J. Bacteriol. *186*, 6430–6436.

Nazarov, S., Schneider, J.P., Brackmann, M., Goldie, K.N., Stahlberg, H., and Basler, M. (2018). Cryo-EM reconstruction of Type VI secretion system baseplate and sheath distal end. EMBO J. *37*.

Nguyen, V.S., Logger, L., Spinelli, S., Legrand, P., Huyen Pham, T.T., Nhung Trinh, T.T., Cherrak, Y., Zoued, A., Desmyter, A., Durand, E., et al. (2017). Type VI secretion TssK baseplate protein exhibits structural similarity with phage receptor-binding proteins and evolved to bind the membrane complex. Nat. Microbiol. *2*, 17103.

Nguyen, V.S., Douzi, B., Durand, E., Roussel, A., Cascales, E., and Cambillau, C. (2018). Towards a complete structural deciphering of Type VI secretion system. Curr. Opin. Struct. Biol. *49*, 77–84.

Nikaido, H. (2003). Molecular basis of bacterial outer membrane permeability revisited. Microbiol. Mol. Biol. Rev. MMBR *67*, 593–656.

Ostrowski, A., Cianfanelli, F.R., Porter, M., Mariano, G., Peltier, J., Wong, J.J., Swedlow, J.R., Trost, M., and Coulthurst, S.J. (2018). Killing with proficiency: Integrated post-translational regulation of an offensive Type VI secretion system. PLoS Pathog. *14*, e1007230.

Park, Y.-J., Lacourse, K.D., Cambillau, C., DiMaio, F., Mougous, J.D., and Veesler, D. (2018). Structure of the type VI secretion system TssK-TssF-TssG baseplate subcomplex revealed by cryo-electron microscopy. Nat. Commun. *9*, 5385.

Parsons, D.A., and Heffron, F. (2005). sciS, an icmF homolog in Salmonella enterica serovar Typhimurium, limits intracellular replication and decreases virulence. Infect. Immun. *73*, 4338–4345.

Patzer, S.I., Baquero, M.R., Bravo, D., Moreno, F., and Hantke, K. (2003). The colicin G, H and X determinants encode microcins M and H47, which might utilize the catecholate siderophore receptors FepA, Cir, Fiu and IroN. Microbiol. Read. Engl. *149*, 2557–2570.

Peraro, M.D., and van der Goot, F.G. (2016). Pore-forming toxins: ancient, but never really out of fashion. Nat. Rev. Microbiol. *14*, 77–92.

Persson, O.P., Pinhassi, J., Riemann, L., Marklund, B.-I., Rhen, M., Normark, S., González, J.M., and Hagström, Å. (2009). High abundance of virulence gene homologues in marine bacteria. Environ. Microbiol. *11*, 1348–1357.

Peskin, C.S., Odell, G.M., and Oster, G.F. (1993). Cellular motions and thermal fluctuations: the Brownian ratchet. Biophys. J. *65*, 316–324.

Pietrosiuk, A., Lenherr, E.D., Falk, S., Bönemann, G., Kopp, J., Zentgraf, H., Sinning, I., and Mogk, A. (2011). Molecular Basis for the Unique Role of the AAA+ Chaperone ClpV in Type VI Protein Secretion. J. Biol. Chem. *286*, 30010–30021.

Pitzschke, A., and Hirt, H. (2010). New insights into an old story: Agrobacterium-induced tumour formation in plants by plant transformation. EMBO J. *29*, 1021–1032.

Planamente, S., Salih, O., Manoli, E., Albesa-Jové, D., Freemont, P.S., and Filloux, A. (2016). TssA forms a gp6-like ring attached to the type VI secretion sheath. EMBO J. *35*, 1613–1627.

Pukatzki, S., Ma, A.T., Sturtevant, D., Krastins, B., Sarracino, D., Nelson, W.C., Heidelberg, J.F., and Mekalanos, J.J. (2006). Identification of a conserved bacterial protein secretion system in Vibrio cholerae using the Dictyostelium host model system. Proc. Natl. Acad. Sci. *103*, 1528–1533.

Pukatzki, S., Ma, A.T., Revel, A.T., Sturtevant, D., and Mekalanos, J.J. (2007). Type VI secretion system translocates a phage tail spike-like protein into target cells where it cross-links actin. Proc. Natl. Acad. Sci. U. S. A. *104*, 15508–15513.

Quentin, D., Ahmad, S., Shanthamoorthy, P., Mougous, J.D., Whitney, J.C., and Raunser, S. (2018). Mechanism of loading and translocation of type VI secretion system effector Tse6. Nat. Microbiol. *3*, 1142–1152.

Rao, P.S.S., Yamada, Y., Tan, Y.P., and Leung, K.Y. (2004). Use of proteomics to identify novel virulence determinants that are required for Edwardsiella tarda pathogenesis. Mol. Microbiol. *53*, 573–586.

Rapisarda, C., Cherrak, Y., Kooger, R., Schmidt, V., Pellarin, R., Logger, L., Cascales, E., Pilhofer, M., Durand, E., and Fronzes, R. (2019). In situ and high-resolution cryo-EM structure of a bacterial type VI secretion system membrane complex. EMBO J.

Redzej, A., Ukleja, M., Connery, S., Trokter, M., Felisberto-Rodrigues, C., Cryar, A., Thalassinos, K., Hayward, R.D., Orlova, E.V., and Waksman, G. (2017). Structure of

a VirD4 coupling protein bound to a VirB type IV secretion machinery. EMBO J. *36*, 3080–3095.

Relman, D.A., Domenighini, M., Tuomanen, E., Rappuoli, R., and Falkow, S. (1989). Filamentous hemagglutinin of Bordetella pertussis: nucleotide sequence and crucial role in adherence. Proc. Natl. Acad. Sci. U. S. A. *86*, 2637–2641.

Renault, M.G., Zamarreno Beas, J., Douzi, B., Chabalier, M., Zoued, A., Brunet, Y.R., Cambillau, C., Journet, L., and Cascales, E. (2018). The gp27-like Hub of VgrG Serves as Adaptor to Promote Hcp Tube Assembly. J. Mol. Biol. *430*, 3143–3156.

Repizo, G.D., Gagné, S., Foucault-Grunenwald, M.-L., Borges, V., Charpentier, X., Limansky, A.S., Gomes, J.P., Viale, A.M., and Salcedo, S.P. (2015). Differential Role of the T6SS in Acinetobacter baumannii Virulence. PloS One *10*, e0138265.

Riley, M.A. (1993). Molecular mechanisms of colicin evolution. Mol. Biol. Evol. *10*, 1380–1395.

Ringel, P.D., Hu, D., and Basler, M. (2017). The Role of Type VI Secretion System Effectors in Target Cell Lysis and Subsequent Horizontal Gene Transfer. Cell Rep. *21*, 3927–3940.

Roest, H.P., Mulders, I.H., Spaink, H.P., Wijffelman, C.A., and Lugtenberg, B.J. (1997). A Rhizobium leguminosarum biovar trifolii locus not localized on the sym plasmid hinders effective nodulation on plants of the pea cross-inoculation group. Mol. Plant-Microbe Interact. MPMI *10*, 938–941.

Rojas, C.M., Ham, J.H., Deng, W.-L., Doyle, J.J., and Collmer, A. (2002). HecA, a member of a class of adhesins produced by diverse pathogenic bacteria, contributes to the attachment, aggregation, epidermal cell killing, and virulence phenotypes of Erwinia chrysanthemi EC16 on Nicotiana clevelandii seedlings. Proc. Natl. Acad. Sci. U. S. A. *99*, 13142–13147.

Rosenberg, O.S., Dovala, D., Li, X., Connolly, L., Bendebury, A., Finer-Moore, J., Holton, J., Cheng, Y., Stroud, R.M., and Cox, J.S. (2015). Substrates control multimerization and activation of the multi-domain ATPase motor of type VII secretion. Cell *161*, 501–512.

Ruhe, Z.C., Low, D.A., and Hayes, C.S. (2013). Bacterial contact-dependent growth inhibition. Trends Microbiol. *21*, 230–237.

Ruhe, Z.C., Nguyen, J.Y., Xiong, J., Koskiniemi, S., Beck, C.M., Perkins, B.R., Low, D.A., and Hayes, C.S. (2017). CdiA Effectors Use Modular Receptor-Binding Domains To Recognize Target Bacteria. MBio *8*, e00290-17.

Ruhe, Z.C., Subramanian, P., Song, K., Nguyen, J.Y., Stevens, T.A., Low, D.A., Jensen, G.J., and Hayes, C.S. (2018). Programmed Secretion Arrest and Receptor-Triggered Toxin Export during Antibacterial Contact-Dependent Growth Inhibition. Cell *175*, 921-933.e14.

Russell, A.B., Hood, R.D., Bui, N.K., LeRoux, M., Vollmer, W., and Mougous, J.D. (2011). Type VI secretion delivers bacteriolytic effectors to target cells. Nature *475*, 343–347.

Russell, A.B., Singh, P., Brittnacher, M., Bui, N.K., Hood, R.D., Carl, M.A., Agnello, D.M., Schwarz, S., Goodlett, D.R., Vollmer, W., et al. (2012). A widespread bacterial type VI secretion effector superfamily identified using a heuristic approach. Cell Host Microbe *11*, 538–549.

Russell, A.B., LeRoux, M., Hathazi, K., Agnello, D.M., Ishikawa, T., Wiggins, P.A., Wai, S.N., and Mougous, J.D. (2013). Diverse type VI secretion phospholipases are functionally plastic antibacterial effectors. Nature *496*, 508–512.

Russell, A.B., Wexler, A.G., Harding, B.N., Whitney, J.C., Bohn, A.J., Goo, Y.A., Tran, B.Q., Barry, N.A., Zheng, H., Peterson, S.B., et al. (2014a). A Type VI Secretion-Related Pathway in Bacteroidetes Mediates Interbacterial Antagonism. Cell Host Microbe *16*, 227–236.

Russell, A.B., Peterson, S.B., and Mougous, J.D. (2014b). Type VI secretion effectors: poisons with a purpose. Nat. Rev. Microbiol. *12*, 137–148.

Salih, O., He, S., Planamente, S., Stach, L., MacDonald, J.T., Manoli, E., Scheres, S.H.W., Filloux, A., and Freemont, P.S. (2018a). Atomic Structure of Type VI Contractile Sheath from Pseudomonas aeruginosa. Structure.

Salih, O., He, S., Planamente, S., Stach, L., MacDonald, J.T., Manoli, E., Scheres, S.H.W., Filloux, A., and Freemont, P.S. (2018b). Atomic Structure of Type VI Contractile Sheath from Pseudomonas aeruginosa. Struct. Lond. Engl. 1993 *26*, 329-336.e3.

Sana, T.G., Flaugnatti, N., Lugo, K.A., Lam, L.H., Jacobson, A., Baylot, V., Durand, E., Journet, L., Cascales, E., and Monack, D.M. (2016). Salmonella Typhimurium utilizes a T6SS-mediated antibacterial weapon to

establish in the host gut. Proc. Natl. Acad. Sci. *113*, E5044–E5051.

Santin, Y.G., and Cascales, E. (2016). Domestication of a housekeeping transglycosylase for assembly of a Type VI secretion system. EMBO Rep. e201643206.

Santin, Y.G., Doan, T., Lebrun, R., Espinosa, L., Journet, L., and Cascales, E. (2018). In vivo TssA proximity labelling during type VI secretion biogenesis reveals TagA as a protein that stops and holds the sheath. Nat. Microbiol. *3*, 1304–1313.

Sassone-Corsi, M., Nuccio, S.-P., Liu, H., Hernandez, D., Vu, C.T., Takahashi, A.A., Edwards, R.A., and Raffatellu, M. (2016). Microcins mediate competition among Enterobacteriaceae in the inflamed gut. Nature *540*, 280–283.

Scholl, D. (2017). Phage Tail–Like Bacteriocins. Annu. Rev. Virol. *4*, 453–467.

Schwarz, S., West, T.E., Boyer, F., Chiang, W.-C., Carl, M.A., Hood, R.D., Rohmer, L., Tolker-Nielsen, T., Skerrett, S.J., and Mougous, J.D. (2010). Burkholderia type VI secretion systems have distinct roles in eukaryotic and bacterial cell interactions. PLoS Pathog. *6*, e1001068.

Schwarz, S., Singh, P., Robertson, J.D., LeRoux, M., Skerrett, S.J., Goodlett, D.R., West, T.E., and Mougous, J.D. (2014). VgrG-5 Is a Burkholderia Type VI Secretion System-Exported Protein Required for Multinucleated Giant Cell Formation and Virulence. Infect. Immun. *82*, 1445–1452.

Sciara, G., Bebeacua, C., Bron, P., Tremblay, D., Ortiz-Lombardia, M., Lichière, J., van Heel, M., Campanacci, V., Moineau, S., and Cambillau, C. (2010). Structure of lactococcal phage p2 baseplate and its mechanism of activation. Proc. Natl. Acad. Sci. U. S. A. *107*, 6852–6857.

Sgro, G.G., Costa, T.R.D., Cenens, W., Souza, D.P., Cassago, A., Coutinho de Oliveira, L., Salinas, R.K., Portugal, R.V., Farah, C.S., and Waksman, G. (2018). Cryo-EM structure of the bacteria-killing type IV secretion system core complex from Xanthomonas citri. Nat. Microbiol. *3*, 1429–1440.

Shalom, G., Shaw, J.G., and Thomas, M.S. (2007). In vivo expression technology identifies a type VI secretion system locus in Burkholderia pseudomallei that is induced upon invasion of macrophages. Microbiol. Read. Engl. *153*, 2689–2699.

Shikuma, N.J., Antoshechkin, I., Medeiros, J.M., Pilhofer, M., and Newman, D.K. (2016). Stepwise metamorphosis of the tubeworm Hydroides elegans is mediated by a bacterial

inducer and MAPK signaling. Proc. Natl. Acad. Sci. U. S. A. *113*, 10097–10102.

Shneider, M.M., Buth, S.A., Ho, B.T., Basler, M., Mekalanos, J.J., and Leiman, P.G. (2013). PAAR-repeat proteins sharpen and diversify the type VI secretion system spike. Nature *500*, 350–353.

Si, M., Zhao, C., Burkinshaw, B., Zhang, B., Wei, D., Wang, Y., Dong, T.G., and Shen, X. (2017). Manganese scavenging and oxidative stress response mediated by type VI secretion system in Burkholderia thailandensis. Proc. Natl. Acad. Sci. U. S. A. *114*, E2233–E2242.

Silverman, J.M., Brunet, Y.R., Cascales, E., and Mougous, J.D. (2012). Structure and regulation of the type VI secretion system. Annu. Rev. Microbiol. *66*, 453–472.

Silverman, J.M., Agnello, D.M., Zheng, H., Andrews, B.T., Li, M., Catalano, C.E., Gonen, T., and Mougous, J.D. (2013). Haemolysin Co-regulated Protein is an Exported Receptor and Chaperone of Type VI Secretion Substrates. Mol. Cell *51*.

Souza, D.P., Oka, G.U., Alvarez-Martinez, C.E., Bisson-Filho, A.W., Dunger, G., Hobeika, L., Cavalcante, N.S., Alegria, M.C., Barbosa, L.R.S., Salinas, R.K., et al. (2015). Bacterial killing via a type IV secretion system. Nat. Commun. *6*, 6453.

Speare, L., Cecere, A.G., Guckes, K.R., Smith, S., Wollenberg, M.S., Mandel, M.J., Miyashiro, T., and Septer, A.N. (2018). Bacterial symbionts use a type VI secretion system to eliminate competitors in their natural host. Proc. Natl. Acad. Sci. U. S. A.

Stanley, S.A., Raghavan, S., Hwang, W.W., and Cox, J.S. (2003). Acute infection and macrophage subversion by Mycobacterium tuberculosis require a specialized secretion system. Proc. Natl. Acad. Sci. *100*, 13001–13006.

Stoodley, P., Sauer, K., Davies, D.G., and Costerton, J.W. (2002). Biofilms as complex differentiated communities. Annu. Rev. Microbiol. *56*, 187–209.

Streatfield, S.J., Sandkvist, M., Sixma, T.K., Bagdasarian, M., Hol, W.G., and Hirst, T.R. (1992). Intermolecular interactions between the A and B subunits of heat-labile enterotoxin from Escherichia coli promote holotoxin assembly and stability in vivo. Proc. Natl. Acad. Sci. U. S. A. *89*, 12140–12144.

Szwedziak, P., and Pilhofer, M. (2019). Bidirectional contraction of a type six secretion system. Nat. Commun. *10*, 1565.

Tauschek, M., Gorrell, R.J., Strugnell, R.A., and Robins-Browne, R.M. (2002). Identification of a protein secretory pathway for the secretion of heat-labile enterotoxin by an enterotoxigenic strain of Escherichia coli. Proc. Natl. Acad. Sci. U. S. A. *99*, 7066–7071.

Taylor, N.M.I., Prokhorov, N.S., Guerrero-Ferreira, R.C., Shneider, M.M., Browning, C., Goldie, K.N., Stahlberg, H., and Leiman, P.G. (2016). Structure of the T4 baseplate and its function in triggering sheath contraction. Nature *533*, 346–352.

Taylor, N.M.I., van Raaij, M.J., and Leiman, P.G. (2018). Contractile injection systems of bacteriophages and related systems. Mol. Microbiol.

Thomas, J., Watve, S.S., Ratcliff, W.C., and Hammer, B.K. (2017). Horizontal Gene Transfer of Functional Type VI Killing Genes by Natural Transformation. MBio *8*.

Townsley, L., Sison Mangus, M.P., Mehic, S., and Yildiz, F.H. (2016). Response of Vibrio cholerae to Low-Temperature Shifts: CspV Regulation of Type VI Secretion, Biofilm Formation, and Association with Zooplankton. Appl. Environ. Microbiol. *82*, 4441–4452.

Trunk, K., Peltier, J., Liu, Y.-C., Dill, B.D., Walker, L., Gow, N.A.R., Stark, M.J.R., Quinn, J., Strahl, H., Trost, M., et al. (2018). The type VI secretion system deploys antifungal effectors against microbial competitors. Nat. Microbiol. *3*, 920.

Typas, A., Banzhaf, M., Gross, C.A., and Vollmer, W. (2011). From the regulation of peptidoglycan synthesis to bacterial growth and morphology. Nat. Rev. Microbiol. *10*, 123–136.

Unnikrishnan, M., Constantinidou, C., Palmer, T., and Pallen, M.J. (2017). The Enigmatic Esx Proteins: Looking Beyond Mycobacteria. Trends Microbiol. *25*, 192–204.

Unterweger, D., Miyata, S.T., Bachmann, V., Brooks, T.M., Mullins, T., Kostiuk, B., Provenzano, D., and Pukatzki, S. (2014). The *Vibrio cholerae* type VI secretion system employs diverse effector modules for intraspecific competition. Nat. Commun. *5*, 3549.

Unterweger, D., Kostiuk, B., Ötjengerdes, R., Wilton, A., Diaz-Satizabal, L., and Pukatzki, S. (2015). Chimeric adaptor proteins translocate diverse type VI secretion system effectors in Vibrio cholerae. EMBO J. *34*, 2198–2210.

Veening, J.-W., and Blokesch, M. (2017). Interbacterial predation as a strategy for DNA acquisition in naturally competent bacteria. Nat. Rev. Microbiol. *15*, 621–629.

Vettiger, A., Winter, J., Lin, L., and Basler, M. (2017). The type VI secretion system sheath assembles at the end distal from the membrane anchor. Nat. Commun. *8*, ncomms16088.

Wagner, S., Grin, I., Malmsheimer, S., Singh, N., Torres-Vargas, C.E., and Westerhausen, S. (2018). Bacterial type III secretion systems: a complex device for the delivery of bacterial effector proteins into eukaryotic host cells. FEMS Microbiol. Lett. *365*.

Waksman, G. (2019). From conjugation to T4S systems in Gram-negative bacteria: a mechanistic biology perspective. EMBO Rep. *20*.

Waldor, M.K., and Mekalanos, J.J. (1996). Lysogenic conversion by a filamentous phage encoding cholera toxin. Science *272*, 1910–1914.

Wang, J., Brackmann, M., Castaño-Díez, D., Kudryashev, M., Goldie, K.N., Maier, T., Stahlberg, H., and Basler, M. (2017). Cryo-EM structure of the extended type VI secretion system sheath-tube complex. Nat. Microbiol. *2*, 1507–1512.

Watnick, P., and Kolter, R. (2000). Biofilm, City of Microbes. J. Bacteriol. *182*, 2675–2679.

Watve, S.S., Thomas, J., and Hammer, B.K. (2015). CytR Is a Global Positive Regulator of Competence, Type VI Secretion, and Chitinases in Vibrio cholerae. PloS One *10*, e0138834.

Weber, B.S., Miyata, S.T., Iwashkiw, J.A., Mortensen, B.L., Skaar, E.P., Pukatzki, S., and Feldman, M.F. (2013). Genomic and functional analysis of the type VI secretion system in Acinetobacter. PloS One *8*, e55142.

Weber, B.S., Hennon, S.W., Wright, M.S., Scott, N.E., de Berardinis, V., Foster, L.J., Ayala, J.A., Adams, M.D., and Feldman, M.F. (2016). Genetic Dissection of the Type VI Secretion System in Acinetobacter and Identification of a Novel Peptidoglycan Hydrolase, TagX, Required for Its Biogenesis. MBio *7*.

Wenren, L.M., Sullivan, N.L., Cardarelli, L., Septer, A.N., and Gibbs, K.A. (2013). Two Independent Pathways for Self-Recognition in Proteus mirabilis Are Linked by Type VI-Dependent Export. MBio *4*, e00374-13.

Wexler, A.G., Bao, Y., Whitney, J.C., Bobay, L.-M., Xavier, J.B., Schofield, W.B., Barry, N.A., Russell, A.B., Tran, B.Q., Goo, Y.A., et al. (2016). Human symbionts inject and

neutralize antibacterial toxins to persist in the gut. Proc. Natl. Acad. Sci. *113*, 3639–3644.

Whitney, J.C., Chou, S., Russell, A.B., Biboy, J., Gardiner, T.E., Ferrin, M.A., Brittnacher, M., Vollmer, W., and Mougous, J.D. (2013). Identification, structure, and function of a novel type VI secretion peptidoglycan glycoside hydrolase effector-immunity pair. J. Biol. Chem. *288*, 26616–26624.

Whitney, J.C., Quentin, D., Sawai, S., LeRoux, M., Harding, B.N., Ledvina, H.E., Tran, B.Q., Robinson, H., Goo, Y.A., Goodlett, D.R., et al. (2015). An Interbacterial NAD(P)+ Glycohydrolase Toxin Requires Elongation Factor Tu for Delivery to Target Cells. Cell *163*, 607–619.

Wiener, M., Freymann, D., Ghosh, P., and Stroud, R.M. (1997). Crystal structure of colicin Ia. Nature *385*, 461–464.

Williams, S.G., Varcoe, L.T., Attridge, S.R., and Manning, P.A. (1996). Vibrio cholerae Hcp, a secreted protein coregulated with HlyA. Infect. Immun. *64*, 283–289.

Wilton, M., Wong, M.J.Q., Tang, L., Liang, X., Moore, R., Parkins, M.D., Lewenza, S., and Dong, T.G. (2016). Chelation of Membrane-Bound Cations by Extracellular DNA Activates the Type VI Secretion System in Pseudomonas aeruginosa. Infect. Immun. *84*, 2355–2361.

Wolf, A.A., Jobling, M.G., Wimer-Mackin, S., Ferguson-Maltzman, M., Madara, J.L., Holmes, R.K., and Lencer, W.I. (1998). Ganglioside Structure Dictates Signal Transduction by Cholera Toxin and Association with Caveolae-like Membrane Domains in Polarized Epithelia. J. Cell Biol. *141*, 917–927.

Wong, M.J.Q., Liang, X., Smart, M., Tang, L., Moore, R., Ingalls, B., and Dong, T.G. (2016). Microbial Herd Protection Mediated by Antagonistic Interaction in Polymicrobial Communities. Appl. Environ. Microbiol. *82*, 6881–6888.

Yang, G., Dowling, A.J., Gerike, U., ffrench-Constant, R.H., and Waterfield, N.R. (2006). Photorhabdus virulence cassettes confer injectable insecticidal activity against the wax moth. J. Bacteriol. *188*, 2254–2261.

Yin, M., Yan, Z., and Li, X. (2019). Architecture of type VI secretion system membrane core complex. Cell Res. *29*, 251.

Zhao, W., Caro, F., Robins, W., and Mekalanos, J.J. (2018). Antagonism toward the intestinal microbiota and its effect on Vibrio cholerae virulence. Science *359*, 210–213.

Zheng, J., and Leung, K.Y. (2007). Dissection of a type VI secretion system in Edwardsiella tarda. Mol. Microbiol. *66*, 1192–1206.

Zheng, J., Shin, O.S., Cameron, D.E., and Mekalanos, J.J. (2010). Quorum sensing and a global regulator TsrA control expression of type VI secretion and virulence in Vibrio cholerae. Proc. Natl. Acad. Sci. U. S. A. *107*, 21128–21133.

Zheng, J., Ho, B., and Mekalanos, J.J. (2011). Genetic Analysis of Anti-Amoebae and Anti-Bacterial Activities of the Type VI Secretion System in Vibrio cholerae. PLoS ONE *6*.

Zheng, S., Sham, L.-T., Rubino, F.A., Brock, K.P., Robins, W.P., Mekalanos, J.J., Marks, D.S., Bernhardt, T.G., and Kruse, A.C. (2018). Structure and mutagenic analysis of the lipid II flippase MurJ from Escherichia coli. Proc. Natl. Acad. Sci. U. S. A. *115*, 6709–6714.

Zoued, A., Durand, E., Bebeacua, C., Brunet, Y.R., Douzi, B., Cambillau, C., Cascales, E., and Journet, L. (2013). TssK Is a Trimeric Cytoplasmic Protein Interacting with Components of Both Phage-like and Membrane Anchoring Complexes of the Type VI Secretion System. J. Biol. Chem. *288*, 27031–27041.

Zoued, A., Durand, E., Brunet, Y.R., Spinelli, S., Douzi, B., Guzzo, M., Flaugnatti, N., Legrand, P., Journet, L., Fronzes, R., et al. (2016). Priming and polymerization of a bacterial contractile tail structure. Nature *531*, 59–63.

Zoued, A., Durand, E., Santin, Y.G., Journet, L., Roussel, A., Cambillau, C., and Cascales, E. (2017). TssA: The cap protein of the Type VI secretion system tail. BioEssays News Rev. Mol. Cell. Dev. Biol. *39*.

Zupan, J., Hackworth, C.A., Aguilar, J., Ward, D., and Zambryski, P. (2007). VirB1* Promotes T-Pilus Formation in the vir-Type IV Secretion System of Agrobacterium tumefaciens. J. Bacteriol. *189*, 6551–6563.

CHAPTER 2

The type VI secretion system sheath assembles at the end distal from the membrane anchor

Andrea Vettiger[1], Julius Winter[1], Lin Lin[1] and Marek Basler[1]*

[1]Focal Area Infection Biology, Biozentrum, University of Basel, Klingelbergstrasse 50/70, 4056 Basel, Switzerland

* Correspondence and requests for materials should be addressed to M.B. (email: marek.basler@unibas.ch)

Supplementary Figures and Tables to this article can be found in Appendix A. Supplementary Video files 1-6 can be found online at the publishers webpage:
https://www.nature.com/articles/ncomms16088#supplementary-information

Statement of contribution:

I designed and performed experiments, analyzed and interpreted results and contributed to paper writing and figure preparation. I also trained and supervised nanoscience MSc student J.W. in standard microbiology techniques as well as fluorescence live-cell microscopy in combination with photobleaching.

ARTICLE

The type VI secretion system sheath assembles at the end distal from the membrane anchor

Andrea Vettiger[1], Julius Winter[1], Lin Lin[1] & Marek Basler[1]

The bacterial Type VI secretion system (T6SS) delivers proteins into target cells using fast contraction of a long sheath anchored to the cell envelope and wrapped around an inner Hcp tube associated with the secreted proteins. Mechanisms of sheath assembly and length regulation are unclear. Here we study these processes using spheroplasts formed from ampicillin-treated *Vibrio cholerae*. We show that spheroplasts secrete Hcp and deliver T6SS substrates into neighbouring cells. Imaging of sheath dynamics shows that the sheath length correlates with the diameter of spheroplasts and may reach up to several micrometres. Analysis of sheath assembly after partial photobleaching shows that subunits are exclusively added to the sheath at the end that is distal from the baseplate and cell envelope attachment. We suggest that this mode of assembly is likely common for all phage-like contractile nanomachines, because of the conservation of the structures and connectivity of sheath subunits.

[1] Focal Area Infection Biology, Biozentrum, University of Basel, Klingelbergstrasse 50/70, 4056 Basel, Switzerland. Correspondence and requests for materials should be addressed to M.B. (email: marek.basler@unibas.ch).
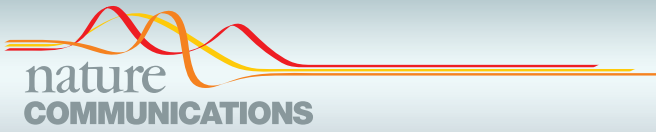
Chapter 2: The type VI secretion system sheath assembles at the end distal from the membrane anchor

Nanomachines related to contractile phage tails share basic components needed for generating mechanical force to puncture target cell membranes and to translocate proteins: a rigid tube with a sharp tip, a contractile sheath and a baseplate[1–4]. The bacterial Type VI secretion systems (T6SS), composed of ∼13 core components, are widely distributed among Gram-negative bacteria and deliver various toxins into both eukaryotic and bacterial cells[5,6]. Current model of T6SS mode of action predicts that the assembly starts by formation of membrane complex formed from TssJLM (ref. 7). Next, TssK protein specifically interacts with the membrane complex and likely recruits TssEFG (ref. 8) to form a baseplate together with VgrG/PAAR spike complex associated with T6SS effectors[9–12]. This likely triggers polymerization of Hcp tube and VipA/VipB (TssB/TssC) sheath wrapped around the tube[13–15]. Interestingly, the sheath assembly in *Escherichia coli* is dependent on the presence of TssA forming a dodecameric structure colocalizing with the end of a polymerizing sheath, which is distal from the assembly initiation[16]. However, TssA1 in *Pseudomonas aeruginosa* was shown to interact with TssK1 and TssF1 in the baseplate[17]. This is likely due to the fact that TssAs of *E. coli* and *P. aeruginosa* share little homology and belong to two different subfamilies[17].

Using live-cell fluorescence microscopy, the sheath dynamics can be characterized by three distinct steps: (i) sheath polymerization into a fully extended state, (ii) rapid contraction and (iii) disassembly by ClpV. In several organisms, T6SS sheaths were observed to assemble across the whole cell suggesting that sheath length is limited only by cell diameter. This was shown by direct observations of TssB in *Vibrio cholerae*, *Serratia marcescens*, and *E. coli*[18–20] as well as indirectly by imaging of ClpV localization in *P. aeruginosa*, *Burkholderia thailandensis* and *Bacteroidetes*[21–24]. The sheath contracts to about half of its initial length, presumably propelling the spike and Hcp with the associated effectors into target cells[11,25–29]. The contracted sheath is immediately recognized and disassembled by the AAA+ ATPase ClpV, making VipA/VipB subunits available for the assembly of new structures[21,30–32]. Even though live-cell imaging of T6SS assembly provided unprecedented insights into the mode of action of the T6SS, it is unclear at which end and how new sheath subunits are incorporated into the growing sheath polymer. Interestingly, even for related phage-like contractile nanomachines, there is no direct evidence for the directionality of the sheath assembly[3,33].

Recently, *V. cholerae* was reported to tolerate cell wall synthesis inhibitors by the formation of viable, although non-dividing spherical cells or spheroplasts[34,35]. This allows *V. cholerae* to survive for up to 6 h in the presence of antibiotics 20 times above the minimal inhibitory concentration (MIC) without osmo-protecting agents in the media[34]. Importantly, unlike L-forms of *E. coli* or *Corynebacterium glutamicum*[36,37], *V. cholerae* spheroplasts increase their size significantly as cells continue to grow without cell division[34].

Here we show that the T6SS of *V. cholerae* remains active in cells exposed to ampicillin. Moreover, increased cell size during spheroplast formation correlates with increased sheath length, which allowed us to partially photobleach assembling sheaths and determine at which end of the sheath the soluble subunits are incorporated.

Results

Sheath length is limited by cell size. It was previously reported that in the presence of β-lactam antibiotics, *V. cholerae* forms viable spheroplasts[34]. To test if T6SS remains active in such cells, we exposed exponentially growing *V. cholerae* cells expressing

VipA-msfGFP to ampicillin (500 µg ml^{-1}, 100× MIC). In agreement with the published observations, cells quickly lost their rod shape and transformed into spheres by blebbing from the mid-cell while simultaneously losing peptidoglycan (PG) as detected using the fluorescent D-amino acid analogue HADA[34,38,39] (Fig. 1a). Importantly, VipA-msfGFP and ClpV-mCherry2 localization dynamics in spheroplasts suggested that T6SS sheaths cycle between assembly, contraction and disassembly similarly to untreated cells (Fig. 1b,c Supplementary Movies 1–3). Quantification of spheroplast induction and T6SS dynamics revealed that exposure to ampicillin for 40 min at 37 °C generated the highest proportion (89.75%) of spheroplasts displaying dynamic T6SS sheaths (1,007 out of 1,122 cells; Fig. 1d, Supplementary Movie 1). Therefore, this time point was chosen for spheroplast induction in all subsequent experiments unless indicated differently. Due to impaired cell division, the cells increased their size during 40 min exposure to ampicillin from normal rod-shaped cells 1.53 µm^2 to spheroplasts 6.59 µm^2 (Fig. 1a,e). Interestingly, the average sheath length increased threefold during ampicillin treatment from 0.85 µm to 2.63 µm. Sheaths often spanned across the entire spheroplast and their length correlated ($R^2 = 0.91$) with cell diameter (Fig. 1a,f,g).

Incubation beyond 60 min in the presence of ampicillin (500 µg ml^{-1}, 100× MIC) resulted in even larger cells and sheaths, however also occasionally led to outer membrane detachment and cells lysis (Supplementary Fig. 1a). When *V. cholerae* cells were incubated with only 100 µg ml^{-1} (20× MIC) ampicillin, most spheroplasts remained intact for up to 6 h and grew to surface area of up to 28.54 µm^2 and assembled sheaths as long as 8.4 µm (Fig. 1h). Overall, these observations indicate that in normal cells the length of T6SS sheaths is limited by available space given by the cell size and when such limitation is absent, the sheaths can assemble to up to ten times longer structures.

Spheroplasts assemble functional T6SS. To test if the observed sheath dynamics in ampicillin treated cells corresponds to a functional T6SS, we first monitored Hcp secretion. Spheroplasts were grown to OD = 1, washed twice, inoculated into fresh LB medium supplemented with ampicillin and incubated for 20 min at 37 °C. Proteins from culture supernatant were precipitated and separated by SDS–polyacrylamide gel electrophoresis for immuno-detection of Hcp. This clearly showed that spheroplasts secreted the same amount of Hcp as the untreated rod-shaped cells. Importantly, no Hcp was detected in the supernatant of spheroplasts or rod-shaped cells lacking *vipB*, *tssM* or *tssJ* (Fig. 2a, Supplementary Fig. 2a). Similarly, deletion of *vipB*, *tssM* and *tssJ* decreased number of T6SS sheaths in the spheroplasts to the levels observed in the untreated cells (Fig. 2b).

Furthermore, we monitored protein translocation from spheroplasts into target cells by two different assays: (i) detection of VgrG2 exchange between sister cells and (ii) permeabilization of *E. coli* prey cells. As reported previously for rod-shaped cells[29], spheroplasts formed from cells lacking the tip protein VgrG2 were unable to assemble sheaths (3,500 cells were analysed). When such spheroplasts (Δ*vgrg2*/*vipA-msfGFP*) were mixed with spheroplasts formed from cells with an intact T6SS (*clpV-mCherry2*), on average one sheath assembly was detected in 15 spheroplasts during 5 min (Fig. 2c,d, Supplementary Movie 4). Such frequency of sheath assembly is comparable to what was previously described for intact cells (1 in 20 cells in 5 min)[29]. None of ∼10,000 spheroplasts imaged under various conditions contained both msfGFP and mCherry2 signals, indicating that no spheroplast fusion occurred. Furthermore, no sheath assembly was detected in spheroplasts lacking VgrG2,
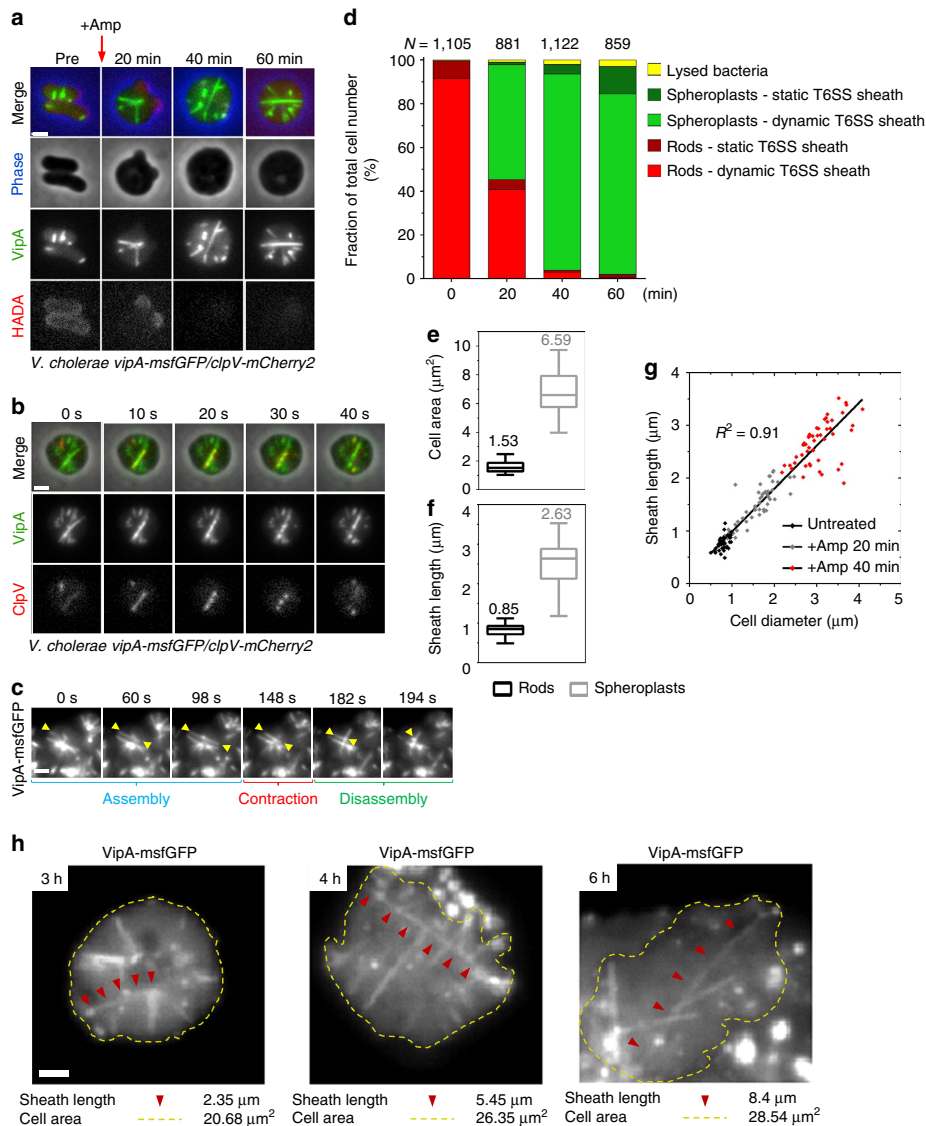
ARTICLE

Figure 1 | V. cholerae spheroplasts assemble long and dynamic T6SS sheaths. (a) Cells were grown in the presence of HADA to OD 0.5 before addition of 500 µg ml^{-1} ampicillin (Amp) and harvested for imaging at indicated time points after antibiotic addition. Cell morphology, VipA-msfGFP localizations (sheath dynamics) and HADA staining (PG) were monitored during spheroplast induction. Top row shows a merge of all three channels (phase contrast is pseudo coloured in blue), channels below are displayed individually as grey scale images. Full time-lapse series of each time point are shown in Supplementary Movie 2. Supplementary Movie 3 shows 50 × 50 µm field of view of spheroplasts after incubation with ampicillin for 40 min. Large fields of view for time points 20 min and 40 min are shown in Supplementary Fig. 1b. **(b)** VipA-msfGFP/ClpV-mCherry2-labelled *V. cholerae* spheroplasts (500 µg ml^{-1} ampicillin, 40 min) were monitored for sheath assembly, contraction and disassembly for 5 min. The top row shows a merge of both fluorescence channels and phase contrast, the fluorescence channels are displayed individually as grey scale images. **(c)** VipA-msfGFP labelled spheroplasts (500 µg ml^{-1} ampicillin, 40 min) were imaged for 5 min at a rate of 2 s per frame. Yellow arrow heads indicate a T6SS sheath undergoing assembly into a fully extended state, contraction and disassembly. **(d)** Cells were grown for indicated time points in presence of 500 µg ml^{-1} ampicillin and analysed for cell morphology (lysed, rod shaped and spheroplast) and T6SS dynamics (dynamic or static VipA-msfGFP localization). All data were acquired from three independent experiments. *N*, total number of cells analysed for each time point. **(e,f)** Cell surface area (**e**) and length (**f**) of the longest fully extended VipA-msfGFP structure was measured for 50 rod-shaped cells or spheroplasts formed during 40 min exposure to ampicillin. Data are represented as box-and-whisker plots with minima and maxima; 75% of all data points lay within the box, horizontal lines and numbers represent median values. **(g)** The coefficient of determination (R^2) between sheath length and cell diameter was calculated from 50 cells in each category. Data are fitted with a linear regression line. All data were acquired from three independent experiments. **(h)** Spheroplasts formation was induced for the indicated time by incubation of cells at 37 °C on 1% agarose pads containing 100 µg ml^{-1} ampicillin. The VipA-msfGFP fluorescence channel is displayed. Cell outlines are shown in yellow, red arrow heads indicate the longest sheath within the observed cell. Scale bars, 1 µm.
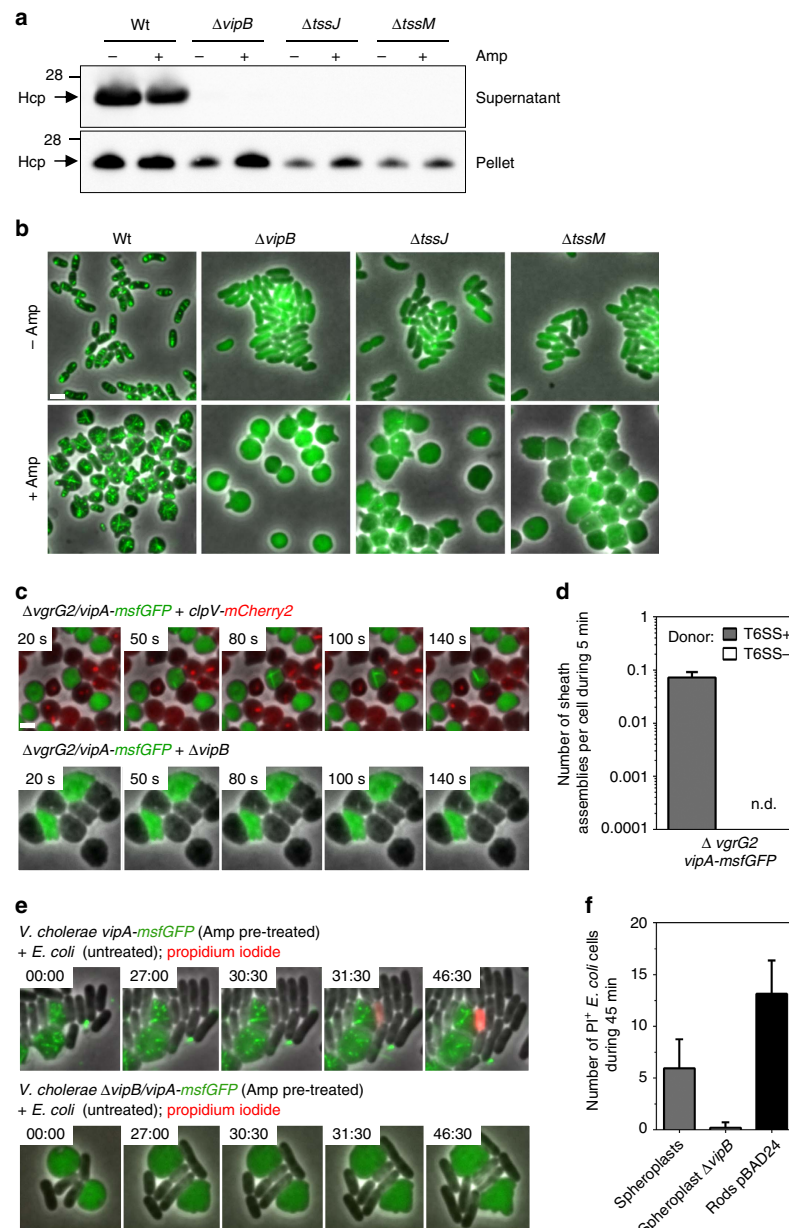
Figure 2 | The T6SS appears to be functional in ampicillin-induced spheroplasts. (**a**) Preinduced spheroplasts (500 μg ml⁻¹ ampicillin for 40 min) and untreated rod-shaped cells were washed twice and inoculated in fresh medium. Presence of Hcp was detected in culture supernatant and cell pellets of indicated strains after 20 min incubation. The molecular weight is indicated on the left in kilodaltons. Full blots and Coomassie Blue stained gels are provided in Supplementary Fig. 2a. (**b**) Indicated strains (all *vipA-msfGFP* background) were monitored for sheath assembly. Representative images of untreated rod-shaped cells and spheroplasts (500 μg ml⁻¹ ampicillin for 40 min) are shown. Scale bar, 2 μm. (**c,d**) VipA-msfGFP labelled recipient spheroplasts (ampicillin 500 μg ml⁻¹, 40 min) lacking VgrG2 were co-incubated with either ClpV-mCherry2 labelled (top) or T6SS-negative (Δ*vipB*; bottom) donor strains. Sheath assembly in recipient cells was monitored (**c**) and quantified (**d**) in $N = 2,000$ VipA-msfGFP cells for each mixture. See Supplementary Movie 4 for complete time-lapse series. Full fields of view are provided in Supplementary Fig. 2b. (**e**) VipA-msfGFP labelled T6SS positive (top) and T6SS-negative (bottom) *V. cholerae* spheroplasts (pretreated in ampicillin 500 μg ml⁻¹ for 40 min, washed in LB) were co-incubated with MG1655 prey cells (grey) on agarose pads containing 100 μg ml⁻¹ ampicillin and 1 μg ml⁻¹ PI. (**f**) Number of PI⁺ *E. coli* cells was quantified from 20 fields of view (30×30 μm) during 45 min co-incubation with indicated *V. cholerae* strains. See Supplementary Movie 5 for complete time-lapse series. Full fields of view are provided in Supplementary Fig. 2c. All data were acquired from three independent biological experiments and are represented as mean ± s.d. Scale bar, 1 μm.

which were co-incubated with spheroplasts formed from a secretion incompetent $\Delta vipB$ strain (Fig. 2c,d).

To test if spheroplasts deliver toxins into prey cells and lyse them, we mixed ampicillin-induced *V. cholerae* spheroplasts with ampicillin resistant *E. coli* (carrying pUC19) at 1:1 ratio on agarose pads containing $100 \mu g ml^{-1}$ ampicillin as well as propidium iodide (PI) to identify permeabilized cells. After 45 min of co-incubation with T6SS positive spheroplasts, we detected on average 5.95 PI-positive *E. coli* cells (out of on average 85 *E. coli* cells in total) in a $30 \times 30 \mu m$ field of view with at least 50% confluence. This was comparable to average 13.15 PI positive *E. coli* cells detected upon co-incubation with rod-shaped *V. cholerae* cells. Importantly, no PI-positive *E. coli* cells were detected in a mixture with T6SS-negative spheroplasts (Fig. 2e,f; Supplementary Movie 5). Overall, these data support that the T6SS is functional in ampicillin-induced *V. cholerae* spheroplasts, suggesting that PG crosslinking is at least partially dispensable for T6SS activity.

Sheaths quickly contract to half their length. Measurement of sheath length in rod-shaped cells is potentially imprecise because it is limited by spatial resolution of an optical microscope. To provide a better estimate for an extent to which sheaths contract, we measured the level of sheath contraction in spheroplasts. Dynamic processes such as sheath polymerization and contraction can be visualized in a kymogram by plotting fluorescence signal as function of distance over time along a designated line profile. This allows to distinguish between distinct steps of sheath dynamics in a single image. We followed 50 sheaths, which transitioned from an extended to a contracted state within two consecutive frames at a frame rate of 2 s frame^{-1}. On average, the comparison of the length of extended and contracted sheaths shows that the sheaths contract to 48.7% of the extended sheath length (Fig. 3, Supplementary Fig. 3).

In addition, to measure speed of contraction, we imaged spheroplasts for 5 s with a frame rate of 500 frames per sec and identified contractions by image analysis (Fig. 3a, Supplementary Fig. 3). Interestingly, in all 5 cases the sheaths contracted between two consecutive frames, therefore faster than in 2 ms (Fig. 3b). The longest observed contracting sheath was 3.29 μm long and

contracted by 1.6 μm to 1.69 μm (Fig. 3a,b). Therefore, we can estimate that sheath contraction occurs faster than 800 nm ms^{-1}.

Sheath polymerizes at the distal end. Live-cell fluorescence microscopy shows that sheath assembly starts from one site in a cell and in time progresses across the whole width of the cell. The initial point of assembly is static, suggesting that this is where the sheath is connected to the membrane anchored baseplate[7,16]. In theory, there are three possible mechanisms how sheath polymers may assemble from soluble subunits: (i) subunits are added at the end distal to the baseplate, (ii) subunits are inserted at the baseplate or (iii) subunits are inserted in between the existing subunits along the whole polymer. To distinguish the three alternative mechanisms, we reasoned that we could photobleach a section of an assembling sheath and then monitor intensity and localization of the photobleached section relative to the rest of the assembling sheath. Depending on the three theoretical mechanisms of sheath assembly described above, these results may be expected: (i) photobleached section of the sheath would be fixed in intensity and relative localization, (ii) photobleached section would have fixed intensity and move away from the site of assembly initiation and (iii) photobleached section would change intensity, localization and size (see the three possible mechanisms in Supplementary Fig. 4).

With our experimental set-up, we estimated the photobleached area to be ∼0.8 μm in diameter, which is an average length of a sheath in a rod shape cell and we were therefore unable to bleach polymerizing sheaths without photobleaching most of the cell (Supplementary Fig. 5). Spheroplasts assemble sheaths that are several times longer therefore such sheaths should be possible to photobleach only partially. However, wild-type spheroplasts assemble multiple sheaths, which are often difficult to resolve and individually track using standard wide field microscopy (Fig. 1d).

Interestingly, the *V. cholerae* strain lacking *vgrG1* and *vasX* was reported to contain about three times less sheaths than wild-type cells, while displaying normal T6SS dynamics (Fig. 4a)[29]. Indeed, deletion of *vgrG1* and *vasX* decreased number of sheaths assembled per cell in 2 min from 4.44 in wild-type rod-shaped cells to 1.57 in double mutant cells and from 7.08 to 2.53 in the respective spheroplasts (Fig. 4b). Importantly, the sheaths often
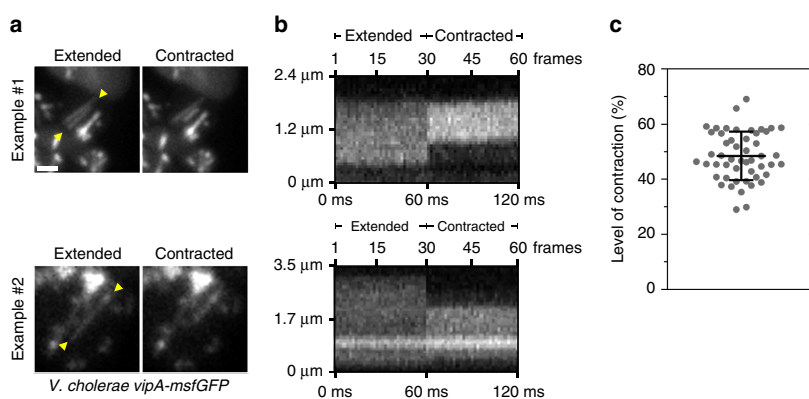
Figure 3 | The sheath contracts within <2 ms to half its extended length. (**a**) High-speed imaging (500 frames per sec) of two representative contraction events in VipA-msfGFP labelled spheroplasts (ampicillin 500 μg ml^{-1}, 40 min). Depicted are maximum intensity projections of 30 frames pre and post sheath contraction. In between the yellow arrow heads a line profile was drawn for subsequent kymogram analysis shown in **b**. Additional examples can be found in Supplementary Fig. 3. Scale bar, 1 μm. (**c**) Level of sheath contraction was measured for 50 individual contraction events in spheroplasts imaged at a rate of 2 s per frame. Contracted sheath length was subtracted from extended state and normalized to extended sheath length. Data were acquired from three independent experiments and are represented as mean ± s.d.
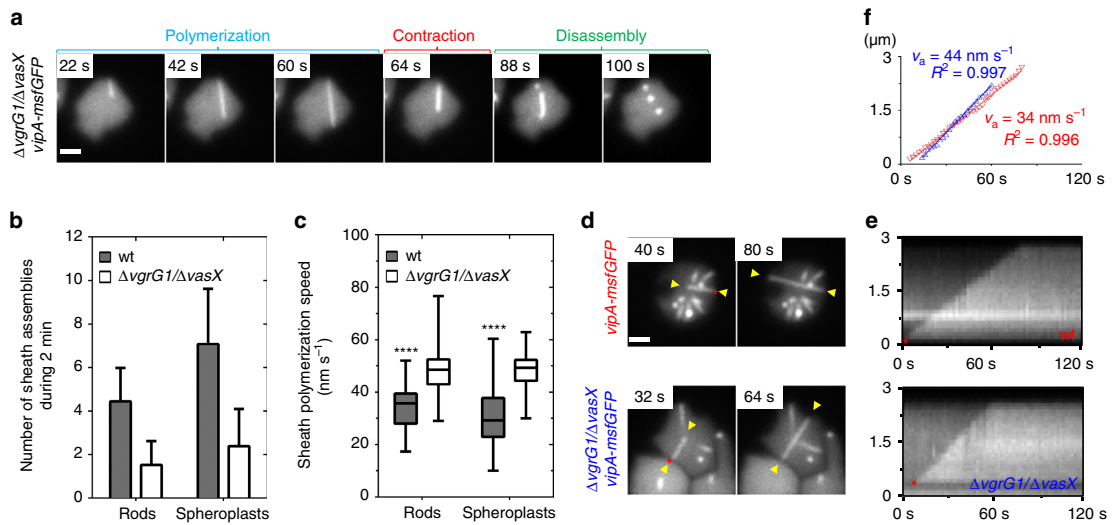
Figure 4 | Sheath polymerization speed negatively correlates with number of sheaths per cell. (**a**) VipA-msfGFP labelled $\Delta vgrG1/\Delta vasX$ spheroplasts (500 µg ml^{-1} ampicillin, 40 min) were imaged for 5 min at an acquisition rate of 2 s per frame. Different steps of T6SS sheath dynamics are labelled. (**b**) Number of sheath assemblies (VipA-msfGFP labelled) was assessed in rod-shaped cells and spheroplasts. For each strain and condition, 50 cells were analysed. Data are represented as mean ± s.d. (**c**) Polymerization speed was calculated from kymograms of 50 sheaths for each strain and condition. Data are represented as box-and-whisker plots with minima and maxima; 75% of all data points lay within the box, horizontal line and numbers represent median values. Two-way ANOVA; ****$P < 0.0001$. (**d–f**) Indicated strains were monitored for sheath assembly for 2 min. Examples of sheath polymerization are shown (**d**). Corresponding kymograms (**e**) and corresponding sheath polymerization speed measurements (**f**) (v_a) of wt (red) and $\Delta vgrG1/\Delta vasX$ (blue) spheroplasts are shown on the right. Linear regression models were fitted and coefficient of determination (R^2) was calculated. Red asterisks indicate the origin of sheath polymerization. Yellow arrow heads indicate polymerizing sheath and were used to draw a straight line for kymogram analyses on the right. Scale bars, 1 µm.

assembled into structures extending across the whole spheroplast (Fig. 4a,d). Based on kymogram analysis, we also noticed that sheath assembly speed increased significantly (two-way analysis of variance (ANOVA), $P < 0.0001$) from 38 nm s^{-1} in wild-type cells to 55 nm s^{-1} in $\Delta vgrG1/\Delta vasX$ cells (Fig. 4c,e,f). However, no significant differences in polymerization speed were found between rod-shaped cells and spheroplasts (two-way ANOVA, $P < 0.58$; Fig. 4c). In all cases sheath polymerization speed was constant over time ($R^2 > 0.99$; Fig. 4f). This suggests that the absence of cross-linked PG and increased sheath length has no impact on sheath assembly kinetics.

To address sheath assembly mechanism, VipA-msfGFP localization was monitored in $\Delta vgrG1/\Delta vasX/vipA-msfGFP$ spheroplasts for 2 min at a frame rate of 2 s per frame (Fig. 5a–d, Supplementary Movie 6). After 30 s (15 frames), cells were partially photobleached using a laser beam following a straight line (Fig. 5a,d). Since the subcellular localization and timing of sheath assembly is random for each individual cell and happens very quickly, we performed the photobleaching randomly across the whole field of view. Later, we analysed the collected time-lapse series and manually searched for sheaths that: (i) were polymerizing during the time before photobleaching, (ii) were only partially photobleached and (iii) kept polymerizing in the same direction after photobleaching. For 25 of such events, we plotted fluorescence intensity along the assembling sheath structure in time (kymogram) (Fig. 5b) and analysed speed of sheath assembly (Fig. 5c) as well as intensity and localization of the photobleached section relative to the point of the sheath assembly initiation (Fig. 5e–g). In all cases, the sheaths polymerized along a straight line and sheath polymerization speed before photobleaching was identical to that after photobleaching as determined by linear regression analysis ($R^2 > 0.99$).

This provides a strong evidence that indeed the same sheath assembly was observed during the whole time lapse (Fig. 5c, Supplementary Fig. 6). Furthermore, we identified few sheaths which contracted after photobleaching (Supplementary Fig. 6), indicating that the photobleaching has no influence on sheath dynamics.

Importantly, the non-bleached section of the sheath assembled before photobleaching as well as the section that was photobleached remained at the same distance from the point of assembly initiation (Fig. 5f). At the same time, low intensity sheath structures extended at the end opposite of the assembly initiation. This section of the sheath was presumably assembled from the partially photobleached subunits that were present in the cell cytosol during laser illumination (Fig. 5e,f). Furthermore, in all cases, the photobleached sections of sheaths retained a fluorescence intensity similar to the intensity of the background cytosolic fluorescence and no recovery of the fluorescence signal was observed (Fig. 5g). Overall, these observations support that sheath subunits are added at the end distal to the baseplate and are not incorporated at the end close to the baseplate or between the subunits of an existing sheath polymer.

Discussion

The remarkable ability of the *V. cholerae* cells to form large viable spheroplasts with functional T6SS allowed us to image assembly of partially photobleached sheaths and show that sheath subunits are added at the end distal from the assembly initiation. The first ring of a sheath assembles on a baseplate and the next sheath rings assemble on the previous sheath rings. Since T6SS sheaths share common fold and inter-subunit connectivity with phage-like sheaths of other contractile nanomachines[3,40–42], we suggest
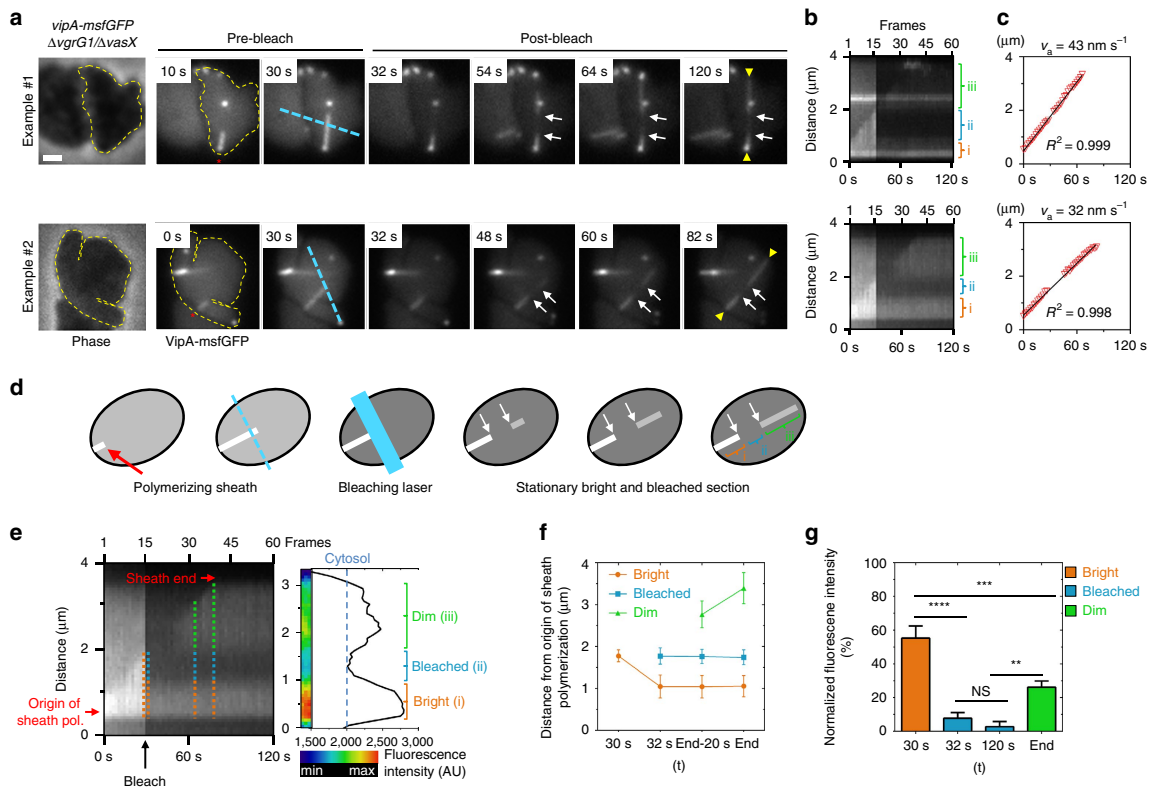
ARTICLE

Figure 5 | Sheath subunits are incorporated at the end distal from the assembly initiation. (**a**) Phase contrast images of VipA-msfGFP labelled $\Delta vgrG1/\Delta vasX$ spheroplasts (500 µg ml^{-1} ampicillin, 40 min) are shown on the left. Cell shapes are outlined by dashed yellow lines based on the phase contrast image. Spheroplasts were monitored for sheath assembly for 2 min at a rate of 2 s per frame. After 30 s of image acquisition, bleaching laser was passed along the indicated line path (dashed turquoise line). Red asterisks indicate the origin of sheath polymerization. White arrows indicate bleached section on the sheath. In between the yellow arrow heads a straight line was drawn for subsequent kymogram analyses and fluorescence intensity measurements (**b**) as well as for the determination of sheath polymerization speed (v_a) (**c**) A linear regression model was fitted and coefficient of determination (R^2) was calculated. Additional examples as well as corresponding time-lapse movies can be found in Supplementary Fig. 6 and Supplementary Movie 6. Scale bar, 1 µm. (**d**) Conceptual representation of results obtained from photo bleaching experiments. (**e**) Detailed analysis of the example #2 in **a**: fluorescence intensity measurements and heat map were generated using Fiji. Based on fluorescence intensity curves, different sections on sheath were classified as 'bright' (i, orange), 'bleached' (ii, turquoise) and 'dim' (iii, light green). (**f**) For each section, corresponding distances from the origin of sheath polymerization was measured as shown by dotted lines on the kymogram in **e**. The first two distance measurements were performed directly before and after photobleaching. The latter two measurements were performed 20 s before the end of sheath polymerization and when sheath polymerization was completed. (**g**) Fluorescence intensity was determined from all 25 line profiles of successfully photobleached sheaths as shown in **e**. Fluorescence intensity of the corresponding section on the sheath was measured at the indicated time points and was normalized for each time point to the cytosolic background fluorescence (defined as 0% fluorescence intensity). Data are represented as mean ± s.e.m. One-way ANOVA; ****$P < 0.0001$, ***$P < 0.001$, **$P < 0.01$, NS, non-significant.

that the same assembly mechanism likely applies to all related contractile tails. This mode of assembly was indeed predicted based on available structures of baseplates and sheaths[3,43] because sheaths strongly attach to baseplates through conserved linkers[14,15,42]. This mode of sheath assembly has important implications for the role of certain TssA proteins in T6SS assembly. The distal end of T6SS sheath in *E. coli* is capped by TssA, which is required for sheath polymerization, interacts with Hcp and TssC, and colocalizes with the distal end of a polymerizing sheath[16]. Our data therefore confirm the previous suggestions that proteins similar to TssA in *E. coli* promote insertion of new sheath and tube subunits[16]. However, since TssA proteins vary in their predicted structure and some T6SS clusters seem to lack TssA proteins similar to TssA in *E. coli*[17], it is therefore likely that certain sheath-tube complexes assemble

without a need for TssA-like cap or that another, yet to be identified protein, fulfills this role.

Ampicillin treatment of *V. cholerae* cells seems to have no obvious effect on T6SS function. The sheaths in spheroplasts undergo assembly, contraction and disassembly by ClpV like sheaths of untreated cells (Fig. 1b,c)[18–21]. Additionally, spheroplasts secrete Hcp, deliver VgrG2 to neighbouring cells and kill target cells (Fig. 2a,c,e). This suggests that T6SS is functional without strong anchoring of the membrane complex to an intact peptidoglycan. Indeed, peptidoglycan has to be cleaved locally to allow for T6SS assembly[44]. Importantly, the spheroplasts have intact inner and outer membranes[35] (Supplementary Fig. 1a) and thus the membrane complex embedded in both membranes[7] likely provides strong enough attachment to allow for T6SS function. Indeed, the sheath

assembly in spheroplasts depends on the presence of both TssM and TssJ (Fig. 2b).

The sheath-tube polymerization in spheroplasts may progress for up to several micrometres, and the sheath length seems to be only limited by the physical space available between the opposing sides of the cell (Fig. 1g). Cells with fewer assembled sheaths, thus presumably with more available soluble subunits, assemble sheaths faster than the cells with many assembled sheaths (Fig. 4c). This suggests that the speed of sheath polymerization may be partially limited by the amount of available soluble subunits. Furthermore, when the amount of sheath or tube subunits is below a certain threshold, only short dynamic sheaths assemble[18,29].

The fact that T6SS sheath length appears to be unregulated (Fig. 1g,h) stands in contrast with the strictly regulated assembly mechanism of most of the related phage-like contractile tails, where a tape measure protein is critical for tail assembly and its length defines the number of tube and sheath rings assembled into the particle[3,43]. Interestingly, shorter T6SS sheaths were suggested to be sufficient for effector delivery by *V. cholerae*[29], however, longer sheaths may increase the efficiency of effector delivery. Longer sheaths would also likely deliver larger amounts of Hcp associated effectors during a single sheath contraction[28]. Overall energy released during sheath contraction is likely proportional to the sheath length[42], therefore long sheaths might also be required for delivery of large folded hydrophilic effectors associated with the spike complex[11,45]. On the other hand, it is possible that after reaching a certain threshold sheath length, the energy of contraction would be greater than the energy needed to destabilize T6SS baseplate or membrane complex and such sheaths would fail to deliver any effectors.

Overall, we show that imaging of large viable spheroplasts provides new opportunities to dissect T6SS assembly, function and dynamics. More generally, large cells lacking cell wall may be used to study systems, which are challenging to visualize by light microscopy in small bacterial cells.

Methods

Strains. Parental *V. cholerae* 2740-80 and VipA-msfGFP labelled derivatives were described previously[15,18,21,29]. *E. coli* MG1655 were used as prey cells for cell permeability assays. A detailed strain list can be found in Supplementary Table 1. Bacteria were grown in Luria–Bertani (LB) broth at 37 °C. Liquid cultures were grown aerobically. Antibiotic concentrations used were streptomycin (100 μg ml^{-1}) and ampicillin (100–500 μg ml^{-1}).

Spheroplast induction. Similar procedures as described recently were applied[34]. Briefly, *V. cholerae* overnight cultures were diluted 1:1,000 into fresh LB and grown until early exponential growth phase (OD ~0.5) before the addition of ampicillin (500 μg ml^{-1}, 100× MIC). If not indicated differently, spheroplast induction cultures were incubated for 40 min at 37 °C, 100 r.p.m. and subsequently harvested by centrifugation (2 min, 3,000g) for further experimental procedures. For incubation times beyond 1 h, 100 μg ml^{-1} (20× MIC) ampicillin was used. Cell diameter and sheath length of the longest structure per cell during the observation period were measured manually using 'straight line' tool in Fiji[46].

HADA staining. For monitoring PG alterations during spheroplast induction blue fluorescent D-amino acid analogue HADA was used[38]. HADA (50 mM) was added to the cultures at OD ~0.2. In *V. cholerae*, D-amino acids analogues are incorporated by penicillin-insensitive L,D transpeptidases allowing to stain PG in the presence of cell wall targeting antibiotics[34]. Before imaging, cells were washed 2x in fresh LB to get rid of excess dye.

Hcp secretion assay. Briefly, cells were grown to OD = 0.8–1.2. Spheroplasts were induced as described above. Subsequently, 1 ml of rod-shaped cells and spheroplasts were harvested by centrifugation (3,000g, 2 min) and washed twice before dilution into 1 ml of fresh medium supplemented with ampicillin (500 μg ml^{-1}) for spheroplasts cultures. Cells were incubated while shaking for 20 min, 100 r.p.m., 37 °C. Bacterial pellets and supernatants were separated by centrifugation (3,000g, 2 min). For detection of secreted Hcp in culture supernatant, 900 μl of supernatant were concentrated by TCA/acetone precipitation[47]. For detection of Hcp in cell

pellets 250 μl cells were harvested and resuspended in 80 μl Laemmli buffer and boiled for 95 °C. Proteins were separated on Novex 4–12% Bis-Tris SDS–polyacrylamide gel electrophoresis gels (Thermo Fisher Scientific) and transferred to nitrocellulose membrane for immuno-detection as previously described[29] or proteins were visualized directly by Coomassie Blue staining.

Interbacterial protein complementation assay. Similar procedures were applied as described previously[29]. Overnight cultures were washed once in LB and diluted 1:100 into fresh medium and cultivated to an OD at 600 nm of 0.5. Spheroplasts were induced as described above. Cells from 1 ml of the culture were concentrated to OD 10, mixed at a ratio of 1:4 (recipient to donor), subsequently spotted on a thin pad of 1% agarose in LB and covered with a glass coverslip. Spheroplasts were immediately imaged during an observation period of 1 h in multiple 5 min time-lapse series. For image analysis, total number of green fluorescent protein (GFP) positive cells were counted using the built in 'find maxima' function in Fiji with a 'noise tolerance' setting of 250 and activated edge maxima exclusion. For quantification of the number of sheath assemblies in recipient cells from time-lapse movies the 'temporal colour code' function was used. Three independent biological replicates were analysed.

Cell permeability assay. *E. coli* MG1655 prey cells, transformed with empty pUC19 vector (Thermo Fisher Scientific) mediating ampicillin resistance, were grown in the presence of ampicillin (100 μg ml^{-1}) to OD 1. Simultaneously, *V. cholerae* spheroplasts and rod-shaped control cells harbouring the pBAD24 vector mediating ampicillin resistance (predators) were grown and induced as described above. For both prey and predator cells, 1 ml of the culture was harvested and concentrated to OD 10. Cells were mixed at a ratio of 1:1 (prey to predator) and subsequently spotted on a thin pad of 1% agarose in LB containing ampicillin (100 μg ml^{-1}) as well as the cell permeability indicator PI (1 μg ml^{-1}) and covered with a glass coverslip. Cells were imaged for 45 min with a 30 s frame rate and the number of PI-positive *E. coli* cells was counted from twenty 30 × 30 μm fields of view with at least 50% confluence of cells.

Fluorescence microscopy and photobleaching. For fluorescence microscopy a Nikon Ti-E inverted motorized microscope with Perfect Focus System and Plan Apo 1003 Oil Ph3 DM (NA 1.4) objective lens was used. SPECTRA X light engine (Lumencore), ET-GFP (Chroma #49002) and ET-mCherry (Chroma #49008) filter set were used to excite and filter fluorescence. sCMOS camera pco.edge 4.2 (PCO, Germany; pixel size 65 nm) and VisiView software (Visitron Systems, Germany) were used to record images. Temperature was regulated to 30 °C and 95% humidity using an Okolab T-unit (Okolab). For high-speed image acquisition of sheath contraction, the field of view on the sCMOS camera was reduced to 400 lines and the image acquisition mode was set to streaming. This allowed image acquisition at a frame rate of 500 frames per second during a total of 5 s observation time.

For photobleaching experiments the GFP fluorescence was diminished using a VS-AOTF 488 nm Laser system mounted with iLas2 laser merge on the microscope, allowing simultaneous LED and laser illumination. Cells were monitored for sheath assembly for 2 min at a frame rate of 2 s per frame. After 30 s the laser was triggered with 100% output power for 0.1 ms per pixel and cells were photobleached along a line profile. Polymerizing sheaths were identified during image analysis and used for the generation of kymograms in Fiji. Polymerization speeds as well as fluorescence intensity profiles to identify 'bright', 'bleached' and 'dim' sections along the sheath were generated from kymograms. Distance from origin of sheath polymerization was measured after 30 s, 32 s, 20 s before end point of sheath assembly as well as the end point for each section. The end point of sheath assembly was identified as the last frame on which an increase of sheath length was clearly detected. Fluorescence intensity measurements were corrected for cytosolic background fluorescence at indicated time points.

Statistical analysis. Statistical parameters such as number of biological replicates and total analysed bacteria as well as levels of significance are reported in the figure legends. Linear regression analyses as well as one-way and two-way ANOVA with multiple comparisons and Tuckey *post hoc* test were calculated using GraphPad Prism version 6.05. If not indicated differently, data are represented as mean ± s.d.

Data availability. The authors declare that all data supporting the findings of this study are available from the corresponding authors upon request.

References

1. Ho, B. T., Dong, T. G. & Mekalanos, J. J. A view to a kill: the bacterial type VI secretion system. *Cell. Host. Microbe.* **15**, 9–21 (2014).
2. Kube, S. & Wendler, P. Structural comparison of contractile nanomachines. *AIMS Biophysics* **2**, 88–115 (2015).
3. Leiman, P. G. & Shneider, M. M. Contractile tail machines of bacteriophages. *Adv. Exp. Med. Biol.* **726**, 93–114 (2012).
4. Zoued, A. *et al.* Architecture and assembly of the Type VI secretion system. *Biochim. Biophys. Acta* **1843**, 1664–1673 (2014).

Chapter 2: The type VI secretion system sheath assembles at the end distal from the membrane anchor

5. Boyer, F., Fichant, G., Berthod, J., Vandenbrouck, Y. & Attree, I. Dissecting the bacterial type VI secretion system by a genome wide in silico analysis: what can be learned from available microbial genomic resources? *BMC Genomics* **10,** 104 (2009).

6. Pukatzki, S. *et al.* Identification of a conserved bacterial protein secretion system in Vibrio cholerae using the Dictyostelium host model system. *Proc. Natl Acad. Sci. USA* **103,** 1528–1533 (2006).

7. Durand, E. *et al.* Biogenesis and structure of a type VI secretion membrane core complex. *Nature* **523,** 555–560 (2015).

8. Brunet, Y. R., Zoued, A., Boyer, F., Douzi, B. & Cascales, E. The type VI secretion TssEFGK-VgrG phage-like baseplate is recruited to the TssJLM membrane complex via multiple contacts and serves as assembly platform for tail tube/sheath polymerization. *PLOS Genet.* **11,** e1005545 (2015).

9. Dong, T. G., Ho, B. T., Yoder-Himes, D. R. & Mekalanos, J. J. Identification of T6SS-dependent effector and immunity proteins by Tn-seq in Vibrio cholerae. *Proc. Natl Acad. Sci. USA* **110,** 2623–2628 (2013).

10. Pukatzki, S., Ma, A. T., Revel, A. T., Sturtevant, D. & Mekalanos, J. J. Type VI secretion system translocates a phage tail spike-like protein into target cells where it cross-links actin. *Proc. Natl Acad. Sci. USA* **104,** 15508–15513 (2007).

11. Shneider, M. M. *et al.* PAAR-repeat proteins sharpen and diversify the type VI secretion system spike. *Nature* **500,** 350–353 (2013).

12. Whitney, J. C. *et al.* An interbacterial NAD(P)(+) glycohydrolase toxin requires elongation factor Tu for delivery to target cells. *Cell* **163,** 607–619 (2015).

13. Brunet, Y. R., Hénin, J., Celia, H. & Cascales, E. Type VI secretion and bacteriophage tail tubes share a common assembly pathway. *EMBO Rep.* **15,** 315–321 (2014).

14. Clemens, D. L., Ge, P., Lee, B.-Y., Horwitz, M. A. & Zhou, Z. H. Atomic structure and mutagenesis of T6SS reveals interlaced array essential to function. *Cell* **160,** 940–951 (2015).

15. Kudryashev, M. *et al.* Structure of the type VI secretion system contractile sheath. *Cell* **160,** 952–962 (2015).

16. Zoued, A. *et al.* Priming and polymerization of a bacterial contractile tail structure. *Nature* **531,** 59–63 (2016).

17. Planamente, S. *et al.* TssA forms a gp6-like ring attached to the type VI secretion sheath. *EMBO J.* **35,** 1613–1627 (2016).

18. Basler, M., Pilhofer, M., Henderson, G. P., Jensen, G. J. & Mekalanos, J. J. Type VI secretion requires a dynamic contractile phage tail-like structure. *Nature* **483,** 182–186 (2012).

19. Brunet, Y. R., Espinosa, L., Harchouni, S., Mignot, T. & Cascales, E. Imaging type VI secretion-mediated bacterial killing. *Cell Rep.* **3,** 36–41 (2013).

20. Gerc, A. J. *et al.* Visualization of the serratia type VI secretion system reveals unprovoked attacks and dynamic assembly. *Cell Rep.* **12,** 2131–2142 (2015).

21. Basler, M. & Mekalanos, J. J. Type 6 secretion dynamics within and between bacterial cells. *Science* **337,** 815 (2012).

22. Mougous, J. D. *et al.* A virulence locus of pseudomonas aeruginosa encodes a protein secretion apparatus. *Science* **312,** 1526–1530 (2006).

23. Russell, A. B. *et al.* A type VI secretion-related pathway in bacteroidetes mediates interbacterial antagonism. *Cell Host Microbe* **16,** 227–236 (2014).

24. Schwarz, S. *et al.* VgrG-5 is a burkholderia type VI secretion system-exported protein required for multinucleated giant cell formation and virulence. *Infect. Immun.* **82,** 1445–1452 (2014).

25. Basler, M., Ho, B. T. & Mekalanos, J. J. Tit-for-tat: type VI secretion system counterattack during bacterial cell-cell interactions. *Cell* **152,** 884–894 (2013).

26. Hood, R. D. *et al.* A type VI secretion system of Pseudomonas aeruginosa targets a toxin to bacteria. *Cell Host Microbe* **7,** 25–37 (2010).

27. Russell, A. B. *et al.* Type VI secretion delivers bacteriolytic effectors to target cells. *Nature* **475,** 343–347 (2011).

28. Silverman, J. M. *et al.* Haemolysin co-regulated protein is an exported receptor and chaperone of type VI secretion substrates. *Mol. Cell* **51,** 584–593 (2013).

29. Vettiger, A. & Basler, M. Type VI secretion system substrates are transferred and reused among sister cells. *Cell* **167,** 99–110.e12 (2016).

30. Bönemann, G., Pietrosiuk, A., Diemand, A., Zentgraf, H. & Mogk, A. Remodelling of VipA/VipB tubules by ClpV-mediated threading is crucial for type VI protein secretion. *EMBO J.* **28,** 315–325 (2009).

31. Förster, A. *et al.* Coevolution of the ATPase ClpV, the sheath proteins TssB and TssC, and the accessory protein TagJ/HsiE1 distinguishes type VI secretion classes. *J. Biol. Chem.* **289,** 33032–33043 (2014).

32. Kapitein, N. *et al.* ClpV recycles VipA/VipB tubules and prevents non-productive tubule formation to ensure efficient type VI protein secretion. *Mol. Microbiol.* **87,** 1013–1028 (2013).

33. Leiman, P. G. *et al.* Morphogenesis of the T4 tail and tail fibers. *Virol. J.* **7,** 355 (2010).

34. Dörr, T., Davis, B. M. & Waldor, M. K. Endopeptidase-mediated beta lactam tolerance. *PLoS Pathog.* **11,** e1004850 (2015).

35. Dörr, T. *et al.* A cell wall damage response mediated by a sensor kinase/response regulator pair enables beta-lactam tolerance. *Proc. Natl Acad. Sci. USA* **113,** 404–409 (2016).

36. Errington, J. L-form bacteria, cell walls and the origins of life. *Open Biol.* **3,** 120143 (2013).

37. Mercier, R., Kawai, Y. & Errington, J. General principles for the formation and proliferation of a wall-free (L-form) state in bacteria. *eLife* **3** doi:10.7554/eLife.04629 (2014).

38. Kuru, E. *et al.* In situ probing of newly synthesized peptidoglycan in live bacteria with fluorescent D-amino acids. *Angew. Chem. Int. Ed.* **51,** 12519–12523 (2012).

39. Lam, H. *et al.* D-amino acids govern stationary phase cell wall remodeling in bacteria. *Science* **325,** 1552–1555 (2009).

40. Aksyuk, A. A. *et al.* The tail sheath structure of bacteriophage T4: a molecular machine for infecting bacteria. *EMBO J.* **28,** 821–829 (2009).

41. Aksyuk, A. A. *et al.* Structural conservation of the myoviridae phage tail sheath protein fold. *Structure* **19,** 1885–1894 (2011).

42. Ge, P. *et al.* Atomic structures of a bactericidal contractile nanotube in its pre- and postcontraction states. *Nat. Struct. Mol. Biol.* **22,** 377–382 (2015).

43. Fokine, A. & Rossmann, M. G. Molecular architecture of tailed double-stranded DNA phages. *Bacteriophage* **4,** e28281 (2014).

44. Santin, Y. G. & Cascales, E. Domestication of a housekeeping transglycosylase for assembly of a Type VI secretion system. *EMBO Rep.* **18,** 138–149 (2017).

45. Alcoforado Diniz, J. & Coulthurst, S. J. Intraspecies competition in serratia marcescens is mediated by type VI-secreted Rhs effectors and a conserved effector-associated accessory protein. *J. Bacteriol.* **197,** 2350–2360 (2015).

46. Schindelin, J. *et al.* Fiji: an open-source platform for biological-image analysis. *Nat. Methods* **9,** 676–682 (2012).

47. Brooks, T. M., Unterweger, D., Bachmann, V., Kostiuk, B. & Pukatzki, S. Lytic activity of the vibrio cholerae type VI secretion toxin VgrG-3 is inhibited by the antitoxin TsaB. *J. Biol. Chem.* **288,** 7618–7625 (2013).

Author contributions

A.V., J.W. and M.B. designed experiments, analysed and interpreted the results. A.V. and J.W. acquired all experimental data. L.L. generated *tssM* and *tssJ* V. *cholerae* strains and performed their initial characterization. A.V. and M.B. wrote the manuscript, which was read and approved by all authors.

Additional information

Competing interests: The authors declare no competing financial interests.

Reprints and permission information is available online at http://npg.nature.com/reprintsandpermissions/

How to cite this article: Vettiger, A. *et al.* The Type VI secretion system sheath assembles at the end distal from the membrane anchor. *Nat. Commun.* **8,** 16088 doi: 10.1038/ncomms16088 (2017).

Publisher's note: Springer Nature remains neutral with regard to jurisdictional claims in published maps and institutional affiliations.

CHAPTER 3

Induction of type VI secretion system contraction through compressive stress

Andrea Vettiger[1] and Marek Basler[1]*

[1]Focal Area Infection Biology, Biozentrum, University of Basel, Klingelbergstrasse 50/70, 4056 Basel, Switzerland

* Correspondence and requests for materials should be addressed to M.B. (email: marek.basler@unibas.ch)

Supplementary Figures and Tables for this manuscript can be found in Appendix B. Supplementary Video file 1 can be found attached on the CD attached to this thesis.

Manuscript in preparation, June 2019

Statement of contribution

I designed and performed experiments, analyzed and interpreted results and wrote the manuscript including figure preparation.

Abstract

Contractile nanomachines, translocate proteins across cellular membranes using force generated by rapid sheath contraction. Unlike for evolutionary related phage T4 where target cell surface receptor binding triggers sheath contraction, it is not known which signal initiates T6SS contraction. Recent studies identified a membrane associated sheath stabilizing protein, TagA, terminating sheath assembly and maintaining the polymer in its extended confirmation for minutes prior to contraction. Importantly, sheath terminator proteins are absent in many T6SS clusters. Interestingly, in these organisms sheaths contract immediately upon cell envelope contact, suggesting that compressive stress is sensed by the baseplate, initiating contraction. Here, we apply microfluidics to study the effect of hyperosmotic shocks to T6SS of V. cholerae. Our findings indicate that a rapid cell volume reduction results in a sharp increase in sheath contractions. This suggests, that despite the presence of TagA, the T6SS baseplate is pressure sensitive and thus compressive stress could be a general trigger for initiating sheath contraction.

3.1 Introduction

Contractile bacteriophages, R-type pyocins, Serratia antifeeding prophage or photorabdus virulence cassette, first attach to target cells loosely with long tail fibers and subsequently tightly bind to their designated surface receptor with short tail fibers (e.g. LPS and OmpC respectively, for phage T4) (Bertozzi Silva et al., 2016). This results in specific conformational changes in the baseplate initiating sheath contraction, which proceeds in a propagating wave along the contractile tail towards the distal end, resulting in rapid expulsion of the inner tube, which is decorated with a sharp tip (Leiman and Shneider, 2012; Taylor et al., 2016, 2018). This mechanism of breaching target cell envelope for substrate translocation, is conserved among all contractile nanomachines (Brackmann et al., 2017).

The T6SS is found in 25% of all sequenced Gram-negative bacteria (Boyer et al., 2009), being an important virulence factor for contact-dependent microbial interference competition as well as for infection of eukaryotic cells (Brodmann et al., 2017; Hood et al., 2010; Pukatzki et al., 2006; Stubbendieck and Straight, 2016). However, unlike beforementioned soluble extracellular contractile nanomachines, T6SS works from within the cell, thus likely different modes of contraction initiation apply. T6SS assembly starts with the insertion of the membrane (TssJ, L, M) complex into the cell envelope onto which the baseplate (TssE, F, G, K), spike proteins (VgrGs, PAAR and effectors) and the cap protein TssA assemble (Brunet et al., 2015; Cherrak et al., 2018; Durand et al., 2015; Zoued et al., 2016). This macromolecular complex serves then as a hub for the assembly of the cytosolic contractile tail. Current models for T6SS tail assembly indicate that TssA incorporates new sheath (VipA/B) and tube (Hcp) subunits at the distal end opposite to the

baseplate (Vettiger et al., 2017; Zoued et al., 2016). Sheath length was found to correlate with cell size; thus, the assembly commonly proceeds across the full cell diameter (Brunet et al., 2013; Gerc et al., 2015; Vettiger et al., 2017). The extended sheath represents a metastable high-energy state conformation, mediating the energy for substrate translocation. During contraction, sheath subunits undergo a conformational change to a low-energy sate. This results in sheath length reduction by 50% within less than 2ms, thereby expelling the inner Hcp tube with associated spike and effectors across the cell envelope into the extracellular space or by-standing target cell (Basler et al., 2012; Kudryashev et al., 2015; Vettiger et al., 2017). The contracted sheath is then specifically recognized and disassembled by the AAA+ ATPase ClpV in order to solubilize sheath subunits for a next round of assembly (Bönemann et al., 2009; Kapitein et al., 2013; Pietrosiuk et al., 2011). T6SS assembly and disassembly dynamics were previously studied by fluorescent live-cell microscopy using fusions of fluorescent proteins to the C-terminus of sheath subunit VipA or the ATPase ClpV, respectively (Basler and Mekalanos, 2012; Ringel et al., 2017).

Currently it is not known, which signal initiates sheath contraction for the T6SS. Recent studies suggest the presence of a membrane associated sheath terminating protein TagA, which was shown to interact with the assembly chaperon TssA in enteroaggregative *Escherichia coli* as well as *Vibrio cholerae* (Santin et al., 2018; Szwedziak and Pilhofer, 2019). Furthermore, as demonstrated by fluorescence microscopy, TagA co-localizes at the intersection between the distal sheath end and the membrane (Santin et al., 2018). Importantly, in tagA encoding T6SS clusters, sheaths remain stalled in this membrane spanning conformation for several minutes prior to contraction. In accordance with this observation, deletion of tagA results in bent sheaths with elevated length as a result of continued polymerization upon membrane contact (Santin et al., 2018; Szwedziak and Pilhofer, 2019). Accordingly, in a tagA mutant in *E. coli*, average sheath stalling time was reduced from 476s to 162s. Importantly, many T6SS clusters do not encode a tagA homologue. Interestingly, absence of TagA correlates with lack of stalling (< 2s) and therefore rapid sheath contraction upon membrane contact as previously shown in *Acinetobacter baylyi* (Ringel et al., 2017). This may suggest a mechanism for sheath contraction in absence of tagA through pressure mediated conformational changes in the baseplate as a consequence of cell envelope contact from the polymerizing distal end.

Here we show using a combination of microfluidics and fluorescence live-cell microscopy, that the tagA encoding organism *V. cholerae*, contracts its T6SS upon application of exogenous pressure. This is mediated by a rapid cell volume reduction upon mild hyperosmotic shocks. We show that this observation results from pressure applied to the distal sheath end opposite the baseplate, since predominately long sheath contract upon hyperosmotic shock. Furthermore, a hypoosmotic shock does not result in an elevated number of sheath contractions. More generally, our data also indicates a relation between

total number of sheath assemblies and overall T6SS secretion rate, which is influenced by presence of TagA stabilizing sheaths in their extended state. We envision a mode for sheath contraction in presence of TagA by a gradual accumulation of compressive stress on stalled sheaths through continued or resumed polymerization at rates below the diffraction limit.

3.1   Results

3.2.1 Cell volume reduction upon hyperosmotic shock triggers sheath contraction

We based our hypothesis that pressure could trigger T6SS contraction based on three previous observations: in presence of the sheath assembly terminator TagA, T6SS assemblies remain stalled for several minutes prior to contraction (i), while in absence of TagA sheaths contract rapidly upon membrane contact (ii). In addition, in *A. baylyi* sheaths were often found to bend upon membrane contact prior to contraction (iii).

Thus, in order to increase the pressure on fully-assembled stalled sheaths, we applied transient hyperosmotic shocks to T6SS positive *V. cholerae* cells using a commercial microfluidic platform (CellAsic®, Merck) (Fig. 1a) similarly as described by (Rojas et al., 2014). This setup allows to quickly exchange growth media with different solute concentration (e.g. LB (170mM NaCl) to high salt LB (340mM NaCl)). Cells react rapidly to a change of the extracellular osmolyte concentration (C_{Osm}) by adapting their turgor pressure (P_{tugor}) accordingly. This results in a rapid efflux of water from cytosol and deflation of the cell envelope (Rojas and Huang, 2018). Thus, cell volume decreased along both major and minor cell axis by 0.14 ± 0.02 μm and 0.11 ± 0.01 μm respectively, resulting in an average cell volume reduction by 22.75%, as determined by phase contrast microscopy (Fig. S1 b-c, f). In addition, we followed T6SS dynamics in these cells using fluorescently labeled sheath component VipA-msfGFP as well as the ATPase ClpV-mCherry2. We searched in time-lapse series for assemblies which were stalled in the frame prior to hyperosmotic shock and found many examples of subsequently contracting sheaths within the consecutive frame after media exchange (Fig. 1b, red arrow heads). Importantly assembling sheaths (turquois arrow head) did not contract during hyperosmotic shock, suggesting that only stalled sheaths are sensitive to compressive stress resulting from cell volume reduction (Fig. 1b). Applying the same hyperosmotic shock to the non-contractile VipA3AA sheath mutant did not result in sheath contractions, however caused frequent sheath buckling (Fig. 1c, yellow arrow heads) (Brackmann et al., 2018). This suggest that that stalled sheaths are indeed attached at both membranes. Manual quantification form 150 cell during 30s before and 30 after hyperosmotic shock suggested that the overall number of sheaths per cell remains same as determined by counting VipA-msfGFP foci (Fig. 1d). Classifying these foci into their respective state (assembling, stalled, contracted) revealed that upon hyperosmotic shock significantly more sheaths are in the contracted state as identified by ClpV co-localization

(Fig. 1e, 2way-ANOVA, $\alpha < 0.05$). Taken together, these finding suggest that increasing pressure on stalled T6SS sheath leads to their contraction despite presence of TagA.
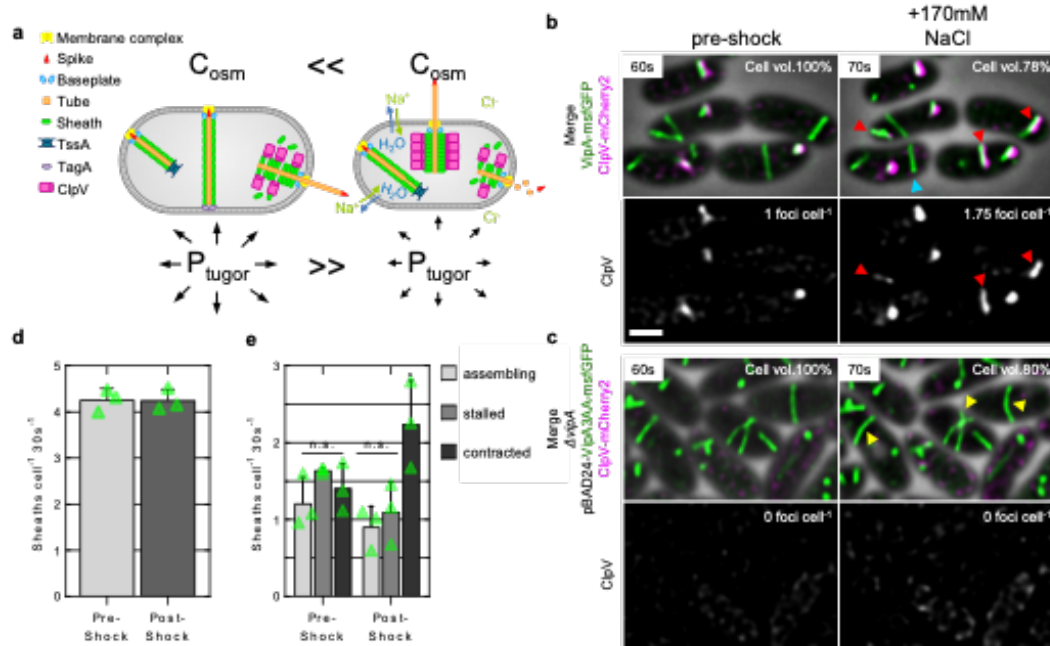
Figure 1: A hyperosmotic shock induces T6SS contraction. **(a)** Experimental approach to study the mechanism of sheath contraction: An increase of the extracellular osmolyte concentration results in cell volume reduction through a decrease in turgor pressure, applying pressure onto stalled T6SS assemblies (center). **(b)** T6SS dynamics were observed in dual labeled VipA-msfGFP (green), ClpV-mCherry2 (magenta and separate grey scale) *V. cholerae* cells grown in a microfluidic flow-cell. The two depicted frames were taken from the last frame before growth media exchange (pre-shock) and the consecutive image upon hyperosmotic shock (+ 170 mM NaCl). Red arrow heads indicate sheath contraction events; turquoise arrow head indicates sheath polymer undergoing active assembly. Scale bar = 1 μm. **(c)** Same procedure was applied to non-contractile *vipA3AA* sheath mutant. Yellow arrow heads indicate buckling sheaths. **(d)** The number of sheaths per cell was quantified manually from in total 150 cells during 30s (3 frames) immediately prior or after hyperosmotic shock (N = 3 biological replicates). **(e)** Sheath assemblies from 150 cells were categorized manually into assembling polymers (displaying sheath displacement above the diffraction limit or an increase in fluorescence over time for vertical assemblies, respectively), stalled assemblies (no sheath displacement) as well as contracted sheath structures (co-localization with ClpV) during 30s immediately prior or after hyperosmotic shock (N = 3 biological replicates). If a sheath was undergoing a dynamic transition (assembling – stalled; stalled – contracting) during this 30s observation period, the assembly was characterized according to its dynamic behavior (assembling; contracted respectively). Data are represented as mean ± one SD; 2way-ANOVA, $\alpha < 0.05$; * = $p < 0.05$, n.s. = non-significant.

3.2.2 Semi-automated quantification of sheath contractions through ClpV tracking

Motivated by our previous finding, we wanted to readout T6SS dynamics in large scale along the entire time-lapse series, impossible to do my manual quantification. Thus, we decided to track ClpV foci over time as an indirect readout for sheath contraction using the Fiji plugin TrackMate (Tinevez et al., 2017). Importantly, we first assessed that the hyperosmotic shock (+ 170mM NaCl) did not result in T6SS independent ClpV-mCherry2 foci formation. Indeed, no ClpV foci were observed in T6SS negative *vgrG2* mutant and non-contractile

sheath mutant *vipA3AA* in more than 10'000 cells upon hyperosmotic shock. In contrast, the parental strain increased the number of ClpV foci upon media exchange on average by 60% from 1.06 ± 0.18 to 1.67 ± 0.32 foci per cell (Fig. 2a-c). The increase in number of ClpV foci strongly correlated with the decrease in cell volume and resumes to pre-osmotic shock levels upon media exchange to isotonic osmolyte concentration (Fig 2c). We then asked, if the increase in ClpV foci indeed corresponds to new T6SS contraction events. Therefore, we quantified rate of ClpV track initiation across the time-lapse series. A ClpV track is defined as at least two successive ClpV foci within less than 0.3μm. Importantly, we found an approximately 300% increase (0.305 ± 0.14) in number of ClpV track initiation per cell within the first two frames (20s) upon hyperosmotic shock as compared to steady-state conditions in high salt (NaCl 340mM) or plain LB (NaCl 170mM) respectively (Fig. 2d, two-sided t-test $p < 0.01$). Upon media exchange back to isotonic osmolyte concentration, resulting in a hypoosmotic shock accompanied by a cell volume increase back to pre-shock level, we also found that that significantly less ClpV track are initiated as compared to steady-state conditions (Fig 2d, two-sided t-test $p < 0.01$). We then asked in which stage of their respective assembly 100 randomly chosen contractions events, as identified by TrackMate, were and measured their sheath length prior to contraction. Based on time-lapse series, we first assessed whether the assembly was horizontal or vertical in respect to the focal plane and whether it was stalled prior to contraction. Vertical sheath assembly can be defined as diffraction limited spots displaying an increase in fluorescent intensity over time, whereas horizontal sheath assemblies are defined by lateral GFP displacement over time. Importantly, we found that all 100 assemblies were stalled prior to contraction and displayed sheath lengths of 0.82 ± 0.23 μm corresponding to full-length assemblies (Fig. 2e) (Vettiger and Basler, 2016). Furthermore, we searched 100 sheath which were undergoing polymerization during the hyperosmotic shock. We found that sheath polymer length increased on average by 0.33 ± 0.20 μm during 30s and only 5 assemblies contracted upon subsequent membrane contact (Fig. 2f).

As further controls for the accuracy of the assay, we used the X, Y, and time coordinates of 1120 identified ClpV foci by TrackMate as seeds for measuring fluorescence intensity in the GFP channel and compared its fluorescence intensity to soluble-cytosolic, assembled-extended or assembled-contracted VipA-msfGFP subunits. This suggested, that the mean fluorescence intensity distribution of ClpV based GFP measurements corresponded to contracted sheaths ($p > 0.99$) and significantly differs from extended sheath assemblies ($p = 0.0013$) and cytosolic VipA sunbunits ($p < 0.0001$) (Fig. S2a, Kurskal-Wallis, N = 2640). Importantly, such a GFP signal distribution does not result by chance as it was found to be significantly different from randomized cytosolic GFP measurements ($p < 0.0001$) (Fig. S2a.) In addition, we also show that the number of ClpV foci correlates strongly with the number of T6SS assembly per cell by performing the hyperosmotic shock experiment in

vgrG1-vasX double mutant assembling around 10 x less T6SSs per cell as compared the parental strain (Fig. S2c) Significantly, higher number of ClpV tracks were initiated upon hyperosmotic shock (Fig. S2d).
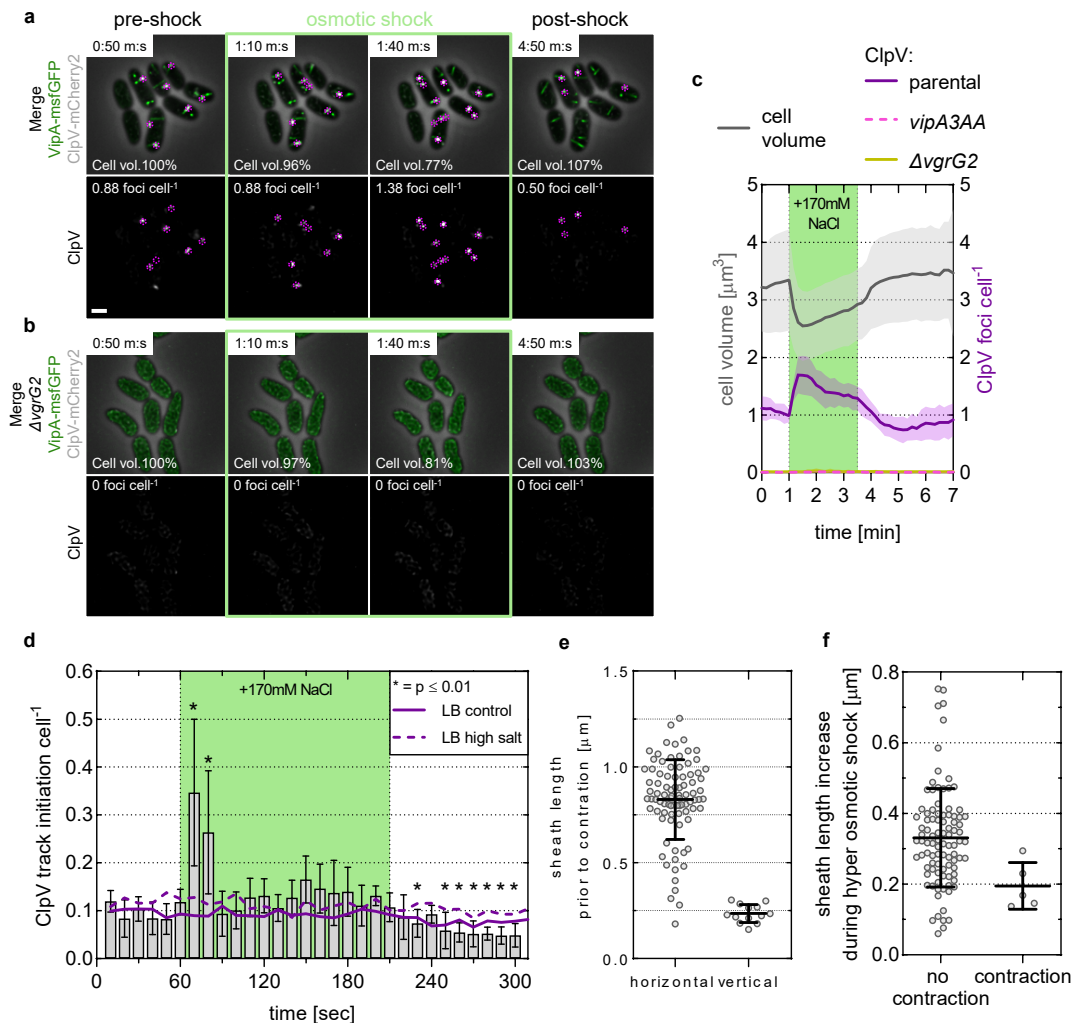
Figure 2: Increase in new sheath contraction events correspond to cell volume reduction. T6SS dynamics were monitored by following VipA-msfGFP (green) and ClpV-mCherry2 (white and separate gray scale image) during 7min at 10s acquisition frame rate in wild-type **(a)**, as well as T6SS negative *vgrG2* deletion mutant **(b)**. Cells were exposed after 1min to a hyperosmotic shock (+ 170 mM NaCl) for 2:30min and subsequently continued to observe for an additional 3:30min. T6SS contraction events were quantified by detecting ClpV foci through TrackMate (see material and methods for details). Dashed magenta circles mark ClpV foci identified by TrackMate. Scale bar = 1 μm. **(c)** Cell volume dynamics (grey curve) from 50 cells in response to hyperosmotic shock (green area) was assessed by measuring difference in major and minor axis length from phase-contrast images as described in material and methods as well as Fig. S1. In addition, the number of ClpV foci per cell for indicated strains is plotted on the right Y-axis. ClpV detection was carried out in > 3'000 cells for each genotype from 5 independent biological replicates. Data is represented as mean ± one SD. **(d)** The number of new arising ClpV tracks per cell was assessed from each frame (bar plot) in response to hyperosmotic shock (green area) and compared to the number for ClpV track initiations under steady-state conditions in LB (170 mM NaCl) or high salt LB (340mM NaCl). Data is presented as mean ± one SD for ClpV track initiation in response to osmotic shock, whereas only the mean is displayed for steady-state conditions. two-sided t-test p < 0.01, N > 3'000 cells from 5 biological replicates. **(e)** Sheath length from the frame prior to contraction, as identified by TrackMate, was measured from 100 randomly chosen contraction events. Data is represented as mean ± one SD. **(f)** Similarly, sheath length increase

during 30s was measured from 100 randomly chosen assembling polymers during hyperosmotic shock.

Furthermore, we also performed ClpV tracking from time-lapse series acquired at 3s acquisition frame rate (Fig. S3a-b). Importantly, we exposed cells to either short (30s) or long (2:30min) hyperosmotic shocks (+ 170mM NaCl). We then asked for the median ClpV track duration initiated before (5s), during (35s) and after hyperosmotic shock (90s), which should directly correspond to sheath disassembly time. We found that ClpV track duration was significantly increased by 12s (p = 0.0002) upon hyperosmotic shock as compared to tracks initiated before or after osmotic shock as well as under state conditions (Fig. S3c, Kruskal-Wallis, N = 3908). This indicates that sheath disassembly is prolonged in shocked cells. Importantly, we found no difference in ClpV track duration between cells grown under steady-state condition in LB or high salt LB (Fig. S3c). However, we also realized that many ClpV tracks were very short (below 15s), which is based on previous reports unlikely to account for a complete disassembly of the contracted sheath polymer. Indeed, when comparing manual tracked sheath disassembly duration to TrackMate measurements we found that median ClpV track duration was 4x higher (15s vs. 64.5s) (Fig. S3d). This suggests that ClpV tracking by TrackMate does not account for the correct sheath disassembly time. There are several explanations for this: sheath often break into multiple fragments upon disassembly (i), imperfection of particle tracking based on fluorescence intensities (ii) as well as the occasional detection of multiple ClpV foci per single sheath contraction event (iii). Nevertheless, this does not influence the capability of TrackMate to correctly identifying overall ClpV foci as well as track initiation events.

Overall, these findings suggest that stalled sheath contract upon cell volume reduction and that this can be reliably identified in by semi-automated ClpV-foci detection using TrackMate.

3.2.3 A hypoosmotic shock does not lead to sheath contraction

A hyperosmotic shock could have secondary effects on cell physiology and thereby perturb our analysis (Delarue et al., 2018). Thus, we performed several control experiments to verify that indeed pressure as a consequence from cell volume reduction triggers the contraction of stalled sheaths.

First, we wanted to verify whether the increase in contraction events was specific to cell volume reduction or could be simply triggered by the baseplate as a consequence reduced membrane tension. Therefore, we decided to perform the invers experiment than before. This time cells are grown in high salt LB medium, which is exchanged to plain LB resulting in a hypoosmotic shock (-170 mM NaCl). As expected, cells increased their turgor pressure in response to the sudden decease extracellular osmolyte concentration, resulting in an 8%
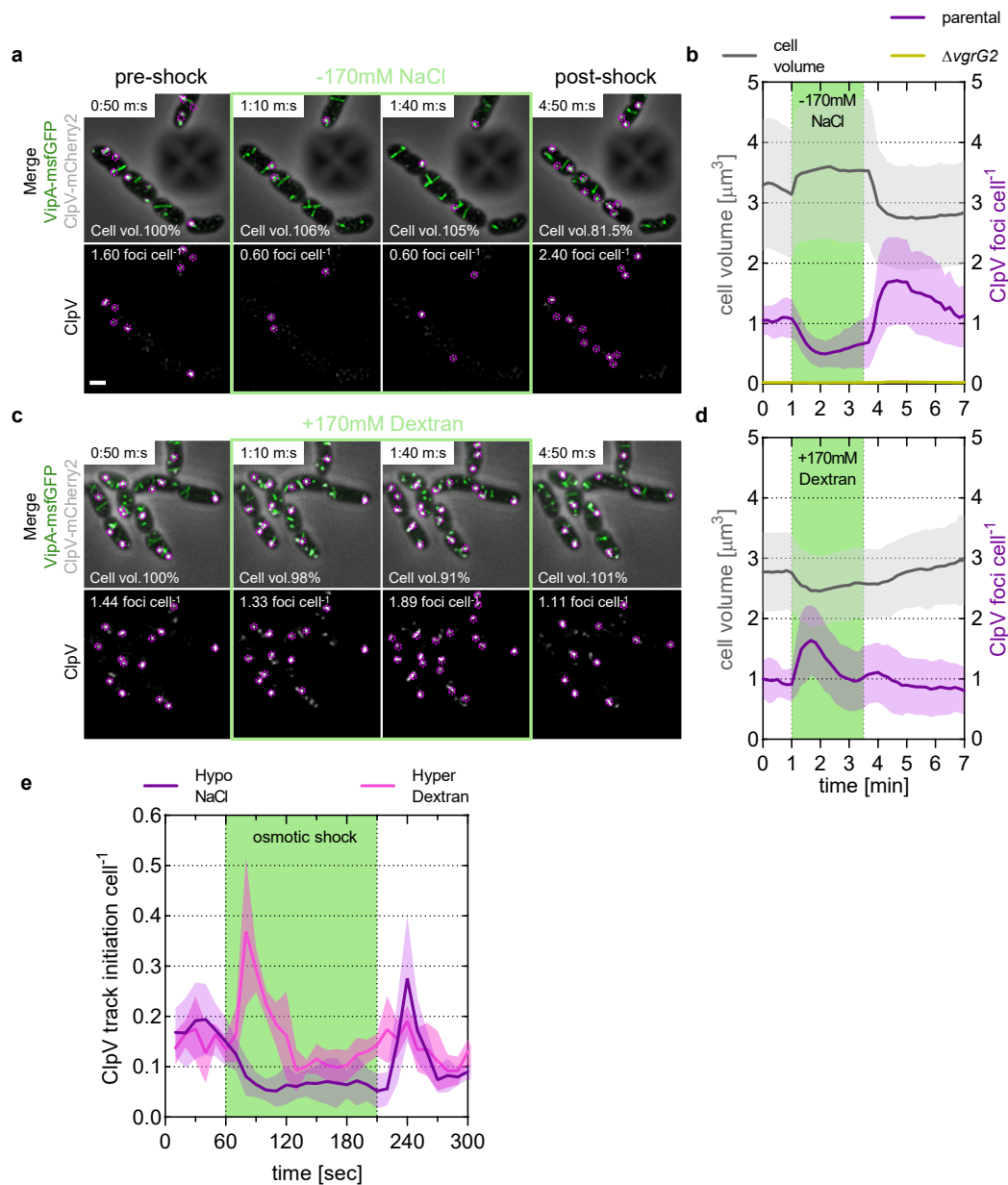
Figure 3: Sheath contractions correlate with cell volume reduction but is independent of osmolyte. T6SS dynamics were monitored by following VipA-msfGFP (green) and ClpV-mCherry2 (white and separate gray scale image) during 7min at 10s acquisition frame rate in *V. cholerae* cells in response to a **(a + b)** hypoosmotic shock (LB, 340 mM NaCl to LB 170 mM NaCl), as well as hyperosmotic shock to dextran **(c + d)** (LB 170 mM dextran to LB 340mM dextran). T6SS contraction events were quantified by detecting ClpV foci through TrackMate (see material and methods for details). Dashed magenta circles mark ClpV foci identified by TrackMate. Scale bar = 1 *μm*. Cell volume dynamics (grey curve) from 50 cells each in response to hypo- **(b)** and hyperosmotic shock **(c)** (green area) were assessed by measuring difference in major and minor axis length from phase-contrast images as described in material and methods as well as Fig. S1. In addition, the number of ClpV foci per cell (purple curve) is plotted on the right Y-axis. ClpV detection was carried out in > 3'000 cells for each genotype from 5 independent biological replicates. Data is represented as mean ± one SD. **(e)** The number of new arising ClpV tracks per cell was assessed from each frame in response to hypo- (purple curve) as well as hyperosmotic shock (pink curve) for NaCl and dextran, respectively. Data is presented as mean ± one SD, N > 3'000 cells from 5 biological replicates.

cell volume expansion (Fig. S1d-f). When following T6SS dynamics, we observed that during cell volume expansion, the total number of ClpV foci per cell as well as the number of newly initiated ClpV tracks decreased by approximately 50% (Fig. 3a-b, e). Importantly,

when the growth medium was switched back to high salt LB, resulting in a hyperosmotic shock, cell volume decreased rapidly (Fig. 3a-b). As previously, this correlated with a sharp increase in newly initiated ClpV tracks (+ 300%) (Fig. 3e) as well as an elevated total number of ClpV foci (1.65±0.71 foci per cell) (Fig 3a-b).

3.2 Osmolyte independent cell volume reduction triggers T6SS contractions

Next, we wondered whether the increase in sheath contractions was osmolyte dependent. Thus, in addition to outer membrane (OM) permeable NaCl, we also used impermeable and slow OM permeable osmolytes dextran and sucrose, respectively.

When exposing *V. cholerae* cells to a hyperosmotic shock with dextran (+170mM), we found the same pattern as previously observed for NaCl. Cell volume decreased to a similar extend by 12% from approximately 2.77 ± 0.65 μm³ to 2.46 ± 0.61 μm³ (Fig. 3c-d). This led to an approximately 200% increase in ClpV track initiations (0.15 ± 0.3 to. 0.33 ± 0.09) (Fig. 3e) resulting in an overall 60% increase of total ClpV foci per cell (0.96 ± 0.31 to 1.56 ± 0.59) (Fig. 3c-d). Analogous patterns were observed for hyperosmotic shock with sucrose (Fig. S4a, c). In addition, we also performed hypoosmotic shocks with sucrose, resulting similar T6SS response as observed for NaCl although to a lower extend. As expected, fewer ClpV foci per cell (1.23 ± 0.23 vs. 1.108 ± 0.23) were observed upon cell volume expansion by 10% accompanied by a subsequent increase of contractions (0.188 ± 0.04) upon media exchange back to isotonic media (Fig. S4b-c).

Taken together, we have demonstrated that exclusively a cell volume reduction leads to an increase in T6SS contractions and that this is osmolyte independent. Based on these results, we believe that our hypothesis for a pressure mediated signal for sheath contraction stands true.

3.3 TagA stabilizes T6SS dynamics

Next, we wondered how the T6SS dynamics of a *tagA* mutant would react upon an exogenous increase of pressure. To this end, we followed sheath assemblies at 2s acquisition frame rate in *tagA* mutant and compared it to the parental strain (Fig. S5). As reported previously, while in parental cells assembled sheaths remained stalled over minutes prior to contraction (Fig. S5a, stalling; b, top), in the *tagA* mutant sheath polymerization proceeded upon membrane contact, albeit at lower polymerization speed. This resulted often in characteristic bending of the sheath polymer (Fig S5a, stalling; S5b bottom). Temporal color coding of the assembly and stalling phase indicates that sheath bending only occurs after initial contact with cell envelope and thus may be interpreted as a result of the force from continued sheath polymerization against cell membrane (Fig. S5a).

We then asked how the *tagA* mutant would react in response to hyperosmotic shock by NaCl (+ 170 mM). Similar to the parental strain, we observed an overall increase in ClpV foci

from 0.76 ± 0.28 to 1.01 ± 33 by 40% upon exchange to high salt LB medium (Fig 4a). Accordingly, we also observed a 100% increase in ClpV track initiations from 0.08 ± 0.02 to 0.17 ± 0.05, which was significantly higher as compared to steady-state conditions (Fig. 4b, two-sided t-test $p < 0.01$). Interestingly, despite an overall lowered number of sheath assemblies (2.64 ± 0.49 vs. 1.89 ± 0.32) and ClpV foci per cell (0.87 ± 0.25 vs. 0.60 ± 0.05) (Fig. 4c-d), the number of ClpV track initiations is same as compared to the parental strain (0.10 ± 0.01 vs. 0.09 ± 0.01) under steady-state conditions (Fig 3d, 4-d). Based on this, the overall T6SS secretion rate was estimated to be 0.83 ± 0.3 contractions per cell per minute in both strains (Fig. 4e).
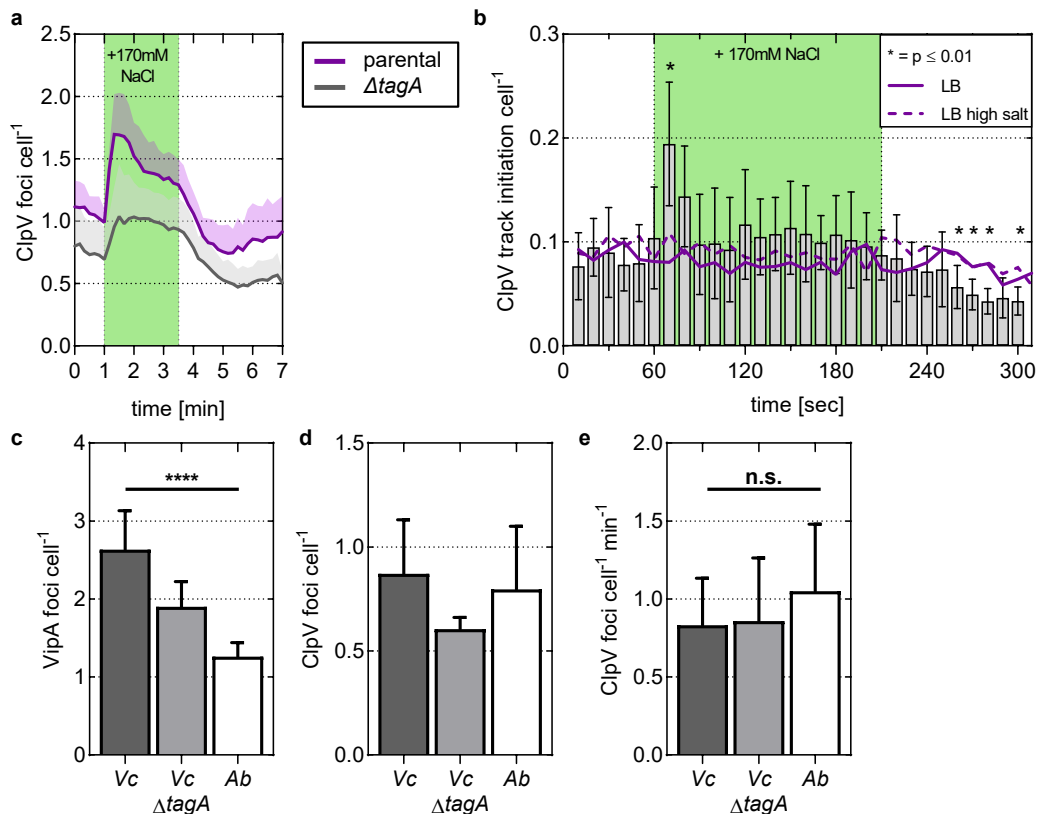
Figure 4: TagA reduces T6SS dynamics by stabilizing sheaths assemblies. **(a)** Number of ClpV foci per cell in response to a hyperosmotic shock (LB, 170 mM NaCl to LB 340 mM NaCl; green area) were monitored in a *tagA* deletion mutant of *V. cholaerae* (grey curve) by following ClpV-mCherry2 during 7min at 10s acquisition frame rate and compared to the parental strain (purple curve, reproduced from Fig. 2c). Data is represented as mean + one SD from 5 biological replicates and N > 3'000 cells for each genotype. **(b)** The number of new arising ClpV tracks per cell was assessed from each frame (bar plot) in response to hyperosmotic shock (green area) and compared to the number for ClpV track initiations under steady-state conditions in LB (170 mM NaCl) or high salt LB (340mM NaCl). Data is presented as mean ± one SD for ClpV track initiation in response to osmotic shock, whereas only the mean is displayed for steady-state conditions. Two-sided t-test $p < 0.01$, N > 3'000 cells from 5 biological replicates. The number of sheaths (VipA-(m)sfGFP) **(c)** as well as the number of ClpV foci (ClpV-mCherry2) per cell **(d)** were analyzed from N > 3'000 cells under steady-state conditions (LB, 170 mM NaCl) for *V. cholerae* (Vc), isogenic *tagA* deletion mutant (Vc Δ*tagA*) and *A. baylyi* (Ab) cells imaged for 7min at 10s acquisition frame rate. **(e)** The number of new arising ClpV tracks per cell per minute was assessed by TrackMate. Data is represented as mean + one SD, one-way ANOVA, $p < 0.0001$, n.s. = non-significant, N = 1'000 from 3 independent biological replicates.

Taken together, this indicates that TagA terminates sheath assemblies upon membrane contact and stabilizes the extended polymer. This results in higher number of stalled sheath assemblies and thereby lowers the section rate. In agreement with this trend, we also analyzed T6SS dynamics in TagA negative *Acinetobacter baylyi* strain (Ringel et al., 2017). As expected, no stalled sheath assemblies in 3000 cells were found and the total number of VipA foci per cell was almost 3x lower as compared to *V. cholerae* (1.26 ± 0.18 vs 2.64 ± 0.49, one-way ANOVA, $p < 0.0001$) (Fig 4c, Fig. S5c). Still, based on assessing the rate of new ClpV track initiation per cell, overall T6SS secretion rate (1.00 ± 0.49) was found to be same as compared to *V. cholerae* strains (one-way ANOVA, $\alpha < 0.05$) (Fig. 4e).

3.3   Discussion

To assess which signal could trigger T6SS contraction, we monitored sheath dynamics at the single cell level in response to mild osmotic shocks. Collectively, our data highlight that the application of compression stress as a result of cell volume reduction can induce T6SS sheath contraction. First, we showed that exclusively stalled sheaths attached with both ends to the cell envelope, but not polymerizing assemblies, contract upon cell volume decrease (Fig. 1b, Fig. 2f). Second, exclusively hyperosmotic shocks resulted in elevated T6SS contractions, indicating that changes in membrane tension as well as differences in flow rate from growth media exchange do not contribute to this (Fig. 3, Fig. S4). Interestingly, we also found a reduced number of sheath contraction in response to hypoosmotic shock. An explanation for this observation could be, that through cell volume expansion the pressure onto stalled T6SS assemblies is released, thereby reducing the likelihood for contraction (Fig 3a, e). Third, hyperosmotic shocks with three different osmolytes displaying distinct OM permeability (NaCl – permeable, sucrose – semi-permeable, dextran – impermeable) all resulted in a similar T6SS response (Fig. 3, Fig. S4). Thereby any secondary effects resulting from the elevated Na+ or Cl- ion concentration can be ruled out. Furthermore, during our experiments we applied only mild osmotic shocks generally not resulting in plasmolysis, hence decreased membrane tension should be irrespective of the OM permeability of the corresponding osmolyte (Pilizota and Shaevitz, 2013). Last, we show that cells lacking the sheath assembly terminator tagA show lower number of sheath contractions in response to hyperosmotic shock, despite displaying same T6SS secretion rate as the parental strain (Fig 4).

Based on our findings we propose a working model for T6SS contraction under steady-state conditions. This hypothesis relies on three assumptions: TssA/TagA interactions with the distal sheath end upon membrane contact are fluctuant (i), while the cell envelope displays high elasticity (ii) allowing for low levels of sheath polymerization below the diffraction limit (iii). According to current model for T6SS assembly TagA most probably functions as a competitive inhibitor for TssA, thereby deviating the substrates from away from the sheath

assembly chaperon terminating the assembly (Santin et al., 2018; Szwedziak and Pilhofer, 2019). However, recent findings in *V. cholerae* have demonstrated that TssA and TagA can fall off and bind again stalled sheaths (Schneider, *accepted*). Moreover, sheath contractions were not found to be correlated with presence of either TagA or TssA at the distal end (Schneider, *accepted*). Thus, we envision that stalled sheaths may resume polymerization by either substituting TagA with TssA or even in absence of any assembly chaperon, allowing to incorporate few sheath and tube subunits. Importantly, the addition of one sheath ring measures will contribute only to an approximately 4nm length increase (Wang et al., 2017), which is 50 times below the diffraction limit of the light microscope. Since both membranes as well as peptidoglycan were found to display remarkable flexibility (Rojas et al., 2018), the resumed polymerization results in a gradual increase of pressure over time following the principles of a Brownian ratchet (Peskin et al., 1993; Ptacin et al., 2010).

Moreover, the T6SS use is generally regulated on the transcriptional level through surface or quorum sensing (Borgeaud et al., 2015; Joshi et al., 2017; Metzger et al., 2016). In addition, some organism such as *Pseudomonas aeruginosa* or *Serratia marcescens*, regulate the assembly of their T6SS on the post-translational level through the threonine phosphorylation pathway (Basler et al., 2013; Gerc et al., 2015; Mougous et al., 2007). However, unlike for sheath assembly initiation, it is improbable that the trigger for contraction comes from extracellular cues. In support for this, it was found that isolated single *V. cholerae* and *A. baylyi* cells fire their T6SS at similar rates as compared to cell which are surrounded by sister or prey cells (Fig. S5c) (Basler et al., 2012; Ringel et al., 2017).

We have shown that the presence of TagA increased the total number sheaths per cell but did result in a similar ClpV track initiation rate (Fig. 4c, e). Correspondingly, this should result in a similar Hcp secretion and effector translocation rate into target cells. However, it was previously found that the tagA mutant reduces prey cells survival 10x less as compared to the wild type (Santin et al., 2018). As an explanation for this, it was found that bent sheath assemblies, which are increased in the tagA mutant, often display non-canonical contraction events (Szwedziak and Pilhofer, 2019). These are defined as sheath contractions towards the distal end opposite to the baseplate. Whether, such non-canonical contraction events result in functional secretion events is not clear. However, the data presented here indeed suggests that TagA increases secretion efficiency by limiting sheath length and preventing polymer bending, thereby ensuring canonical contraction events.

Unlike for phages and other contractile nanomachines, which always assemble particles with identical sheath length using a tape-measure protein, T6SS sheath length is not regulated (Leiman and Shneider, 2012; Vettiger et al., 2017). Increasing cell size by forming *V. cholerae* spheroplasts resulted in sheath assemblies, which were on average 3x longer as

compared to rod shaped cells (2.63 μm vs. 0.85 μm) (Vettiger et al., 2017). Since sheath assembly polymerization speed was found to be linear, it takes longer to assemble long sheath. Furthermore, based on the wide distribution of stalling times in both *E. coli* and *V. cholerae*, we believe that a 'timer' or 'spontaneous instability' based mechanism for sheath contraction is unlikely under physiological conditions (Santin et al., 2018; Vettiger et al., 2017).

Last, we have also previously shown that Hcp limited as well as tssA mutant *V. cholerae* cells, assembling on average 4x shorter sheaths as compared to wild type (0.25 μm vs. 0.62 μm), are capable of inducing prey cell lysis (Schneider, *accepted*; Vettiger and Basler, 2016). Likely, distal sheath ends in these assemblies were not in contact with the cell envelope, thus a different mechanism for sheath contraction must apply. In absence of sufficient Hcp or sheath subunit precursor, or the assembly chaperon TssA respectively, sheath polymerization speed is low. Sheath contraction in phage T4 and R-type pyocins occurs in a wave of several sheath rings contracting simultaneously (Maghsoodi et al., 2017). Therefore, if sheath length is below the number of rings which contract during the initial wave of contraction, the assembly is instable and prone to contract prematurely. However, under physiological conditions, sheath polymerization occurs much faster (38 nm s^{-1}), thus bypassing the period of instability rapidly. This stabilizes the T6SS assembly and allows sheath polymerization across the entire cytosol until the perpendicular cell membrane.

Still, further approaches will be needed for understanding the complete mechanism for T6SS sheath contraction. A crucial step towards this would be elucidating the structure of the contracted baseplate, which is currently absent from isolated sheaths. This would enable the comparison to extended conformation, allowing to calculating energy coefficients during contraction using molecular dynamics and thus could indicate which signal is sensed for contraction initiation.

Author contributions

AV designed and performed the experiments, analyzed and interpreted the data and wrote the manuscript. MB designed the experiments, analyzed and interpreted the data, wrote the manuscript and acquired funding.

Acknowledgments

Declaration of interest

The authors declare no competing interests.

3.4 Material and Methods

3.4.1 Bacterial strains and growth conditions

Parental *V. cholerae* 2740-80 and *A. baylyi* ADP1 strains were described previously here (Basler et al., 2012; Ringel et al., 2017). A detailed strain list used in this study can be found in Table S1. Bacteria were grown shaking at 200rpm in Luria-Bertani (LB) broth (NaCl 170mM, 1% (w/v)) at 37°C. All cultures were grown aerobically. Antibiotic concentrations used were streptomycin (50 µg ml^{-1}) and ampicillin (300 µg ml^{-1}).

3.4.2 DNA manipulations

In-frame deletions and chromosomal mutations in *V. cholerae* were generated by allelic exchange method using the suicide plasmid pWM91. For experiments with the non-contractile sheath mutant, VipA-3AA-msfGFP was expressed from inducible vector pBAD24 by the addition of 0.1% (w/v) L-arabinose to the growth medium for 40min (Brackmann et al., 2018; Wang et al., 2017).

3.4.3 Microfluidic setup for application of osmotic shocks

Bacteria from o/n cultures were diluted 1:500 into fresh LB and grown at 37 °C, 200rpm until an optical density (OD) measured at 600 nm of approximately 0.8-1.2. Then, cells were harvested by centrifugation (1 min, 16'000 x g), washed once in LB and adjusted to an OD of 0.2. From this cell suspension, 50 μl were loaded into the cell inlet of a bacterial CellASIC® plate (B04A-03, Merck, Germany). An ONIX perfusion platform (Merck, Germany) was used to control flow. Prior to loading the cells into the flow chambers, PBS storage solution was replaced by LB and the respective test media. Subsequently, inlets were primed for 5min at 8psi (30 μl h^{-1}) to ensure later for rapid medium exchange. Cells were then loaded according to the manufacture protocol. Prior to exposure to osmotic shocks, cells were grown for 1 h in LB at 30 °C and 1psi flow rate (approx. 2.5 μl h^{-1}). If not indicated differently, all osmotic shock experiments were carried out using the same flow protocol. First, cells were in presence of isotonic growth medium (e.g. LB, 170 mM NaCl) for 1 min at 1 psi flow rate, followed by an exchange to hypertonic media (e.g. high salt LB, 340 mM NaCl) for 2:30 min indicated by the green area in graphs. To ensure rapid media exchange the flow was set to 8psi during the first minute and then subsequently lowered back to 1 psi for the remaining 1:30min. Then the medium was exchanged back to isotonic LB and cells were continued monitoring during 3:30min at 1psi. All hyperosmotic shocks were carried out by increasing the initial osmolyte concentration (c_i = 170mM) by 170mM (c_f = 340). The same procedure was used for hypoosmotic shocks; however, there cells were first adapted

to hypertonic medium by growing them for 60 min in presence of elevated osmolyte concentration (340 mM). Then, the growth media was exchanged back to hypotonic osmolyte concentration (170 mM) resulting in a hypoosmotic shock. After any osmotic shock, cells were allowed to recover for 15 min prior to the next exposure. For steady-state experiments, cells were adapted to the respective growth medium as explained previously. Importantly, the same flow protocol was applied, except that the growth media was switched to identical medium from a different inlet.

3.4.4   Imaging bacterial cells on agar pads

For comparing T6SS dynamics of *V. cholerae*, the isogenic tagA deletion mutant and *A. baylyi* cells similar techniques were applied as by (Ringel et al., 2017). Briefly, bacteria were grown as for microfluidic experiment, however cells were concentrated to an OD = 10 by centrifugation. Of this cell suspension, 3 μl were spotted onto a thin 1% agarose (w/v) in LB pad and covered with a coverslip for imaging.

3.4.5   Fluorescence microscopy

Images were acquired using a Nikon Ti-E inverted motorized microscope with Perfect Focus System and Plan Apo 1003 Oil Ph3 DM (NA 1.4) objective lens. If not indicated differently, time-lapse series were acquired at 10s acquisition frame rate during 7min. SPECTRA X light engine (Lumencore), ET-GFP (Chroma #49002) filter set was used to excite and filter fluorescence. sCMOS camera pco.edge 4.2 (PCO, Germany) (pixel size 65 nm) and VisiView software (Visitron Systems, Germany) were used to record images. The power output of the SPECTRA X light engine was set to 20% for all excitation wavelengths. VipA-GFP derivates and phase-contrast images were acquired with 50-100ms exposure, whereas ClpV-mCherry2 was acquired with 200ms exposure time. Temperature and humidity were set to 30 °C, 95% respectively, using an Okolab T-unit objective heating collar as well as a climate chamber (Okolab).

3.4.6   Image analysis

Quantification of T6SS dynamics in response to osmotic shocks was carried out exclusively on deconvolved time-lapse series using the Huygens Remote Manager (Ponti et al., 2007). Parameters for image reconstruction were set as described by Schneider, *accepted*. All other imaging processing was carried out in Fiji (Schindelin et al., 2012). Acquired time-lapse series were drift corrected using a custom StackReg based software (Ringel et al., 2017; Thevenaz et al., 1998). Total cell number was assessed from phase contrast image using the 'find maxima' options with noise tolerance setting set to 1000. Total number of sheath foci was quantified the same way using a noise tolerance setting of 750 and activated 'light background' function. These measurements were carried out for each frame of the respective time-lapse series. All quantifications were verified manually and carried out using the "edge

maxima exclusion" function. For quantification of sheath contractions, rate of new ClpV tracks, as well as total foci number were detected using TrackMate (Tinevez et al., 2017). Total number ClpV foci were detected using the 'Log detector' function with a 'blob diameter' of 0.4 μm and subsequently filtered using the quality threshold, which was set same for sets of images which were directly compared with each other. ClpV foci tracking was performed using the 'Simple LAP tracker' by setting the maximal linking distance to 0.3 μm, while not allowing for any gap closure events. ClpV tracks were filtered based on a total track displacement below 0.7 μm. Additionally, all tracks which started or ended on the first or the last frame, respectively, were excluded from the analysis.

Specificity for identifying sheath contraction events using ClpV foci detection was carried out by extracting respective X, Y, and time (frame) coordinate for each foci. This data was then loaded into the ROI manager and was used as centre of mass coordinates for creating an oval with a radius of 0.2 μm from which mean fluorescence intensity was measured in the GFP channel. GFP intensity was calibrated by performing 100 manual fluorescence intensity measurements each for background, cytosolic, assembled and contracted sheaths along random timepoints of the time-lapse series. Contracted sheaths were identified based on ClpV co-localization. Photobleaching did not seem to interfere with GFP intensity measurements (Fig. S2b). Randomized fluorescence intensity measurements were carried out by applying random noise ('Salt and Pepper') function to segmented cell outlines (Otsu) based on phase contrast images. This results in 2.5% saturated pixels per frame. Again, X, Y and time coordinates were extracted from segmented saturated pixels and used as seeds for measuring mean fluorescence GFP intensity within an oval with a radius of 0.2 μm. Importantly, this results in a higher number per cell than one would get based on ClpV detection.

Form 100 sheath contraction events, identified by Trackmate, sheath length from the frame prior to contraction was measured using the 'straight line' tool. Moreover, also the respective stage of the assembly (actively polymerizing or stalled) prior to contraction was addressed. In addition, we measured the average increase in sheath length during the first 30s of hyperosmotic shock form 100 assembling polymers.

Quantification of cell volume dynamics in response to osmotic shock were carried similar as described by (Pilizota and Shaevitz, 2013; Rojas et al., 2014). Cells were segmented from phase contrast images using Otsu algorithm (Otsu, 1979). 'Watershed' algorithm was used to split dividing cells. To the segmented cells an ellipse was fitted from which the major (h) and minor (D) axis was computed (Fig. S1a). Cell volume (V_{Cell}) was calculated assuming the cell body behaves like a tube following the equation: $V_{cell} = (\pi \times D^2 \times h)/4$.

Time-lapse series, 'temporal color coding' and kymograms, generated as described previously (Vettiger et al., 2017), were used to compare T6SS dynamics of *A. baylyi*, *V.*

cholerae and *tagA* deletion mutant on agar pads. Contrast on all compared sets of images was adjusted equally.

3.4.7 Statistics

All calculations were carried out using Microsoft Excel 2016 and GraphPad Prism version 8.0.2. Statistical parameters such as type of analysis and total number of analysed bacteria as well as levels of significance are reported in the figure legends. If not indicated differentially, all data are represented as mean +/- 1 SD. Normal distribution was checked by using the D'Agostino-Pearson omnibus K2 normality test. Each experiment was carried out at least in biological triplicates.

The datasets generated during this study are available from the corresponding author upon request.

3.5 References

Basler, M., and Mekalanos, J.J. (2012). Type 6 secretion dynamics within and between bacterial cells. Science 337, 815.

Basler, M., Pilhofer, M., Henderson, G.P., Jensen, G.J., and Mekalanos, J.J. (2012). Type VI secretion requires a dynamic contractile phage tail-like structure. Nature 483, 182–186.

Basler, M., Ho, B.T., and Mekalanos, J.J. (2013). Tit-for-tat: Type VI secretion system counterattack during bacterial cell-cell interactions. Cell 152, 884–894.

Bertozzi Silva, J., Storms, Z., and Sauvageau, D. (2016). Host receptors for bacteriophage adsorption. FEMS Microbiol. Lett. 363.

Bönemann, G., Pietrosiuk, A., Diemand, A., Zentgraf, H., and Mogk, A. (2009). Remodelling of VipA/VipB tubules by ClpV-mediated threading is crucial for type VI protein secretion. The EMBO Journal 28, 315–325.

Borgeaud, S., Metzger, L.C., Scrignari, T., and Blokesch, M. (2015). The type VI secretion system of Vibrio cholerae fosters horizontal gene transfer. Science 347, 63–67.

Boyer, F., Fichant, G., Berthod, J., Vandenbrouck, Y., and Attree, I. (2009). Dissecting the bacterial type VI secretion system by a genome wide in silico analysis: what can be learned from available microbial genomic resources? BMC Genomics 10, 104.

Brackmann, M., Nazarov, S., Wang, J., and Basler, M. (2017). Using Force to Punch Holes: Mechanics of Contractile Nanomachines. Trends in Cell Biology 27, 623–632.

Brackmann, M., Wang, J., and Basler, M. (2018). Type VI secretion system sheath inter-subunit interactions modulate its contraction. EMBO Rep 19, 225–233.

Brodmann, M., Dreier, R.F., Broz, P., and Basler, M. (2017). Francisella requires dynamic type VI secretion system and ClpB to deliver effectors for phagosomal escape. Nat Commun 8, 15853.

Brunet, Y.R., Espinosa, L., Harchouni, S., Mignot, T., and Cascales, E. (2013). Imaging type VI secretion-mediated bacterial killing. Cell Rep 3, 36–41.

Brunet, Y.R., Zoued, A., Boyer, F., Douzi, B., and Cascales, E. (2015). The Type VI Secretion TssEFGK-VgrG Phage-Like Baseplate Is Recruited to the TssJLM Membrane Complex via Multiple Contacts and Serves As Assembly Platform for Tail Tube/Sheath Polymerization. PLOS Genetics 11, e1005545.

Cherrak, Y., Rapisarda, C., Pellarin, R., Bouvier, G., Bardiaux, B., Allain, F., Malosse, C., Rey, M., Chamot-Rooke, J., Cascales, E., et al. (2018). Biogenesis and structure of a type VI secretion baseplate. Nature Microbiology 1.

Delarue, M., Brittingham, G.P., Pfeffer, S., Surovtsev, I.V., Pinglay, S., Kennedy, K.J., Schaffer, M., Gutierrez, J.I., Sang, D., Poterewicz, G., et al. (2018). mTORC1 Controls Phase Separation and the Biophysical Properties of the Cytoplasm by Tuning Crowding. Cell 174, 338-349.e20.

Durand, E., Nguyen, V.S., Zoued, A., Logger, L., Péhau-Arnaudet, G., Aschtgen, M.-S., Spinelli, S., Desmyter, A., Bardiaux, B., Dujeancourt, A., et al. (2015). Biogenesis and structure of a type VI secretion membrane core complex. Nature 523, 555–560.

Gerc, A.J., Diepold, A., Trunk, K., Porter, M., Rickman, C., Armitage, J.P., Stanley-Wall, N.R., and Coulthurst, S.J. (2015). Visualization of the Serratia Type VI Secretion System Reveals Unprovoked Attacks and Dynamic Assembly. Cell Rep 12, 2131–2142.

Hood, R.D., Singh, P., Hsu, F., Güvener, T., Carl, M.A., Trinidad, R.R.S., Silverman, J.M., Ohlson, B.B., Hicks, K.G., Plemel, R.L., et al. (2010). A Type VI Secretion System of Pseudomonas aeruginosa Targets a Toxin to Bacteria. Cell Host Microbe 7, 25–37.

Joshi, A., Kostiuk, B., Rogers, A., Teschler, J., Pukatzki, S., and Yildiz, F.H. (2017). Rules of Engagement: The Type VI Secretion System in Vibrio cholerae. Trends in Microbiology 25, 267–279.

Kapitein, N., Bönemann, G., Pietrosiuk, A., Seyffer, F., Hausser, I., Locker, J.K., and Mogk, A. (2013). ClpV recycles VipA/VipB tubules and prevents non-productive tubule formation to ensure efficient type VI protein secretion. Mol. Microbiol. 87, 1013–1028.

Kudryashev, M., Wang, R.Y.-R., Brackmann, M., Scherer, S., Maier, T., Baker, D., DiMaio, F., Stahlberg, H., Egelman, E.H., and Basler, M. (2015). Structure of the Type VI Secretion System Contractile Sheath. Cell 160, 952–962.

Leiman, P.G., and Shneider, M.M. (2012). Contractile tail machines of bacteriophages. Adv. Exp. Med. Biol. 726, 93–114.

Maghsoodi, A., Chatterjee, A., Andricioaei, I., and Perkins, N.C. (2017). Dynamic Model Exposes the Energetics and Dynamics of the Injection Machinery for Bacteriophage T4. Biophys J 113, 195–205.

Metzger, L.C., Stutzmann, S., Scrignari, T., Van der Henst, C., Matthey, N., and Blokesch, M. (2016). Independent Regulation of Type VI Secretion in Vibrio cholerae by TfoX and TfoY. Cell Rep 15, 951–958.

Mougous, J.D., Gifford, C.A., Ramsdell, T.L., and Mekalanos, J.J. (2007). Threonine phosphorylation post-translationally regulates protein secretion in Pseudomonas aeruginosa. Nat. Cell Biol. 9, 797–803.

Otsu, N. (1979). A Threshold Selection Method from Gray-Level Histograms. IEEE Transactions on Systems, Man, and Cybernetics 9, 62–66.

Peskin, C.S., Odell, G.M., and Oster, G.F. (1993). Cellular motions and thermal fluctuations: the Brownian ratchet. Biophys J 65, 316–324.

Pietrosiuk, A., Lenherr, E.D., Falk, S., Bönemann, G., Kopp, J., Zentgraf, H., Sinning, I., and Mogk, A. (2011). Molecular Basis for the Unique Role of the AAA+ Chaperone ClpV in Type VI Protein Secretion. J. Biol. Chem. 286, 30010–30021.

Pilizota, T., and Shaevitz, J.W. (2013). Plasmolysis and Cell Shape Depend on Solute Outer-Membrane Permeability during Hyperosmotic Shock in E. coli. Biophysical Journal 104, 2733–2742.

Ponti, A., Schward, P., Gulati, A., and Bäcker, V. (2007). Huygens remote manager: A web interface for high-volume batch deconvolution. Imaging & Microscopy 9, 57–58.

Ptacin, J.L., Lee, S.F., Garner, E.C., Toro, E., Eckart, M., Comolli, L.R., Moerner, W.E., and Shapiro, L. (2010). A spindle-like apparatus guides bacterial chromosome segregation. Nat. Cell Biol. 12, 791–798.

Pukatzki, S., Ma, A.T., Sturtevant, D., Krastins, B., Sarracino, D., Nelson, W.C., Heidelberg, J.F., and Mekalanos, J.J. (2006). Identification of a conserved bacterial protein secretion system in Vibrio cholerae using the Dictyostelium host model system. PNAS 103, 1528–1533.

Ringel, P.D., Hu, D., and Basler, M. (2017). The Role of Type VI Secretion System Effectors in Target Cell Lysis and Subsequent Horizontal Gene Transfer. Cell Rep 21, 3927–3940.

Rojas, E.R., and Huang, K.C. (2018). Regulation of microbial growth by turgor pressure. Curr. Opin. Microbiol. 42, 62–70.

Rojas, E., Theriot, J.A., and Huang, K.C. (2014). Response of Escherichia coli growth rate to osmotic shock. Proc. Natl. Acad. Sci. U.S.A. 111, 7807–7812.

Rojas, E.R., Billings, G., Odermatt, P.D., Auer, G.K., Zhu, L., Miguel, A., Chang, F., Weibel, D.B., Theriot, J.A., and Huang, K.C. (2018). The outer membrane is an essential load-bearing element in Gram-negative bacteria. Nature 559, 617–621.

Santin, Y.G., Doan, T., Lebrun, R., Espinosa, L., Journet, L., and Cascales, E. (2018). In vivo TssA proximity labelling during type VI secretion biogenesis reveals TagA as a protein that stops and holds the sheath. Nature Microbiology 3, 1304–1313.

Schindelin, J., Arganda-Carreras, I., Frise, E., Kaynig, V., Longair, M., Pietzsch, T., Preibisch, S., Rueden, C., Saalfeld, S., Schmid, B., et al. (2012). Fiji: an open-source platform for biological-image analysis. Nat. Methods 9, 676–682.

Stubbendieck, R.M., and Straight, P.D. (2016). Multifaceted Interfaces of Bacterial Competition. J. Bacteriol. 198, 2145–2155.

Szwedziak, P., and Pilhofer, M. (2019). Bidirectional contraction of a type six secretion system. Nature Communications 10, 1565.

Taylor, N.M.I., Prokhorov, N.S., Guerrero-Ferreira, R.C., Shneider, M.M., Browning, C., Goldie, K.N., Stahlberg, H., and Leiman, P.G. (2016). Structure of the T4 baseplate and its function in triggering sheath contraction. Nature 533, 346–352.

Taylor, N.M.I., van Raaij, M.J., and Leiman, P.G. (2018). Contractile injection systems of bacteriophages and related systems. Mol. Microbiol.

Thevenaz, P., Ruttimann, U.E., and Unser, M. (1998). A pyramid approach to subpixel registration based on intensity. IEEE Transactions on Image Processing 7, 27–41.

Tinevez, J.-Y., Perry, N., Schindelin, J., Hoopes, G.M., Reynolds, G.D., Laplantine, E., Bednarek, S.Y., Shorte, S.L., and Eliceiri, K.W. (2017). TrackMate: An open and extensible platform for single-particle tracking. Methods 115, 80–90.

Vettiger, A., and Basler, M. (2016). Type VI Secretion System Substrates Are Transferred and Reused among Sister Cells. Cell 167, 99-110.e12.

Vettiger, A., Winter, J., Lin, L., and Basler, M. (2017). The type VI secretion system sheath

assembles at the end distal from the membrane anchor. Nature Communications 8, ncomms16088.

Wang, J., Brackmann, M., Castaño-Díez, D., Kudryashev, M., Goldie, K.N., Maier, T., Stahlberg, H., and Basler, M. (2017). Cryo-EM structure of the extended type VI secretion system sheath-tube complex. Nat Microbiol 2, 1507–1512.

Zoued, A., Durand, E., Brunet, Y.R., Spinelli, S., Douzi, B., Guzzo, M., Flaugnatti, N., Legrand, P., Journet, L., Fronzes, R., et al. (2016). Priming and polymerization of a bacterial contractile tail structure. Nature 531, 59–63

CHAPTER 4

Type VI secretion system substrates are transferred and reused among sister cells

Andrea Vettiger[1] and Marek Basler[1]*

[1]Focal Area Infection Biology, Biozentrum, University of Basel, Klingelbergstrasse 50/70, 4056 Basel, Switzerland

* Correspondence and requests for materials should be addressed to M.B. (email: marek.basler@unibas.ch)

Supplementary Figures and Tables to this article can be found in Appendix C. Supplementary Video files 1-8 can be found online at the publishers webpage:
https://www.sciencedirect.com/science/article/pii/S0092867416310741?via%3Dihub#app2

Statement of contribution

I designed and performed experiments, analyzed and interpreted results and contributed to the manuscript as well as figure preparation.

Cell

Type VI Secretion System Substrates Are Transferred and Reused among Sister Cells

Graphical Abstract
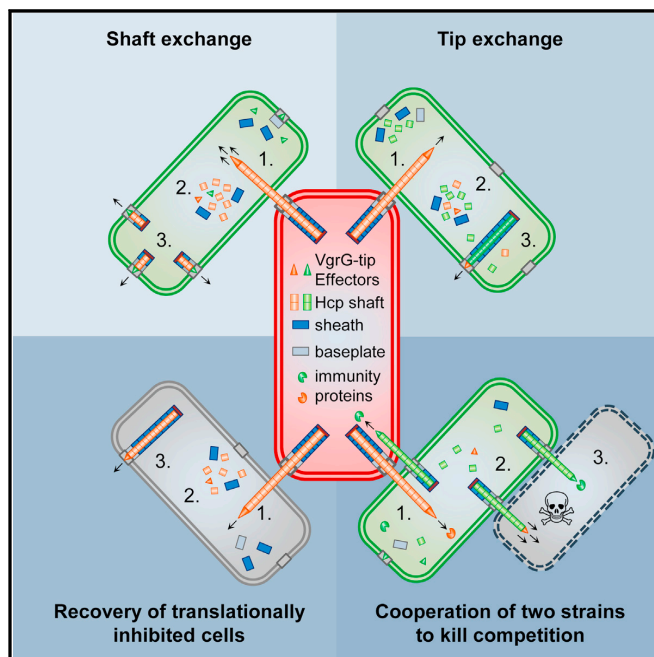
Authors
Andrea Vettiger, Marek Basler

Correspondence
marek.basler@unibas.ch

In Brief
Bacteria use proteinaceous spear guns to attack one another and can reuse the components that entered their cytosol in this manner.

Highlights

- Proteins secreted by T6SS are exchanged among cells and reused for T6SS assembly

- Amount of VgrG limits number of T6SS assemblies and Hcp limits the sheath length

- T6SS-dependent exchange of secreted proteins increases chances to kill competition

- Efficiency of protein exchange depends on precise aiming of T6SS

CrossMark

CellPress

Article

Cell

Type VI Secretion System Substrates Are Transferred and Reused among Sister Cells

Andrea Vettiger[1] and Marek Basler[1,2,*]
[1]Focal Area Infection Biology, Biozentrum, University of Basel, Basel, Switzerland
[2]Lead Contact
*Correspondence: marek.basler@unibas.ch
http://dx.doi.org/10.1016/j.cell.2016.08.023

SUMMARY

Bacterial type VI secretion system (T6SS) is a nanomachine that works similarly to a speargun. Rapid contraction of a sling (sheath) drives a long shaft (Hcp) with a sharp tip and associated effectors through the target cell membrane. We show that the amount and composition of the tip regulates initiation of full-length sheath assembly and low amount of available Hcp decreases sheath length. Importantly, we show that both tip and Hcp are exchanged by T6SS among by-standing cells within minutes of initial cell-cell contact. The translocated proteins are reused for new T6SS assemblies suggesting that tip and Hcp reach the cytosol of target cells. The efficiency of protein translocation depends on precise aiming of T6SS at the target cells. This inter-bacterial protein complementation can support T6SS activity in sister cells with blocked protein synthesis and also allows cooperation between strains to increase their potential to kill competition.

INTRODUCTION

Membranes play an important role in protecting cellular contents from the outside environment. However, sophisticated mechanisms evolved to overcome the protection. One such mechanism is mechanical breach of the membrane by puncturing using a sharp tip. This principle is used by many systems related to contractile phage tails such as bacterial type VI secretion system (T6SS) or R-type pyocins (Cianfanelli et al., 2016; Leiman and Shneider, 2012; Zoued et al., 2014). T6SS was identified in many gram-negative bacteria and its expression as well as subcellular localization is regulated by several different mechanisms (Ho et al., 2014; Silverman et al., 2012). The different T6SSs secrete wide variety of effector molecules into both bacterial and eukaryotic targets making T6SS essential for bacterial competition and pathogenesis (Alcoforado Diniz et al., 2015; Durand et al., 2014; French et al., 2011; Hachani et al., 2016; Hood et al., 2010; Ma et al., 2014; MacIntyre et al., 2010; Pukatzki et al., 2006; Russell et al., 2014). An explanation for such a remarkable flexibility of T6SS could be its unique mode of action, which resembles a spear gun. T6SS is composed of a shaft with a sharp tip carrying a payload, a sling and a baseplate attached to the

bacterial cell envelope. The shaft is a hollow tube built from rings of Hcp hexamers and is surrounded by a contractile sling called sheath composed of six helical strands of VipA/VipB (or TssB/TssC) heterodimers (Bönemann et al., 2009; Brunet et al., 2014; Kudryashev et al., 2015; Mougous et al., 2006). The tube begins with a tip complex composed of VgrG trimer, PAAR protein, and various effectors (Dong et al., 2013; Flaugnatti et al., 2016; Hachani et al., 2014; Pukatzki et al., 2007; Shneider et al., 2013; Unterweger et al., 2014). The tube-sheath complex assembles in the cytoplasm from a cell envelope-associated baseplate and can be as long as the width of the cell (Basler et al., 2012; Brunet et al., 2015; Durand et al., 2015; Gerc et al., 2015; Zoued et al., 2016). Upon an unknown signal from the baseplate, the sheath rapidly contracts to about half of its length and ejects the tube with the associated effectors out of the cell and across a target cell membrane (Basler et al., 2012). The contracted sheath is specifically recognized by a T6SS-associated ATPase, ClpV, which unfolds VipB to allow for new sheath assembly (Basler and Mekalanos, 2012; Bönemann et al., 2009; Kapitein et al., 2013; Pietrosiuk et al., 2011). VipA and ClpV fluorescent protein fusions were shown to be fully functional and their dynamic localization correlates with T6SS activity (Basler and Mekalanos, 2012; Basler et al., 2012; Brunet et al., 2013; Clemens et al., 2015; Gerc et al., 2015; Kapitein et al., 2013; Kudryashev et al., 2015).

T6SS activity is regulated on transcriptional level in a response to wide variety of signals (Miyata et al., 2013; Silverman et al., 2012). For example, certain *Vibrio cholerae* strains grown to a high cell density in presence of chitin co-regulate DNA uptake machinery and T6SS activity to acquire new genes (Borgeaud et al., 2015). Assembly of H1-T6SS of *Pseudomonas aeruginosa* is localized subcellularly with a high precision to direct the secretion toward the target cells for their efficient killing (Basler et al., 2013; Ho et al., 2013; LeRoux et al., 2012). Additionally, in *V. cholerae* secreted proteins VgrG2 and Hcp as well as VasX and VgrG3 effectors were shown to be required for proper T6SS assembly (Dong et al., 2013; Kapitein et al., 2013; Pukatzki et al., 2006, 2007). Many anti-bacterial effectors have periplasmic targets, such as peptidoglycan or membrane (Russell et al., 2014), however, some others, such as DNases, clearly need to reach the bacterial cytosol (Koskiniemi et al., 2013; Ma et al., 2014). It is unclear if T6SS is capable to breach both membranes and peptidoglycan at the same time or if cytosolic effectors use separate mechanism to translocate from periplasm to cytosol similarly to the recently described effector of *P. aeruginosa*, which requires EF-Tu to cross inner membrane (Whitney et al., 2015).

Here, we show that Hcp, VgrG2, and T6SS effectors of *V. cholerae* are exchanged between neighboring cells and can be efficiently reused for a new T6SS assembly. We further show that availability of tip complex limits number of T6SS assemblies per cell and Hcp concentration regulates length of T6SS sheaths. Our data also suggest that both Hcp tube and tip complex are delivered to the cytosol of a target cell and both are disassembled to be reused for a new functional T6SS assembly. We show that efficiency of this interbacterial protein complementation depends on accurate aiming of T6SS activity and may under certain conditions help cells to fight competition.

RESULTS

Hcp and VgrG2 Are Exchanged between Cells and Reused for a New T6SS Assembly

We designed our experiments to test if VgrG and Hcp proteins are exchanged between bacteria based on two previous observations: (1) T6SS sheath assembles into a long dynamic structure, which is a hallmark of a functional T6SS, and (2) some T6SS substrates are necessary for T6SS function. Here, we observed that *V. cholerae* cells with a fully functional T6SS contained on average 3.2 VipA-msfGFP sheath structures per cell at any given time and assembled on average 5.6 structures per 5 min. In contrast, no sheaths were assembled in cells lacking *vgrG2*, *hcp1/hcp2*, or *vgrG2/hcp1/hcp2*, respectively in more than 20,000 cells (Figures 1A and S1; Movie S1; for a complete strain list, see Table S1). Importantly, these cells were also unable to kill *Escherichia coli* prey cells or secrete Hcp (Figures S2A–S2C). We mixed these cells deficient in sheath assembly (recipient) with T6SS+ (donor) cells at a ratio of 1:4 and monitored localization of VipA-msfGFP in the recipient cells by fluorescence microscopy (Figure 1B). Surprisingly, the sheath assembly was restored in the recipient strain as more than 1 in 20 cells assembled at least one sheath structure within 5 min of imaging (Figures 1C–1E and 1H; Movies S2, S3, and S4). This was fully dependent on a functional T6SS in the donor cells because no sheath assembly was detected in the recipient cells mixed with donor cells lacking *vipB* (Figure 1F). Importantly, T6SS+ donor cells failed to rescue sheath assembly in recipient cells lacking non-secreted VipB sheath component (Figure 1G). The recipient cells were also unable to directly uptake VgrG and Hcp proteins from the environment as no sheath assembly was detected upon incubation with 10-fold concentrated supernatant of wild-type cells containing both VgrG2 and Hcp (Figure S3). Furthermore, distance measurement between donor and recipient cells showed that sheath assembly was ten times more frequent in the recipient cells that were in a direct contact to T6SS+ donor cells than in those that were further away (Figure 1I) and reached ~2% of the frequency of sheath assembly in the wild-type cells (Figures 1H and 1I).

To test if DNA, RNA, or protein transfer was responsible for restoring sheath assembly, we inhibited protein synthesis in the recipient cells lacking *vgrG2* by 30 min pre-incubation in the presence of chloramphenicol. Such treatment failed to inhibit sheath assembly in the recipient cells mixed with wild-type cells (Figures S4B and S4C). In contrast, chloramphenicol treatment fully blocked sheath assembly in the recipient cells after expression of *vgrG2* was induced from pBAD24 plasmid (Figure S4A).

Taken together, this indicates that secreted proteins such as VgrG2 and Hcp can be exchanged between cells by T6SS-dependent translocation and that the exchanged proteins can be reused for a new T6SS assembly.

Availability of VgrG2 Limits the Number of Sheath Assemblies and Hcp Limits the Sheath Length

A detailed comparison of length and number of T6SS sheaths assembled in the recipient cells after complementation of VgrG2 or Hcp revealed unexpected differences (Figures 1C and 1E). In case of VgrG2, the sheath structures that formed in the recipient cells were stretching from one side of a cell to another and were on average 0.60 μm long. These structures were therefore indistinguishable from structures assembled in the wild-type cells that were on average 0.62 μm long (Figure 2A). However, mostly only a single structure assembled in the recipient cell during 5 min (Figure 2B). In case of Hcp complementation, the average length of assembled sheath structures was 0.25 μm, which is less than half of the length in wild-type cells. Because this length is close to the diffraction limit of the optical microscope, it is likely that many of these sheath structures were in fact even shorter. The number of structures assembled during Hcp complementation was on average 3.1 and thus significantly higher than in case of VgrG2 complementation and similar to number of assemblies in wild-type cells (Figures 2A and 2B). During simultaneous complementation of VgrG2 and Hcp, 1.7 structures per cells assembled on average and the average sheath length was 0.36 μm (Figures 1D, 2A, and 2B).

Interestingly, the first sheath assembly in *vgrG2*-negative recipient cells was detected as quickly as 2 min after mixing with T6SS+ donor cells (Figure 2C). This is remarkable considering that at these imaging conditions the wild-type cells contract T6SS sheath on average approximately once per minute as estimated from ClpV-mCherry2 localization (Movies S2, S3, and S4). Because close contact is necessary for the protein transfer, a recipient cell can be within a reach of only limited number of cells and thus could receive only few VgrG complexes in 2 min. On the other hand, sheath assembly during Hcp complementation was first detected after 28 min of incubation (Figure 2C). This suggests that even though protein transfer starts immediately after the cells are in close contact, the concentration of Hcp in the cytosol has to reach certain threshold to initiate sheath assembly or be sufficient for assembly of sheaths detectable by fluorescence microscopy.

To test how amount of available VgrG2 and Hcp influences T6SS assembly, we expressed Hcp or VgrG2 from an inducible pBAD plasmid in cells lacking *hcp1/hcp2* or *vgrG2*, respectively. The protein expression was induced at the same time as imaging was initiated by spotting the cells on an agarose pad containing 0.1% L-arabinose. Shortly after induction of VgrG2, only few full-length sheath assemblies were detected in the cells, however, after 40 min of induction, the number of full-length structures reached wild-type levels (Figure 2D; Movie S5). On the other hand, short induction of Hcp resulted in assembly of multiple short sheath structures and longer induction only increased the sheath length without further increasing the number of structures per cell (Figure 2E; Movie S5). Small amounts of Hcp or VgrG2 protein, barely detectable using western blot analysis, are
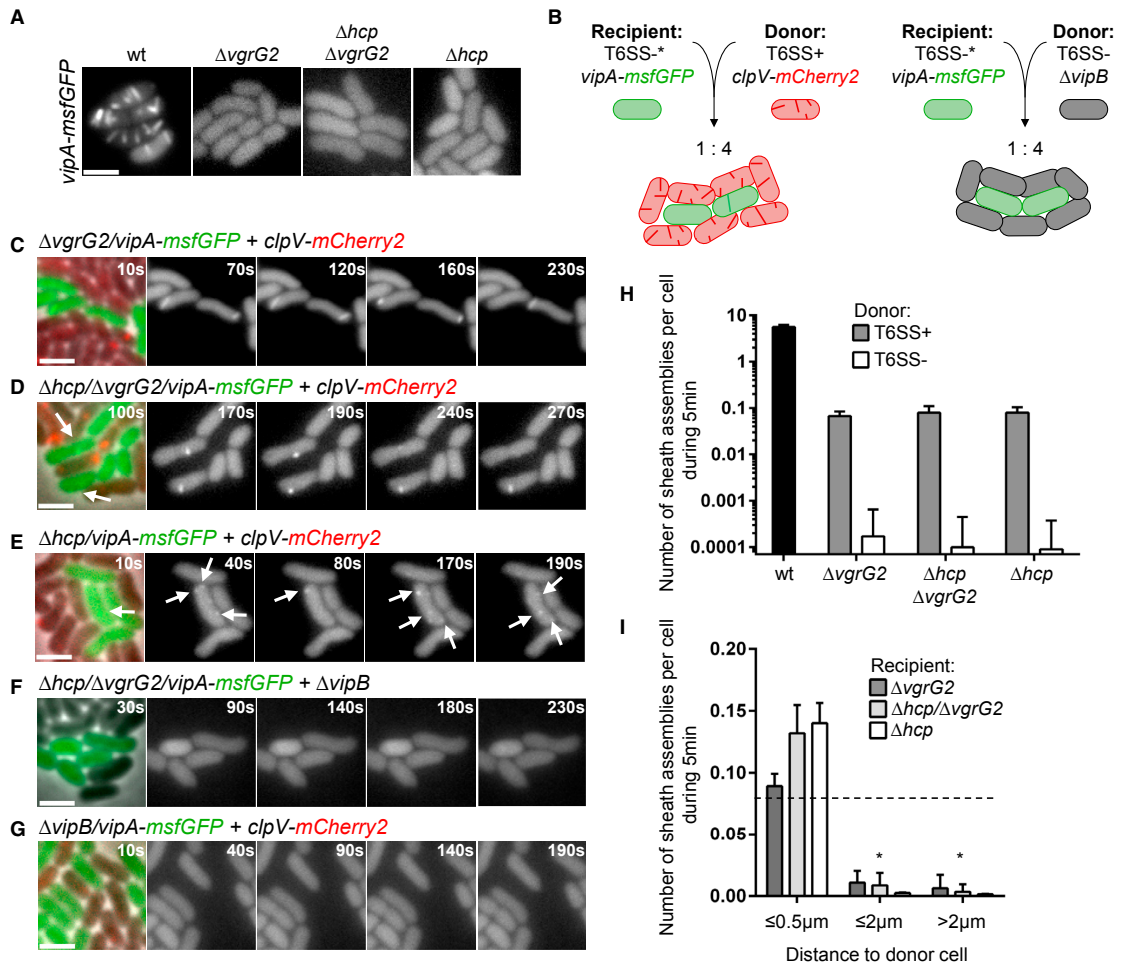
Figure 1. T6SS Activity Can Be Partially Restored in T6SS⁻ Cells by Interbacterial Protein Complementation from T6SS⁺ Cells

(A) VipA-msfGFP localization (sheath assembly) was monitored in at least 20,000 cells of the indicated strains over 5 min. Representative images of GFP fluorescence channel are shown. Additional images with a bigger field of view can be found in Figure S1 and Movie S1.

(B) The interbacterial protein complementation assay: Bacterial mixtures were spotted on a 1% LB-agarose pad and imaged during 2 hr at 25°C. Asterisk marks T6SS⁻ strains with deleted secreted components.

(C–G) Indicated recipient strains (green, T6SS⁻) were mixed with donor strains (unlabeled, T6SS⁻; red, T6SS⁺) and monitored for sheath assembly for 2 hr. Depicted are individual frames of a 5-min time-lapse movie. The first frame shows all cells and is a merge of phase contrast, GFP, and mCherry2 fluorescence channels (where applicable). The next four frames only show GFP fluorescence channel to clearly visualize sheath dynamics. Arrows highlight dynamics of short VipA-msfGFP structures. See Movies S2, S3, and S4 for complete time-lapse movies.

(H) Sheath assembly was monitored in the indicated strains for 5 min after 30 min co-incubation with either T6SS⁺ or T6SS⁻ donor cells. Total number of sheath assemblies was counted for at least 5,000 GFP⁺ cells for each combination of indicated strains. Black bar depicts T6SS assembly rate in wild-type.

(I) For a total number of 20,915 GFP⁺ cells distance to the next donor cell was analyzed. GFP⁺ cells were grouped into three indicated categories based on the distance. Sheath assembly was monitored in the indicated strains for 5 min. Dashed line represents mean protein complementation frequency for total cell number as depicted in Figure 1H. *p < 0.0001 as compared to ≤0.5 μm; two-way ANOVA with multiple comparison and Tuckey post hoc correction; number of cells per category: ≤0.5 μm, N = 14,388; ≤2 μm, N = 4,356; >2 μm, N = 3,639.

All data represented in this figure are shown as mean ± SD were acquired from six independent biological replicates. Scale bar, 2 μm on all images.
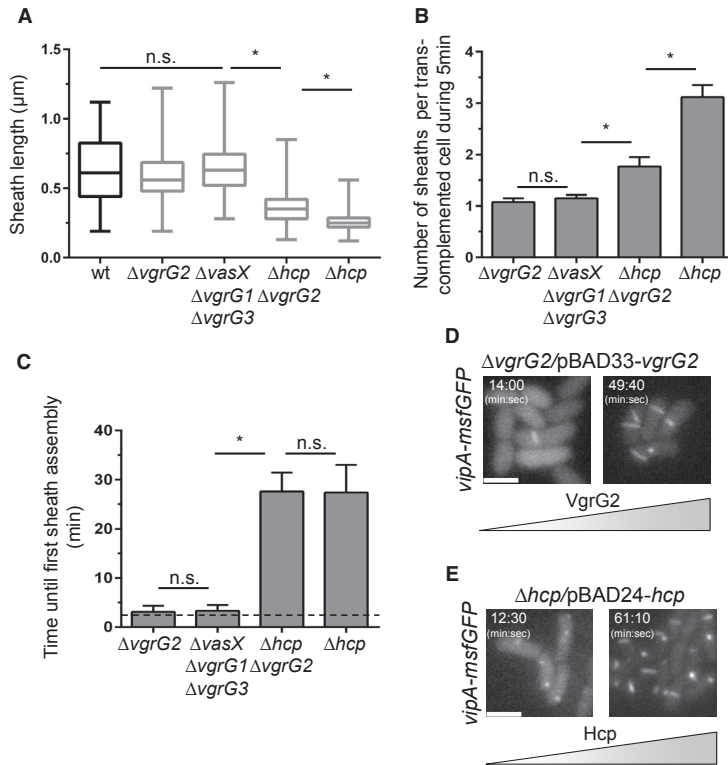
See also Figures S2, S3, and S4.

Figure 2. Tip Protein Concentration Dictates Number of Sheaths per Cell, whereas Hcp Determines Sheath Length

(A) Sheath length was measured from 100 fully extended structures in wild-type *vipA-msfGFP* strain (black graph) and in the indicated recipient strains (all *vipA-msfGFP* background) mixed with T6SS⁺ donor strain (protein complementation, gray graphs). Depicted are whiskers plots with minima and maxima; 75% of all data points lay within the box, horizontal line represents the median.

(B) Number of sheath assemblies during 5 min as a result of interbacterial protein complementation was assessed for each indicated strain within 200 recipient cells displaying T6SS activity. Data are represented as mean ± SD.

(C) Time until the first detection of sheath assembly by interbacterial protein complementation was measured for each indicated strain co-incubated with T6SS⁺ donor cells. Dashed line indicates time prior to imaging. Data are represented as mean ± SD.

(D and E) VgrG2 (D) or Hcp (E) was expressed from pBAD vectors in *vipA-msfGFP* background strains lacking *vgrG2* or *hcp1/hcp2*, respectively. The time after cells were spotted on a pad with 0.1% L-arabinose is indicated. Images show representative cells in GFP fluorescence channel to visualize sheath assembly. See Movie S5 for full time-lapse movies.

All data shown in this figure were acquired from three independent biological replicates. For statistical analysis one-way ANOVA with multiple comparison using Tuckey post hoc test was performed, *p < 0.0001; n.s., non-significant. Scale bar, 2 μm on all images.

See also Figure S5.

sufficient for sheath assembly; however, to fully restore T6SS activity, both Hcp and VgrG2 proteins have to be expressed to a level that is close to the wild-type level (Figure S5). Taken together, these observations suggest that during interbacterial protein complementation the frequency of assembly and sheath length are limited by the amount of Hcp and VgrG2 proteins delivered into the recipient cells.

T6SS Effectors Are Exchanged between Cells

Hcp secretion in *V. cholerae* was previously shown to be abolished in the absence of VgrG3 and VasX (Dong et al., 2013). We reasoned that this was likely a consequence of an aberrant T6SS assembly and created strains lacking *vgrG1*, *vgrG3*, and/or *vasX* in *vipA-msfGFP* background. Indeed, the frequency of sheath assembly was significantly decreased in strains lacking one or any combination of two of these three effectors. For example, deletion of *vgrG3* and *vasX* lowered T6SS activity 300-fold to a frequency of one sheath assembly in 100 cells and additional deletion of *vgrG1* further decreased the activity 10-fold (Figures 3A and S1). To test if the tip-associated effectors VgrG1, VgrG3, and VasX are also transferred between cells, we mixed *vgrG1/vgrG3/vasX* triple mutant recipient cells with T6SS⁺ donor cells. Similarly to VgrG2 transfer, single sheath structures were first detected after 2 min and the average sheath length was

indistinguishable from the sheath length in wild-type cells (Figures 2A–2C). Sheath assembly was restored also in *vgrG1/vgrG2/vgrG3* cells mixed with T6SS⁺ donor cells (Figure 3B).

Sheath assembly in *vgrG1/vgrG3/vasX* triple mutant could be triggered either by transfer of a whole tip complex or any combination of VgrG1, VgrG3, or VasX effectors because the corresponding double or single mutants all assemble the sheath with a higher frequency than the triple mutant (Figure 3A). To test if transfer of VgrG3 effector alone could restore the activity, we mixed the triple effector mutant recipient cells with double mutant *vgrG1/vasX* donor cells, which transfer VgrG2/VgrG3 complex at approximately ten times lower rate than wild-type (Figure 3A; Movie S6). Indeed, the frequency of sheath assembly was significantly increased in the *vgrG1/vgrG3/vasX* recipient cells (Figures 3C and 3D; Movie S6). This suggests that in addition to VgrG2, the whole tip complex with associated effectors is transferred between cells and can be reused to initiate new T6SS assembly.

Translocated and Cytosolic Proteins Mix to Assemble Functional T6SS

To test if the T6SS assembled from complemented components is functional, we generated two reporter strains that are sensitive to delivery of T6SS substrates TseL (targets lipids) or VgrG3 (targets peptidoglycan) (Brooks et al., 2013; Dong et al., 2013; Unterweger
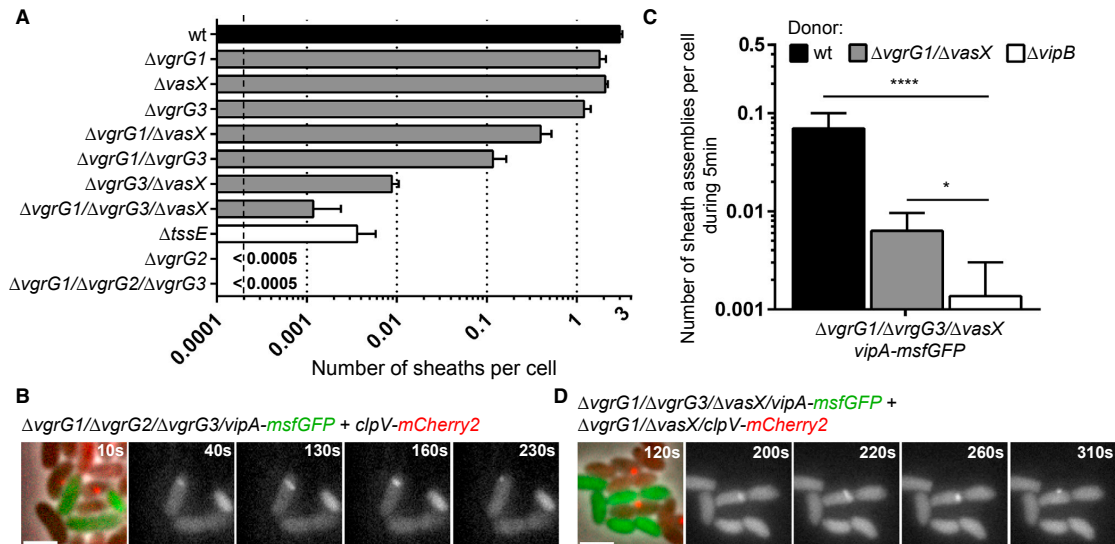
Cell

Figure 3. T6SS Effectors Are Efficiently Exchanged among Neighboring Cells

(A) Total number of sheath assemblies detected in 5,000 cells of each indicated strain (all *vipA-msfGFP* background) at a given point of time was divided by number of cells. Dashed line represents detection limit for this analysis and is given by number of analyzed cells. Black bar represents wild-type, gray bars represent strains lacking one or several T6SS effectors, white bars represent strains lacking a structural component. No structures were detected in 20,000 *vgrG2* and *vgrG1/vgrG2/vgrG3* triple mutants. Representative images can be found in Figure S1.

(B) Full VgrG tip interbacterial protein complementation: depicted are individual frames of a 5-min time-lapse. The first frame shows all cells and is a merge of phase contrast, GFP (*ΔvgrG1/ΔvgrG2/ΔvgrG3*, T6SS⁻ recipient) and mCherry2 (wild-type donor) fluorescence channels. The following four frames only show GFP fluorescence channel to visualize sheath dynamics.

(C) Sheath assembly was monitored in the *ΔvgrG1/ΔvgrG3/ΔvasX/vipA-msfGFP* strain for 5 min after 30 min co-incubation either with *clpV-mCherry2* (wild-type T6SS activity), *ΔvgrG1/ΔvasX/clpV-mCherry2* (around 10× reduced T6SS activity), or *ΔvipB* (T6SS⁻) donor cells. Total number of sheath assemblies was counted in at least 10,000 GFP⁺ cells for indicated strains. **** $p < 0.0001$, * $p < 0.05$; one-way ANOVA and Tuckey post hoc test for multiple comparison.

(D) VgrG3-specific interbacterial protein complementation using *vgrG1/ΔvgrG3/ΔvasX* as recipient and *ΔvgrG1/ΔvasX* as donor. See Movie S6 for full time-lapse movie.

All data shown in this figure were acquired from three independent biological replicates and are represented as mean ± SD. Scale bar, 2 μm on all images.

et al., 2014). These reporter strains were used as donor cells in two different assays. In the first assay, we tested delivery of TseL from recipient cells into *tseL-tsiV1*-negative donor cells by monitoring their lysis (Figure 4A). The donor cells expressed LacZ from an inducible pBAD33 plasmid and the level of LacZ release was monitored by placing the donor-recipient cell mixture on an agar containing a cell impermeable substrate of LacZ, chlorophenol red-β-D-galactopyranoside (CPRG), which can be used to monitor integrity of LacZ⁺ cells (Paradis-Bleau et al., 2014). Indeed, when such TseL-sensitive and LacZ⁺ reporter cells were mixed with wild-type cells, the LacZ was released as documented by increase in 572 nm absorbance upon CPRG hydrolysis to chlorophenol red (Figures 4B and 4C). This was clearly a result of T6SS-dependent delivery of TseL because the CPRG conversion was abolished by deleting *vipB* or *tseL*. Interestingly, lysis of the T6SS⁺ reporter cells was detected when the cells were mixed with *hcp1/hcp2*, *vgrG2*, or *vgrG2/hcp1/hcp2* recipient strains (Figures 4B and 4C). On the other hand, inactivating T6SS in the reporter cells blocked their lysis, confirming that the recipient cells lacking VgrG2 or Hcp are unable to lyse the reporter cells unless VgrG2 or Hcp proteins are first delivered from the reporter cells (Figure S2D).

To estimate the detection limit of the CPRG-based assay, we tested lysis of LacZ⁺ *E. coli* and the *V. cholerae* reporter by *V. cholerae* lacking *tssE*. This mutant was previously shown to assemble the sheath with a low frequency but had undetectable killing activity using competition assays that measure survival of prey *E. coli* (Basler et al., 2012). Here, we show that in the absence of *tssE*, the sheath assembly rate decreased ~1,000-fold and on average only one sheath assembled per 300 cells (Figure 3A). When *tssE*-negative strain was mixed with *E. coli*, significant LacZ release was observed after 160 min of incubation on CPRG containing agar (Figure S2B). Similarly, significant lysis of *V. cholerae* reporter strain was observed after 160 min (Figure 4C). This confirms that the residual sheath assembly in *tssE*-negative strain is functional and the CPRG assay detects up to 1,000-fold decreased T6SS activity. Importantly, the cells lacking VgrG2 or Hcp were indistinguishable from a strain lacking VipB and induced no detectable lysis of *E. coli* even upon extended incubation (Figure S2B).

In the second assay, we tested VgrG3 translocation using a reporter strain lacking *vgrG3-tsiV3* (Figure 4D). When VgrG3-sensitive reporter cells were incubated with wild-type cells for 1 hr,
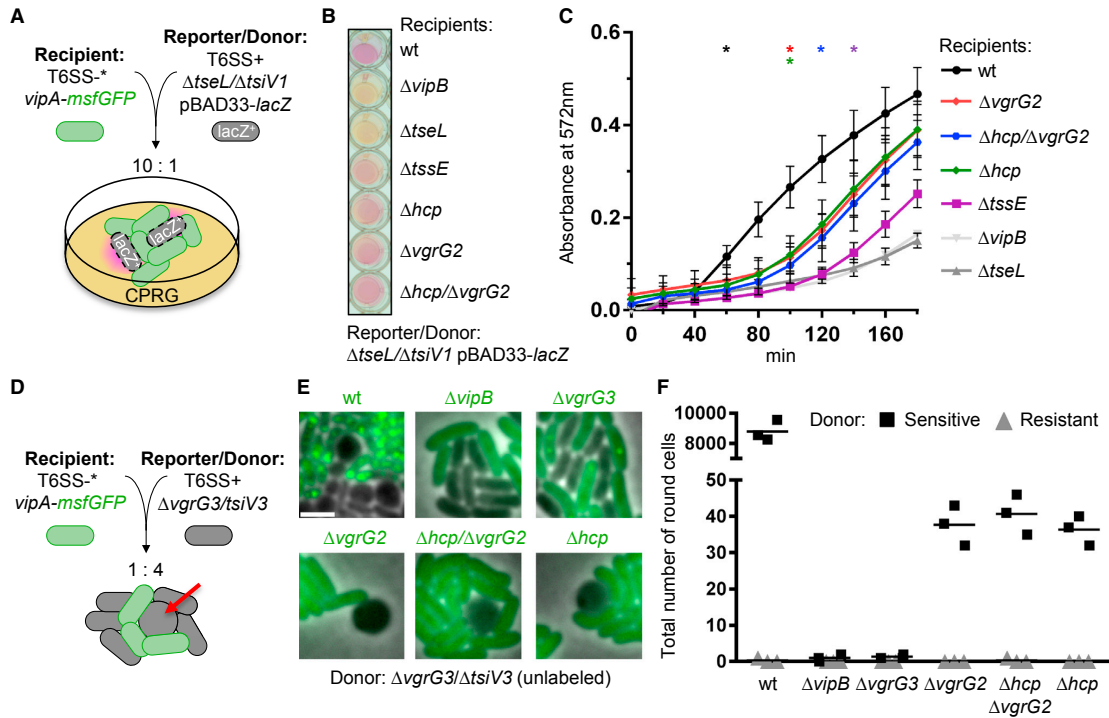
Figure 4. Translocated Proteins Are Reused to Form a Functional T6SS

(A) T6SS$^+$ donor cells lacking the effector TseL and its associated immunity protein TsiV1, as well as harboring the pBAD33-*lacZ* vector were used for inter-bacterial protein complementation assay. Cell mixtures were plated on a LB agar plate containing 20 μg/ml CPRG and 0.1% L-arabinose. Cell-impermeable CPRG is converted by released β-galactosidase to chlorophenol red with an absorbance maximum at 572 nm.

(B) A representative image of a CPRG-based cell permeability assay on 96-well plate is shown after 180 min co-incubation of indicated strains with LacZ$^+$ Δ*tseL*/Δ*tsiV1* donor strain.

(C) Indicated recipient strains were mixed with the donor strain and incubated for 3 hr at 37°C in 96-well plate. Absorbance was measured in 20 min intervals at 572 nm. Colored asterisks mark time point from which chlorophenol red absorbance was significantly higher as compared to background absorbance (Δ*vipB* + reporter) determined by unpaired t test.

(D) T6SS$^+$ donor cells lacking the effector VgrG3 and its associated immunity protein TsiV3 were used for interbacterial protein complementation. Bacterial mixtures were co-incubated on LB agarose pad under a glass coverslip for 1 hr prior to screening for cell-rounding.

(E) Representative images of cells are shown and are a merge of phase contrast and GFP fluorescence channels depicting cell-rounding in VgrG3-sensitive donor cells (black label, no fluorescence) and indicated *vipA-msfGFP* background strains (green label, GFP fluorescence). Scale bar, 2 μm.

(F) Cell-rounding was assessed in 40,000 donor cells being either sensitive (Δ*vgrG3*/Δ*tsiV3*, black squares) or resistant (Δ*vgrG3*, gray triangles) to VgrG3-specific T6SS attack from indicated recipient strain.

All data were acquired from three independent experiments and are represented as mean ± SD.
See also Figure S2.

approximately one in five reporter cells lost their characteristic curved-rod shape and rounded up (Figure 4E). No round cells were detected when wild-type cells were in close contact with wild-type sister cells or when the reporter cells were mixed with *vgrG3*- or *vipB*-deficient strains (Figures 4E and 4F). Interestingly, after 1 hr of incubation of *vgrG3/tsiV3*-negative cells, with *hcp1/ hcp2* and/or *vgrG2*-negative recipient cells, ~1 in 1,000 sensitive cells were round (Figure 4F). The frequency of round cell formation dependent on protein complementation was ~200-fold lower than the frequency observed when wild-type cells were mixed with VgrG3-sensitive cells. This is, however, expected considering two important facts. First, as shown above, recipient cells

assemble T6SS using *trans*-complemented proteins at a rate that is ~50-fold lower than that of wild-type cells (Figure 1H). Second, *vgrG3-tsiV3* donor strain has three times reduced T6SS dynamics compared to the wild-type donor cells and it is therefore also likely complementing VgrG2 and Hcp at three times lower rate (Figure 3A). When T6SS was inactivated in the donor cells, no cell rounding was observed (Figure S2E). As in the case of TseL, this excludes an alternative delivery mechanism of VgrG3 in the absence of VgrG2 or Hcp proteins in the recipient cells.

Taken together, these two assays clearly indicate that the T6SS assembly in the recipient cells resulting from interbacterial protein complementation of Hcp or VgrG2 is functional and can
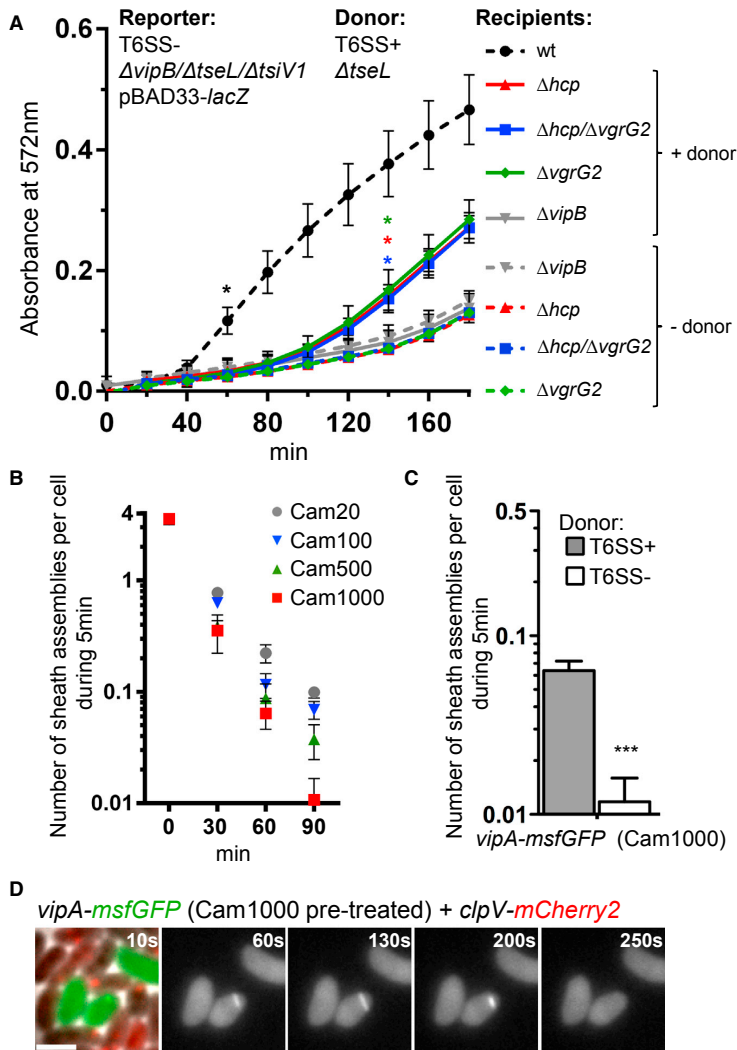
Cell

Figure 5. Cooperation Dependent on Inter-bacterial Protein Complementation

(A) T6SS+ donor cells lacking the effector TseL and indicated recipient strains were mixed with a lipase-sensitive, T6SS−, LacZ+ reporter strain at a ratio of 5:5:1 (donor/recipient/reporter) for the detection of cell lysis. Dashed lines indicate co-incubation of only recipient and reporter strains in the absence of donor. Solid lines indicate a complete three strain mixture. Colored asterisks mark time point from which chlorophenol red absorbance was significantly higher as compared to background absorbance (ΔvipB + donor + reporter) determined by un-paired t test.

(B) Wild-type *vipA-msfGFP*-labeled *V. cholerae* cells were grown to an optical density (OD) of 0.8 prior to the addition of 20, 100, 500, or 1,000 μg/ml chloramphenicol to the culture and continued incubating (200 rpm, 37°C) for up to 90 min. At indicated time points a sample was taken for the analysis of T6SS activity. For each time point and antibiotic concentration, the sheath assemblies were counted in 500 cells.

(C) Sheath assembly was monitored in chloramphenicol-treated wild-type cells upon co-incubation with untreated T6SS+ or T6SS− donor cells. Total number of sheath assemblies was counted for 5,000 GFP+ cells.

(D) Interbacterial protein complementation in translationally inhibited cells. Depicted are individual frames of a 5-min time-lapse. The first frame shows all cells and is a merge of phase contrast, GFP (T6SS substrate-depleted wild-type, T6SS− recipient) and mCherry2 (untreated wild-type donor) fluorescence channels. The following four frames only show GFP fluorescence channel to visualize sheath dynamics. See Movie S7 for full time-lapse movie. Scale bar, 2 μm.

All data were acquired from three independent experiments and are represented as mean ± SD.

Interbacterial Protein Complementation Increases Chances to Kill Competition

Exchange of secreted T6SS components between neighboring cells could provide a benefit to a bacterial community of strains with structurally compatible T6SSs. To test efficiency of such cooperation, we generated a reporter strain, which is only sensitive to TseL delivery and releases LacZ upon lysis, however, is itself unable to secrete any T6SS substrates. When such reporter strain was mixed with a strain that lacks TseL but is capable of delivering other T6SS substrates (donor), no reporter lysis was observed (Figure 5A). Similarly, if the reporter was mixed with a strain that expresses TseL but lacks the structural components Hcp or VgrG2 (recipient), no lysis was observed (Figure 5A). However, when all three strains (reporter, donor, and recipient) were mixed together LacZ was released from lysed reporter cells (Figure 5A). This indicates that donor cells translocated Hcp or VgrG2

deliver both TseL and VgrG3 into neighboring target cells. Interestingly, these experiments also showed that the composition of the tip complex had to change after translocation. The donor cells lacked TseL or VgrG3, however, both TseL and VgrG3 were clearly secreted by the recipient cells after Hcp and VgrG2 complementation. This suggests that the tube-tip complex delivered by the donor cells disassembles after translocation into recipient cells and forms again during new T6SS assembly. Interestingly, Hcp complementation supports formation of T6SS capable of substrate delivery even though most sheath structures are shorter than wild-type (Figure 2A), suggesting that the full-length T6SS sheath is not strictly required for substrate delivery (Figures 4C and 4F).

A Δhcp1/clpV1-*GFP*/pPSV35-*hcp1* + 1mM IPTG

Δhcp1/clpV1-*GFP*/pPSV35-*hcp1* - no IPTG

B Donor: ΔretS

C Donor: ΔretS/ΔpppA

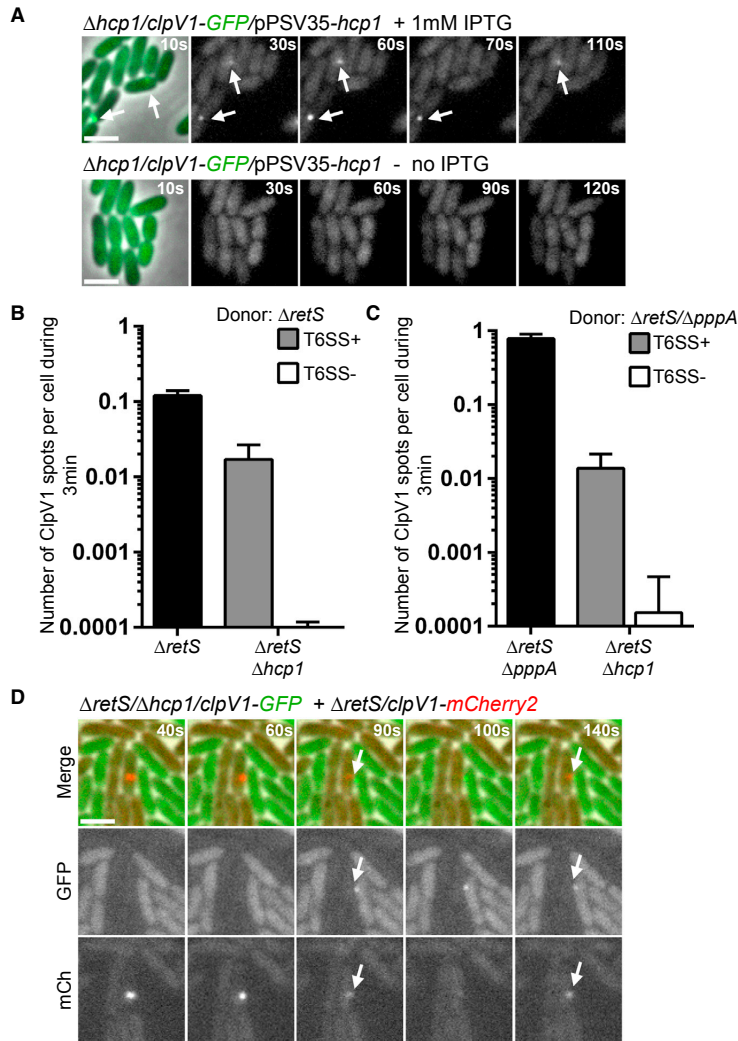**D** ΔretS/Δhcp1/clpV1-*GFP* + ΔretS/clpV1-*mCherry2*

Figure 6. T6SS Mediated Hcp1 Complementation among *P. aeruginosa* Cells

(A) ClpV1-GFP-labeled cells lacking *hcp1* were complemented from pPSV35-*hcp1*. Protein expression was either induced by the addition of 1 mM IPTG for 1 hr at OD of 0.5 to the culture (top) or left uninduced (bottom). Subsequently cells were monitored for ClpV1 spot formation. Depicted are individual time points from a 3-min time-lapse movie. The first frame is a merge of phase contrast and GFP signal. The following four frames only show GFP fluorescence channel to visualize ClpV1 spots.

(B and C) Number of ClpV1 spots in 5,000 GFP⁺ cells was monitored in the Δhcp1 strain (ΔretS/ clpV1-GFP background) for 3 min after 45 min co-incubation either with T6SS⁺ or T6SS⁻ donor cells. Black bar indicates number of ClpV1 spots per cell in ΔretS/clpV1-mCherry2 (B) or ΔretS/ΔpppA/ clpV1-mCherry2 (C) donor strain. Data are represented as mean ± SD and were acquired from four independent biological replicates.

(D) *P. aeruginosa* interbacterial protein complementation: Depicted are individual frames of a 3-min time-lapse. The top row shows all cells and is a merge of phase contrast, GFP (ΔretS/ Δhcp1, T6SS⁻ recipient) and mCherry2 (ΔretS donor) fluorescence channels. The middle and bottom rows only show GFP and mCherry2 fluorescence channel respectively, to clearly identify ClpV1 spots. Arrows highlight ClpV1 spots in donor and recipient as a result of interbacterial protein complementation. Image series were corrected to reduce effects of photo-bleaching. See Movie S8 for complete time-lapse movie. Scale bar, 2 μm.

See also Figure S6.

proteins into the recipient cells that then used these proteins to deliver TseL into the reporter strain to lyse it. This experiment provides a proof of concept that in polymicrobial communities cooperation between two strains based on T6SS dependent protein exchange could contribute to killing of a third strain.

Many anti-bacterial toxins cleave RNA or DNA of target cells. This blocks protein synthesis and presumably decreases the ability of the cells to defend themselves. Indeed, when wild-type *V. cholerae* cells were incubated with chloramphenicol at increasing concentration for extended period of time, the number of sheath assemblies and thus T6SS activity decreased to up to 300 times lower levels (Figure 5B). Interestingly, when such cells were mixed with sister cells with active T6SS, the activity in the inhibited cells was partially restored (Figures 5C

and 5D; Movie S7). This suggests that on-going protein translation is mainly required for synthesis of T6SS substrates and if this is inhibited, the available substrates are secreted out of the cells and T6SS activity decreases. Protein complementation from neighboring sister cells can however prolong T6SS activity and thus potentially increase the chance to successfully fight competition.

The Efficiency of T6SS-Dependent Protein Delivery Depends on Precise Aiming of T6SS

Activity of *P. aeruginosa* H1-T6SS, manifested by dynamic formation of ClpV1-GFP spots, is increased by deletion of *retS* and depends on presence of Hcp1 (Basler and Mekalanos, 2012; Mougous et al., 2006) (Figure 6A). The H1-T6SS assembly is regulated by the TagQRST/PpkA/PppA signaling cascade through phosphorylation and dephosphorylation of Fha1 protein (Basler et al., 2013; Mougous et al., 2007). Importantly, cells with the intact signaling cascade show only low level of H1-T6SS activity, however, can quickly assemble and subcellularly localize
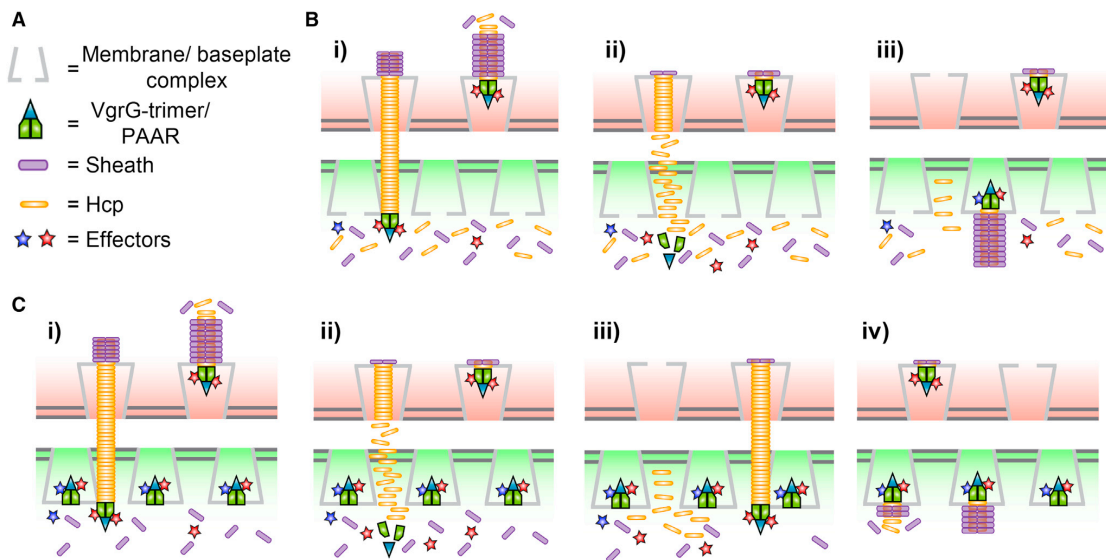
Figure 7. Model for Interbacterial Protein Complementation of Secreted T6SS Components

(A) Overview of depicted T6SS components (not shown in scale).

(B) Tip complementation. VgrGs and associated effectors are translocated from a T6SS+ donor cell (red shade) into a T6SS− recipient cell (green shade) (i), the translocated tip structure rapidly dissociates (ii) and reassembles into a functional T6SS (iii). The assembly of a single full-length Hcp-sheath complex is initiated because sufficient Hcp and sheath subunits are available in the recipient cell and only single tip complex is formed. Translocated tip complexes dissociate in the recipient cells or can be modified by the addition of effector molecules prior to the next round of secretion.

(C) Hcp complementation. Multiple translocation events (i–iv) are needed during Hcp complementation to detect sheath assembly. Recycled Hcp subunits are used for several Hcp-sheath assemblies that are initiated from many functional baseplates, thus leading to multiple significantly shorter sheath assemblies. Hcp-tip complex dissociates in the recipient cells.

See also Figure S7.

their T6SS in the response to external stimuli. In the absence of phosphatase PppA, the T6SS assembly is constitutive, however, the cells are unable to efficiently reposition the H1-T6SS assembly and its subcellular localization seems constant (Basler et al., 2013; Ho et al., 2013). These properties of H1-T6SS allowed us to assess the role of T6SS aiming in T6SS-dependent protein transfer.

To estimate the efficiency Hcp1 transfer between *P. aeruginosa* cells, we mixed *retS/hcp1*-negative recipient strain (*clpV1-GFP* background) with *retS*-negative or *retS/pppA*-negative donor strains (*clpV1-mCherry2* background). After 45 min of co-incubation, ClpV1 localization was monitored for 3 min in both donor and recipient cells (Figures 6B–6D and S6). ClpV1-GFP spot formation was restored in 1.5% of the recipient cells mixed with either one of the two T6SS+ donors, but no ClpV1-GFP spots were detected in a control mixture with *retS/tssC1*- or *retS/pppA/tssB1*-negative donor cells (Figures 6B and 6C). This shows that *P. aeruginosa* is capable of exchanging Hcp1 in a T6SS-dependent manner. The efficiency of Hcp1 transfer was at least six times lower in the mixtures with *pppA*-negative donors than with *pppA*-positive donors because the T6SS activity in the recipients was the same despite the fact that the deletion of *pppA* increased the number of cells with ClpV1 spots more than six times from 12% to 78% (Figures

6B, 6C, and S6; Movie S8). This suggests that the ability to aim T6SS at the target cells is crucial for efficient effector delivery.

DISCUSSION

We show here that measuring frequency of sheath assembly by live-cell microscopy and lysis of target cells are sensitive methods to detect T6SS activity. We used these methods to provide evidence that secreted T6SS components, such as VgrG, Hcp, and effectors, are exchanged between neighboring cells in a T6SS-dependent manner and can be directly reused for a new assembly of a functional T6SS (Figure 7).

T6SS effector translocation was so far detected by live-cell imaging of morphological changes or lysis of target cells (Basler et al., 2013; Borenstein et al., 2015; Brunet et al., 2013; Ho et al., 2013; LeRoux et al., 2012). From these experiments it was, however, unclear how quickly and with what efficiency the T6SS substrates were translocated because the target cells had to be significantly damaged to detect any change. Similarly to phage, T6SS sheath polymerization is initiated by baseplate, which assembles around a single tip complex (Brunet et al., 2015; Durand et al., 2015; Leiman and Shneider, 2012; Taylor et al., 2016). Therefore, imaging sheath assembly in cells that lack tip proteins could detect a consequence of translocation

Cell

of a single tip complex from neighboring cells (Figure 7). Interestingly, we show that T6SS protein translocation can be detected already 2 min after mixing the donor and recipient *V. cholerae* cells (Figure 2C). Protein transfer efficiency can be up to 2% in cells with random localization of T6SS assembly but can be higher if T6SS is properly aimed at the target cells (Figures 1I, 3C, 5A, 6B, and 6C). This efficiency is higher than that of interbacterial protein transfer that was previously measured for T4SS substrates. Frequency of a recombination event upon transfer of a substrate protein fused to Cre recombinase was shown to be $\sim 10^{-3}$ for RP4-dependent MobA translocation and $<10^{-5}$ for Dot/Icm of *Legionella pneumophila* (Luo and Isberg, 2004).

The fact that Hcp and VgrG proteins can be reused for new T6SS assemblies together with the following observations suggest that the proteins are delivered into the cytosol of the target cells. Hcp protein was detected in all cellular fractions with the majority being in the cytosol (Lin et al., 2014; Mougous et al., 2007). T6SS tail assembly is similar to that of phage thus the tube subunits likely assemble on the end of the tube polymer that is distal to the baseplate (Brunet et al., 2014; Leiman and Shneider, 2012; Zoued et al., 2016). Because assembly of T6SS starts from membrane-associated baseplate complex and progresses across the whole cytosol (Durand et al., 2015), most, if not all, of the Hcp protein would be needed in the cytosol. The VgrG proteins were never detected in the periplasm and, similarly to Hcp, lack canonical secretion signal (Boyer et al., 2009). Furthermore, the recently resolved structure of the membrane complex shows that the periplasmic part the T6SS machine is rather small and tightly packed, which suggests that the secreted substrates are loaded onto the tip from the cytosol (Durand et al., 2015). Together, this indicates that VgrG, Hcp, and effectors are likely assembled onto the functional T6SS machine from the cytosol and therefore, at least during interbacterial protein complementation, both Hcp and VgrGs can be delivered to the cytosol of target cells (Figure 7). Our data support a parsimonious explanation that tip and Hcp proteins are directly translocated to the cytosol of target cells by T6SS. Even though another mechanism in the target cells may translocate Hcp and VgrGs from periplasm to the cytosol, such mechanism would have to be able to efficiently and quickly translocate both Hcp and VgrG proteins and be present in both *V. cholerae* and *P. aeruginosa*.

In a single layer of cells with random orientations of their T6SSs, most of the translocation events will likely miss target cells. Assuming that the reach of T6SS is up to a half width of a cell and taking the cell geometry into account, only a maximum of one in six events has a potential to hit a neighboring target cell (Figure S7) (Ho et al., 2014). The observed efficiency of protein complementation in *V. cholerae* is, however, lower, which suggests that only fraction of Hcp or tip secretion results in a new T6SS assembly in the cytosol. Indeed, T6SS may deliver substrates more frequently to the periplasm than to cytosol because many T6SS effectors, including both VgrG3 and TseL, target substrates in the periplasm (Brooks et al., 2013; Dong et al., 2013; Liang et al., 2015; Unterweger et al., 2014). Direct labeling of T6SS substrates or a method for detection of a single molecule transfer is needed for precise quantification of delivery to

cytosol and periplasm, however, it is likely that the T6SS substrates are stochastically delivered to both periplasm and cytosol. The approaches developed in this study will allow further understanding of T6SS-dependent protein transfer.

STAR★METHODS

Detailed methods are provided in the online version of this paper and include the following:

- KEY RESOURCES TABLE
- CONTACT FOR REAGENT AND RESOURCE SHARING
- EXPERIMENTAL MODEL AND SUBJECT DETAILS
  - ○ Bacterial Strains and Growth Conditions
- METHOD DETAILS
  - ○ DNA Manipulations
  - ○ Bacterial Competition Assays
  - ○ Antibodies
  - ○ Western Blotting
  - ○ Fluorescence Microscopy
  - ○ Chloramphenicol Depletion of T6SS-Positive Cells
  - ○ Image Analysis
- QUANTIFICATION AND STATISTICAL ANALYSIS

AUTHOR CONTRIBUTIONS

A.V. designed and performed the experiments, analyzed and interpreted the data, and wrote the manuscript. M.B. designed the experiments, analyzed and interpreted the data, and wrote the manuscript.

REFERENCES

Alcoforado Diniz, J., Liu, Y.-C., and Coulthurst, S.J. (2015). Molecular weaponry: diverse effectors delivered by the Type VI secretion system. Cell. Microbiol. *17*, 1742–1751.

Basler, M., and Mekalanos, J.J. (2012). Type 6 secretion dynamics within and between bacterial cells. Science *337*, 815.

Basler, M., Pilhofer, M., Henderson, G.P., Jensen, G.J., and Mekalanos, J.J. (2012). Type VI secretion requires a dynamic contractile phage tail-like structure. Nature *483*, 182–186.

Basler, M., Ho, B.T., and Mekalanos, J.J. (2013). Tit-for-tat: type VI secretion system counterattack during bacterial cell-cell interactions. Cell *152*, 884–894.

Bina, X.R., Wong, E.A., Bina, T.F., and Bina, J.E. (2014). Construction of a tetracycline inducible expression vector and characterization of its use in *Vibrio cholerae*. Plasmid *76*, 87–94.

Bönemann, G., Pietrosiuk, A., Diemand, A., Zentgraf, H., and Mogk, A. (2009). Remodelling of VipA/VipB tubules by ClpV-mediated threading is crucial for type VI protein secretion. EMBO J. *28*, 315–325.

Borenstein, D.B., Ringel, P., Basler, M., and Wingreen, N.S. (2015). Established microbial colonies can survive Type VI secretion assault. PLoS Comput. Biol. *11*, e1004520.

Borgeaud, S., Metzger, L.C., Scrignari, T., and Blokesch, M. (2015). The type VI secretion system of *Vibrio cholerae* fosters horizontal gene transfer. Science *347*, 63–67.

Boyer, F., Fichant, G., Berthod, J., Vandenbrouck, Y., and Attree, I. (2009). Dissecting the bacterial type VI secretion system by a genome wide in silico analysis: what can be learned from available microbial genomic resources? BMC Genomics *10*, 104.

Brooks, T.M., Unterweger, D., Bachmann, V., Kostiuk, B., and Pukatzki, S. (2013). Lytic activity of the *Vibrio cholerae* type VI secretion toxin VgrG-3 is inhibited by the antitoxin TsaB. J. Biol. Chem. *288*, 7618–7625.

Brunet, Y.R., Espinosa, L., Harchouni, S., Mignot, T., and Cascales, E. (2013). Imaging type VI secretion-mediated bacterial killing. Cell Rep. *3*, 36–41.

Brunet, Y.R., Hénin, J., Celia, H., and Cascales, E. (2014). Type VI secretion and bacteriophage tail tubes share a common assembly pathway. EMBO Rep. *15*, 315–321.

Brunet, Y.R., Zoued, A., Boyer, F., Douzi, B., and Cascales, E. (2015). The Type VI secretion TssEFGK-VgrG phage-like baseplate is recruited to the TssJLM membrane complex via multiple contacts and serves as assembly platform for tail tube/sheath polymerization. PLoS Genet. *11*, e1005545.

Cianfanelli, F.R., Monlezun, L., and Coulthurst, S.J. (2016). Aim, load, fire: the Type VI secretion system, a bacterial nanoweapon. Trends Microbiol. *24*, 51–62.

Clemens, D.L., Ge, P., Lee, B.-Y., Horwitz, M.A., and Zhou, Z.H. (2015). Atomic structure of T6SS reveals interlaced array essential to function. Cell *160*, 940–951.

Dong, T.G., Ho, B.T., Yoder-Himes, D.R., and Mekalanos, J.J. (2013). Identification of T6SS-dependent effector and immunity proteins by Tn-seq in *Vibrio cholerae*. Proc. Natl. Acad. Sci. USA *110*, 2623–2628.

Durand, E., Cambillau, C., Cascales, E., and Journet, L. (2014). VgrG, Tae, Tle, and beyond: the versatile arsenal of Type VI secretion effectors. Trends Microbiol. *22*, 498–507.

Durand, E., Nguyen, V.S., Zoued, A., Logger, L., Péhau-Arnaudet, G., Aschtgen, M.-S., Spinelli, S., Desmyter, A., Bardiaux, B., Dujeancourt, A., et al. (2015). Biogenesis and structure of a type VI secretion membrane core complex. Nature *523*, 555–560.

Flaugnatti, N., Le, T.T.H., Canaan, S., Aschtgen, M.-S., Nguyen, V.S., Blangy, S., Kellenberger, C., Roussel, A., Cambillau, C., Cascales, E., and Journet, L. (2016). A phospholipase A1 antibacterial Type VI secretion effector interacts directly with the C-terminal domain of the VgrG spike protein for delivery. Mol. Microbiol. *99*, 1099–1118.

French, C.T., Toesca, I.J., Wu, T.-H., Teslaa, T., Beaty, S.M., Wong, W., Liu, M., Schröder, I., Chiou, P.-Y., Teitell, M.A., and Miller, J.F. (2011). Dissection of the *Burkholderia* intracellular life cycle using a photothermal nanoblade. Proc. Natl. Acad. Sci. USA *108*, 12095–12100.

Gerc, A.J., Diepold, A., Trunk, K., Porter, M., Rickman, C., Armitage, J.P., Stanley-Wall, N.R., and Coulthurst, S.J. (2015). Visualization of the *Serratia* Type VI secretion system reveals unprovoked attacks and dynamic assembly. Cell Rep. *12*, 2131–2142.

Guzman, L.M., Belin, D., Carson, M.J., and Beckwith, J. (1995). Tight regulation, modulation, and high-level expression by vectors containing the arabinose PBAD promoter. J. Bacteriol. *177*, 4121–4130.

Hachani, A., Allsopp, L.P., Oduko, Y., and Filloux, A. (2014). The VgrG proteins are "à la carte" delivery systems for bacterial type VI effectors. J. Biol. Chem. *289*, 17872–17884.

Hachani, A., Wood, T.E., and Filloux, A. (2016). Type VI secretion and anti-host effectors. Curr. Opin. Microbiol. *29*, 81–93.

Ho, B.T., Basler, M., and Mekalanos, J.J. (2013). Type 6 secretion system-mediated immunity to type 4 secretion system-mediated gene transfer. Science *342*, 250–253.

Ho, B.T., Dong, T.G., and Mekalanos, J.J. (2014). A view to a kill: the bacterial type VI secretion system. Cell Host Microbe *15*, 9–21.

Hood, R.D., Singh, P., Hsu, F., Güvener, T., Carl, M.A., Trinidad, R.R.S., Silverman, J.M., Ohlson, B.B., Hicks, K.G., Plemel, R.L., et al. (2010). A type VI secretion system of *Pseudomonas aeruginosa* targets a toxin to bacteria. Cell Host Microbe *7*, 25–37.

Kapitein, N., Bönemann, G., Pietrosiuk, A., Seyffer, F., Hausser, I., Locker, J.K., and Mogk, A. (2013). ClpV recycles VipA/VipB tubules and prevents non-productive tubule formation to ensure efficient type VI protein secretion. Mol. Microbiol. *87*, 1013–1028.

Koskiniemi, S., Lamoureux, J.G., Nikolakakis, K.C., t'Kint de Roodenbeke, C., Kaplan, M.D., Low, D.A., and Hayes, C.S. (2013). Rhs proteins from diverse bacteria mediate intercellular competition. Proc. Natl. Acad. Sci. USA *110*, 7032–7037.

Kudryashev, M., Wang, R.Y.-R., Brackmann, M., Scherer, S., Maier, T., Baker, D., DiMaio, F., Stahlberg, H., Egelman, E.H., and Basler, M. (2015). Structure of the type VI secretion system contractile sheath. Cell *160*, 952–962.

Leiman, P.G., and Shneider, M.M. (2012). Contractile tail machines of bacteriophages. Adv. Exp. Med. Biol. *726*, 93–114.

LeRoux, M., De Leon, J.A., Kuwada, N.J., Russell, A.B., Pinto-Santini, D., Hood, R.D., Agnello, D.M., Robertson, S.M., Wiggins, P.A., and Mougous, J.D. (2012). Quantitative single-cell characterization of bacterial interactions reveals type VI secretion is a double-edged sword. Proc. Natl. Acad. Sci. USA *109*, 19804–19809.

Liang, X., Moore, R., Wilton, M., Wong, M.J.Q., Lam, L., and Dong, T.G. (2015). Identification of divergent type VI secretion effectors using a conserved chaperone domain. Proc. Natl. Acad. Sci. USA *112*, 9106–9111.

Lin, J.-S., Wu, H.-H., Hsu, P.-H., Ma, L.-S., Pang, Y.-Y., Tsai, M.-D., and Lai, E.-M. (2014). Fha interaction with phosphothreonine of TssL activates type VI secretion in *Agrobacterium tumefaciens*. PLoS Pathog. *10*, e1003991.

Luo, Z.-Q., and Isberg, R.R. (2004). Multiple substrates of the *Legionella pneumophila* Dot/Icm system identified by interbacterial protein transfer. Proc. Natl. Acad. Sci. USA *101*, 841–846.

Ma, L.-S., Hachani, A., Lin, J.-S., Filloux, A., and Lai, E.-M. (2014). *Agrobacterium tumefaciens* deploys a superfamily of type VI secretion DNase effectors as weapons for interbacterial competition in planta. Cell Host Microbe *16*, 94–104.

MacIntyre, D.L., Miyata, S.T., Kitaoka, M., and Pukatzki, S. (2010). The *Vibrio cholerae* type VI secretion system displays antimicrobial properties. Proc. Natl. Acad. Sci. USA *107*, 19520–19524.

Metcalf, W.W., Jiang, W., Daniels, L.L., Kim, S.K., Haldimann, A., and Wanner, B.L. (1996). Conditionally replicative and conjugative plasmids carrying *lacZ* alpha for cloning, mutagenesis, and allele replacement in bacteria. Plasmid *35*, 1–13.

Miyata, S.T., Bachmann, V., and Pukatzki, S. (2013). Type VI secretion system regulation as a consequence of evolutionary pressure. J. Med. Microbiol. *62*, 663–676.

Mougous, J.D., Cuff, M.E., Raunser, S., Shen, A., Zhou, M., Gifford, C.A., Goodman, A.L., Joachimiak, G., Ordoñez, C.L., Lory, S., et al. (2006). A virulence locus of *Pseudomonas aeruginosa* encodes a protein secretion apparatus. Science *312*, 1526–1530.

Mougous, J.D., Gifford, C.A., Ramsdell, T.L., and Mekalanos, J.J. (2007). Threonine phosphorylation post-translationally regulates protein secretion in *Pseudomonas aeruginosa*. Nat. Cell Biol. *9*, 797–803.

Paradis-Bleau, C., Kritikos, G., Orlova, K., Typas, A., and Bernhardt, T.G. (2014). A genome-wide screen for bacterial envelope biogenesis mutants identifies a novel factor involved in cell wall precursor metabolism. PLoS Genet. *10*, e1004056.

Pietrosiuk, A., Lenherr, E.D., Falk, S., Bönemann, G., Kopp, J., Zentgraf, H., Sinning, I., and Mogk, A. (2011). Molecular basis for the unique role of the AAA+ chaperone ClpV in type VI protein secretion. J. Biol. Chem. *286*, 30010–30021.

Pukatzki, S., Ma, A.T., Sturtevant, D., Krastins, B., Sarracino, D., Nelson, W.C., Heidelberg, J.F., and Mekalanos, J.J. (2006). Identification of a conserved bacterial protein secretion system in *Vibrio cholerae* using the *Dictyostelium* host model system. Proc. Natl. Acad. Sci. USA *103*, 1528–1533.

Pukatzki, S., Ma, A.T., Revel, A.T., Sturtevant, D., and Mekalanos, J.J. (2007). Type VI secretion system translocates a phage tail spike-like protein into target cells where it cross-links actin. Proc. Natl. Acad. Sci. USA *104*, 15508–15513.

Rietsch, A., Vallet-Gely, I., Dove, S.L., and Mekalanos, J.J. (2005). ExsE, a secreted regulator of type III secretion genes in *Pseudomonas aeruginosa*. Proc. Natl. Acad. Sci. USA *102*, 8006–8011.

Russell, A.B., Peterson, S.B., and Mougous, J.D. (2014). Type VI secretion system effectors: poisons with a purpose. Nat. Rev. Microbiol. *12*, 137–148.

Schindelin, J., Arganda-Carreras, I., Frise, E., Kaynig, V., Longair, M., Pietzsch, T., Preibisch, S., Rueden, C., Saalfeld, S., Schmid, B., et al. (2012). Fiji: an open-source platform for biological-image analysis. Nat. Methods *9*, 676–682.

Shneider, M.M., Buth, S.A., Ho, B.T., Basler, M., Mekalanos, J.J., and Leiman, P.G. (2013). PAAR-repeat proteins sharpen and diversify the type VI secretion system spike. Nature *500*, 350–353.

Silverman, J.M., Brunet, Y.R., Cascales, E., and Mougous, J.D. (2012). Structure and regulation of the type VI secretion system. Annu. Rev. Microbiol. *66*, 453–472.

Taylor, N.M.I., Prokhorov, N.S., Guerrero-Ferreira, R.C., Shneider, M.M., Browning, C., Goldie, K.N., Stahlberg, H., and Leiman, P.G. (2016). Structure of the T4 baseplate and its function in triggering sheath contraction. Nature *533*, 346–352.

Unterweger, D., Miyata, S.T., Bachmann, V., Brooks, T.M., Mullins, T., Kostiuk, B., Provenzano, D., and Pukatzki, S. (2014). The *Vibrio cholerae* type VI secretion system employs diverse effector modules for intraspecific competition. Nat. Commun. *5*, 3549.

Whitney, J.C., Quentin, D., Sawai, S., LeRoux, M., Harding, B.N., Ledvina, H.E., Tran, B.Q., Robinson, H., Goo, Y.A., Goodlett, D.R., et al. (2015). An interbacterial NAD(P)(+) glycohydrolase toxin requires elongation factor Tu for delivery to target cells. Cell *163*, 607–619.

Zoued, A., Brunet, Y.R., Durand, E., Aschtgen, M.-S., Logger, L., Douzi, B., Journet, L., Cambillau, C., and Cascales, E. (2014). Architecture and assembly of the Type VI secretion system. Biochim. Biophys. Acta *1843*, 1664–1673.

Zoued, A., Durand, E., Brunet, Y.R., Spinelli, S., Douzi, B., Guzzo, M., Flaugnatti, N., Legrand, P., Journet, L., Fronzes, R., et al. (2016). Priming and polymerization of a bacterial contractile tail structure. Nature *531*, 59–63.

STAR★METHODS

KEY RESOURCES TABLE

REAGENT or RESOURCE	SOURCE	IDENTIFIER
Antibodies		
Rabbit polyclonal anti-Hcp	This paper	N/A
Rabbit polyclonal anti-VgrG2	This paper	N/A
Rabbit polyclonal anti-VipB	(Kudryashev et al., 2015)	N/A
Chemicals, Peptides, and Recombinant Proteins		
Streptomycin	AppliChem	A1852,0052; CAS: 3810-74-0
Ampicillin	AppliChem	A0839,0025; CAS: 69-52-3
Chloramphenicol	Sigma Aldrich	C1919; CAS: 56-75-7
Gentamicin	AppliChem	A1492,0025; CAS: 1405-41-0
Chlorophenol red-β-D-galactopyranoside	Sigma-Aldrich	59767-100MG-F; CAS: 99792-79-7
L-(+)-Arabinose	Sigma-Aldrich	A3256-25G; CAS: 5328-37-0
Isopropyl β-D-1-thiogalactopyranoside	AppliChem	A1008,0005; CAS: 367-93-1
Experimental Models: Organisms/Strains		
Vibrio cholerae 2740-80	(Basler et al., 2012)	PRJNA18253
Pseudomonas aeruginosa PAO1	(Mougous et al., 2006)	PRJNA331
A detailed strain list can be found in Table S1A.	this study	N/A
Recombinant DNA		
A detailed plasmid list can be found in Table S1B.	this study	N/A
Software and Algorithms		
Fiji	(Schindelin et al., 2012)	https://fiji.sc/
GraphPad Prism	http://www.graphpad.com	version 6.05 Windows
Other		
Nikon Ti-E inverted motorized microscope	Visitron	N/A

CONTACT FOR REAGENT AND RESOURCE SHARING

Further information and requests for reagents may be directed to, and will be fulfilled by the corresponding author Marek Basler (marek.basler@unibas.ch).

EXPERIMENTAL MODEL AND SUBJECT DETAILS

Bacterial Strains and Growth Conditions

A detailed strain list used in this study can be found in Table S1A. Bacteria were grown in Luria-Bertani (LB) broth at 37°C. Liquid cultures were grown aerobically. Antibiotic concentrations used were streptomycin (100 μg/ml), ampicillin (200 μg/ml), chloramphenicol (20 μg/ml) and gentamicin (15 μg/ml).

METHOD DETAILS

DNA Manipulations

All in-frame deletions and chromosomal mutations were generated by allelic exchange method using suicide plasmids pWM91 (*V. cholerae*) or pEXG2 (*P. aeruginosa*) (Metcalf et al., 1996; Rietsch et al., 2005). A list of plasmids and sequences of the peptides that replaced the indicated genes can be found in Table S1B. For plasmid complementation experiments in *V. cholerae* standard techniques were used to clone *hcp2* and *vgrG2* into L-arabinose inducible vectors pBAD24 and pBAD33 respectively (Guzman et al., 1995). For the detection of T6SS-mediated lysis in *V. cholerae*, *lacZ* was re-cloned from pXB308 (Bina et al., 2014) into pBAD33. For plasmid complementation in *P. aeruginosa*, *hcp1* was cloned into IPTG inducible vector pPSV35 (Rietsch et al., 2005). All cloning products were sequence verified. Chromosomal mutations were verified by PCR using primers outside of the replaced region.

Bacterial Competition Assays

For quantitative killing assays, bacteria were diluted from overnight culture 1:1000 (*V. cholerae*) or 1:200 (*E. coli*) into fresh LB medium supplemented with the appropriate antibiotics and incubated shaking at 37°C, 200 rpm. If indicated, protein expression was induced at OD = 0.2 by the addition of 0.1% L-arabinose to the culture. Bacteria were harvested at OD ≈ 1 and concentrated 10 times, mixed at ratio of 10:1 (*V. cholerae* to *E. coli*) and incubated on dry LB plates for 2 hr at 37°C. Surviving bacteria were counted by 10-fold serial dilutions on selective recovery plates (streptomycin for *V. cholerae*, gentamicin for *E. coli*). Three independent biological replicates were analyzed.

For the detection of T6SS mediated lysis of target cells a LacZ based detection assay was used. Lipase sensitive *V. cholerae* donor strain (*ΔtseL-ΔtsiV1*) harboring the pBAD33-*lacZ* vector was grown in the presence of 10 μg/ml chloramphenicol until OD ≈ 1, washed once and resuspended in 1 ml LB. Recipient cells were grown until OD ≈ 1 and concentrated 10 times. Indicated strains were mixed at a ratio of 10:1 (T6SS- recipients to *ΔtseL-ΔtsiV1*, LacZ+, T6SS+ donors), and 3 μl of the mixtures were spotted on dry 96-well LB plates containing 100 μl of LB agar supplemented with 20 μg/ml CPRG and 0.1% L-arabinose. For three strain lysis assays, strains were mixed at a ratio of 5:5:1 (recipient/donor/reporter). For the detection of *E. coli* lysis, strains were incubated on CPRG plates containing 100 μM IPTG for the induction of β-galactosidase. Bacteria were incubated up to 4 hr at 37°C and absorbance of chlorophenol red was measured every 20 min at 572 nm using an Epoch-2 plate reader (BioTek).

Antibodies

Antigen-purified rabbit polyclonal antibodies raised against VgrG2 peptide NGDPDQPIITGRTY and recombinant full-length Hcp protein were obtained commercially (GenScript, USA). Specificity of the antibodies was tested on *V. cholerae* strains expressing or lacking VgrG2 or Hcp, respectively.

Western Blotting

Bacteria were cultivated as described for the bacterial killing assay. For detection of secreted proteins 450 μl culture supernatant were concentrated by TCA/acetone precipitation, separated on Novex 4%–12% Bis-Tris SDS-PAGE gels (Life Technologies), and transferred to nitrocellulose membrane for immuno-detection. Primary antibodies were used at final concentration of 1 μg/ml in 5% milk in Tris buffered saline (pH 7.4) containing Tween 0.1% (TBST). Primary antibodies were incubated for 1.5 hr with horseradish peroxidase-labeled anti-rabbit antibody (Jackson Lab), washed with TBST, and peroxidase was detected by LumiGLO Chemiluminescent Substrate (Cell Signaling Technology, USA) on a gel imager (GE ImageQuant LAS 4000).

Fluorescence Microscopy

For interbacterial protein complementation experiments overnight cultures were washed once in LB and diluted 1:100 into fresh medium supplemented with appropriated antibiotics, and cultivated to an optical density (OD) at 600 nm of about 0.8–1.2. Cells from 1 ml of the culture were concentrated to OD 10, mixed at a ratio of 1:4 (recipient to donor), subsequently spotted on a thin pad of 1% agarose in LB and covered with a glass coverslip. Bacteria were immediately imaged during an observation period of 2 hr at 25°C using a Nikon Ti-E inverted motorized microscope with Perfect Focus System and Plan Apo 1003 Oil Ph3 DM (NA 1.4) objective lens. SPECTRA X light engine (Lumencore), ET-GFP (Chroma #49002) and ET-mCherry (Chroma #49008) filter sets were used to excite and filter fluorescence. sCMOS camera pco.edge 4.2 (PCO, Germany) (pixel size 65 nm) and VisiView software (Visitron Systems,Germany) were used to record images. Humidity was regulated to 95% using an Okolab T-unit (Okolab). For trans-complementation experiments from pBAD vectors, protein expression was induced by placing cells on a LB 1% agarose pad containing 0.1% L-arabinose. In *P. aeruginosa* protein induction from pPSV35 vector was induced by the addition of 1 mM IPTG to bacterial culture. Bacteria were immediately imaged during an observation period of 2 hr at 25°C. For functional testing of interbacterial protein complementation of secreted T6SS components, *V. cholerae ΔvgrG3/tsiV3* were used as donor cells and mixed with recipient strains as indicated. Prior to screening for cell-rounding, cells were incubated for 1 hr at 37°C.

Chloramphenicol Depletion of T6SS-Positive Cells

Wild-type *vipA-msfGFP* labeled bacteria were grown to an OD of 0.8 prior to the addition of up to 1 mg/ml chloramphenicol (diluted from stock of 200 mg/mL in 100% DMSO) to the culture. Cells were incubated further for 90 min and then 1 ml of culture was harvested and washed three times in 1 ml LB and subsequently concentrated to OD 10. Translationally inhibited cells were then mixed with untreated donor cells for interbacterial protein complementation assay. The final concertation of DMSO during 90 min chloramphenicol pre-incubation was up to 5%, which had no significant influence on T6SS sheath dynamics.

Image Analysis

Fiji (Schindelin et al., 2012) was used for all image analysis and manipulations. For quantification of T6SS activity total cell number was assessed from phase contrast image using the "find maxima" options with noise tolerance setting set to 3000. GFP positive cells were counted the same way using a noise tolerance setting of 250. Sheath number was assessed using a noise tolerance setting of 400. All quantifications were verified manually and carried out using the "edge maxima exclusion" function. For quantification of T6SS activity from time-lapse movies the "temporal color code" function was used. This procedure allows to reliably identifying low-frequency events such as sheath assembly by interbacterial protein complementation but becomes more imprecise with

increasing frequency (e.g., estimation of wild-type T6SS activity) due to overlapping signals. Sheath length measurements were performed exclusively on fully extended structures using the "straight line" tool in Fiji. Contrast on compared sets of images was adjusted equally. All imaging experiments were performed with at least three biological replicates.

QUANTIFICATION AND STATISTICAL ANALYSIS

Statistical parameters such as number of biological replicates and total analyzed bacteria as well as levels of significance are reported in the figure legends. Unpaired t test, ordinary one-way ANOVA or two-way ANOVA with multiple comparisons and Tuckey post hoc test was used to determine significance between all groups using GraphPad Prism version 6.05. If not indicated differently, data are represented as mean ± standard deviation (SD).

CHAPTER 5

The evolution of the type VI secretion system as a lytic weapon

William P. J. Smith[1,2]*, Andrea Vettiger[3]*, Julius Winter[3,4], Till Ryser[3], Laurie E. Comstock[5], Marek Basler[3†] and Kevin R. Foster[1,2†‡]

[1]Department of Biochemistry, University of Oxford, OX1 3QU, UNITED KINGDOM

[2]Department of Zoology, University of Oxford, OX1 3SZ, UNITED KINGDOM

[3]Biozentrum, University of Basel, Klingelbergstrasse 50/70, CH-4056 Basel, SWITZERLAND

[4]École Polytechnique Fédérale de Lausanne, CH-1015 Lausanne, SWITZERLAND

[5]Division of Infectious Diseases, Brigham and Women's Hospital, Harvard Medical School, Boston, MA 02115l, UNITED STATES

* These authors contributed equally to this work

† Corresponding authors. Email: marek.basler@unibas.ch, kevin.foster@zoo.ox.ac.uk

Correspondence and requests for materials should be addressed to K.RF. (email: kevin.foster@zoo.ox.ac.uk)

Supplementary Figures and Tables for this manuscript can be found in Appendix D. Supplementary Video files 1-6 as well as the complete phylogenetic tree can be found attached on the CD attached to this thesis.

Manuscript currently under consideration at *Nature* in a slightly shortened version to meet the journal specific criteria. June, 2019

Statement of contribution

I designed and performed all in vitro experiments as well as analyzed and interpreted their results. I supervised nanoscience MSc students J.W. and T.R. for establishing microfluidics. Further, I contributed genomic analyses as well as to manuscript and figure preparation.

Abstract

The toxin-injecting Type-6 Secretion System (T6SS) is used by Gram-negative bacteria to kill competing bacteria. Here we present a new agent-based model that enables detailed study of the evolutionary costs and benefits of the T6SS as a weapon. Our model predicts that the T6SS's short range creates a fundamental problem: it is rapidly self-limiting because dead cells accumulate in its way, blocking further attacks. We explore solutions using our model, which predicts that inducing rapid lysis in target cells greatly improves killing. We test this prediction and show that Acinetobacter baylyi rapidly eliminates Escherichia coli through T6SS-dependent delivery of lytic toxins, while non-lytic toxins leave large patches of E. coli alive. Genomic data further suggests that most T6SS-wielding species use lytic toxins, indicative of a general principle underlying T6SS evolution. Our work reveals a crucial interplay between toxins' modes of action and their delivery mechanism, with implications for the design of probiotic strategies.

5.1 Introduction

Resembling a spring-loaded spear-gun, the Type-6 Secretion System (T6SS) is an intricate nanomachine found in many Gram-negative bacteria (Boyer et al., 2009; Coulthurst, 2013). Its primary function is the injection of toxic effector proteins into prokaryotic and eukaryotic cells. When a bacterial cell's T6SS is fired, a molecular spring drives a poison-tipped needle outwards, potentially piercing and intoxicating a nearby target cell. Clonemates are spared damage from neighbours' T6SS attacks through the expression of immunity proteins, but other cells lacking immunity risk subsequent cell death. While dependent on cell-cell contact, this delivery route confers a broad target spectrum, enabling toxin translocation without relying on victim cells' surface receptors or transport systems (Stubbendieck and Straight, 2016). Whereas exogenous toxins can be degraded via extracellular enzymes, or excluded via receptor modification (Frost et al., 2018; García-Bayona and Comstock, 2018), the T6SS bypasses victims' defenses, delivering lethal toxins directly to periplasmic or cytoplasmic targets.

Commensurate with these advantages, there is growing evidence of the important roles the T6SS plays in microbial ecosystems. The T6SS appears to be a powerful mediator of interbacterial competition across a broad range of contexts, including plant- and human-associated communities (Bernal et al., 2017; Chassaing and Cascales, 2018; Drebes Dörr and Blokesch, 2018). In these settings, it facilitates pathogen invasion through the killing of commensal species—but, conversely, also empowers commensals to defend ecological niches from competitors and pathogens (Abt and Pamer, 2014; Chatzidaki-Livanis, Geva-Zatorsky and Comstock, 2016; Wexler et al., 2016; Verster et al., 2017).

The importance of the T6SS and its elaborate form has led to extensive study of its structure and function at the molecular level (Cianfanelli, Monlezun and Coulthurst, 2016; Brackmann et al., 2017; Nguyen et al., 2018). However, we still understand little of the factors that drove its evolution as a mechanism for interference competition. The T6SS has a widespread distribution and is found in many Gram-negative bacteria. Nevertheless, many bacteria do not carry it (Chen et al., 2015; Joshi et al., 2017), and those that do typically restrict expression to particular conditions and environments (Basler, Ho and Mekalanos, 2013; Leroux et al., 2015; Metzger et al., 2016; Lazzaro, Feldman and García Véscovi, 2017). Moreover, in addition to its benefits, it is clear that there are potential costs to the T6SS, as usage likely comes with high material overheads, and with only limited scope for component recycling (Basler, 2015; Vettiger and Basler, 2016). The arrangement of different genotypes in space can also affect its utility by changing the proportion of attacks directed against non-kin cells (Borenstein et al., 2015; McNally et al., 2017). This prompts the question: under what conditions do benefits outweigh costs, favoring T6SS use and evolution?

To explore this question, we developed a detailed agent-based model of T6SS competition. A key strength of this model is that it allows one to freely alter both environmental and weapon parameters, such as cell density, firing rate, the cost of firing, and toxin potency, in a manner impossible with experiments. We use this model to explore where and how T6SS use affects bacterial fitness, across a wide range of conditions. Our approach reveals a major limitation to the T6SS's contact-dependent mode of killing. While increasing the rate of T6SS needle firing can benefit a cell through the elimination of competitors, killing rapidly becomes self-limiting, because dead cells accumulate to form protective barriers around groups of T6SS-sensitive cells. This led to a key prediction on the design of the T6SS as a weapon: it will only function effectively if it delivers lytic toxins that clear dead cells. We tested this prediction in competition experiments, both in microfluidic devices and on plates, between *E. coli* and T6SS+ *Acinetobacter baylyi* bacteria secreting different toxins. We also investigated the distribution of lytic toxins across a wide range of T6SS-wielding bacterial species. Our work reveals that the T6SS suffers a major design constraint, but that this can be overcome by the delivery of toxins with a particular mechanism of action. We discuss the implications of our findings both for T6SS evolution and for the goal of using biotherapeutic strains to deliver antimicrobials.

5.2 Results

5.2.1 Agent-based modelling of T6SS competition

When is the T6SS favored by natural selection as a mechanism to kill bacterial competitors? To address this question, we created an agent-based model (ABM) incorporating T6SS

dynamics. Figure 1A provides an overview of our ABM, detailed further in Materials and Methods. As in previous studies (Rudge et al., 2013; Nuñez et al., 2016; Smith et al., 2016; Frost et al., 2018), we consider rod-shaped bacterial cells that push on one another as they grow and divide (Figure 1A, 'Dynamics'). Simulations begin with cells randomly scattered on a flat surface (t_{start}), and end once the cell population reaches a user-defined maximum (t_{end}). To this established framework, we added a discrete representation of T6SS firing and response. T6SS+ 'attacker' cells (green) fire needles from randomly-chosen sites on their surface, at an average rate k_{fire}. T6SS- 'susceptible' cells (magenta) become intoxicated after being struck by N_{hits} needles; intoxicated 'victims' (black) are disabled and lyse at rate k_{lysis}. T6SS+ cells pay a fractional growth cost proportional to their firing rate, so that the average per capita T6SS+ growth rate is $k_{grow}(1 - ck_{fire})$. Our model is implemented as GPU-compatible Python/OpenCL software, expanding on an existing simulation framework (CellModeller). The new model offers the possibility to study the functioning of the T6SS system across a vast range of conditions, and its source code is available to download (Smith, 2019). Further details are provided in the Materials and Methods section, and in Figure S1.

5.2.2 Theory predicts strongly diminishing returns from T6SS investments

We illustrate the model's dynamics with magnified colony views (Figure 1B), showing expansion of cell groups over the course of a simulation. T6SS-mediated killing becomes significant as the colony approaches confluency, with susceptible cells becoming intoxicated—and subsequently lysing—at the inter-strain boundary. In this way, our framework can be used to simulate simple competition scenarios between T6SS+ strains and their susceptible competitors. With it, we can ask: how much T6SS use maximizes attacker fitness?

To determine the optimal firing rate in the presence of weapon costs, we ran competitions like those shown in Figure 1B (100-cell, 1:1 inoculum; 10,000-cell carrying capacity), for increasing values of T6SS firing rate k_{fire}, using the relative fitness of the attacker strain (see Materials and Methods) as a measure of competition outcome. Figure 1C shows that relative fitness increases from 1 for low values of k_{fire}, before peaking and dropping below 1 for higher values (shown here: $N_{hits} = 1, c = 0.001, k_{lysis} = 0.8$ h[-1]; additional parameter combinations are shown in Figures S1 and S2). The three example simulations from Figure 1C are shown in Movie S1. The model predicts the expected fitness benefit of using the T6SS to eliminate a susceptible strain. However, surprisingly, for high T6SS activity the attacker strain can lose, such that the T6SS is counter-selected.
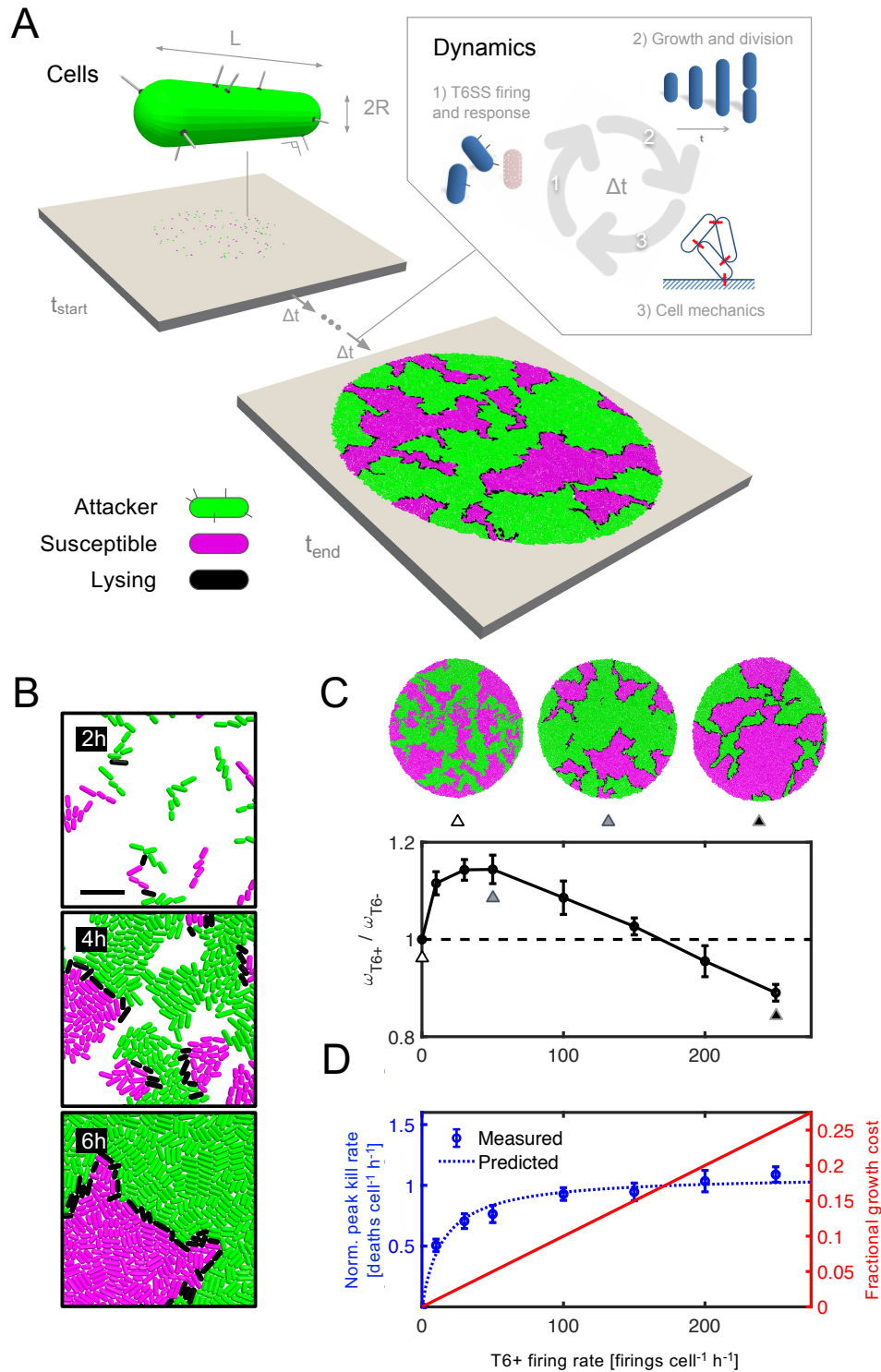
Figure 1: Agent-based model predicts saturation of T6SS benefits. **(A)** Diagram of 2-D competition simulation showing initial (tstart; 100 cells), and final (tend; ~10,000 cells) cell configurations. **(B)** Magnified boxes show typical cell arrangements after 2, 4 and 6 hours of co-culture. Cells are colored by type according to the legend shown; scalebar=10μm. **(C)** Variation in relative fitness of T6SS+ strain ($\omega_{T6+}/\omega_{T6-}$) is shown as a function of T6SS firing rate k_{fire}. Simulation snapshots show final cell configuration for firing rates 0, 50 and 250 firings cell-1 h-1, respectively (triangular markers). Full simulations shown in Movie S1. **(D)** Peak rates of susceptible cell killing, normalized by the number of T6+ cells on the inter-strain boundary (left axis), are compared against fractional growth costs (right axes, equivalent to ck_{fire}) measured at each of the above firing rates. Sample of 5 simulations per

firing rate value depicted in C, D. Parameter values: N_{hits} = 1, c = 0.001, k_{lysis}= 0.8 h-1; additional values shown in Figure S1.

To understand this result, we sought to quantify the benefits of T6SS activity as a function of attacker cells' firing rate. We measured the peak T6SS killing rate in each competition and normalized it by the number of cells on inter-strain boundaries (see Materials and Methods). Plotted in Figure 1D (blue traces, left axis), these measurements show a diminishing returns relationship between increasing T6SS investment (k_{fire}) and the rate of killing achieved in confluent communities. Taken alongside the rising costs of investment (red trace, right axis), these measurements provide a rationale for the observed fitness landscape: for a given inoculum density and composition, saturating benefits of T6SS use are always eventually overtaken by rising costs.

5.2.3   Diminishing fitness returns are due to the accumulation of dead cells

Our model predicts a diminishing-returns relationship between T6SS use and its fitness benefit, which will strongly influence its evolution as an antibacterial weapon. To understand the basis for this relationship, we performed in-depth analyses of the dynamics of T6SS-dependent killing (Figure 2). This revealed that, as T6SS firing increases, so too does the number of dead 'victim' cells found at the inter-strain boundary (Fig. 2A). The same trend was found when the rate of dead cell lysis was increased 10-fold (k_{lysis} = 8.0 h-1, Figure 2B), which substantially lowered the amount of victim cells at the inter-strain boundary. To quantify these trends, we analyzed cell-cell contact patterns in our simulations (see Materials and Methods and Figure S2). We identified attacker cells as being on the inter-strain boundary (bT6SS+) if they touched at least one T6SS- cell, either living or dead, and then measured the fraction of all bT6SS+|T6SS- contacts that involved dead cells. We call this fraction the 'interfacial saturation'. Plotting its values as a function of simulation time (Figure 2C, left column, blue circles) shows that, as the competition progresses, inter-strain boundaries become increasingly populated with dead victims, i.e. interfacial saturation increases. Raising the firing rate (Figure 2C, middle and right columns) substantially increased the final saturation, to the point where > 95 % of all susceptible cells within range of T6SS attacks were already dead. Conversely, increasing the victim lysis rate reduced the average saturation at all time-points and for each firing rate (Figure 2C, red circles).

These trends can be seen more clearly in Figure 2D, which shows measurements of interfacial saturation taken at the time of peak T6SS killing, for increasing T6SS firing rates. Data for slow and fast lysis (k_{lysis} = 0.8, 8.0 h-1 respectively) both showed a saturating, Monod-like dependency on k_{fire} (fitted curves, black). Finally, to test whether interfacial saturation could be used to predict T6SS killing rate, we compared our peak-time saturation measurements (Figure 2D) with peak time killing measurements, plotted previously in Figure 1C. We found that interfacial saturation could be used to predict T6SS killing using

a simple formula, $k_{kill} = f_{interface} \, k_{fire} \, p_{hit}$, where k_{kill} is the rate of victim cell death per unit interface, $f_{interface}$ is the interfacial saturation, k_{fire} is the attacker firing rate, and p_{hit} is the probability of a successful T6SS attack on the interface (Materials and Methods). The predicted kill rates from this simple model are in good agreement with the T6SS kill rates measured in simulations (Figure 1E).
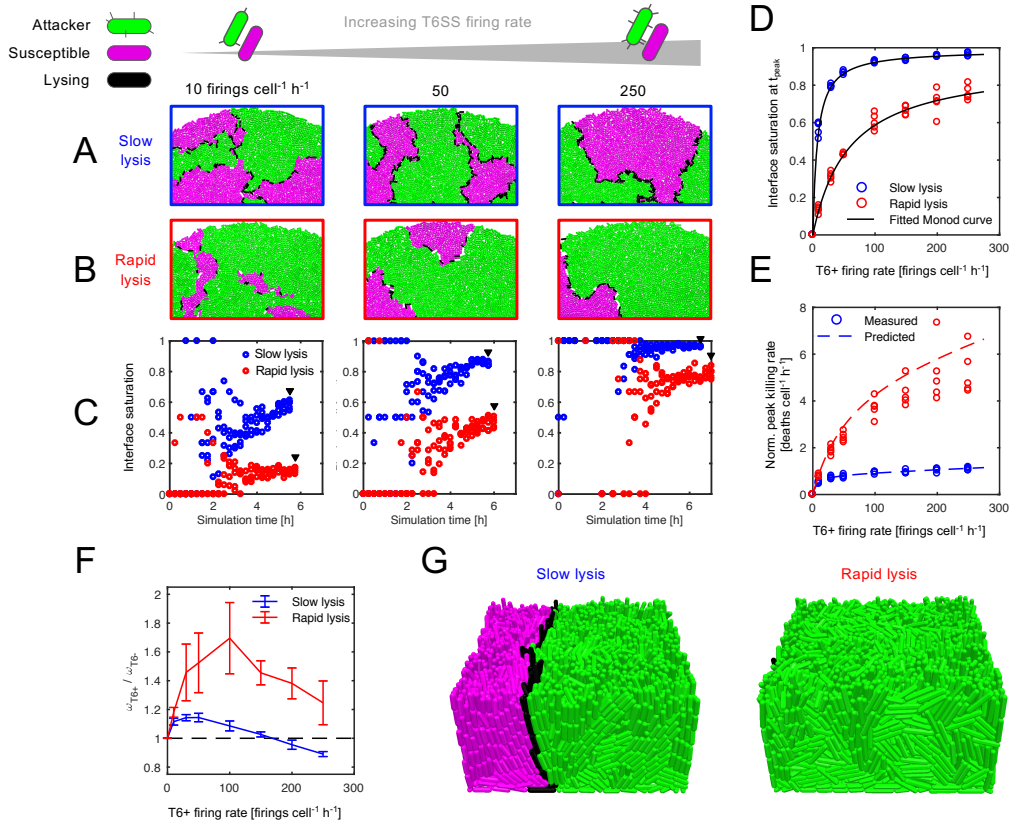

Figure 2: Modelling predicts that victim cell lysis rate determines T6SS killing efficiency. (A, B) Magnified sections of simulated communities show occupation of inter-strain boundary by lysing cells (see legend) at increasing T6SS firing rates. 'Slow lysis' and 'Rapid lysis' cases correspond to k_{lysis} = 0.8, 8.0 h⁻¹ respectively. (C) Interfacial saturation, computed as the fraction of inter-strain boundaries occupied by lysing cells, is shown as a function of simulation time, for each firing and lysis rate in A, B. Arrows indicate timepoints depicted in snapshots. (D) Interfacial saturation measured at time of peak killing (circles) is shown for increasing firing rates k_{fire}, alongside fitted Monod curves (solid lines). (E) Comparison of measured normalized peak killing rates (circles) with those predicted from interfacial saturation (dashed lines), using the formula shown in the main text. (F) Relative fitness of the T6+ attacker strain ($\omega_{T6+}/\omega_{T6-}$, equivalent to ratio of strain division rates) shown for the same conditions as in D, E. (G) 3-D simulations using the same parameters show similar outcomes (k_{fire}= 100 firings cell⁻¹ h⁻¹, comparison at 12.5h growth). Sample of 5 simulations per firing rate value depicted in C-F.

In sum, the diminishing returns relationship between T6SS investment and benefit (Figure 1C) is caused by interfacial saturation. Mechanistically, initial increases in T6SS firing rate accelerate killing and curb competitor growth – but as the firing rate is increased further, the blocking of T6SS attacks by victim cells at the group interface becomes a rate-limiting

factor, and fewer and fewer additional kills are achieved per unit firing rate. We refer to this process as the 'corpse barrier effect', and its existence is consistent with previous empirical observations of dead cells between mutually-vulnerable T6SS+ strains (Alteri et al., 2013; Wong et al., 2016). Our analyses led us to the following key prediction: accelerating victim lysis will improve the value of the T6SS during interference competition. Parameter sweeps using the model support this prediction (Figure 2F), which also holds in 3-dimensional simulations (Figure 2G). Rapid lysis increases the relative fitness of the attacker strain compared with slow lysis, particularly at higher firing rates where the corpse barrier effect is predicted to be stronger. Further, the diminishing returns trend is robust to variation in weapon cost (Figure S2E), and in the number of strikes required to kill a cell (Figure S2F).

5.2.4   Target lysis accelerates T6SS killing of *Escherichia coli* by *Acinetobacter baylyi*

We next sought to test the predictions of our model using competition experiments in microfluidic chambers, which enable single-cell imaging and real-time analysis of T6SS activity, inter-strain boundaries, and victim lysis (Figures 3 and S3). We competed a naturally constitutively-active T6SS+ attacker strain *Acinetobacter baylyi* against a T6SS-susceptible strain, *Escherichia coli* (Ringel, Hu and Basler, 2017). Normally *A. baylyi* uses its T6SS to inject a cocktail of at least 5 different toxins, whose molecular targets and activities differ substantially. For instance, Tae1 is an amidase toxin that targets victims' cell walls, and induces lysis following intoxication. By contrast, toxin Tse2 lyses target cells slowly, but still kills cells efficiently through a mechanism yet unknown. Importantly, it is possible to engineer *A. baylyi* strains that carry only single effector toxins while maintaining the same T6SS assembly rate (Ringel, Hu and Basler, 2017). This allows us to test our predictions by comparing the killing abilities of single-effector mutants bearing lytic (Figure 3, B, D, F) and non-lytic (Figure 3, C, E, G) toxins, during T6SS competition.

First, to verify that both Tae1 and Tse2 toxins can kill *E. coli*, we carried out competition experiments in the presence of propidium iodide, which cannot enter intact cells but increases its fluorescence when bound to DNA upon disruption of membrane integrity (Crowley et al., 2016). Fluorescently-tagged strains of *A. baylyi* (green), expressing only the fast-lysing toxin Tae1, and unlabeled T6SS-sensitive *E. coli* bacteria, were loaded into rectangular microfluidic chambers such that *E. coli* was flanked on two sides by *A. baylyi* (Figure 3A). The competing strains were then allowed to grow and contact one another, forming an interface between the two species (Figure 3B). *A. baylyi* with Tae1 caused *E. coli* cell rounding followed by lysis and release of DNA into the chamber, producing a diffuse cloud of fluorescence (Figure 3B, bottom). *A. baylyi* carrying only toxin Tse2 also caused increase in propidium iodide fluorescence (Figure 3C) but the fluorescence signal

largely remained inside *E. coli* cells at the interface, suggesting that, while the membrane was disrupted, the cells remained physically intact.
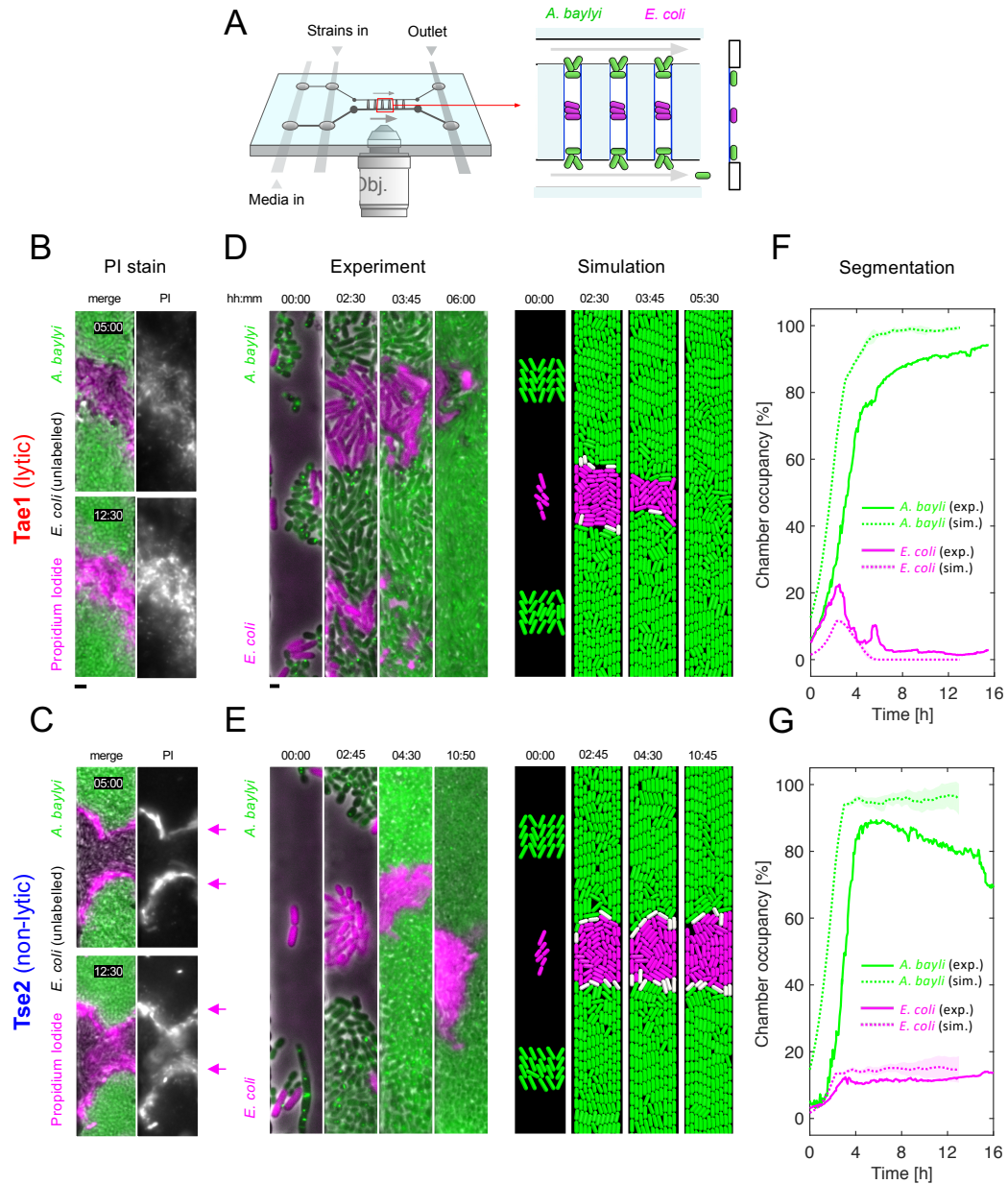

Figure 3: Attackers with lytic T6SS effectors outperform non-lytic analogs in a microfluidic competition assay. Comparison of T6SS competition dynamics in microfluidic chambers, varying T6SS effector type: T6SS+ attacker *A. baylyi* with lytic effector Tae1 (B, D, F), or non-lytic effector Tse2 (C, E, G). **(A)** Diagram of microfluidic chip (left), showing inlets, outlets, flow and observation channels; zoomed section (right) shows observation channels loaded with *A. baylyi* and T6SS- *E. coli*. Diagram not to scale. **(B, C)** Fluorescent microscopy images (B, C, 'PI stain') show unlabeled *E. coli* victim cells between two groups of T6SS+ *A. baylyi* (green) within observation channels. Propidium iodide (PI) labels DNA (shown in magenta) released from lysed cells (Tae1, B), or DNA inside cells upon membrane permeabilization (Tse2, C). **(D, E)** Fluorescent microscopy time-lapse series ('Experiment', left column) show dynamics of competition (*A. baylyi*, green; *E. coli*, magenta); images are representative of 16 biological replicates. Simulations of chamber competitions using the agent-based model from Figures 1-2 are shown alongside ('Simulation', right column; attacker, susceptible and lysing cells shown in green, magenta and white respectively.). **(F, G)** Channel occupancy of each

strain was measured in 5 min intervals based on fluorescence signal and plotted (*E. coli* in magenta, *A. baylyi* in green) as percentage of the whole chamber (solid lines). These data are shown alongside analogous plots for chamber simulations (dashed lines; lines and patches respectively denote means and standard deviations of 5 simulation replicates). Scale bars: 2µm.

Next, we tested whether the mechanism of target cell killing influences growth of the competing bacteria in the microfluidic chambers. Indeed, *A. baylyi* parental strain rapidly eliminated the *E. coli* cell population, whereas no killing was observed for *A. baylyi* lacking *hcp (Δhcp* T6SS-) control (Figure S4, Movie S4). In addition, *A. baylyi* cells carrying only Tae1 were able to largely clear the chamber of *E. coli* cells within 6 hours of inoculation (Figure 3D, 3.93% *E. coli* occupancy), as quantified using automated image analysis (Figure S3, Materials and Methods). In contrast, *A. baylyi* secreting only the non-lytic toxin Tse2 (Figure 3E) were unable to clear *E. coli* from the chambers even after up to 18h co-incubation (14.25% *E. coli* occupancy) despite efficiently killing cells on the boundary (see Movie S3 for side-by-side comparisons of the two toxins; five replicates shown).

The microfluidic experiments support the general prediction from the model that causing cell lysis greatly improves the functioning of the T6SS. To further test the fit between the model and the data, we ran a new version of the T6SS competition simulation using the specific geometry of the microfluidic system, and compared the dynamics of killing between the model and the experiments. Importantly, this exercise was not carried out by simply fitting the model to the data using free parameters in the model. Specifically, the majority of parameters remained unchanged from our earlier models ($N_{hits} = 1, c = 0.001, k_{lysis} = 0.8, 8.0$ h^{-1}). Firing rate k_{fire} is an independent variable in our models and we set this to 50.0 firings cell^{-1} h^{-1}, based on *A. baylyi's* firing rate under these conditions (see Materials and Methods). The one model parameter that, in a sense, was fitted was the degree of mechanical growth restriction (the degree to which dense cell packing causes a slowing in growth), which was increased moderately ($1/\gamma = 0.1$). We found this was necessary to stop susceptible cells from rapidly pushing attackers out of the openings of the chamber in the new geometry.

Running the new model with these parameters revealed a good fit between the predicted dynamics and those seen in the experiments, for both the low and the high rate of cell lysis (Figure 3F, G; Figure S4 and Movie S2). Additional simulations performed for different k_{fire}, k_{lysis} values produced qualitatively similar outcomes, with rapid lysis consistently leading to complete elimination of the susceptible strain (Figure S4E). Overall, this suggests that the dynamics of T6SS-dependent elimination of susceptible cells indeed depend critically on the rate of target cell lysis.

5.2.5 Lytic effectors prevent microcolony survival in competitions on agar surface

Our microfluidic system allows observation of T6SS competition dynamics at single cell resolution, allowing a direct comparison to our models. However, these experiments also confine bacteria in narrow chambers in a manner that may influence the outcome of experiments.
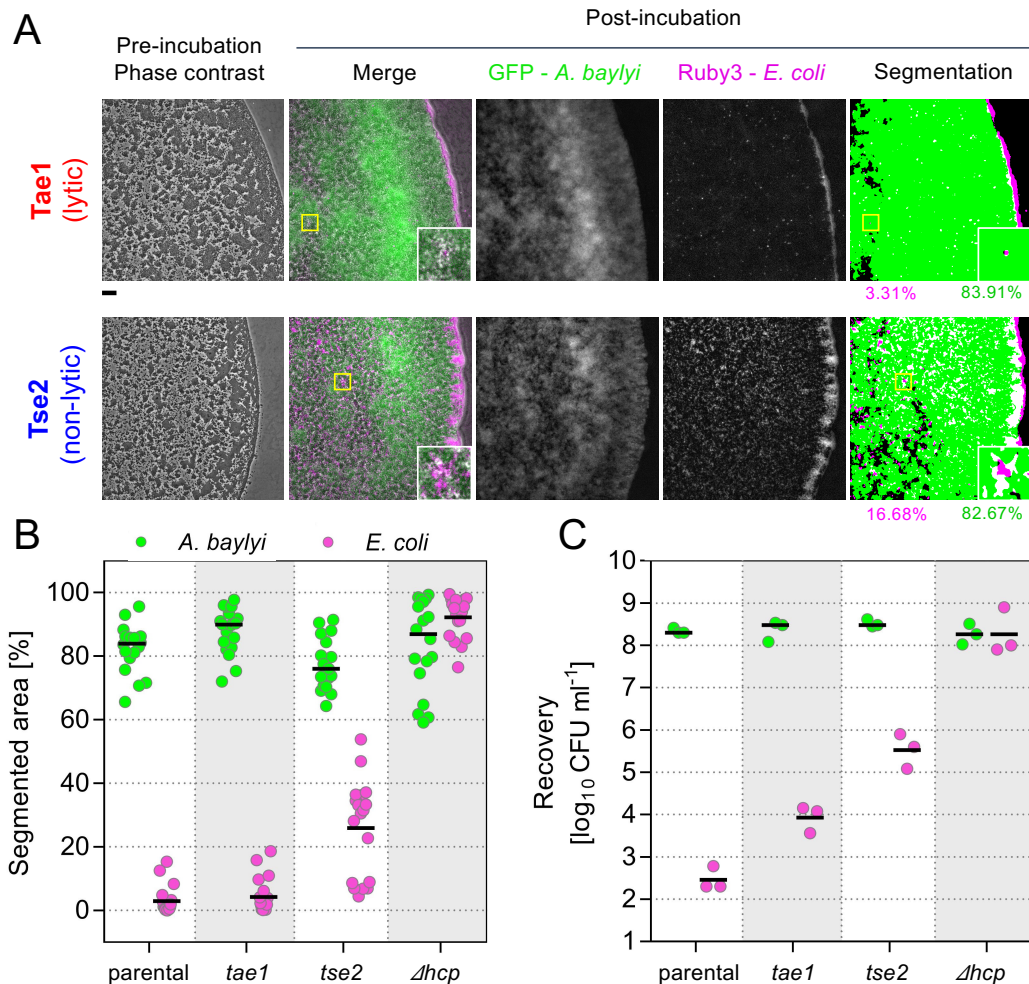

Figure 4: Lytic T6SS effectors outperform non-lytic analogs in competition on agarose surfaces. Surface competition assays comparing performance of T6SS+ attacker *A. baylyi* (vipA-sfGFP, green) armed with lytic (Tae1) and non-lytic (Tse2) effectors, competing with susceptible *E. coli* (mRuby3, magenta). **(A)** Representative phase-contrast and fluorescence micrographs show pre- and post- 3h, 37°C co-incubation distributions of *A. baylyi* and *E. coli* cells, for mixtures of *A. baylyi* secreting Tae1 (top row, red) and Tse2 (bottom row, blue). Fluorescence signal for each channel was blurred and background subtracted prior to Otsu segmentation (right-most column). Based on this, the respective area occupancies of *A. baylyi* and *E. coli* within the community was quantified (percentage occupancy of each strain shown below panel). White pixels indicate overlapping signals for both attacker and susceptible strain. Scale bar = 50µm; inserts depict a 50 x 50µm field of view. **(B)** Segmented areas as percentage of total colony surface are plotted for the two effectors, alongside parental and T6SS-knockout (*Δhcp*) controls. Two-way ANOVA (a = 0.01) with Tuckey post-hoc test; **** = $p \leq 0.0001$; n = 18 spot competitions were analyzed per group. **(C)** Cell recovery data for these assays quantify *A. baylyi* and *E. coli* survival for the same four treatment groups; subsample of 3 replicates per case.

We therefore sought also to test our predictions by co-culturing cells on agarose pads (Figure 4, Materials and Methods). *A. baylyi* and *E. coli* cells were mixed in 1:1 ratio and micrographs showed large numbers of surviving *E. coli* microcolonies at the end of the experiment when competed with *A. baylyi* secreting only non-lytic Tse2. By contrast, there was little evidence of *E. coli* survival when incubated with *A. baylyi* secreting Tae1 (Figures 4A, 4B, S5). To verify that reduced *E. coli* fluorescence did indeed correspond to increased *E. coli* killing, we also performed a cell recovery assay following competitions. These data confirm that ~30x more *E. coli* cells survive in the presence of effector Tse2 than with effector Tae1 (Figure 4C). As expected, the parental *A. baylyi* strain carrying all effectors showed effective *E. coli* killing, while the T6SS- (*Δhcp*) control showed extensive *E. coli* survival (Figure S5).

5.2.6   Osmo-protective conditions show lysis is central to T6SS effectiveness

We have shown—both in microfluidic chambers and on agarose surfaces—that the lytic T6SS toxin Tae1 outperforms its non-lytic counterpart Tse2. Moreover, we observe the build-up of large clumps of victim cells in the absence of cell lysis, as predicted by the corpse barrier effect. These findings, which compare two naturally occurring toxins, support our model's predictions that slow victim lysis blocks effective functioning of the T6SS. However, if the toxins kill at different rates, this may also influence the competition outcomes in addition to the effects of lysis. We, therefore, devised a second experimental strategy to modulate victim lysis without changing the toxin secreted by the attacker. We reasoned that, since Tae1 causes cell lysis by degrading peptidoglycan (Figure 3), it ought to be possible to prevent this by the addition of osmo-protectant (sucrose and $MgSO_4$), which would stabilize the intoxicated cells as spheroplasts (Lederberg, 1956; Leaver et al., 2009).

As anticipated, in the presence of osmo-protectant, *E. coli* cells incubated with Tae1-armed *A. baylyi* blebbed and formed spheroplasts with intact membranes. This was in contrast with the rapid *E. coli* cell lysis observed in the absence of osmo-protectant (Figure 5A, Movie S5). Importantly, the presence of the osmo-protectant had no effect on the T6SS activity of *A. baylyi*, as under both conditions we detected equal amounts of secreted Hcp in the culture supernatant (Figure 5B). Furthermore, image analysis revealed no significant difference in the rates of *E. coli* cell intoxication, as evidenced by an equal number of cell lysis or blebbing events per number of contacts between cells of the two species (Figure 5C). This shows that osmo-protective conditions specifically block target cell lysis without altering T6SS activity and potency or delivery of toxin Tae1.
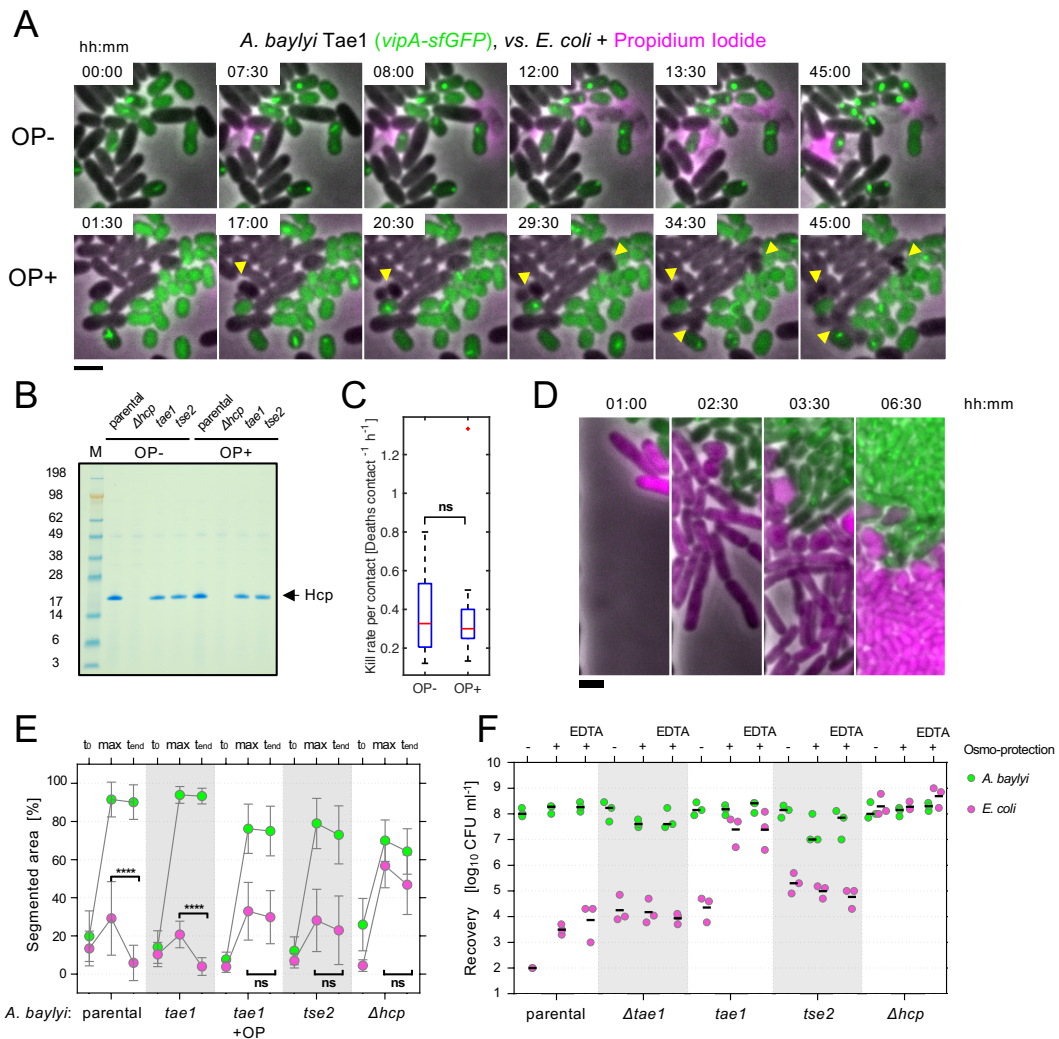
Figure 5: Osmo-protective conditions prevent victim cell lysis and killing without affecting toxin activity. **(A)** Time-lapse images show T6SS firing and killing dynamics between cells grown on agar pads in presence and absence of osmo-protectant (OP+, OP- respectively). Propidium iodide stain (magenta) labels DNA released from susceptible *E. coli* (unlabeled) upon T6SS attack from *A. baylyi* cells (vipA-sfGFP, green) armed with Tae1. Arrowheads mark formation of spheroplasts upon T6SS intoxication. **(B)** Hcp was precipitated from culture supernatants of *A. baylyi* with and without OP, proteins separated by SDS-PAGE, and stained using Coomassie Blue. Column 'M' contains protein reference ladder; axis values show approximate protein molecular weight in kDa. **(C)** Image analysis of time lapses comparing toxin translocation rates, normalized by *E. coli*–*A. baylyi* initial contact counts, in the presence and absence of OP (2-group t-test; p-value = 0.9027). Data originates from ten 45min time-lapses as in A, also shown in Movie S6. **(D)** Fluorescence time-lapse series of microfluidic competition assay between *A. baylyi* armed withTae1 and *E. coli* in the presence of OP at indicated time points (hh:min). Images are representative for 16 biological replicates. **(E)** Quantification of chamber dynamics plot initial ('t_0'), maximum ('t_{max}') and final ('t_{end}') area occupancies of *E. coli* (magenta) and *A. baylyi* (green) from microfluidic competition assays. Data for indicated *A. baylyi* strains and treatments are displayed. Two-way ANOVA ($\alpha = 0.01$) with Tuckey post-hoc test; **** = $p \leq 0.0001$; ns = non-significant; n = 16 channel competitions were analyzed per group. **(F)** *A. baylyi* and *E. coli* recovery data for agarose competition experiments are shown in presence or absence of OP. For each OP+ condition, we show an additional treatment with 20mM EDTA added to ensure lysis of spheroplasts pre-recovery. Scale bar: 2µm.

We applied our osmo-protective assay with *A. baylyi* armed with Tae1 to the microfluidic competition assay. Strikingly, the addition of osmo-protectant resulted in outcomes that appear very similar to competitions with the non-lytic effector Tse2 (Figure 3B), with a visible corpse barrier of spheroplasts forming at the *A. baylyi-E. coli* interface (Figure 5D, Movie S6) and the inability to clear prey cells in the microfluidic device (Figure 5E). Taken together, these data show that both the parental and Tae1 strains lyse target cells and thus eliminate *E. coli* from the chamber upon contact, while preventing *E. coli* lysis by either limiting the toxin to Tse2 or osmo-protecting the *E. coli* cells generates a 'corpse barrier', which prevents elimination of the target cells (Figures 3D-G, 5E).

We also repeated the competition experiments on agar plates under osmo-protective conditions. In these experiments, our assessment of competitive ability comes from plating out cells rather than from direct observation with microscopy; it is therefore possible that spheroplasts would regrow under those conditions, potentially skewing our results. To guarantee that no spheroplasts that were formed by intoxication with Tae1 regrow, we incubated the cells with the membrane-destabilizing ion chelator Ethylene Diamine Tetraacetic Acid (EDTA; see Materials and Methods) during cell recovery. This approach was based on experiments showing that EDTA overrides osmo-protective stabilization of spheroplasts formed using the antibiotic ampicillin (Figure S6). Recovery of E. coli from mixtures with T6SS- *A. baylyi* upon EDTA treatment was unchanged (Figure 5F) indicating that the treatment has no effect on *E. coli* viability and, therefore, that spheroplasts do not survive to form colonies after plating without EDTA. Importantly, in agreement with our microfluidic assays, osmo-protection treatment significantly increased *E. coli* survival when incubated with *A. baylyi* secreting lytic toxin Tae1. However, osmo-protection had no effect on *E. coli* survival in mixtures with *A. baylyi* secreting the non-lytic toxin Tse2. Indeed, in the absence of cell lysis, Tae1 was less effective at clearing *E. coli* than Tse2, although it still killed *E. coli* significantly more than T6SS- (Δhcp) control.

Finally, to exclude the possibility that the osmoprotectant affects additional aspects of T6SS activity beyond lysis of target cells by Tae1, we tested killing of *E. coli* by *A. baylyi* lacking only Tae1. *A. baylyi Δtae1* strain has lytic effectors (e.g. the phospholipase Tle1) that target cell membranes rather than the cell wall, which are expected to induce lysis even under osmo-protective conditions, which only protects cells with intact membranes. As expected, *E. coli* killing was unaffected by osmo-protection in mixtures with *A. baylyi Δtae1* strain. *E. coli* recovery was similar to both the parental strain under osmo-protection conditions as well as to the Tae1 single effector mutant in the absence of osmo-protection (Figure 5F). The effects of osmo-protectant, therefore, are specific to the cell wall targeting effector Tae1.

In summary: as predicted by the model, we found that naturally-occurring lytic and non-lytic effectors differ greatly in their ability to clear corpse barriers. By comparing a single effector with and without osmo-protectant, we further showed that the T6SS functions far better as a lytic weapon than as a general mechanism for the delivery of antimicrobials.

5.3 Discussion

There is growing evidence that bacteria rely on the T6SS as a means to eliminate rivals across diverse ecological contexts (Sassone-Corsi and Raffatellu, 2016; Bernal et al., 2017; Sana, Lugo and Monack, 2017; Drebes Dörr and Blokesch, 2018). While the T6SS offers clear advantages in this capacity, it has also specific limitations, requiring cell-cell contact for toxin delivery. Here, we have developed a new agent-based model and used it to survey the fitness costs and benefits of the T6SS as an anti-competitor weapon. The model predicts, as expected, that a cell can gain territory by using the T6SS against susceptible cells. However, it also predicts that the benefits of increasing T6SS activity are rapidly saturated and even offset by the associated costs. Further analyses revealed that the cause of the saturating benefits is the accumulation of dead cells at inter-strain boundaries, which prevent attacking cells from reaching new targets. We tested these predictions using single-cell and population level experiments, which demonstrated the importance of clearing dead cells for the efficacy of the T6SS as a weapon. Moreover, in both models and experiments, barrier effects appeared mechanically robust: attacker cells could not easily push past dead cells to access fresh susceptible targets. Overall, this suggests that the formation of a barrier of dead cells is a general and fundamental limitation of T6SS-mediated antagonism.

Our work therefore suggests that natural selection should drive a strong association between the use of the T6SS and delivery of effectors that cause rapid lysis in victims. Indeed, many T6SS effectors are known to target the cell wall or membrane (Russell et al., 2011; Durand et al., 2014; Russell, Brook Peterson and Mougous, 2014; LaCourse et al., 2018). The cell wall is the key structure in the bacterial cell for resisting turgor pressure, and its disruption is expected to leave a cell particularly prone to lysis (Huang et al., 2008; Vollmer, Blanot and De Pedro, 2008; Kohanski, Dwyer and Collins, 2010). Consistent with this, we found that delivery of the amidase toxin Tae1 rapidly induces cell lysis (Figure 3). Disruption to cell membranes can also lead to lysis, particularly for phospholipid-targeting toxins that break down the membrane itself (Titball, 1993; Russell et al., 2013; Benz and Meinhart, 2014). This contrasts with pore-forming toxins, which function by inserting themselves into intact membranes (Russell, Brook Peterson and Mougous, 2014). This allows solutes to diffuse across the membranes and disrupts the proton-motive force, but without rapidly reducing the structural integrity of the cell. Similarly, nuclease toxins, which degrade genetic material in the cytosol, are expected to disable bacterial targets without inducing lysis (Cascales et al., 2007; Sharp et al., 2017).
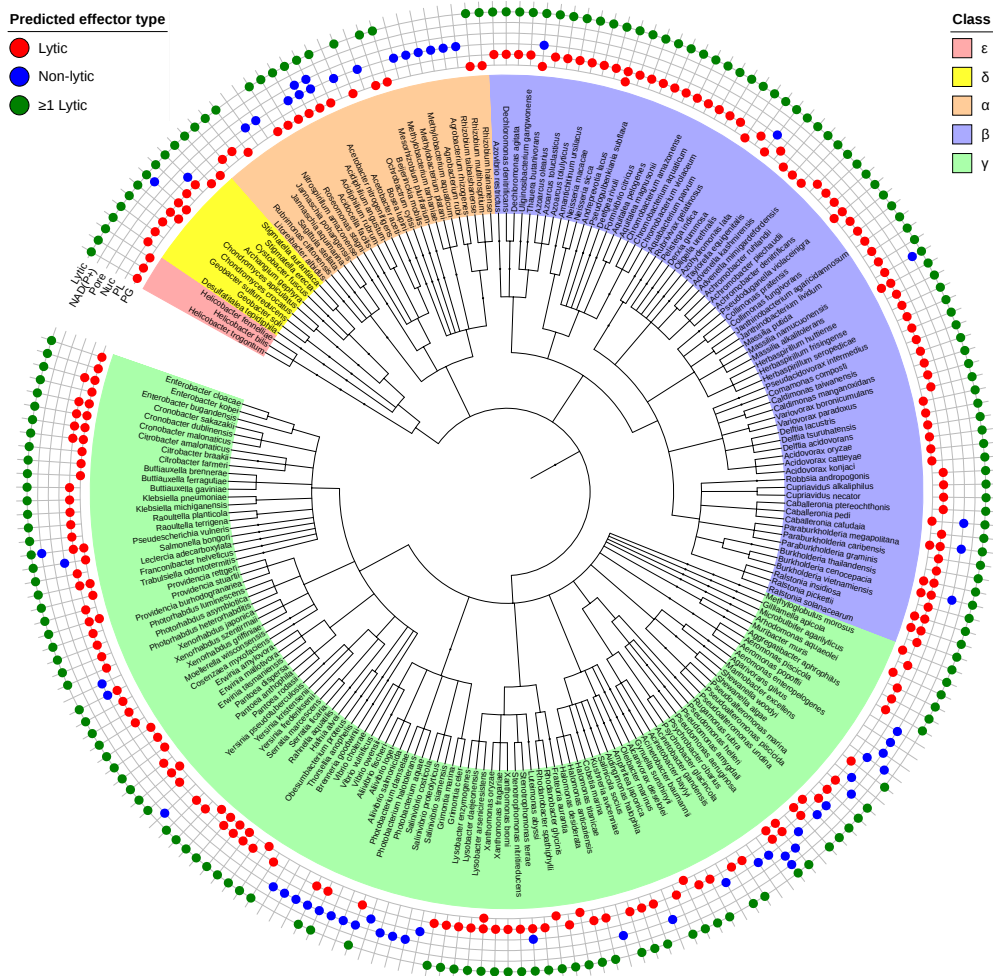
Figure 6: Representative phylogenetic tree showing distribution of lytic and non-lytic T6SS effectors among Proteobacteria. Each species is positioned in the tree according to its taxonomic classification in the NCBI taxonomy database, and colored according to Proteobacterial Class (α, ß, γ, δ, ε). Circles indicate the T6SS effectors associated with a single, randomly-chosen strain from each species. These effectors are classified according to their molecular target: PG=peptidoglycan, PL=phospholipids, DNA=deoxyribonucleic acid, Pore=membrane pore-forming, NAD(P+)= nicotinamide adenine dinucleotide phosphate. A marker in any of these five categories signifies that the corresponding strain has one or more effectors active against that target. Effectors expected to induce rapid cell lysis (PG-, PL-targeting, 'Lytic') are marked in red; those expected to lyse cells only slowly (DNA, Pore, NAD(P+), 'Non-lytic') are marked in blue. A green marker signifies that a given strain has at least one lytic effector in its repertoire. Plotting data from all 474 species was not feasible in one figure, so we plot approximately half (222) of the strains here, but each genus remains represented. The full tree is available to download as a separate file (FullPhyloTree.svg). Data from LaCourse et al.; reanalyzed and simplified here.

In order to further test our prediction that lytic toxins should be commonly secreted by the T6SS, we reanalysed recently-published genomic data (LaCourse et al., 2018). We performed a detailed phylogenetic analysis on the composition of recognized T6SS effectors found in randomly-chosen strains of 474 bacterial species (Figure 6). Each species in this dataset is represented by one strain only, and so these data are not representative of the full toxin repertoire of any given species. However, by comparing example strains across many

species, one can robustly assess preference for known lytic toxins. We divided effectors into those that are more likely to promote cell lysis (peptidoglycan- and membrane-targeting) and those less likely to cause lysis (pore formers, nucleases and glycohydrolases). Of the 1,134 identified effectors, 83.2% (943) are peptidoglycan- or cell-membrane-targeting. Moreover, looking at individual strains, the data suggest that 84.8% (402) carry at least one effector that is peptidoglycan- or cell-membrane-targeting.

Apart from overcoming barrier effects, there are evidently other potential advantages associated with lytic toxins in general: lysed victim cells can release valuable nutrients and DNA for uptake (Borgeaud et al., 2015; Ringel, Hu and Basler, 2017; Veening and Blokesch, 2017; Troselj et al., 2018). However, the patterns seen with T6SS effectors are not common to all bacterial toxins. In particular, the best-studied set of bacterial toxins, the colicins, are released to diffuse in the environment and, there, DNAse and pore-forming mechanisms of action predominate (Riley and Wertz, 2002; Cascales et al., 2007). Lytic toxins, therefore, are not universally favored by bacteria as a means to kill competitors.

Envelope-damaging toxins represent the great majority of T6SS effectors. However, effectors with other mechanisms of action are also found, such as nucleases and glycohydrolases. Other selective pressures will act on the T6SS in a manner that can favor the use of a range of toxins, including the evolution of resistance that can favor the use of uncommon toxins (Biernaskie, Gardner and West, 2013; Granato, Meiller-Legrand and Foster, 2019), and interactions whereby a combination of toxins functions better in inhibiting competitors than one toxin alone (Russell, Brook Peterson and Mougous, 2014; LaCourse et al., 2018). Furthermore, our models predict that lytic effectors are less important if bacteria use the T6SS in conditions where corpse barriers are rare, such as when cells of different genotypes are typically well-mixed, or if the function of the T6SS is to kill the occasional cell that lands upon an existing community. Interestingly, a second, rarer contact-dependent mechanism, Contact-Dependent growth Inhibition (CDI), appears to often deliver non-lytic toxins (Aoki et al., 2010, 2011). This suggests that CDI may function in different ecological contexts, and in potentially different ways, to the T6SS (Ruhe, Low and Hayes, 2013). Indeed, several authors have suggested that a major function of CDI may be signaling within a genotype rather than interference with other genotypes (Danka, Garcia and Cotter, 2017).

The prevalence of the T6SS in bacterial communities is testament to its importance as a mechanism for bacterial competition. A much-discussed strength of the system is that it can directly deliver a wide range of toxins that would otherwise be unable to cross the membranes of target cells (Ho, Dong and Mekalanos, 2014; Basler, 2015; Rüter et al., 2018; Granato, Meiller-Legrand and Foster, 2019). A corollary is that T6SS-wielding bacteria have the potential to serve as powerful probiotics, which deliver a chosen antimicrobial to harmful bacteria (Rüter and Hardwidge, 2014; Rüter, Schmidt and Schmidt, 2017; Raffatellu, 2018).

However, we have shown the T6SS can be ineffective at clearing bacteria if it carries toxins that fail to lyse victim cells. This suggests that the design of biotherapeutics will require an antimicrobial's mechanism of delivery to be matched to its mechanism of action, in a manner not true for the design of conventional antibiotics. More generally, our work emphasizes the need to understand the evolutionary costs and benefits of bacterial weapons if we are to use them to manipulate microbial communities.

Acknowledgements

Declaration of interests

The authors declare no competing interests.

Author contributions

Conceptualization, WPJS, AV, LEC, MB, and KRF; Methodology, WPJS, AV, JW, TR, and MB; Investigation, WPJS, AV, MB, and KRF; Writing – Original Draft, WPJS and AV; Writing – Review & Editing, WPJS, AV, LEC, MB, and KRF; Funding Acquisition, LEC, MB, and KRF; Resources, LEC, MB, and KRF; Supervision, LEC, MB, and KRF.

5.4 Material and Methods

5.4.1 Agent-based modelling

Our agent-based model is based on an existing framework, previously described in detail (Rudge et al., 2012, 2013; Nuñez et al., 2016; Smith et al., 2016), which we have extended to incorporate T6SS firing and killing. Here we provide an overview of the model, and our additions to it. Model parameters and variables are summarized in Tables S1 and S2, respectively.

Cell growth and division. We assume throughout that nutrients are always available in excess, so that all cells have access to the same nutrient concentrations. This simplification obviates the need to explicitly simulate nutrient gradients. In this regime, each cell's volume

V_i bincreases exponentially through elongation, from birth volume V_0, according to the equation $dV_i/dt = k_{grow,i} V_i$; cell volumes are updated iteratively using the discretized form $\Delta V_i = k_{grow,i} V_i dt$, where dt represents the simulation timestep and $k_{grow,i}$ the cell's growth rate. Cells divide lengthwise into two identical daughter cells once they reach volume $2V_0 + \eta_{division}$, where $\eta_{division}$ represents uniform random noise in the cell cycle. Each daughter's axis vector $\hat{a}_i$ is perturbed slightly by a noise term with weight $\eta_{orientations}$, to represent spatial imperfections in the division process.

Cell movement. Following the cell-growth phase, the cell configuration is returned to a quasi-stationary mechanical equilibrium using an energy minimization algorithm, described in previous publications (Rudge et al., 2012; Smith et al., 2016). Briefly, any pair of cells whose surfaces are within 0.01μm of each other are deemed to be overlapping and subject to mutual repulsion. Overlaps between neighboring cells are identified and summarized in a contact matrix A and a distance vector d, along with a regularizing matrix M representing the energetic cost of cell movement, weighted by a scalar factor α. Cell impulses p satisfying the equation $(A^T A + \alpha M)p = -Ad$ are calculated using an iterated conjugate gradients method (Fletcher and Reeves, 1964), such that the application of the impulses moves the cells back to an equilibrium configuration whilst minimizing cell displacement, to within an absolute tolerance ϵ_{CG}. New overlaps created by movement are resolved sequentially, adding sets of impulses together until either their application produces no additional detectable overlaps, or until the iteration count exceeds the maximum iteration number $M_{iter,max}$.

T6SS firing and costs. We model T6SS activity in terms of discrete, spatially-explicit firing events (See Figure 1A, 'cells'). Every simulation timestep dt, each T6SS+ cell i fires $N_{firings,i}$ times, with $N_{firings,i}$ being drawn at random from a Poisson distribution with mean k_{fire} (SI Figure 1A). For each of these firings, a point x on the surface of cell i is chosen at random. A vector, with origin x, orientation $\hat{u}(x)$, and length L_{needle} is constructed, where $\hat{u}(x)$ corresponds to the unit outward normal vector at point p on the cell. We assume that $L_{needle} = R$ (the cell radius), based on the observations that a) extended T6SS sheaths often span the diameter of producing cells, and that b) contraction roughly halves the sheaths' length (Basler et al., 2012; Vettiger et al., 2017; Wang et al., 2017). Firing is assumed to be rapid compared with cell movement timescales, such that firing occurs in essentially static cell configurations. We assume a linear relationship between T6SS firing rate and growth costs (SI Figure 1B): $N_{firings,i}$ times on a given timestep dt reduces the growth rate of cell i by factor $1 - c_{Total,i}$ where cost $c_{Total,i} = c(N_{firings,i}/dt)$.

T6SS hit detection and response. Following firing, each T6SS needle vector is checked to see if it passes through any other cell in the current configuration (a needle never strikes the cell that produced it). Geometrically, this is equivalent to checking whether two line

segments come within distance R of one another, where R is the cell radius. This computationally-intensive process is accelerated using spatial sorting algorithms and parallel implementation, described previously for computing cell-cell mechanical interactions (Rudge et al., 2012). Tallies of successful needle hits are kept to track each cell's intoxication. We assume a step-wise toxin response (SI Figure 1C) with cells dying after being struck by N_{hits} needles. To model immunity, a separate tally is kept for each type of cell in the simulation. For example, given two mutually-susceptible T6SS+ strains A and B, A would ignore its tally of hits from other A cells (self-immunity), but respond to those from B cells.

Model parameterization. The model has a total of 17 parameters, whose names and values are summarized in Table S1. Mechanical and numerical parameters, governing cell movement during growth, were taken from previous publications. Whenever possible, parameters governing T6SS firing and response were estimated directly from experimental observations of *A. baylyi* / *E. coli* competition, detailed below. This was not possible in the case of the cost parameter c, and so we performed a broad parameter sweep to test its influence in our competition simulations from Figures 1 and 2. Figure S1E summarizes this parameter sweep, plotting final attacker frequency ($Total\ attacker\ cell\ volume\ /\ Total\ cell\ volume$) as a metric of competition outcome. Following this sweep, we set the cost factor to the intermediate value of 0.001, for which the optimum firing rate (i.e. the k_{fire} value maximizing final attacker frequency) approximately coincides with the observed A. baylyi firing rate (50 firings cell^{-1} h^{-1}).

5.4.2 Simulation protocols

Computation and post-processing. Agent-based model simulations were run on a 2017 Apple® MacBook Pro laptop computer, with simulations distributed between Intel® 3.1GHz quadcore i7-7920HQ CPU, Intel® HD 630 Graphics card, and AMD Radeon Pro® 560 Compute Engine. Simulation data was analyzed using custom Matlab® scripts, and visualized using Paraview (Ahrens, Geveci and Law, 2005).

2-D disc simulations (Figures 1 and 2). Here we used 100-cell inocula consisting of a 1:1 mix of T6SS+ 'attacker' and T6SS- 'susceptible' cells, randomly scattered and oriented within a 100μm circle. Cell coordinates were restricted to a 2-D plane, producing a confluent monolayer of cells ~180μm in diameter. Simulations were set to terminate once the cell population exceeded 10,000 individuals (living or dead), representing an ecological niche with limited space.

3-D biofilm simulations (Figure 2). Here we instead began with 1 cell of each type, but allowed cells to move and rotate freely within a walled box with base dimensions 40 by 40 μm. To model cell detachment from the mature biofilm, a cell 'slougher' was added to

remove cells positioned $> 20\mu$m from the biofilm's base. Simulations were set to terminate after 13h of growth.

Simulations of microfluidic chambers (Figure 3). In this case, we grow cells from the initial cell arrangement shown in Figure 3A (t = 00:00), in walled, open-ended chambers measuring 10 by 100 μm, with cells being removed from the simulation after being forced out of the chamber's ends. The simulations shown in Figure 3 use the same parameters as in Figure 2 (with k_{fire} set at 50.0 firings cell^{-1} h^{-1}, coinciding approximately with *A. baylyi's* observed firing rate), except that we used CellModeller's default level of mechanical growth restriction ($\gamma = 10, \alpha = 0.1$) to capture observed cell growth reduction in saturated chambers. Chamber simulations began with a fixed arrangement of cells, created by placing a susceptible cell in the center of the chamber, flanking it with 2 rows of 5 attacker cells, and then allowing 3h growth. Simulations terminated after 13h of growth following this starting point, shown in Movie S2 as t = 0.0h.

5.4.3 Simulation metrics

Strain relative fitness. We used the relative fitness of the T6SS+ strain, $\omega_{T6+}/\omega_{T6-}$, to quantify simulation outcome. This quantity is defined as

$$\frac{\omega_{T6+}}{\omega_{T6-}} = \frac{log_2\left(V_{total,T6+}(t_{end}) \,/\, V_{total,T6+}(t_{start})\right)}{log_2\left(V_{total,T6-}(t_{end}) \,/\, V_{total,T6-}(t_{start})\right)},$$

where $V_{total,T6+}$, $V_{total,T6-}$ correspond to the total volumes of T6+ (attacker) and T6- (susceptible) cells, and where t_{start}, t_{end} are the simulation start and end times, respectively.

Inter-strain boundaries. As discussed in the main text, we define T6SS+ cells as lying on the inter-strain boundary if they are touching, and therefore within T6SS firing range of, any T6SS-susceptible cell, whether living or dead (see Figure S2B). As shown in Figure S2A, the number of boundary cells, $N_{boundary}$, varies both within and between simulations, and so it is important to normalize out this variation when comparing T6SS kill rate measurements, as discussed below.

Confluency. Analysis of cell-cell contacts can also be used to define the point at which disc colonies become confluent. At this time, most cells become surrounded on all sides, and so the median cell coordination number (Figure S2A, S2C) plateaus.

Normalized peak kill rate. At a given simulation time-point t, we compute the net victim death rate, $k_{death}(t)$ as the gradient of the cumulative susceptible cell death count $N_{death}(t)$: $k_{death}(t) = (dN_{death}(t)/dt)_t$. Figure S2D shows plots of both $N_{death}(t)$ (red) and $k_{death}(t)$ (blue) for reference. In Figures 1 and 2, we use $max\left(k_{death}(t)\right)$, normalized by the number of boundary cells $N_{boundary}$ at the corresponding time-point, as a measure of the post-confluency kill rate per unit inter-strain boundary,

$$Normalised\ peak\ killing\ rate\ =\ max\big(k_{death}(t)\big)/\ N_{boundary}.$$

Computed in this way, normalized peak T6- kill rates function as an intrinsic metric of T6SS effectiveness: plotting these rates against T6SS firing rate (Figure S2E) produces the same saturating curve for different weapon costs.

T6SS hit probability. To compute the probability that an attacker cell (situated on an inter-strain boundary) hits a non-kin cell with a T6SS needle, we used our model to simulate rounds of firing in fixed cell configurations. For each of the simulations shown in Figure 2, the final cell configuration was extracted. Boundary attacker cells were identified (see *'inter-strain boundaries'* above; Figure S2) and allowed to fire N needles at random. Needle hits were computed, and the proportion of needles striking non-kin (susceptible or victim) cells measured and averaged over the set of configurations. These mean values were found to be invariant with respect to the firing rate used to generate the input cell configurations. The data reported in the main text were measured for simulations with $k_{fire}\ =\ 50.0$ firings cell^{-1} h^{-1}, N $=\ 100$.

5.4.4 Bacterial strains and cultivation

All strains were grown at 37ºC on LB agar plates or by shaking at 200 rpm in LB broth. Growth media were supplemented with appropriate antibiotics where indicated. To gentamycin resistant *E. coli* MG1655 and isogenic mutant constitutively expressing mRuby3 derivate, 15 μg/mL gentamicin was added, for *A. baylyi* ADP1 rpsL-K88R derivatives, 50 μg/mL streptomycin was added. Mutagenesis in *A. baylyi* was carried out as described previously (Ringel, Hu and Basler, 2017). The strains used in this study are listed in Table S3.

5.4.5 Microfluidics

Microfluidic platform. A custom-built polydimethylsiloxane-based microfluidic device was used for all microfluidic experiments. As shown in Figure S3, two individual flow channels are linked by narrow observation channels 10 x 30-150 x 1 μm in dimension (width x length x height). This design allows observation of competition dynamics in cell monolayer, as clonal groups of bacteria grow and come into contact. During design iterations, we realized that *A. baylyi* is slightly thicker than *E. coli*, and so was prone to be trapped at observation channel entrances, while *E. coli* cells could readily enter the channels. On the other hand, *E. coli* grows faster than *A. baylyi* and so could potentially expel the latter from chambers, interfering with the outcome of the contact-dependent competitions. Adjustments to the loading procedure helped to overcome this problem: first, we loaded *A. baylyi* by applying a higher flow rate to the top flow channel (top channel 0.001 μL/s, bottom 0.003 μL/s for 30s), thereby forcing *A. baylyi* cells into the tops of the observation channels. Next, *E. coli* cells were loaded from the opposite side using the same principle but with inverted flow

pressures. Most *E. coli* cells therefore became trapped inside the central regions of the observation channels. Last, the bottom cell inlet was exchanged from *E. coli* to *A. baylyi* cells, allowing us to load a second layer of *A. baylyi* to block the exit of the observation channel (Figure S3). Using this procedure, a prey cell population was trapped in between two layers of *A. baylyi* cells. The chip was perfused with LB medium at 0.005 μL/s using a Nemesys syringe pump, and incubated at 30°C inside an Oko-lab incubation chamber. Competition experiments were run for up to 18h.

Imaging setup. Cells were imaged on an inverted Nikon Ti Eclipse epifluorescence microscope equipped with a fully motorized stage and perfect focus system for multi-position time-lapse imaging. Images were acquired at a 5min acquisition frame rate using a 1.42 numerical aperture Plan Apo 100x oil immersion objective. Fluorescence was excited using a SPECTRA X light engine and filtered using ET-GFP (Chroma #49002), and ET-mCherry (Chroma #49008) filter set and recorded on a pco.edge 4.2 (PCO, Germany) scientific complementary metal-oxide-semiconductor (sCMOS) camera (pixel size 65nm) using VisiView software (Visitron Systems, Germany). For all excitations, output power of the SPECTRA X light engine was set to 20%. Phase contrast, GFP and PI were recorded at 100ms exposure, whereas mRuby3 was recorded at 250ms exposure.

Image analysis. Recorded time-lapse series were post-processed with Fiji (Schindelin et al., 2012). Stage drift was corrected using a customized StackReg plugin (Ringel, Hu and Basler, 2017). Observation channels were selected manually based on initial cell density (<40% occupancy) and a 2:1 (*A. baylyi* : *E. coli*) cell ratio. Next, an automated macro was generated to split fluorescence channels, normalize single intensity to 0.1% saturated pixels per frame, and to reduce noise by blurring images using a Gaussian blur filter (sigma: 2px). If necessary, mRuby3 signal background fluorescence was subtracted (50px rolling ball radius, sliding paraboloid, disabled smoothing). For signal segmentation, a global Otsu thresholding algorithm (Otsu, 1979) was applied to plot growth trajectories for each strain. Total occupancy calculated as measured occupancy of *A. baylyi* + *E. coli* at confluency (assessed from phase contrast image) and served as internal quality control for segmentation (Figure S4), which was not allowed to be higher than 110% (10% error above expected 100% *A. baylyi* + *E. coli* channel occupancy).

5.4.6 Microbial competition assays

Overnight cultures of *A. baylyi* and *E. coli* were diluted 1 to 20 and 1 to 100 respectively into fresh LB, and grown to an optical density (OD, measured at 600nm) of 1. VipA-sfGFP-labeled *A. baylyi* strains served as a T6SS-positive parental strain, while an isogenic *hcp* deletion mutant was used as T6SS-negative control. *E. coli* served as the T6SS-susceptible strain; attacker and susceptible cells were concentrated to indicated ODs, and mixed at 1:1 ratio. Five microliters of cell mixtures were spotted on pre-dried LB plates. After spots were

completely absorbed, the competition was carried out for 3h at 37°C. Subsequently, spots were excised from LB plates and bacterial cells were resuspended in 500 μL LB and subjected to 7 rounds of 10-fold serial dilution. CFUs (colony forming units) of *A. baylyi* and *E. coli* cells were enumerated respectively by plating on streptomycin (100μg/mL) or gentamycin (30μg/mL) media, incubated at 37°C.

For low-magnification microscopy of spot competition assays, cells were grown and prepared as indicated above. 0.5 μL of cell mixture was spotted on a 2.5mm thick 1%-agarose (w/v) and LB pad, and allowed to dry. The spots were imaged with a 10x (numerical aperture 0.25) air objective lens, using the same microscope set-up as above. At this point, fluorescent signal from bacterial cells was too low to be reliably distinguished from background noise. The position was marked, and agar pads were incubated in a humidified chamber (100% relative humidity) at 37°C for 3h. Subsequently, phase contrast images, GFP (1s exposure) and mRuby3 (2s exposure) fluorescence images were acquired for the same positions. Images were background-corrected (50px rolling ball radius, sliding paraboloid, enabled smoothing), blurred (Sigma 2px). Fluorescent signal of both channels was segmented using a global Otsu thresholding algorithm in Fiji (Otsu, 1979; Schindelin et al., 2012). Percentage occupancy was reported for each strain; overlay masks of the segmented signal were generated and compared to the original image as a quality control.

5.4.7 Hcp secretion assay

For detecting Hcp secretion into culture supernatant, indicated *A. baylyi* strains were regrown as described for the quantitative competition assay. Thereafter, 2 mL of fresh LB, or LB + Osmo-protectant (see below), were inoculated at OD600 0.5 and incubated shaking at 37°C, 200rpm for 2h. Subsequently, 1 mL of culture was centrifuged for 1min at 10,000g and 4°C. After centrifugation, 900 μL of culture supernatant were transferred into a fresh tube and proteins were precipitated by adding 100 μL ice-cold 100% TCA (w/v; Sigma-Aldrich). The samples were incubated on ice for 10min with regular mixing and then centrifuged for 5min at 14,000g and 4°C. The pellets were washed with ice-cold acetone, dried at room temperature, and then resuspended in 20 μL 1x NuPAGE LDS sample buffer (Thermo Fisher Scientific); 2 μL 1M dithiothreitol was added and then incubated at 70°C for 10min. Samples were loaded onto NuPAGE 4%–12% Bis-Tris 1.0-mm, 12-well protein gels (Thermo Fisher Scientific), which were run in MES buffer (Thermo Fisher Scientific) for 50min at 150V. The gels were stained with InstantBlue Coomassie protein stain (Expedeon) for 1h at room temperature and subsequently de-stained with distilled water. The results are representative for biological duplicates.

5.4.8 Osmo-protection assay

Cell-wall-damaged *E. coli* cells were stabilized as spheroplasts (Lederberg, 1956; Errington, 2013) by the addition of 0.4M sucrose and 8mM MgSO4 (Sigma-Aldrich) to the growth

medium (designated as osmo-protection, OP). For Hcp secretion assays, cells were pre-grown in absence of osmo-protective medium. For microbial competition experiments, LB plates as well as recovery media were supplemented with OP. To prevent spheroplast regrowth after competition experiments, cells were recovered in LB-OP supplemented with 20mM EDTA and incubated for 45min at 37°C, which causes spheroplast lysis.

For comparison of T6SS intoxication rates in presence or absence of osmo-protectant, we competed unlabeled *E. coli* with vipA-sfGFP labeled *A. baylyi tae1* single effector mutant. Cells were grown and prepared as indicated for microbial competition assays. 2.5μL of cell mixture was spotted onto fresh 1%-agarose (w/v) in LB pads containing 2μg/mL propidium iodide and covered with a glass coverslip, and subsequently imaged for 45min at 30°C at a 30s acquisition frame rate using the same microscope setup as for microfluidic competition assay. From recorded time-lapse series, we manually counted T6SS intoxication events, logging any instance of cell lysis, blebbing, or other sudden morphological change as indicating successful intoxication by Tae1. To account for variation in *A. baylyi - E. coli* cell contact between treatments, we then normalized intoxication counts by the number of unique *A. baylyi - E. coli* cell contacts visible at the start of each time-lapse. These measurements were repeated for all 10 time-lapses; Presence (OP+) and absence (OP-) of OP were compared with a 2-sample t-test performed in Matlab®.

5.4.9   Determination of T6SS firing rate in *A. baylyi*

The rate of T6SS firing in *A. baylyi* was measured from 1,000 vipA-sfGFP, clpV-mCherry2-labeled cells via automated detection of ClpV foci, using Trackmate software (Tinevez et al., 2017). Each new ClpV focus was assumed to mark one T6SS contraction event in a focal cell (Ringel, Hu and Basler, 2017). Time-lapse series were recorded for 7min at a 10sec acquisition frame rate, at 30°C, giving an average measurement of 0.8 firings cell^{-1} min^{-1} (48 firings cell^{-1} h^{-1}).

5.4.10   Survey of T6SS effector repertoire across Proteobacteria

The dataset of LaCourse et al. (LaCourse et al., 2018) lists the distribution of 16 known T6SS toxin domains (Tae1-4, Tge1-3, Tle1-5, Tse4 and VasX effectors; Tox46 and Tox34 motifs) across the genomes of 474 bacterial species, spanning the phyla Proteobacteria (466 species) and Bacteroidetes (8 species). Each species is represented by a single randomly-chosen strain, and so the effectors listed for any one strain are not necessarily representative of the effector variety seen within that species. We used the NCBI common tree tool to arrange these strains in a phylogenetic tree, according to their taxonomic classification in the NCBI taxonomy database (National Center for Biotechnology Information, 2019). We then annotated each strain according to the effectors found in its genome, grouping by molecular target: Peptidoglycan, Phospholipids, DNA, Membrane pore-forming and NAD(P+). The complete (474-species) tree is available to download as an SI file; Figure 6

depicts a pruned (222-species) version of this tree in which up to 3 randomly-chosen species from each represented genus are retained. For ease of reference, the species *K. pneumoniae*, *S. marcescens*, *V. cholerae*, *A. baylyi*, *A. baumannii*, *P. aeruginosa* and *B. thailandensis* are protected from this pruning. Tree visualizations produced using EMBL's interactive Tree of Life (iToL) viewer.

5.4.11 Statistical analyses

Unless indicated otherwise, the number of biological replicates is three for each experiment. For assessing CFUs/mL, the decadic logarithm was taken. Average and standard deviation were calculated from logarithmic values. Normal distribution of values was checked using a D'Agostino-Pearson omnibus normality test. For comparative statistics, we used two-way ANOVA ($\alpha = 0.05$). Multiple comparisons were corrected for using a Tuckey post-hoc test. With the exception of Figure 5C, all such calculations were performed in GraphPad Prism (v7.0).

5.5 References

Abt, M. C. and Pamer, E. G. (2014) 'Commensal bacteria mediated defenses against pathogens', Current Opinion in Immunology. Elsevier Current Trends, 29, pp. 16–22. doi: 10.1016/J.COI.2014.03.003.

Ahrens, J., Geveci, B. and Law, C. (2005) 'ParaView: An End-User Tool for Large Data Visualization', in Visualization Handbook. Elsevier. Available at: www.paraview.org. (Accessed: 19 October 2018).

Alteri, C. J. et al. (2013) 'Multicellular Bacteria Deploy the Type VI Secretion System to Preemptively Strike Neighboring Cells', PLoS Pathogens. Edited by T. Kubori. Public Library of Science, 9(9), p. e1003608. doi: 10.1371/journal.ppat.1003608.

Aoki, S. K. et al. (2010) 'A widespread family of polymorphic contact-dependent toxin delivery systems in bacteria', Nature. Nature Publishing Group, 468(7322), pp. 439–442. doi: 10.1038/nature09490.

Aoki, S. K. et al. (2011) 'Toxin on a stick', Virulence. PMID, 2(4), p. 21085179. doi: 10.4161/viru.2.4.16463.

Basler, M. et al. (2012) 'Type VI secretion requires a dynamic contractile phage tail-like structure', Nature, 483. doi: 10.1038/nature10846.

Basler, M. (2015) 'Type VI secretion system: secretion by a contractile nanomachine', Phil. Trans. R. Soc. B, 370, pp. 1–11. doi: 10.1098/rstb.2015.0021.

Basler, M., Ho, B. T. and Mekalanos, J. J. (2013) 'Tit-for-Tat: Type VI Secretion System Counterattack during Bacterial Cell-Cell Interactions', Cell, 152, pp. 884–894. doi: 10.1016/j.cell.2013.01.042.

Benz, J. and Meinhart, A. (2014) 'Antibacterial effector/immunity systems: it's just the tip of the iceberg', Current Opinion in Microbiology. Elsevier Current Trends, 17, pp. 1–10. doi: 10.1016/J.MIB.2013.11.002.

Bernal, P. et al. (2017) 'The Pseudomonas putida T6SS is a plant warden against phytopathogens', The ISME Journal. Nature Publishing Group, 11(4), pp. 972–987. doi: 10.1038/ismej.2016.169.

Biernaskie, J. M., Gardner, A. and West, S. A. (2013) 'Multicoloured greenbeards, bacteriocin diversity and the rock-paper-scissors game', J. Evol. Biol., 26, pp. 2081–2094. doi: 10.1111/jeb.12222.

Borenstein, D. B. et al. (2015) 'Established Microbial Colonies Can Survive Type VI Secretion Assault', PLoS Comput Biol, 11(10). doi: 10.1371/journal.pcbi.

Borgeaud, S. et al. (2015) 'The type VI secretion system of Vibrio cholerae fosters horizontal gene transfer', Science, 347(6217), pp. 63–67. doi: 10.1126/science.1260064.

Boyer, F. et al. (2009) 'Dissecting the bacterial type VI secretion system by a genome wide in silico analysis: what can be learned from available microbial genomic resources?', BMC Genomics, 10(104), pp. 1–14. doi: 10.1186/1471-2164-10-104.

Brackmann, M. et al. (2017) 'Using Force to Punch Holes: Mechanics of Contractile Nanomachines', Trends in Cell Biology, 27(9), pp. 623–632. doi: 10.1016/j.tcb.2017.05.003.

Cascales, E. et al. (2007) 'Colicin biology.', Microbiology and molecular biology reviews : MMBR. American Society for Microbiology, 71(1), pp. 158–229. doi: 10.1128/MMBR.00036-06.

Chassaing, B. and Cascales, E. (2018) 'Antibacterial Weapons: Targeted Destruction in the Microbiota', Trends in Microbiology, 26(4), pp. 329–338. doi: 10.1016/j.tim.2018.01.006.

Chatzidaki-Livanis, M., Geva-Zatorsky, N. and Comstock, L. E. (2016) 'Bacteroides fragilis type VI secretion systems use novel effector and immunity proteins to antagonize human gut Bacteroidales species', Proceedings of the National Academy of Sciences, 113(13), pp. 3627–3632. doi: 10.1073/pnas.1522510113.

Chen, L. et al. (2015) 'Composition, function, and regulation of T6SS in Pseudomonas aeruginosa', Microbiological Research, 172, pp. 19–25. doi: 10.1016/j.micres.2015.01.004.

Cianfanelli, F. R., Monlezun, L. and Coulthurst, S. J. (2016) 'Aim, Load, Fire: The Type VI Secretion System, a Bacterial Nanoweapon', Trends in Microbiology, 24(1), pp. 51–62. doi: 10.1016/j.tim.2015.10.005.

Coulthurst, S. J. (2013) 'The Type VI secretion system - a widespread and versatile cell targeting system', Research in Microbiologoy, 164, pp. 640–654. doi: 10.1016/j.resmic.2013.03.017.

Crowley, L. C. et al. (2016) 'Measuring Cell Death by Propidium Iodide Uptake and Flow Cytometry.', Cold Spring Harbor protocols. Cold Spring Harbor Laboratory Press, 2016(7), p. pdb.prot087163. doi: 10.1101/pdb.prot087163.

Danka, E. S., Garcia, E. C. and Cotter, P. A. (2017) 'Special Issue: From One to Many Are CDI Systems Multicolored, Facultative, Helping Greenbeards?', Trends in Microbiology, 25, pp. 391–401. doi: 10.1016/j.tim.2017.02.008.

Drebes Dörr, N. C. and Blokesch, M. (2018) 'Bacterial type VI secretion system facilitates niche domination', Proceedings of the National Academy of Sciences, 115(36), pp. 8855–8857. doi: 10.1073/pnas.1812776115.

Durand, E. et al. (2014) 'VgrG, Tae, Tle, and beyond: the versatile arsenal of Type VI secretion effectors', Trends in Microbiology. Elsevier Current Trends, 22(9), pp. 498–507. doi: 10.1016/J.TIM.2014.06.004.

Errington, J. (2013) 'L-form bacteria, cell walls and the origins of life', Open Biology, 3(1), pp. 120143–120143. doi: 10.1098/rsob.120143.

Fletcher, R. and Reeves, C. M. (1964) 'Function minimization by conjugate gradients', The Computer Journal. Oxford University Press, 7(2), pp. 149–154. doi: 10.1093/comjnl/7.2.149.

Frost, I. et al. (2018) 'Cooperation, competition and antibiotic resistance in bacterial colonies', The ISME Journal. Nature Publishing Group, 12(6), pp. 1582–1593. doi: 10.1038/s41396-018-0090-4.

García-Bayona, L. and Comstock, L. E. (2018) 'Bacterial antagonism in host-associated microbial communities', Science. American Association for the Advancement of Science, 361(6408), p. eaat2456. doi: 10.1126/SCIENCE.AAT2456.

Granato, E. T., Meiller-Legrand, T. A. and Foster, K. R. (2019) 'The Evolution and Ecology of Bacterial Warfare', Current Biology.

Ho, B. T., Dong, T. G. and Mekalanos, J. J. (2014) 'A View to a Kill: The Bacterial Type VI Secretion System', Cell Host & Microbe, 15, pp. 9–21. doi: 10.1016/j.chom.2013.11.008.

Huang, K. C. et al. (2008) 'Cell shape and cell-wall organization in Gram-negative bacteria', Proceedings of the National Academy of Sciences, 105(49), pp. 19281–19286. Available at: www.pnas.org/cgi/content/full/ (Accessed: 4 March 2019).

Joshi, A. et al. (2017) 'Rules of Engagement: The Type VI Secretion System in Vibrio cholerae', Trends in Microbiology, 25(4), pp. 267–279. doi: 10.1016/j.tim.2016.12.003.

Kohanski, M. A., Dwyer, D. J. and Collins, J. J. (2010) 'How antibiotics kill bacteria: from targets to networks', Nature Reviews Microbiology. Nature Publishing Group,

8(6), pp. 423–435. doi: 10.1038/nrmicro2333.

LaCourse, K. D. et al. (2018) 'Conditional toxicity and synergy drive diversity among antibacterial effectors', Nature Microbiology. Nature Publishing Group, 3(4), pp. 440–446. doi: 10.1038/s41564-018-0113-y.

Lazzaro, M., Feldman, M. F. and García Véscovi, E. (2017) 'A Transcriptional Regulatory Mechanism Finely Tunes the Firing of Type VI Secretion System in Response to Bacterial Enemies.', mBio. American Society for Microbiology, 8(4), pp. e00559-17. doi: 10.1128/mBio.00559-17.

Leaver, M. et al. (2009) 'Life without a wall or division machine in Bacillus subtilis', Nature. Nature Publishing Group, 457(7231), pp. 849–853. doi: 10.1038/nature07742.

Lederberg, J. (1956) 'Bacterial Protoplasts Induced by Penicillin', Proc. Nat. Acad. Sci. Available at: https://www.ncbi.nlm.nih.gov/pmc/articles/PMC534253/pdf/pnas00712-0007.pdf (Accessed: 19 March 2019).

Leroux, M. et al. (2015) 'Kin cell lysis is a danger signal that activates antibacterial pathways of Pseudomonas aeruginosa', eLIFE, 4, pp. 1–25. doi: 10.7554/eLife.05701.001.

McNally, L. et al. (2017) 'Killing by Type VI secretion drives genetic phase separation and correlates with increased cooperation', Nature Communications. doi: 10.1038/ncomms14371.

Metzger, L. C. et al. (2016) 'Independent Regulation of Type VI Secretion in Vibrio cholerae by TfoX and TfoY', Cell Reports, 15, pp. 951–958. doi: 10.1016/j.celrep.2016.03.092.

National Center for Biotechnology Information (2019) NCBI common tree tool. Available at: https://www.ncbi.nlm.nih.gov/Taxonomy/CommonTree/wwwcmt.cgi (Accessed: 1 March 2019).

Nguyen, V. S. et al. (2018) 'Towards a complete structural deciphering of Type VI secretion system', Current Opinion in Structural Biology, 49, pp. 77–84. doi: 10.1016/j.sbi.2018.01.007.

Nuñez, I. N. et al. (2016) 'Artifical Symmetry-Breaking for Morphogenetic Engineering Bacterial Colonies', ACS Synthetic Biology. UTC, 6, pp. 256–265. doi: 10.1021/acssynbio.6b00149.

Otsu, N. (1979) 'A Threshold Selection Method from Gray-Level Histograms', IEEE Transactions on Systems, Man and Cybernetics, 9(1). Available at: https://projects.iq.harvard.edu/imagenesmedi

cas/publications/threshold-selection-method-gray-level-histograms (Accessed: 11 January 2019).

Raffatellu, M. (2018) 'Learning from bacterial competition in the host to develop antimicrobials', Nature Medicine. Nature Publishing Group, 24(8), pp. 1097–1103. doi: 10.1038/s41591-018-0145-0.

Riley, M. A. and Wertz, J. E. (2002) 'Bacteriocin diversity: ecological and evolutionary perspectives', Biochimie. Elsevier, 84(5–6), pp. 357–364. doi: 10.1016/S0300-9084(02)01421-9.

Ringel, P. D., Hu, D. and Basler, M. (2017) 'The Role of Type VI Secretion System Effectors in Target Cell Lysis and Subsequent Horizontal Gene Transfer', Cell Reports, 21(13), pp. 3927–3940. doi: 10.1016/j.celrep.2017.12.020.

Rudge, T. J. et al. (2012) 'Computational Modeling of Synthetic Microbial Biofilms', ACS Synthetic Biology. UTC, 1, pp. 345–352. doi: 10.1021/sb300031n.

Rudge, T. J. et al. (2013) 'Cell Polarity-Driven Instability Generates Self-Organized, Fractal Patterning of Cell Layers', ACS Synth. Biol, (2), pp. 705–714. doi: 10.1021/sb400030p.

Ruhe, Z. C., Low, D. A. and Hayes, C. S. (2013) 'Bacterial contact-dependent growth inhibition', Trends in Microbiology. Elsevier Current Trends, 21(5), pp. 230–237. doi: 10.1016/J.TIM.2013.02.003.

Russell, A. B. et al. (2011) 'Type VI secretion delivers bacteriolytic effectors to target cells', Nature. Nature Publishing Group, 475(7356), pp. 343–347. doi: 10.1038/nature10244

Russell, A. B. et al. (2013) 'Diverse type VI secretion phospholipases are functionally plastic antibacterial effectors', Nature, 469, pp. 508–515. doi: 10.1038/nature12074.

Russell, A. B., Brook Peterson, S. and Mougous, J. D. (2014) 'Type VI secretion system effectors: poisons with a purpose', Nature Reviews Microbiology, 12, pp. 137–148. doi: 10.1038/nrmicro3185.

Rüter, C. et al. (2018) 'All in—Multiple parallel strategies for intracellular delivery by bacterial pathogens', International Journal of Medical Microbiology. Urban & Fischer, 308(7), pp. 872–881. doi: 10.1016/J.IJMM.2018.06.007.

Rüter, C. and Hardwidge, P. R. (2014) '"Drugs from Bugs": bacterial effector proteins as promising biological (immune-) therapeutics', FEMS Microbiology Letters. Oxford University Press, 351(2), pp. 126–132. doi: 10.1111/1574-6968.12333.

Rüter, C., Schmidt, M. A. and Schmidt, M. A. (2017) 'Cell-Penetrating Bacterial Effector Proteins: Better Tools than Targets', Trends in Biotechnology, 35(2), pp. 109–120. doi: 10.1016/j.tibtech.2016.08.002.

Sana, T. G., Lugo, K. A. and Monack, D. M. (2017) 'T6SS: The bacterial "fight club" in the host gut', PLoS Pathogens, 13(6), pp. 1–5. doi: 10.1371/journal.ppat.1006325.

Sassone-Corsi, M. and Raffatellu, M. (2016) 'Close encounters of the type-six kind: injected bacterial toxins modulate gut microbial composition', EMBO Reports. doi: 10.15252/embr.201643036.

Schindelin, J. et al. (2012) 'Fiji: an open-source platform for biological-image analysis', Nature Methods, 9(7), pp. 676–682. doi: 10.1038/nmeth.2019.

Sharp, C. et al. (2017) 'Diversity and distribution of nuclease bacteriocins in bacterial genomes revealed using Hidden Markov Models', PLOS Computational Biology. Edited by C. A. Orengo. Public Library of Science, 13(7), p. e1005652. doi: 10.1371/journal.pcbi.1005652.

Smith, W. P. J. et al. (2016) 'Cell morphology drives spatial patterning in microbial communities', Proceedings of the National Academy of Sciences, pp. E280–E286. doi: 10.1073/pnas.1613007114.

Smith, W. P. J. (2019) CellModeller T6SS Module - code repository, Github. Available at: https://github.com/WilliamPJSmith/CM4-A (Accessed: 27 March 2019).

Stubbendieck, R. M. and Straight, P. D. (2016) 'Multifaceted Interfaces of Bacterial Competition.', Journal of bacteriology. American Society for Microbiology Journals, 198(16), pp. 2145–55. doi: 10.1128/JB.00275-16.

Tinevez, J.-Y. et al. (2017) 'TrackMate: An open and extensible platform for single-particle tracking', Methods, 115, pp. 80–90. doi: 10.1016/j.ymeth.2016.09.016.

Titball, R. W. (1993) 'Bacterial phospholipases C.', Microbiological reviews. American Society for Microbiology Journals, 57(2), pp. 347–66. Available at: http://www.ncbi.nlm.nih.gov/pubmed/8336671 (Accessed: 28 February 2019).

Troselj, V. et al. (2018) 'Physiological Heterogeneity Triggers Sibling Conflict Mediated by the Type VI Secretion System in an Aggregative Multicellular Bacterium.', mBio. American Society for Microbiology, 9(1), pp. e01645-17. doi: 10.1128/mBio.01645-17.

Veening, J.-W. and Blokesch, M. (2017)
'Interbacterial predation as a strategy for
DNA acquisition in naturally competent
bacteria', Nature Reviews Microbiology.
Nature Publishing Group, 15(10), pp. 629–
629. doi: 10.1038/nrmicro.2017.89.

Verster, A. J. et al. (2017) 'The Landscape of
Type VI Secretion across Human Gut
Microbiomes Reveals Its Role in Community
Composition.', Cell host & microbe.
Elsevier, 22(3), p. 411–419.e4. doi:
10.1016/j.chom.2017.08.010.

Vettiger, A. et al. (2017) 'The type VI secretion
system sheath assembles at the end distal
from the membrane anchor', Nature
Communications, 8, p. 16088. doi:
10.1038/ncomms16088.

Vettiger, A. and Basler, M. (2016) 'Type VI
Secretion System Substrates Are Transferred
and Reused among Sister Cells', Cell,
167(1), p. 99–110.e12. doi:
10.1016/j.cell.2016.08.023.

Vollmer, W., Blanot, D. and De Pedro, M. A.
(2008) 'Peptidoglycan structure and
architecture', FEMS Microbio. Rev., 32(2),
pp. 149–167. doi: 10.1111/j.1574-
6976.2007.00094.x.

Wang, J. et al. (2017) 'Cryo-EM structure of the
extended type VI secretion system sheath–
tube complex', Nature Microbiology, 2(11),
pp. 1507–1512. doi: 10.1038/s41564-017-
0020-7.

Wexler, A. G. et al. (2016) 'Human symbionts
inject and neutralize antibacterial toxins to
persist in the gut.', Proceedings of the
National Academy of Sciences of the United
States of America. National Academy of
Sciences, 113(13), pp. 3639–44. doi:
10.1073/pnas.1525637113.

Wong, M. J. Q. et al. (2016) 'Microbial Herd
Protection Mediated by Antagonistic
Interaction in Polymicrobial Communities',
American Society for Microbiology, 82(23),
pp. 6881–6888. doi: 10.1128/AEM.02210-
16.

CHAPTER 6

Discussion and Outlook

The T6SS field is evolving rapidly and several key discoveries were made during the course of my thesis. Most structural and functional aspects have been elucidated. In particular, the architecture of the sheath (Clemens et al., 2015; Kudryashev et al., 2015; Salih et al., 2018; Wang et al., 2017), the baseplate (Brunet et al., 2015; Cherrak et al., 2018; Logger et al., 2016; Nazarov et al., 2018; Nguyen et al., 2017; Park et al., 2018) and the membrane complex (Durand et al., 2015; Rapisarda et al., 2019; Yin et al., 2019) were resolved. This allowed for critical insights into T6SS mode of action and biogenesis. Still, the major conundrum of how the six-fold symmetrical baseplate connects to the 5-fold symmetrical membrane complex awaits to be answered. Future studies may address this problem by analyzing native T6SS assemblies *in situ* through a combination of cryo-FIB milling, cryo-ET and subtomogram averaging (Beck and Baumeister, 2016).

This thesis aimed at elucidating fundamental aspects of T6SS dynamics within single cells and bacterial communities through the use of fluorescence microscopy. Here, I will provide a brief discussion of our findings as well as an outlook for future microscopy-based projects.

6.1 T6SS dynamics at the single-cell level

The remarkable dynamics of the T6SS were first described by Basler et al., 2012, and provided the frame work for this thesis. Based on this data, it was known that sheath polymerization proceeds in a linear fashion, where new subunits are incorporated either at the membrane complex and baseplate associated end or at the distal cytosolic end, across the entire cell body. Using photobleaching, we were able to unambiguously show that new subunits are exclusively added to the end opposite the membrane anchor (Vettiger et al., 2017). Importantly, in enteroaggregative *E. coli* as well as *V. cholerae*, it was shown that the cap protein TssA2 localizes at the distal end during sheath assembly (Zoued et al., 2016; Schneider et al., *accepted*). TssA2 was also shown to interact with sheath component VipB and Hcp. Taken together, this suggests that in *E. coli* and *V. cholerae* the assembly of the contractile tail is carried out by TssA2 incorporating new sheath and tube subunits to the distal end opposite the baseplate. Accordingly, deletion of TssA2 in *V. cholerae* results in assemblies of very short and slow polymerizing sheaths (Schneider et al., *accepted*).

However, it should be noted that several T6SS clusters do not encode a TssA2 homologue, such as the H1-T6SS of *P. aeruginosa*, but contain a baseplate localized TssA1 copy instead (Dix et al., 2018; Planamente et al., 2016). Strikingly, in *P. aeruginosa*, the sheath polymerization speed is almost two-fold higher (60 nm s^{-1} vs. 34 nm s^{-1}) as compared to *V. cholerae*. This questions the role of TssA2 as being indeed an essential tail assembly chaperon.

Commonly, the membrane complex is anchored to the cell wall via TagN, TagL or PG binding motifs on TssL (Aschtgen et al., 2010a, 2010b; Ma et al., 2009). However, these accessory proteins and motives are absent in *V. cholerae*. Accordingly, it is not surprising that ampicillin-induced spheroplasts of *V. cholerae* continue to express a functional T6SS in the absence of PG (Vettiger et al., 2017). This suggests that the membrane complex and baseplate interactions with the Gram-negative cell envelope are strong enough to withstand the force generated during sheath contraction. In the light of the recent findings, it may be inferred that the Gram-negative OM serves not only as a permeability barrier, but also as a major loadbearing structure through ionic charge interactions between LPS molecules (Rojas et al., 2018). Thus, it can be assumed that the membrane complex might be simply held in place through its interactions with the OM and IM via TssJ and TssL/M respectively.

Enlarging cell volume revealed that the length of the contractile sheath is not regulated through a tape measure protein as in other CISs or a timer-based mechanism, where the assembly becomes instable after a specific amount of time, and thus prone to contraction (Leiman et al., 2009; Stietz et al., 2018), but instead corelates with cell size (Vettiger et al., 2017). This mechanism for sheath length regulation through continuous polymerization until the distal end contacts with the with the opposite cell envelope, seems to be conserved also in T6SSs of *P. aeruginosa* and *A. baylyi* (data not shown). The overall amount of energy released by sheath contraction is likely proportional to its length. It has been hypothesized on the other hand, that the force generated during contraction is independent of total polymer length but should rather depend on how many sheath rings contract simultaneously, since only these contribute to force generation (Ringel, 2017).

Additionally, while elongating sheath length was critical for studying aspects of its assembly, it did only marginally improve our estimate for the speed of its contraction (Basler et al., 2012; Vettiger et al., 2017). However, resolving the speed of sheath contraction is critical for calculating the overall force generated by the polymer. In my opinion, it is unlikely that the current measurement can be further improved by future *in vivo* measurements. Rather molecular dynamics simulations will provide these answers.

We have shown that the amount and composition of tip proteins limits the number of T6SS assemblies per cell, whereas the amount Hcp limits sheath length. Thus, by complementing these components at different expression levels, it is possible to fine tune either the number

or the length of T6SS assemblies. Accordingly, we have shown that Hcp-limited cells assembling sheath barely above the diffraction limit (< 250 nm) were still able to kill target cells (Vettiger and Basler, 2016). Sheath contraction results in a polymer length reduction by approximately 50 % propelling the Hcp tube into the extracellular space. Thus, the contraction of a 200 nm long sheath pushes the Hcp tube 100 nm far. Consequently, such an assembly should still be able to translocate its substrate through its own as well as the target cell envelope as the periplasmic space just spans approximately 25 nm (Asmar et al., 2017). Thus, it remains elusive to me why the T6SS tail assembles such long structures in the first place. Clearly, the benefits must outweigh the additional costs of recycling larger sheaths by ClpV and replenishing secreted proteins. Importantly, it should be mentioned that in mature biofilms, individual cells can be separated from each other though the deposition of extracellular matrix components or dead cells (Dragoš et al., 2018; Nadell et al., 2016). Thus, longer sheaths might be of advantage under these conditions by increasing the reach of the T6SS apparatus. However, it should be noted that prey cell killing efficiency of *V. cholerae* spheroplasts assembling ~ 3x longer sheaths was lower as compared to rod-shaped cells (Vettiger et al., 2017). Similarly, it was shown that *V. cholera* and *E. coli* lacking the assembly terminator TagA, displayed reduced killing efficiency (Santin et al., 2018; Schneider et al. *accepted*; Szwedziak and Pilhofer, 2019). Interestingly, in these cells sheath polymerization continued upon membrane contact, leading to longer and often curved T6SS assemblies as sheaths are further pushed along the cell envelope. Thus, compared to wildtype, *tagA* deletion mutant sheath assemblies were reported to often contract aberrantly. In particular, it appears as if the sheath would snap of the baseplate either due to exceeding energy release during contraction or a non-perpendicular angle between the baseplate and the sheath polymer (Santin et al., 2018; Schneider et al. *accepted*; Szwedziak and Pilhofer, 2019). Furthermore, the presence of an evolutionary conserved sheath assembly terminator protein in some organisms highlights the fact that accurate sheath length as well as a perpendicular angle (90°) to the baseplate during contraction is critical for T6SS function. Whether the stability of sheath to baseplate and baseplate to membrane complex interactions specifically co-evolved to withstand the contraction of ~ 0.8 μm long sheaths corresponding to the diameter of bacterial cells, remains to be seen.

Chapter 3 focused on elucidating one of the remaining major question in the T6SS field, the signal for initiation of sheath contraction. The presence of the assembly chaperon TssA2 and the terminator protein TagA can be correlated with sheaths residing for several minutes in an extended cell body spanning conformation prior to their contraction as shown here for *V. cholerae* as well as for *E. coli* by others (Santin et al., 2018). Furthermore, such stalled sheath showed no detectable signs of lateral or longitudinal displacement during this time as determined by fluorescence microscopy. In contrast, the absence of these proteins results in immediate contraction of sheath upon membrane contact as shown for *F. tularensis*, *A.*

baylyi and *P. aeruginosa* (Brodmann et al., 2017; Ringel et al., 2017; Schneider et al., *accepted*). In addition, T6SS assemblies of *A. baylyi* were sometimes observed to buckle upon membrane contact prior to their contraction. Moreover, unlike sheath assembly, which depends on extracellular signals and can be further regulated at the posttranslational level in some organisms (Basler et al., 2013; Brown et al., 2015; Ostrowski et al., 2018), single *V. cholerae* and *E. coli* cells contract their T6SS at similar rates than cells surrounded by either their clone mates or prey cells (Basler and Mekalanos, 2012; Basler et al., 2012; Brunet et al., 2013). Thus, I firmly believe that the signal for sheath contraction comes from within the cell. Whether posttranslational modifications or indeed a physical trigger as suggested here, are responsible for initiating the T6SS contraction will need further clarification. Most promising candidates for posttranslational regulation of sheath contractions could be Fha, whose phosphorylation was shown to be essential for sheath assembly in *P. aeruginosa* (Mougous et al., 2007) or Walker A and B motifs of TssM in *A. tumefaciens,* whose ATPase activity was essential for Hcp secretion (Ma et al., 2012). However, unpublished data of imaging *fha* deletion mutants as well as TssM Walker A mutants in *V. cholerae* revealed an absence of sheath assemblies rather than prevented contraction. Thus, our findings that compressive stress can induce sheath contraction supports a hypothesis of continued slow-rate sheath polymerization upon membrane contact at levels below the diffraction limit. This will result in the accumulation of pressure at the baseplate and may initiate its contraction.

In order to support this hypothesis, we aimed at showing *in vivo* that a polymerizing sheath creates pressure onto membranes using the mechano-sensitive FlipTR probe in combination with fluorescence life-time imaging (Colom et al., 2018). This probe was shown the report changes in membrane tension in yeast and HEK cells upon osmotic shocks (Colom et al., 2018). However, despite our hardest efforts, its application to Gram-negative cells remained unsuccessful, most probably due to the altered chemical properties of the LPS containing OM as compared to eukaryotic plasma membranes. Thus, now as an alternative strategy, we aim at elucidating the spring constant of the T6SS sheath through the use of atomic force microscopy (AFM) as previously utilized for collagen fibrils (Staple et al., 2009). Importantly, a non-contractile *vipA3AA* sheath mutant will be used for these measurements as wildtype sheath contract during the isolation procedure (Brackmann et al., 2018). Moreover, based on hyperosmotic shock experiments with this mutants, one can observe how these sheath buckle under the pressure created from the collapsing cell envelope. Thus, combing data on the spring constant with measuring the torsion angle from buckling sheath during osmotic shocks, will give us an estimate on how much pressure is applied onto the sheath during cell volume reduction. Even though this number will be based on an aberrantly connected sheath mutant (Wang et al., 2017), this will still allow us to estimate whether this amount of force is even feasible to be generated from a polymerizing sheath under steady state conditions.

6.2 T6SS substrate delivery into target cells

The finding that secreted T6SS components reach cytosol of target cells and thus, can be reused among sister-cells (Vettiger and Basler, 2016) was a major breakthrough at the time for the T6SS community. Although, it can be hypothesized that this contributes to lowering the overall costs of active type VI secretion over the entire bacterial community, since peripheral cells could potentially be armed by their clone mates (Koskiniemi and Elf, 2016), still remains to be confirmed experimentally. Despite clear indications of regulating T6SS expression only based on permissive cues for target cell killing (e.g. surface growth, QS, etc.) (Joshi et al., 2017), measuring its costs under laboratory conditions revealed no difference in growth rate between strains expressing activated and repressed T6SS mutants in pandemic *V. cholerae* strains (Zheng et al., 2010). This stands in contrast to T3SS of *S. typhimurium* (Diard et al., 2013; Sturm et al., 2011) or *Shigella sonnei* (McVicker and Tang, 2016) and may suggest that T6SS usage comes at a relatively low cost, potentially contributing to its high prevalence among both environmental and pathogenic bacteria. Furthermore, it is not trivial to find mutants, which would still be capable of displaying an active T6SS without being able to reuse the secreted components form sister cells.

Similarly, the hypothesis that T6SS mediated interactions among sister cells could be used as a form of contact-dependent signaling mechanism (Gallique et al., 2017) remains elusive. RNA sequencing of *V. cholerae*, *A. baylyi* and *P. aeruginosa* strains grown on solid surfaces did not reveal any indication of altered transcripts among T6SS positive and negative mutants (data not shown). Strains lacking QS components might be considered for repeating these experiments, as the contribution of T6SS mediated signaling could be marginal in comparison to previously identified QS modules such as homoserine lactones (Schuster and Greenberg, 2007) or *Pseudomonas* quinolone signaling (Cao et al., 2001).

Although, based on different target sites for T6SS effectors (e.g. nucleases vs. PG hydrolases), it was for a long time not clear whether the T6SS is indeed capable of translocating its substrate across the entire Gram-negative cell envelope or only across the OM. Thus, the establishment of a cell death independent assay for T6SS translocation enabled us to demonstrate that approximately 1 in 50 secretion events delivers its cargo into target cell cytosol. Moreover, we found that the ability of *P. aeruginosa* to aim its T6SS onto target cells (Basler et al., 2013) increased the cytosolic delivery efficiency even more, pointing to the importance of increasing T6SS efficiency through posttranslational modifications (Basler et al., 2013; Ostrowski et al., 2018; Vettiger and Basler, 2016). Our findings were indirectly corroborated by the observation that effectors with periplasmic targets are capable of being exported back to their designated compartment in case of cytosolic delivery (Ho et al., 2017). In addition, we have recently adapted a Cre recombinase assay for translocation (CRAfT) originally develop for the T4SS (Harms et al., 2017) to the

T6SS. Briefly, together with my current MSc student, Andreas Keppler, we engineered a C-terminal fusion of VgrG3 to Cre in an effectorless background of *A. baylyi*. Similar to the interbacterial protein complementation assay, this allows to detect cytosolic T6SS-dependent protein delivery into target cells in absence of any inflicted damage (Ringel et al., 2017). The results of this assay confirmed that about 1 in 10 to 1 in 100 recipient cells display a recombination event after 4h of co-incubation with *A. baylyi* donor cells. This recombination frequency is higher than what was previously reported for DotU/IcmF T4SS of *L. pneumophilla* (Luo and Isberg, 2004) or Vbh T4SS of *Bartonella schoenbuchensis* (Harms et al., 2017). Moreover, it was recently demonstrated the T6SS is capable of translocating its substrates into fungal cells (Trunk et al., 2018), extending the target cell spectrum further. Similarly, we found that also *Mycobacterium smegmatis* and S-layer containing *Caulobacter crescentus* are killed in a T6SS-dependent manner (data not shown). However, despite our best efforts we were not able to show neither T6SS-depenendent protein translocation nor killing of Gram-positive cells. Our current efforts center on using PG deprived L-forms of *B. subtilis* to determine whether resistance of Gram-positive cells is due to inability of breaching the thick cell wall or due to intrinsic resistance mechanism to T6SS effectors. Taken together, these data point out that the T6SS is a powerful drill enabling efficient translocation of large hydrophobic effectors across cellular membranes and the Gram-negative PG layer. However, it becomes apparent that strong structural features such as multiple layers PG or lignin, the major component of plant cell walls (Keegstra, 2010), remain an unpassable barrier for T6SSs. In agreement with this, it was recently published that extracellular matrix production in *V. cholerae* increases the resistance to T6SS killing between 10 and 100-fold (Toska et al., 2018).

6.3 T6SS-mediated interactions in bacterial communities

Further major drawbacks of T6SS mediated competition is the strict contact dependence for prey cell killing and the short range of its attacks. As shown both theoretically and experimentally, prey cells may easily compensate the effect of T6SS killing if their net growth rate is higher than the killing rate at the boundary between the strains. This explains why prey cell survival depends on both growth and kill rates resulting in a critical micro colony size radius determining prey cell survival (Borenstein et al., 2015). Furthermore, it was shown that the spatial organization and the initial inoculum size further predict T6SS killing efficiency (Borenstein et al., 2015; McNally et al., 2017; Wong et al., 2016). This may be explained as follows: Prey cells residing behind other prey cells are physically protected from contact-dependent T6SS attacks. Thus, when a population starts out homogeneously mixed at high density, most prey cells will be in contact with a predator and thus, efficiently eliminated. However, if the initial space occupancy is low or the different populations are not mixed homogenously, prey and predator strains must first form

microcolonies before encountering one another and therefore, will restrict killing to much fewer contact sites. Also, this phenomenon explains why competition generally leads to segregation of competing organisms (Alteri et al., 2013; McNally et al., 2017; Wenren et al., 2013; Wong et al., 2016).

In chapter 5, we present evidence on how the T6SS may overcome some of these limitations. We show that in addition to the above-mentioned parameters, also target cell lysis rate heavily influences the outcomes of T6SS mediated competition. If intoxicated prey cells are lysed efficiently, then the physical barrier protecting further prey cells is strongly reduced at the boundary between strains, thus driving T6SS killing efficiency. In addition to experimental support, we found a strong overrepresentation of lytic T6SS effectors (> 83 %) in genome of hundreds of analyzed proteobacterial species (LaCourse et al., 2018). This stands in contrast to contact-independent bacteriocin such as colicins (Cascales et al., 2007) or pyocins (Michel-Briand and Baysse, 2002), which use non-lytic effectors, such as pore-forming toxins and nucleases. Although this trend of employing lytic effectors seems to be also true for the anti-prokaryotic T4SS of *X. citri* (Souza et al., 2015), it does not generally apply all contact-dependent interference system. Importantly, CDIs of *E. coli* inflict cell death through the use of non-lytic effectors (Ruhe et al., 2013). However, it should be noted that unlike the T4SS and T6SS, which are both injection systems translocating substrates from their own cytosol through their secretion apparatus into target cells (Costa et al., 2015), CDI rely on target cells surface receptors for their translocation (Ruhe et al., 2017). This creates a strong evolutionary bottleneck for the diversification of its effector arsenal, as the same protein (CdiA) needs to full-fill multiple functions at once. However, T6SS effectors have undergone rapid evolution and are highly diverse even among close isolates (Kostiuk et al., 2017; Unterweger et al., 2014). This could be achieved, since the spike (VgrGs/PAAR) offers an ideal platform for rapidly exchanging different variants of toxins while fusing them to structural T6SS components (Brooks et al., 2013; Liang et al., 2015; Russell et al., 2011; Unterweger et al., 2015). Moreover, the operon organization of T6SS effector often being encoded as a separate domain or in direct vicinity to secreted structural component further facilitates this process (Boyer et al., 2009; Kirchberger et al., 2017; Ringel et al., 2017). However, still due to T6SS mode of action several restrictions for effector evolution remain, such as spatial constrains at the spike (~ 0.5 MDa) (Nazarov et al., 2018) or tube (~ 40 Å diameter) (Mougous et al., 2006; Silverman et al., 2013) as well as the low number translocated effectors creating a strong selection for high potency. This is supported by single cell analysis of fluorescence microscopy, where it appears as only a couple T6SS translocation events are sufficient to induce target cell death (Basler et al. 2013, Ringel et al., 2017). Consequently, it is not surprising that the effector repertoire of many T4SSs is higher as compared to the T6SS, since these proteins only need to be fused to a T4CP for

secretion without additional constraints (Christie, 2016; Wagner and Dehio, 2019) and may explain why *L. pneumophilla* encodes up to 300 different T4SS effectors (Hofer, 2016).

The importance of T6SS mediated antagonism is now also being recognized as a major player for shaping microbial communities *in vivo* (Anderson et al., 2017; Chatzidaki-Livanis et al., 2016; Speare et al., 2018; Wexler et al., 2016; Zheng et al., 2018) and first steps towards utilizing T6SS positive organism as probiotics are under its way (Hecht et al., 2016). However, it should be noted that most of these experiments were carried out in germ-free mouse models, lacking an adapted resident microbiota. Instead, one to two days prior infection, these mice were gavaged with *E. coli* or a defined microbiota drastically reduced in species number. I personally would argue that such studies should be interpreted carefully, as the complex composition and spatial organization of the natural microbiota, both critical parameters for contact-dependent antagonism as discussed above, cannot be reflected properly in such experiments. Thus, whenever possible, infection models harboring a natural host associated microbiota should be utilized instead such as exemplified by Speare et al., 2018.

6.4 Fluorescence microscopy as a tool for studying prokaryotic cell biology and bacterial communities

In order to understand the basic principles of living cells, one needs to be able to identify their components, their reciprocal interactions as well as their spatial organization to one another (Schneider and Basler, 2016). Imaging techniques, such as cryo-ET, can provide detailed insights into the nano-scale architecture of cells and their components (Beck and Baumeister, 2016). However, although unprecedented in resolution, EM techniques lack the ability to visualize the underlying dynamics of cellular processes. Thus, light- and in particular fluorescence live-cell microscopy is the most commonly used technique to obtain such insights. Already 350 years ago, Antoni van Leeuwenhoek discovered bacteria in different environmental water samples using his custom built single-lens microscope and accurately described their morphology and ability to rapidly move in solution (Lane, 2015; Leeuwenhoek Antoni Van, 1677). Only few years later, van Leeuwenhoek was also first in observing bacteria isolated from human origin, in particular from his own teeth (Leewenhoeck Anthony, 1684). However, due to the lack of contrast, most cellular components are indistinguishable from each other limiting light microscopy to primarily morphological studies of bacterial cell shape and motility. Thus, discovery of GFP in combination with the advent of fluorescence microscopy was a major breakthrough, as it allowed to specifically label designated proteins or other cellular components (Shimomura et al., 1962; Tsien, 1998). Now, it was possible to follow the dynamics of individual proteins in real-time in live cells. Recently, even the diffraction barrier has been overcome through the use of different localization microscopy techniques, allowing nanometer resolution

(Godin et al., 2014). However, despite tremendous technological advancement in current microscopes, it remains challenging to image bacterial cells. The major limitations remain their inherently small size, typically ranging from 0.5-5 μm as well as weak signal intensities from low-copy number proteins (Schneider and Basler, 2016).

Success in live-cell imaging relies on four aspects: (i) the use of bright and photostable fluorescent proteins, (ii) choosing the appropriate imaging system for answering the designated biological question in combination with the adequate (iii) image analysis pipeline. Moreover, if processes in response changing environmental conditions are of interest or long-term imaging of single cells is required, then the application of (iv) microfluidics should be taken into account. In addition, biological sample must be accessible for genetic manipulations in order to engineer the fusion of fluorescent proteins to the substrates of interest. With regards to imaging systems, widefield microscopes are most suitable for short-term imaging of bacterial cells, due to their large field of view, rapid image acquisition and gentle illumination. If dealing with weak signal intensities, deconvolution approaches are particular helpful enhancing signal to noise ratio based on image reconstruction algorithms (Swedlow, 2013). Similarly, structured illumination microscopy (SIM) increases the optical transfer function in reciprocal space, thereby making normally inaccessible high frequency information visible in the reconstructed image. Overall, this technology allows a two-fold lateral and axial increase in resolution as well as a two times higher signal to noise ratio as compared to a standard wide field microscope (Gustafsson, 2000). Still, in order to obtain a reconstructed SIM image at the current inhouse system (GE®, OMX-Blaze v4), at least 135 single acquisitions (5 phases x 3 angles x 9 z-planes) have to be collected, thereby lowering the acquisition frame rate and increasing phototoxicity. Importantly, newest generation SIM systems now reduce the number of necessary images to be taken 9-fold, due to the use of different image reconstruction algorithms. For long-term imaging of multilayer biofilms, spinning disc confocal systems are most appropriate due to their improved optical sectioning quality reducing out of focus blur. Nowadays, image analysis may take as much, or even more time than originally spent to acquire the data on the microscope. The ability to automatically segment features of interest and track them over time, transformed traditional microscopy into a highly quantitative technique. To this end automated workflows are crucial for being able to handle large dataset efficiently. Machine learning will continue to pave its way into biological imaging analyses allowing for unprecedented precision for accurate cell segmentation (Falk et al., 2019). Last, I personally believe that the combination of live-cell microscopy with microfluidics offers tremendous potential for biological studies, as it allows to manipulate the spatial organization of cells as well as their chemical environment in real-time in combination with the ability to follow single cells over many generations (Eland et al., 2016; Wu and Dekker, 2016).

This doctoral thesis primarily made use of fluorescence live-cell microscopy and revealed several crucial insights into T6SS biology and thus, serves an example of illustrating the power of these techniques. We mostly followed dynamics of T6SS sheath and the ATPase ClpV, which are both ideal proteins as they are permissive for the addition of fluorescent proteins and oligomerize into large macromolecular complexes. Accordingly, a 1 μm long consists of approximately 1500 sheath subunits (Basler, 2015). Importantly, it should be noted that it is also possible to detect as little as 4 copies of mNeonGreen (e.g. $VgrG_3$ + $PAAR_1$) on our current microscope setup (Shaner et al., 2013, Schneider et al., *unpublished*). This makes it possible to follow the dynamics of membrane complex and baseplate components. Moreover, although not presented in this thesis, I have acquired many 3D-SIM datasets of T6SS dynamics in *P. aeruginosa*, *A. baylyi* and *V. cholerae*. These suggest the existence of potential preassemblies of sheath and baseplate in both *P. aeruginosa* and *A. baylyi*, but not *V. cholerae*. Similar preassemblies of the sorting platform were previously reported for T3SSs (Diepold et al., 2015; Rocha et al., 2018) and could enhance the efficiency of the T6SS attack retaliation of *P. aeruginosa* by allowing for faster T6SS assemblies. Furthermore, this may also suggest a role for posttranslational regulation of sheath assemblies. As mentioned previously, a primer candidate could be Fha, which was shown to remain essential, even in absences of TPP, for T6SS activity in *V. cholerae* (Zheng et al., 2011). However, its phosphorylation status remains in most organisms unknown. Moreover, many TssM variants carry a Walker A and B, however its function are still poorly understood (Ma et al., 2012). Single-molecule tracking in combination with Förster resonance energy transfer (FRET) could reveal the abundance of these preassemblies and identify potential interaction partners or conformational changes prior to sheath polymerization initiation.

Additional microfluidic devices based on designs of the dual input mother machine (Kaiser et al., 2018), will allow for media switching and the cultivation of bacterial biofilms. Therefore, this could be utilized to perform multi-species competition experiments similar as described in chapter 5, however now in 3D and under changing environmental conditions. Based on recent reports it is possible to track single cells in 3D biofilms (Hartmann et al., 2019; Yan et al., 2016), thus allowing for novel insights into T6SS mediated competition. Also, these microfluidic chips could be used to study other strategies for microbial interference competition, such as T4SSs, CDIs or soluble bacteriocins. Further investment into microfluidics could aim applying the gut-on-a-chip technique (Bein et al., 2018) for following microbial competition real-time under physiological conditions.

Thus, I am certain that in light of the quote from Richard Feynman at the start of this thesis, indeed many more exciting biological questions can be solved in the future by simply looking at these phenomena using a combination of imaging techniques. Of course, microscopy alone cannot solve all biological problems and thus should be incorporated to

wider multidisciplinary approaches, including genetics, biochemistry as well as *in vivo* and *in silico* models.

6.5 References

Alteri, C.J., Himpsl, S.D., Pickens, S.R., Lindner, J.R., Zora, J.S., Miller, J.E., Arno, P.D., Straight, S.W., and Mobley, H.L.T. (2013). Multicellular Bacteria Deploy the Type VI Secretion System to Preemptively Strike Neighboring Cells. PLoS Pathog. 9.

Anderson, M.C., Vonaesch, P., Saffarian, A., Marteyn, B.S., and Sansonetti, P.J. (2017). Shigella sonnei Encodes a Functional T6SS Used for Interbacterial Competition and Niche Occupancy. Cell Host Microbe 21, 769-776.e3.

Aschtgen, M.-S., Thomas, M.S., and Cascales, E. (2010a). Anchoring the type VI secretion system to the peptidoglycan: TssL, TagL, TagP... what else? Virulence 1, 535–540.

Aschtgen, M.-S., Gavioli, M., Dessen, A., Lloubès, R., and Cascales, E. (2010b). The SciZ protein anchors the enteroaggregative Escherichia coli Type VI secretion system to the cell wall. Mol. Microbiol. 75, 886–899.

Asmar, A.T., Ferreira, J.L., Cohen, E.J., Cho, S.-H., Beeby, M., Hughes, K.T., and Collet, J.-F. (2017). Communication across the bacterial cell envelope depends on the size of the periplasm. PLoS Biol. 15.

Basler, M. (2015). Type VI secretion system: secretion by a contractile nanomachine. Phil Trans R Soc B 370, 20150021.

Basler, M., and Mekalanos, J.J. (2012). Type 6 secretion dynamics within and between bacterial cells. Science 337, 815.

Basler, M., Pilhofer, M., Henderson, G.P., Jensen, G.J., and Mekalanos, J.J. (2012). Type VI secretion requires a dynamic contractile phage tail-like structure. Nature 483, 182–186.

Basler, M., Ho, B.T., and Mekalanos, J.J. (2013). Tit-for-tat: Type VI secretion system counterattack during bacterial cell-cell interactions. Cell 152, 884–894.

Beck, M., and Baumeister, W. (2016). Cryo-Electron Tomography: Can it Reveal the Molecular Sociology of Cells in Atomic Detail? Trends Cell Biol. 26, 825–837.

Bein, A., Shin, W., Jalili-Firoozinezhad, S., Park, M.H., Sontheimer-Phelps, A., Tovaglieri, A., Chalkiadaki, A., Kim, H.J., and Ingber, D.E. (2018). Microfluidic Organ-on-a-Chip Models of Human Intestine. Cell. Mol. Gastroenterol. Hepatol. 5, 659–668.

Borenstein, D.B., Ringel, P., Basler, M., and Wingreen, N.S. (2015). Established Microbial Colonies Can Survive Type VI Secretion Assault. PLoS Comput Biol 11, e1004520.

Boyer, F., Fichant, G., Berthod, J., Vandenbrouck, Y., and Attree, I. (2009). Dissecting the bacterial type VI secretion system by a genome wide in silico analysis: what can be learned from available microbial genomic resources? BMC Genomics 10, 104.

Brackmann, M., Wang, J., and Basler, M. (2018). Type VI secretion system sheath inter-subunit interactions modulate its contraction. EMBO Rep. 19, 225–233.

Brodmann, M., Dreier, R.F., Broz, P., and Basler, M. (2017). Francisella requires dynamic type VI secretion system and ClpB to deliver effectors for phagosomal escape. Nat. Commun. 8, 15853.

Brooks, T.M., Unterweger, D., Bachmann, V., Kostiuk, B., and Pukatzki, S. (2013). Lytic Activity of the Vibrio cholerae Type VI Secretion Toxin VgrG-3 Is Inhibited by the Antitoxin TsaB. J. Biol. Chem. 288, 7618–7625.

Brown, L., Wolf, J.M., Prados-Rosales, R., and Casadevall, A. (2015). Through the wall: extracellular vesicles in Gram-positive bacteria, mycobacteria and fungi. Nat. Rev. Microbiol. 13, 620–630.

Brunet, Y.R., Espinosa, L., Harchouni, S., Mignot, T., and Cascales, E. (2013). Imaging type VI secretion-mediated bacterial killing. Cell Rep. 3, 36–41.

Brunet, Y.R., Zoued, A., Boyer, F., Douzi, B., and Cascales, E. (2015). The Type VI Secretion TssEFGK-VgrG Phage-Like Baseplate Is Recruited to the TssJLM Membrane Complex via Multiple Contacts and Serves As Assembly Platform for Tail Tube/Sheath Polymerization. PLOS Genet. 11, e1005545.

Cao, H., Krishnan, G., Goumnerov, B., Tsongalis, J., Tompkins, R., and Rahme, L.G. (2001). A quorum sensing-associated virulence gene of Pseudomonas aeruginosa encodes a LysR-like transcription regulator with a unique self-regulatory mechanism. Proc. Natl. Acad. Sci. U. S. A. 98, 14613–14618.

Cascales, E., Buchanan, S.K., Duché, D., Kleanthous, C., Lloubès, R., Postle, K., Riley, M., Slatin, S., and Cavard, D. (2007). Colicin biology. Microbiol. Mol. Biol. Rev. MMBR 71, 158–229.

Chatzidaki-Livanis, M., Geva-Zatorsky, N., and Comstock, L.E. (2016). Bacteroides fragilis type VI secretion systems use novel effector and immunity proteins to antagonize human gut Bacteroidales species. Proc. Natl. Acad. Sci. 113, 3627–3632.

Cherrak, Y., Rapisarda, C., Pellarin, R., Bouvier, G., Bardiaux, B., Allain, F., Malosse, C., Rey, M., Chamot-Rooke, J., Cascales, E., et al. (2018). Biogenesis and structure of a type VI secretion baseplate. Nat. Microbiol. 1.

Christie, P.J. (2016). The Mosaic Type IV Secretion Systems. EcoSal Plus 7.

Clemens, D.L., Ge, P., Lee, B.-Y., Horwitz, M.A., and Zhou, Z.H. (2015). Atomic structure of T6SS reveals interlaced array essential to function. Cell 160, 940–951.

Colom, A., Derivery, E., Soleimanpour, S., Tomba, C., Molin, M.D., Sakai, N., González-Gaitán, M., Matile, S., and Roux, A. (2018). A fluorescent membrane tension probe. Nat. Chem. 10, 1118–1125.

Costa, T.R.D., Felisberto-Rodrigues, C., Meir, A., Prevost, M.S., Redzej, A., Trokter, M., and Waksman, G. (2015). Secretion systems in Gram-negative bacteria: structural and mechanistic insights. Nat. Rev. Microbiol. 13, 343–359.

Diard, M., Garcia, V., Maier, L., Remus-Emsermann, M.N.P., Regoes, R.R., Ackermann, M., and Hardt, W.-D. (2013). Stabilization of cooperative virulence by the expression of an avirulent phenotype. Nature 494, 353–356.

Diepold, A., Kudryashev, M., Delalez, N.J., Berry, R.M., and Armitage, J.P. (2015). Composition, formation, and regulation of the cytosolic c-ring, a dynamic component of the type III secretion injectisome. PLoS Biol. 13, e1002039.

Dix, S.R., Owen, H.J., Sun, R., Ahmad, A., Shastri, S., Spiewak, H.L., Mosby, D.J., Harris, M.J., Batters, S.L., Brooker, T.A., et al. (2018). Structural insights into the function of type VI secretion system TssA subunits. Nat. Commun. 9, 4765.

Dragoš, A., Kiesewalter, H., Martin, M., Hsu, C.-Y., Hartmann, R., Wechsler, T., Eriksen, C., Brix, S., Drescher, K., Stanley-Wall, N., et al. (2018). Division of Labor during Biofilm Matrix Production. Curr. Biol. 28, 1903-1913.e5.

Durand, E., Nguyen, V.S., Zoued, A., Logger, L., Péhau-Arnaudet, G., Aschtgen, M.-S., Spinelli, S., Desmyter, A., Bardiaux, B., Dujeancourt, A., et al. (2015). Biogenesis and structure of a type VI secretion membrane core complex. Nature 523, 555–560.

Eland, L.E., Wipat, A., Lee, S., Park, S., and Wu, L.J. (2016). Chapter 3 - Microfluidics for bacterial imaging. In Methods in Microbiology, C. Harwood, and G.J. Jensen, eds. (Academic Press), pp. 69–111.

Falk, T., Mai, D., Bensch, R., Çiçek, Ö., Abdulkadir, A., Marrakchi, Y., Böhm, A., Deubner, J., Jäckel, Z., Seiwald, K., et al. (2019). U-Net: deep learning for cell counting, detection, and morphometry. Nat. Methods 16, 67.

Gallique, M., Bouteiller, M., and Merieau, A. (2017). The Type VI Secretion System: A Dynamic System for Bacterial Communication? Front. Microbiol. 8.

Godin, A.G., Lounis, B., and Cognet, L. (2014). Super-resolution Microscopy Approaches for Live Cell Imaging. Biophys. J. 107, 1777–1784.

Gustafsson, M.G.L. (2000). Surpassing the lateral resolution limit by a factor of two using structured illumination microscopy. J. Microsc. 198, 82–87.

Harms, A., Liesch, M., Körner, J., Québatte, M., Engel, P., and Dehio, C. (2017). A bacterial toxin-antitoxin module is the origin of inter-bacterial and inter-kingdom effectors of Bartonella. PLOS Genet. 13, e1007077.

Hartmann, R., Singh, P.K., Pearce, P., Mok, R., Song, B., Díaz-Pascual, F., Dunkel, J., and Drescher, K. (2019). Emergence of three-dimensional order and structure in growing biofilms. Nat. Phys. 15, 251.

Hecht, A.L., Casterline, B.W., Earley, Z.M., Goo, Y.A., Goodlett, D.R., and Bubeck Wardenburg, J. (2016). Strain competition restricts colonization of an enteric pathogen and prevents colitis. EMBO Rep. 17, 1281–1291.

Ho, B.T., Fu, Y., Dong, T.G., and Mekalanos, J.J. (2017). Vibrio cholerae type 6 secretion system effector trafficking in target bacterial cells. Proc. Natl. Acad. Sci. 201711219.

Joshi, A., Kostiuk, B., Rogers, A., Teschler, J., Pukatzki, S., and Yildiz, F.H. (2017). Rules of Engagement: The Type VI Secretion System in Vibrio cholerae. Trends Microbiol. 25, 267–279.

Kaiser, M., Jug, F., Julou, T., Deshpande, S., Pfohl, T., Silander, O.K., Myers, G., and van Nimwegen, E. (2018). Monitoring single-cell gene regulation under dynamically controllable conditions with integrated microfluidics and software. Nat. Commun. 9, 212.

Keegstra, K. (2010). Plant Cell Walls. Plant Physiol. 154, 483–486.

Kirchberger, P.C., Unterweger, D., Provenzano, D., Pukatzki, S., and Boucher, Y. (2017). Sequential displacement of Type VI Secretion System effector genes leads to evolution of diverse immunity gene arrays in Vibrio cholerae. Sci. Rep. 7, 45133.

Koskiniemi, S., and Elf, J. (2016). Arming the Neighborhood. Dev. Cell 39, 5–6.

Kostiuk, B., Unterweger, D., Provenzano, D., and Pukatzki, S. (2017). T6SS intraspecific competition orchestrates Vibrio cholerae genotypic diversity. Int. Microbiol. Off. J. Span. Soc. Microbiol. 20, 130–137.

Kudryashev, M., Wang, R.Y.-R., Brackmann, M., Scherer, S., Maier, T., Baker, D., DiMaio, F., Stahlberg, H., Egelman, E.H., and Basler, M. (2015). Structure of the Type VI Secretion System Contractile Sheath. Cell 160, 952–962.

LaCourse, K.D., Peterson, S.B., Kulasekara, H.D., Radey, M.C., Kim, J., and Mougous, J.D. (2018). Conditional toxicity and synergy drive diversity among antibacterial effectors. Nat. Microbiol. 1.

Lane, N. (2015). The unseen world: reflections on Leeuwenhoek (1677) 'Concerning little animals.' Philos. Trans. R. Soc. B Biol. Sci. 370.

Leeuwenhoek Antoni Van (1677). Observations, communicated to the publisher by Mr. Antony van Leewenhoeck, in a dutch letter of the 9th Octob. 1676. here English'd: concerning little animals by him observed in rain-well-sea- and snow water; as also in water wherein pepper had lain infused. Philos. Trans. R. Soc. Lond. 12, 821–831.

Leewenhoeck Anthony (1684). An abstract of a letter from Mr. Anthony Leevvenhoeck at Delft, dated Sep. 17. 1683. Containing some microscopical observations, about animals in the scurf of the teeth, the substance call'd worms in the nose, the cuticula consisting of scales. Philos. Trans. R. Soc. Lond. 14, 568–574.

Leiman, P.G., Basler, M., Ramagopal, U.A., Bonanno, J.B., Sauder, J.M., Pukatzki, S., Burley, S.K., Almo, S.C., and Mekalanos, J.J. (2009). Type VI secretion apparatus and phage tail-associated protein complexes share a common evolutionary origin. Proc. Natl. Acad. Sci. U. S. A. 106, 4154–4159.

Liang, X., Moore, R., Wilton, M., Wong, M.J.Q., Lam, L., and Dong, T.G. (2015). Identification of divergent type VI secretion effectors using a conserved chaperone domain. Proc. Natl. Acad. Sci. U. S. A. 112, 9106–9111.

Logger, L., Aschtgen, M.-S., Guérin, M., Cascales, E., and Durand, E. (2016). Molecular Dissection of the Interface between the Type VI Secretion TssM Cytoplasmic Domain and the TssG Baseplate Component. J. Mol. Biol. 428, 4424–4437.

Luo, Z.-Q., and Isberg, R.R. (2004). Multiple substrates of the Legionella pneumophila Dot/Icm system identified by interbacterial protein transfer. Proc. Natl. Acad. Sci. 101, 841–846.

Ma, L.-S., Lin, J.-S., and Lai, E.-M. (2009). An IcmF family protein, ImpLM, is an integral inner membrane protein interacting with ImpKL, and its walker a motif is required for type VI secretion system-mediated Hcp secretion in Agrobacterium tumefaciens. J. Bacteriol. 191, 4316–4329.

Ma, L.-S., Narberhaus, F., and Lai, E.-M. (2012). IcmF family protein TssM exhibits ATPase activity and energizes type VI secretion. J. Biol. Chem. 287, 15610–15621.

McNally, L., Bernardy, E., Thomas, J., Kalziqi, A., Pentz, J., Brown, S.P., Hammer, B.K., Yunker, P.J., and Ratcliff, W.C. (2017). Killing by Type VI secretion drives genetic phase separation and correlates with increased cooperation. Nat. Commun. 8, 14371.

McVicker, G., and Tang, C.M. (2016). Deletion of toxin-antitoxin systems in the evolution of Shigella sonnei as a host-adapted pathogen. Nat. Microbiol. 2, 16204.

Michel-Briand, Y., and Baysse, C. (2002). The pyocins of Pseudomonas aeruginosa. Biochimie 84, 499–510.

Mougous, J.D., Cuff, M.E., Raunser, S., Shen, A., Zhou, M., Gifford, C.A., Goodman, A.L., Joachimiak, G., Ordoñez, C.L., Lory, S., et al. (2006). A Virulence Locus of Pseudomonas aeruginosa Encodes a Protein Secretion Apparatus. Science 312, 1526–1530.

Nadell, C.D., Drescher, K., and Foster, K.R. (2016). Spatial structure, cooperation and competition in biofilms. Nat. Rev. Microbiol. 14, 589–600.

Nazarov, S., Schneider, J.P., Brackmann, M., Goldie, K.N., Stahlberg, H., and Basler, M. (2018). Cryo-EM reconstruction of Type VI secretion system baseplate and sheath distal end. EMBO J. 37.

Nguyen, V.S., Logger, L., Spinelli, S., Legrand, P., Huyen Pham, T.T., Nhung Trinh, T.T., Cherrak, Y., Zoued, A., Desmyter, A., Durand, E., et al. (2017). Type VI secretion TssK baseplate protein exhibits structural similarity with phage receptor-binding proteins and evolved to bind the membrane complex. Nat. Microbiol. 2, 17103.

Ostrowski, A., Cianfanelli, F.R., Porter, M., Mariano, G., Peltier, J., Wong, J.J., Swedlow, J.R., Trost, M., and Coulthurst, S.J. (2018). Killing with proficiency:

Integrated post-translational regulation of an offensive Type VI secretion system. PLoS Pathog. 14, e1007230.

Park, Y.-J., Lacourse, K.D., Cambillau, C., DiMaio, F., Mougous, J.D., and Veesler, D. (2018). Structure of the type VI secretion system TssK-TssF-TssG baseplate subcomplex revealed by cryo-electron microscopy. Nat. Commun. 9, 5385.

Planamente, S., Salih, O., Manoli, E., Albesa-Jové, D., Freemont, P.S., and Filloux, A. (2016). TssA forms a gp6-like ring attached to the type VI secretion sheath. EMBO J. 35, 1613–1627.

Rapisarda, C., Cherrak, Y., Kooger, R., Schmidt, V., Pellarin, R., Logger, L., Cascales, E., Pilhofer, M., Durand, E., and Fronzes, R. (2019). In situ and high-resolution cryo-EM structure of a bacterial type VI secretion system membrane complex. EMBO J.

Ringel, P.D. (2017). Mechanisms of delivery and mode of action of type VI secretion system effectors. Thesis. University_of_Basel.

Ringel, P.D., Hu, D., and Basler, M. (2017). The Role of Type VI Secretion System Effectors in Target Cell Lysis and Subsequent Horizontal Gene Transfer. Cell Rep. 21, 3927–3940.

Rocha, J.M., Richardson, C.J., Zhang, M., Darch, C.M., Cai, E., Diepold, A., and Gahlmann, A. (2018). Single-molecule tracking in live Yersinia enterocolitica reveals distinct cytosolic complexes of injectisome subunits. Integr. Biol. 10, 502–515.

Rojas, E.R., Billings, G., Odermatt, P.D., Auer, G.K., Zhu, L., Miguel, A., Chang, F., Weibel, D.B., Theriot, J.A., and Huang, K.C. (2018). The outer membrane is an essential load-bearing element in Gram-negative bacteria. Nature 559, 617–621.

Ruhe, Z.C., Low, D.A., and Hayes, C.S. (2013). Bacterial contact-dependent growth inhibition. Trends Microbiol. 21, 230–237.

Ruhe, Z.C., Nguyen, J.Y., Xiong, J., Koskiniemi, S., Beck, C.M., Perkins, B.R., Low, D.A., and Hayes, C.S. (2017). CdiA Effectors Use Modular Receptor-Binding Domains To Recognize Target Bacteria. MBio 8, e00290-17.

Russell, A.B., Hood, R.D., Bui, N.K., LeRoux, M., Vollmer, W., and Mougous, J.D. (2011). Type VI secretion delivers bacteriolytic effectors to target cells. Nature 475, 343–347.

Salih, O., He, S., Planamente, S., Stach, L., MacDonald, J.T., Manoli, E., Scheres, S.H.W., Filloux, A., and Freemont, P.S. (2018). Atomic Structure of Type VI

Contractile Sheath from Pseudomonas aeruginosa. Struct. Lond. Engl. 1993 26, 329-336.e3.

Santin, Y.G., Doan, T., Lebrun, R., Espinosa, L., Journet, L., and Cascales, E. (2018). In vivo TssA proximity labelling during type VI secretion biogenesis reveals TagA as a protein that stops and holds the sheath. Nat. Microbiol. 3, 1304–1313.

Schneider, J.P., and Basler, M. (2016). Shedding light on biology of bacterial cells. Philos. Trans. R. Soc. Lond. B. Biol. Sci. 371.

Schuster, M., and Greenberg, E.P. (2007). Early activation of quorum sensing in Pseudomonas aeruginosa reveals the architecture of a complex regulon. BMC Genomics 8, 287.

Shaner, N.C., Lambert, G.G., Chammas, A., Ni, Y., Cranfill, P.J., Baird, M.A., Sell, B.R., Allen, J.R., Day, R.N., Israelsson, M., et al. (2013). A bright monomeric green fluorescent protein derived from Branchiostoma lanceolatum. Nat. Methods 10, 407–409.

Shimomura, O., Johnson, F.H., and Saiga, Y. (1962). Extraction, Purification and Properties of Aequorin, a Bioluminescent Protein from the Luminous Hydromedusan, Aequorea. J. Cell. Comp. Physiol. 59, 223–239.

Silverman, J.M., Agnello, D.M., Zheng, H., Andrews, B.T., Li, M., Catalano, C.E., Gonen, T., and Mougous, J.D. (2013). Haemolysin Co-regulated Protein is an Exported Receptor and Chaperone of Type VI Secretion Substrates. Mol. Cell 51, 10.1016/j.molcel.2013.07.025.

Souza, D.P., Oka, G.U., Alvarez-Martinez, C.E., Bisson-Filho, A.W., Dunger, G., Hobeika, L., Cavalcante, N.S., Alegria, M.C., Barbosa, L.R.S., Salinas, R.K., et al. (2015). Bacterial killing via a type IV secretion system. Nat. Commun. 6, 6453.

Speare, L., Cecere, A.G., Guckes, K.R., Smith, S., Wollenberg, M.S., Mandel, M.J., Miyashiro, T., and Septer, A.N. (2018). Bacterial symbionts use a type VI secretion system to eliminate competitors in their natural host. Proc. Natl. Acad. Sci. U. S. A.

Staple, D.B., Loparic, M., Kreuzer, H.J., and Kreplak, L. (2009). Stretching, unfolding, and deforming protein filaments adsorbed at solid-liquid interfaces using the tip of an atomic-force microscope. Phys. Rev. Lett. 102, 128302.

Stietz, M.S., Liang, X., Wong, M., Hersch, S., and Dong, T.G. (2018). The double tubular contractile structure of the type VI secretion

system displays striking flexibility and elasticity. BioRxiv 470229.

Sturm, A., Heinemann, M., Arnoldini, M., Benecke, A., Ackermann, M., Benz, M., Dormann, J., and Hardt, W.-D. (2011). The cost of virulence: retarded growth of Salmonella Typhimurium cells expressing type III secretion system 1. PLoS Pathog. 7, e1002143.

Swedlow, J.R. (2013). Quantitative fluorescence microscopy and image deconvolution. Methods Cell Biol. 114, 407–426.

Szwedziak, P., and Pilhofer, M. (2019). Bidirectional contraction of a type six secretion system. Nat. Commun. 10, 1565.

Toska, J., Ho, B.T., and Mekalanos, J.J. (2018). Exopolysaccharide protects Vibrio cholerae from exogenous attacks by the type 6 secretion system. Proc. Natl. Acad. Sci. 201808469.

Trunk, K., Peltier, J., Liu, Y.-C., Dill, B.D., Walker, L., Gow, N.A.R., Stark, M.J.R., Quinn, J., Strahl, H., Trost, M., et al. (2018). The type VI secretion system deploys antifungal effectors against microbial competitors. Nat. Microbiol. 3, 920.

Tsien, R.Y. (1998). The green fluorescent protein. Annu. Rev. Biochem. 67, 509–544.

Unterweger, D., Miyata, S.T., Bachmann, V., Brooks, T.M., Mullins, T., Kostiuk, B., Provenzano, D., and Pukatzki, S. (2014). The Vibrio cholerae type VI secretion system employs diverse effector modules for intraspecific competition. Nat. Commun. 5, 3549.

Unterweger, D., Kostiuk, B., Ötjengerdes, R., Wilton, A., Diaz-Satizabal, L., and Pukatzki, S. (2015). Chimeric adaptor proteins translocate diverse type VI secretion system effectors in Vibrio cholerae. EMBO J. 34, 2198–2210.

Vettiger, A., and Basler, M. (2016). Type VI Secretion System Substrates Are Transferred and Reused among Sister Cells. Cell 167, 99-110.e12.

Vettiger, A., Winter, J., Lin, L., and Basler, M. (2017). The type VI secretion system sheath assembles at the end distal from the membrane anchor. Nat. Commun. 8, ncomms16088.

Wagner, A., and Dehio, C. (2019). Role of distinct type-IV-secretion systems and secreted effector sets in host adaptation by pathogenic Bartonella species. Cell. Microbiol. 21, e13004.

Wang, J., Brackmann, M., Castaño-Díez, D., Kudryashev, M., Goldie, K.N., Maier, T., Stahlberg, H., and Basler, M. (2017). Cryo-EM structure of the extended type VI secretion system sheath-tube complex. Nat. Microbiol. 2, 1507–1512.

Wenren, L.M., Sullivan, N.L., Cardarelli, L., Septer, A.N., and Gibbs, K.A. (2013). Two Independent Pathways for Self-Recognition in Proteus mirabilis Are Linked by Type VI-Dependent Export. MBio 4, e00374-13.

Wexler, A.G., Bao, Y., Whitney, J.C., Bobay, L.-M., Xavier, J.B., Schofield, W.B., Barry, N.A., Russell, A.B., Tran, B.Q., Goo, Y.A., et al. (2016). Human symbionts inject and neutralize antibacterial toxins to persist in the gut. Proc. Natl. Acad. Sci. 113, 3639–3644.

Wong, M.J.Q., Liang, X., Smart, M., Tang, L., Moore, R., Ingalls, B., and Dong, T.G. (2016). Microbial Herd Protection Mediated by Antagonistic Interaction in Polymicrobial Communities. Appl. Environ. Microbiol. 82, 6881–6888.

Wu, F., and Dekker, C. (2016). Nanofabricated structures and microfluidic devices for bacteria: from techniques to biology. Chem. Soc. Rev. 45, 268–280.

Yan, J., Sharo, A.G., Stone, H.A., Wingreen, N.S., and Bassler, B.L. (2016). Vibrio cholerae biofilm growth program and architecture revealed by single-cell live imaging. Proc. Natl. Acad. Sci. U. S. A. 113, E5337-5343.

Yin, M., Yan, Z., and Li, X. (2019). Architecture of type VI secretion system membrane core complex. Cell Res. 29, 251.

Zheng, J., Shin, O.S., Cameron, D.E., and Mekalanos, J.J. (2010). Quorum sensing and a global regulator TsrA control expression of type VI secretion and virulence in Vibrio cholerae. Proc. Natl. Acad. Sci. U. S. A. 107, 21128–21133.

Zheng, J., Ho, B., and Mekalanos, J.J. (2011). Genetic Analysis of Anti-Amoebae and Anti-Bacterial Activities of the Type VI Secretion System in Vibrio cholerae. PLoS ONE 6.

Zheng, S., Sham, L.-T., Rubino, F.A., Brock, K.P., Robins, W.P., Mekalanos, J.J., Marks, D.S., Bernhardt, T.G., and Kruse, A.C. (2018). Structure and mutagenic analysis of the lipid II flippase MurJ from Escherichia coli. Proc. Natl. Acad. Sci. U. S. A. 115, 6709–6714.

Zoued, A., Durand, E., Brunet, Y.R., Spinelli, S., Douzi, B., Guzzo, M., Flaugnatti, N., Legrand, P., Journet, L., Fronzes, R., et al. (2016). Priming and polymerization of a bacterial contractile tail structure. Nature 531, 59–63.

APPENDIX A

Supplementary material to chapter 2

The type VI secretion system sheath assembles at the end distal from the membrane anchor

Andrea Vettiger, Julius Winter, Lin Lin and Marek Basler

Supplementary Information

File name: Supplementary Movie 1

Description: T6SS remains dynamic during spheroplast formation. VipA-msfGFP and ClpVmCherry2 labeled *V. cholerae* cells were grown to OD = 0.8 and imaged on a 1 % agarose LB pad containing 500 μg ml^{-1} ampicillin. Five representative 90 min time lapse series acquired with a rate of 1 min frame^{-1} for each time point are shown. Field of view is 20 x 20 μm and shows a merge of phase contrast and two fluorescent channels: VipA-msfGFP and ClpV-mCherry2. Furthermore, GFP and mCherry2 fluorescence channels are depicted individually on the right as grey scale images. The video plays at a rate of 10 frames per second.

File name: Supplementary Movie 2

Description: T6SS dynamics in rod shaped cells are comparable to spheroplasts. Spheroplast were induced by the addition of 500 μg ml^{-1} ampicillin for indicated time points. Cells were imaged on a 1% agarose LB pad. Three representative 5 min time lapse series acquired with a rate of 10 sec frame-1 for each time-point are shown. Field of view is 5 x 5 μm and shows a merge of phase contrast and three fluorescent channels: VipA-msfGFP, ClpV-mCherry2 and HADA labeling of PG. Furthermore, GFP and mCherry2 fluorescence channels are depicted individually on the right as grey scale images. The video plays at a rate of 10 frames per second.

File name: Supplementary Movie 3

Description: T6SS dynamics in ampicillin induced *V. cholerae* spheroplasts. Spheroplasts were induced by the addition of 500 µg ml^{-1} ampicillin for 40 min and subsequently imaged on a 1 % agarose LB pad. Three representative 5 min time lapse series acquired with a rate of 10 sec frame^{-1} are shown. Field of view is 50 x 50 µm and shows a merge of phase contrast and three fluorescent channels: VipA-msfGFP, ClpV-mCherry2 and HADA labeling of PG. The video plays at a rate of 10 frames per second.

File name: Supplementary Movie 4

Description: T6SS in spheroplasts is capable of translocating VgrG2 into cytosol of recipient cells. Recipient *ΔvgrG2/vipA-msfGFP* spheroplasts were co-incubated with T6SS+ *clpVmCherry2* donor cells on a 1 % agarose LB pad. The sheath assembly was monitored in GFP channel. Five representative time-lapse image series acquired for 5 min with a rate of 10 sec frame^{-1} are shown. Field of view is 10 x 10 µm and shows a merge between bright-field, mCherry2 and GFP fluorescence channels on the left; right field shows only GFP fluorescence channel. The video plays at a rate of 7 frames per second.

File name: Supplementary Movie 5

Description: T6SS in spheroplasts is capable of killing target cells. *V. cholerae* VipA-msfGFP labeled spheroplasts were co-incubated with *E. coli* MG1655 prey cells on agarose pads containing 100 µg ml^{-1} ampicillin and 1 µg ml^{-1} propidium iodide. Cell death was identified by detection of propidium iodide staining. Five representative time-lapse image series acquired for 45 min with a rate of 30 sec frame-1 are shown. Field of view is 10 x 10 µm and shows a merge between bright-field, propidium iodide and GFP fluorescence channels. The video plays at a rate of 10 frames per second.

File name: Supplementary Movie 6

Description: New sheath subunits are incorporated at the end distal from the assembly initiation. VipA-msfGFP labeled *ΔvgrG1/ΔvasX* spheroplasts (ampicillin 500 µg ml^{-1}, 40 min) were monitored for sheath assembly for 2 min at a rate of 2 sec frame^{-1}. After 30 sec of image acquisition, the bleaching laser was triggered. Ten representative time-lapse series are shown. Field of view is 5 x 5 µm. The video plays at a rate of 10 frames per second.
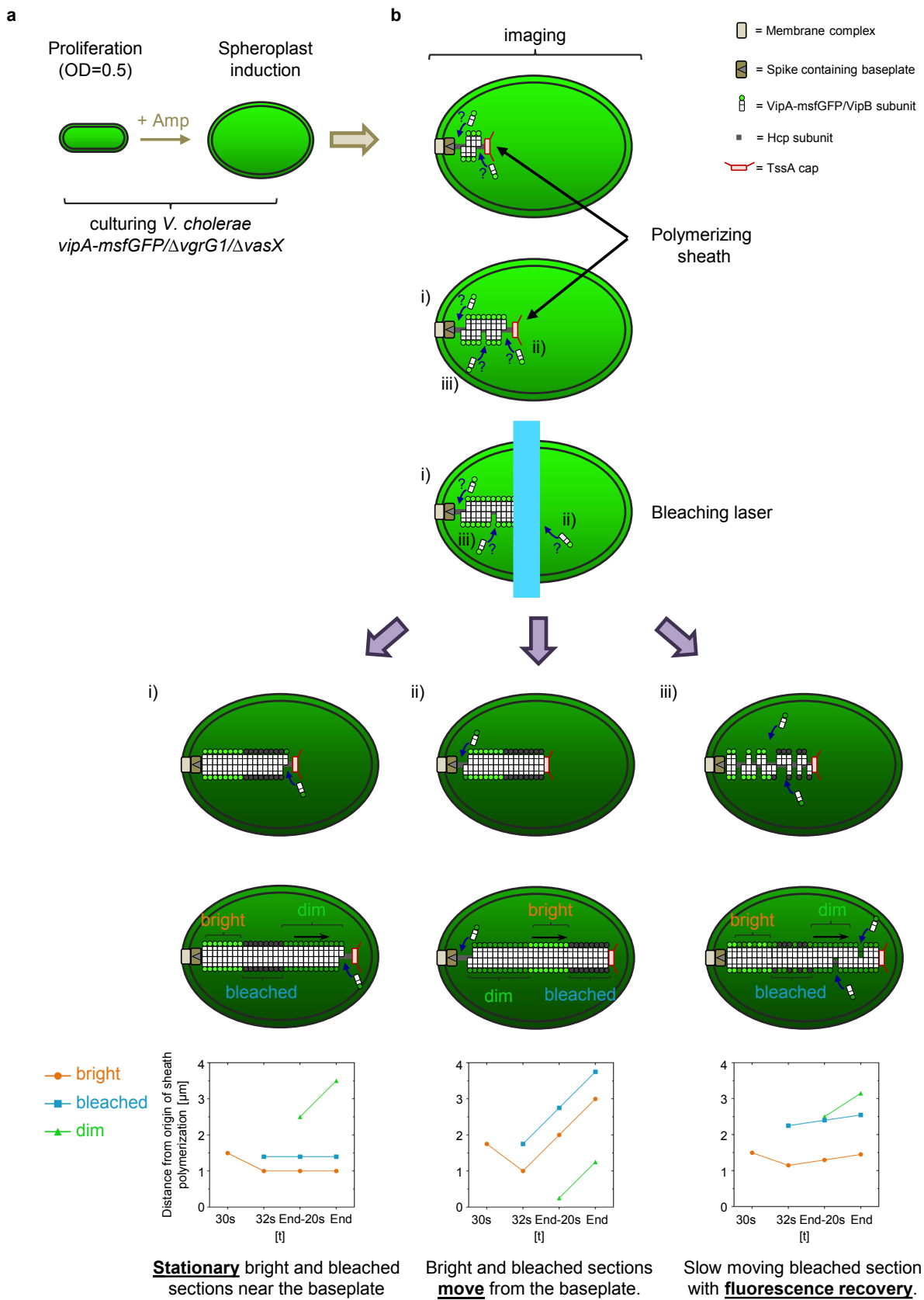
a *V. cholerae vipA-msfGFP/clpV-mCherry2*

b *V. cholerae vipA-msfGFP/clpV-mCherry2* (Amp pre-treated)
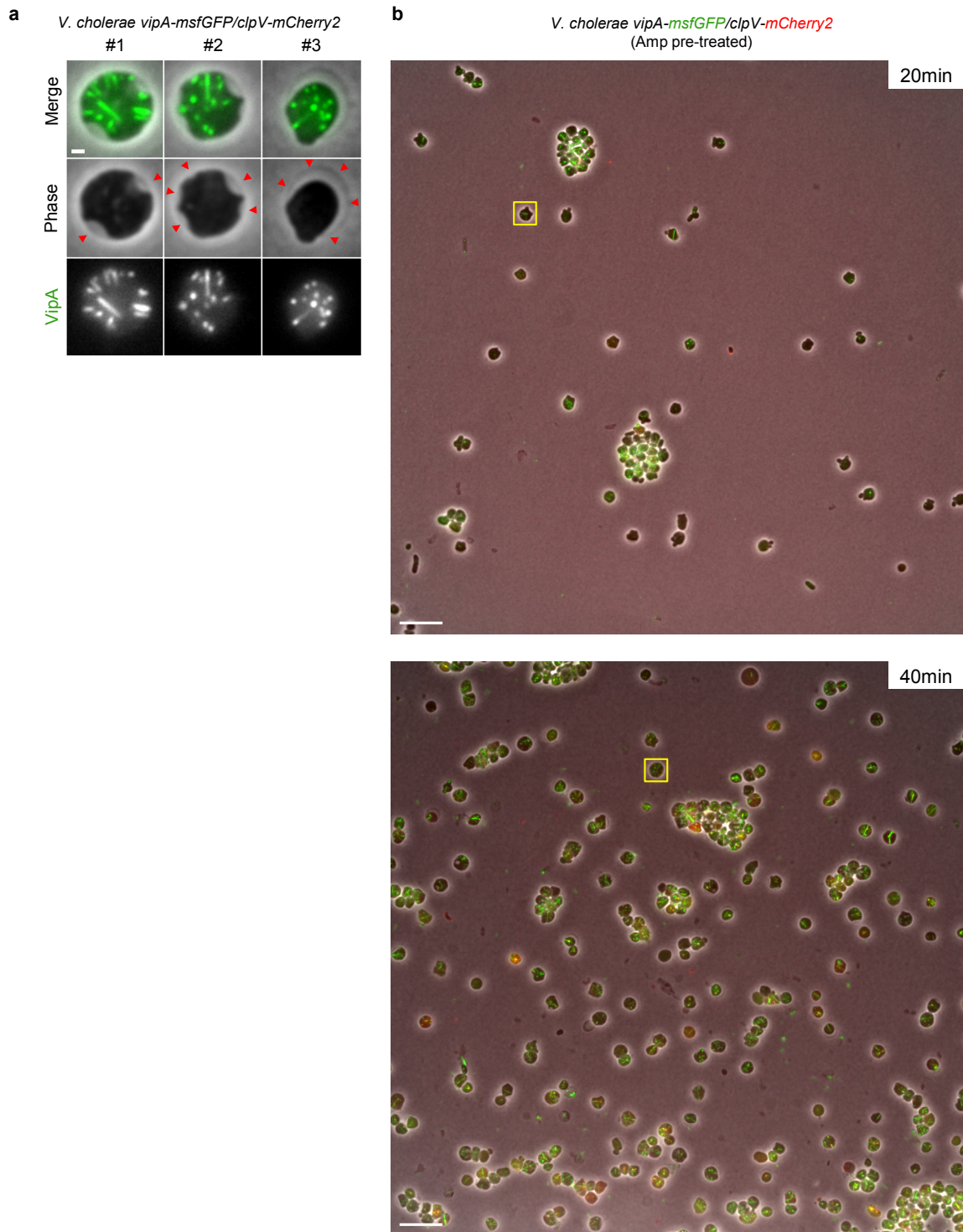
Supplementary Figure 1: T6SS dynamics in spheroplasts. (a) Examples of membrane detachment (arrow heads) in spheroplasts (*vipA-msfGFP* background) that were incubated for 60 min in the presence of ampicillin (500 µg ml^{-1}). Scale bar = 1 µm. **(b)** Full (133 x 133 µm) fields of view are shown for cells that were incubated either for 20 min (top) or 40 min (bottom) in the presence of ampicillin. Yellow boxes mark the cropped regions shown in Figure 1a. Scale bar = 10 µm.
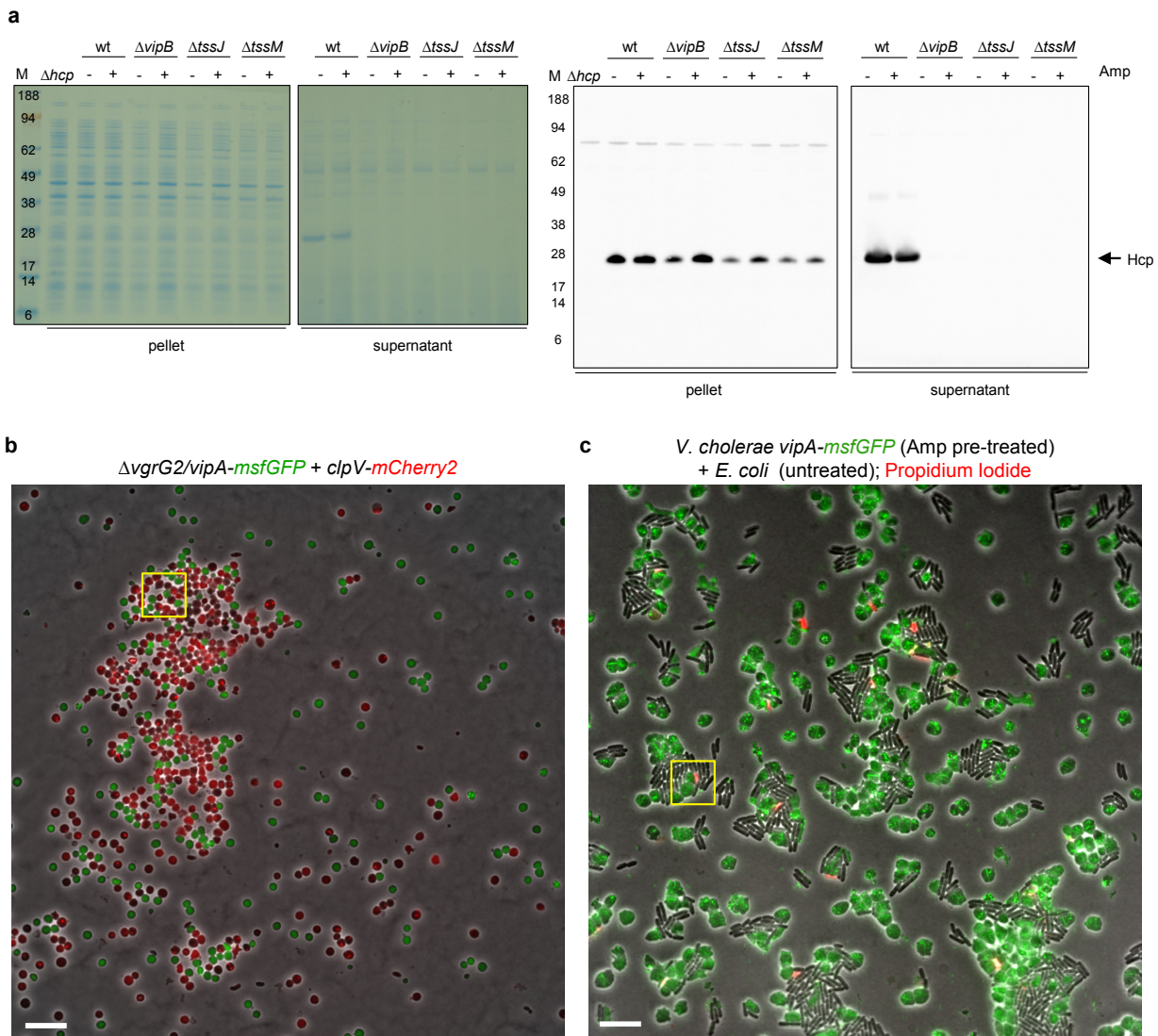
Supplementary Figure 2: The T6SS apparently remains functional in ampicillin-induced spheroplasts. (a) Cell lysates and precipitated culture supernatants of spheroplasts and rod shaped cells of indicated strains were separated by SDS-PAGE and stained with Coomassie Blue (left) or probed with polyclonal antibody raised against recombinant full-length Hcp (right). Arrows point towards specific bands for Hcp (theoretical MW = 19.1 kDa). Marker for molecular weight is indicated on the right in kDa. **(b-c)** Full (133 x 133 µm) fields of view are shown for VgrG2 interbacterial protein complementation assay **(b)** and *E. coli* cell permeabilization assay **(c)**. Yellow boxes mark cropped regions shown in Figure 2b and d respectively. Scale bar = 10 µm
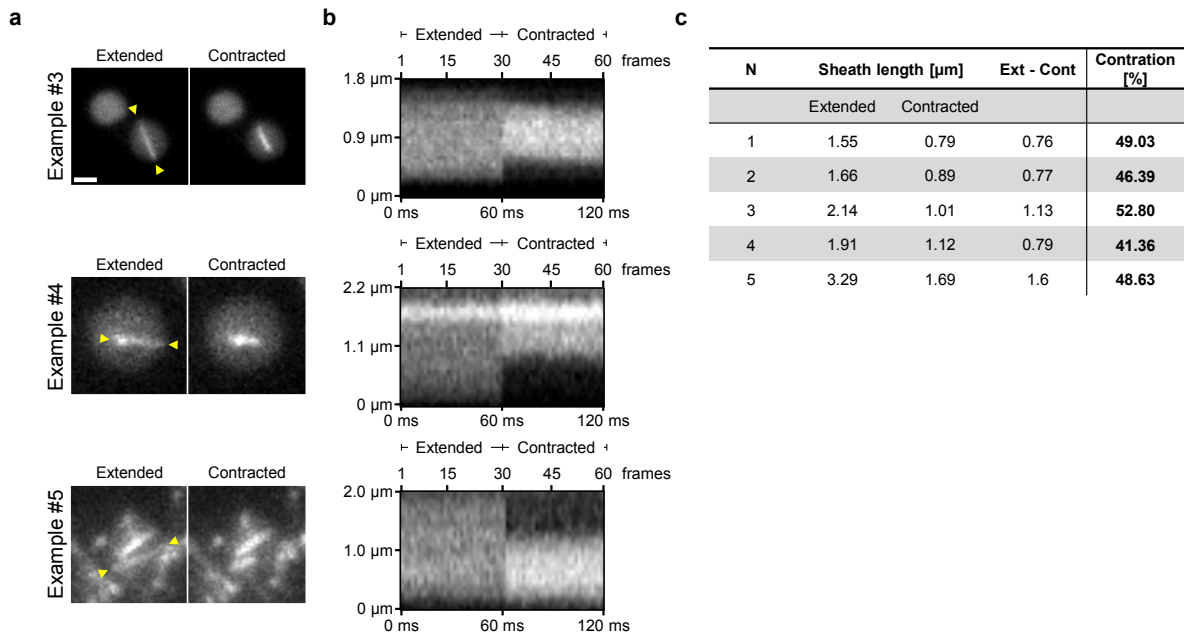
Supplementary Figure 3: Additional examples of sheath contractions. (a) Additional examples of sheath contraction acquired at a rate of 500 frames sec^{-1} and corresponding **(b)** kymograms are depicted as shown in Figure 3. **(c)** Corresponding measurements to determine level of contraction. Sheath length from the last frame prior to contraction and the first frame after contraction were measured. Calculated length difference was normalized to the extended sheath length.

a

Proliferation
(OD=0.5)

Spheroplast
induction

+ Amp

culturing *V. cholerae*
vipA-msfGFP/ΔvgrG1/ΔvasX

b

imaging

= Membrane complex

= Spike containing baseplate

= VipA-msfGFP/VipB subunit

= Hcp subunit

= TssA cap

Polymerizing
sheath

Bleaching laser

i)

ii)

iii)

bright

dim

bleached

bright

dim

bleached

bright

dim

bleached

bright
bleached
dim

Distance from origin of sheath
polymerization [µm]

30s   32s End-20s End
[t]

30s   32s End-20s End
[t]

30s   32s End-20s End
[t]

Stationary bright and bleached
sections near the baseplate

Bright and bleached sections
move from the baseplate.

Slow moving bleached section
with **fluorescence recovery**.

Supplementary Figure 4: Experimental approach to determine site of sheath subunit incorporation. (a) VipA-msfGFP labeled *V. cholerae* lacking *vgrG1* and *vasX* were grown to an OD = 0.5 and exposed to 500 µg ml^{-1} ampicillin to induce spheroplast formation. **(b)** Three models were tested by monitoring sheath polymerization after photobleaching: (i) incorporation of new subunits at the distal cytosolic end, (ii) at the baseplate and (iii) random incorporation along the entire polymer. After photobleaching, 3 signal intensities should be identified: (i) the "bright" section consisting of assembled sheath subunits prior to bleaching; (ii) the "bleached" section representing the part of the sheath, which was directly hit by the bleaching laser and (iii) the "dim" section consisting of partially bleached sheath subunits present in the cytosol. Based on the localization and fluorescence intensity changes of these sections in time, the three proposed models for sheath assembly can be distinguished.
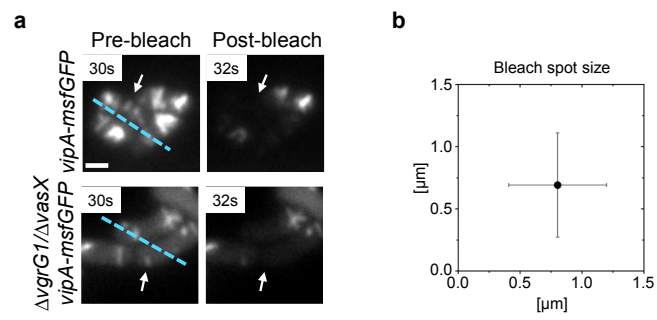
Supplementary Figure 5: Photobleaching experiments are impossible to perform on rod shaped cells. (a) Polymerizing sheaths (arrows) of indicated strains were imaged for 2 min and photobleached (λ = 488 nm; 100 % laser power; 0.1 ms pixel^{-1}) after 30 sec. The last frame prior and the first frame after photobleaching are depicted. **(b)** The bleach spot size was measured in spheroplasts from 25 successfully photobleached sheaths. Data are represented as mean +/- SD. Scale bar = 1 µm.
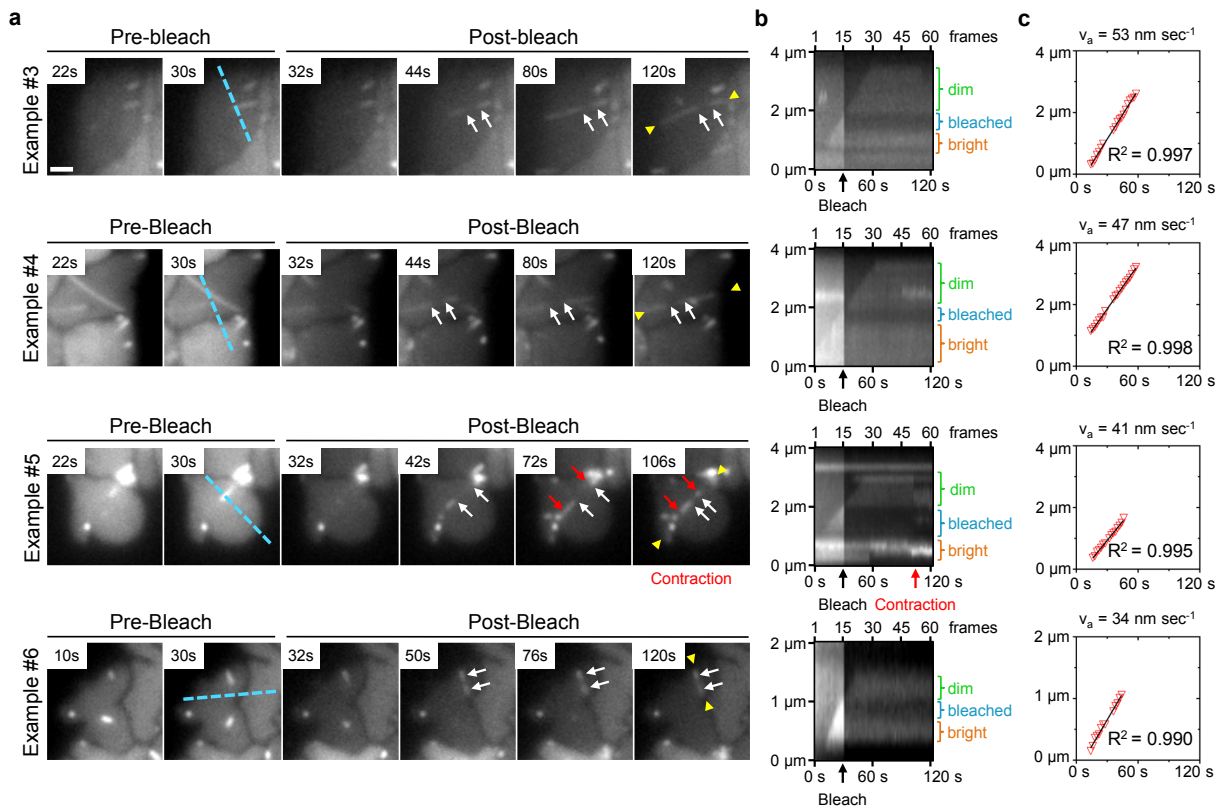
Supplementary Figure 6: Photobleached sections of sheaths remain stationary and with unchanged intensity after photobleaching. (a) Additional examples of successfully photobleached polymerizing sheaths as well as corresponding **(b)** kymograms and polymerization speed measurements **(c)** as shown in Figure 5. Red arrows indicated sheath contraction of a photo bleached polymer.

Supplementary Table 1: Strains used in this study, related to Methods

Organism	Genotype	Plasmid	Relevant features	Source
V. cholerae 2740-80	lacZ-, Str^r		Parental strain	(Basler et al., 2012)
	lacZ-, Str^r	pBAD24	Parental strain, Amp^r	This study
	lacZ-, Str^r, ΔvipB		Deletion of *vipB*; T6SS negative	(Basler et al., 2012)
	lacZ-, Str^r, ΔvipB, vipA-msfGFP		Deletion of *vipB*; T6SS negative in *vipA-msfGFP* background	(Kudryashev et al., 2015)
	lacZ-, Str^r, ΔtssJ, vipA-msfGFP		Deletion of outer membrane protein *tssJ* in *vipA-msfGFP* background	This study
	lacZ-, Str^r, ΔtssM, vipA-msfGFP		Deletion of membrane protein *tssM* in *vipA-msfGFP* background	This study
	lacZ-, Str^r, vipA-msfGFP, clpV-mCherry2		C-terminal chromosomal fusions of *msfGFP* to *vipA* and *mCherry2* to *clpV*	(Basler and Mekalanos, 2012)
	lacZ-, Str^r, clpV-mCherry2		C-terminal chromosomal fusion of *mCherry2* to *clpV*	(Basler and Mekalanos, 2012)
	lacZ-, Str^r, vipA-msfGFP		C-terminal chromosomal fusion of *msfGFP* to *vipA*	(Kudryashev et al., 2015)
	lacZ-, Str^r, vipA-msfGFP, ΔvipB		Deletion of *vipA*; T6SS negative	(Kudryashev et al., 2015)
	lacZ-, Str^r, vipA-msfGFP, ΔvgrG2		Deletion of *vgrG2* in *vipA-msfGFP* background	(Vettiger and Basler, 2016)
	lacZ-, Str^r, vipA-msfGFP, ΔvgrG1, ΔvasX		Combination of *vgrG1* and *vasX* deletions in *vipA-msfGFP* background	(Vettiger and Basler, 2016)
E. coli MG1655	K-12, F-, λ-, ilvG-, rfb-50, rph-1, lacZ+	pUC19	Used for quantitative killing assays, Amp^r	(Kudryashev et al., 2015)

APPENDIX B

Supplementary material to chapter 3

Induction of type VI secretion system contraction through compressive stress

Andrea Vettiger and Marek Basler

Manuscript in preparation, 2019

Supplementary information

Supplementary movie S1 associated with this manuscript can be found in on the attached CD under the folder, Chapter 3.

File name: Supplementary Movie S1

Description: A hyper osmotic shock induces T6SS sheath contraction. T6SS dynamics was monitored in VipA-msfGFP (green), ClpV-mCherry2 (magenta) *V. cholerae* cells in response to a hyperosmotic shock (+ 170 mM NaCl). Five representative time-lapse image series acquired during 7 min with a 10 s frame-rate are shown. The video plays at a rate 12 frames per second. Left field shows a merge between bright-field, mCherry2 and GFP fluorescence channels; right field shows mCherry2 signal as grey scale. ClpV foci detected by TrackMate are marked with a purple circle.
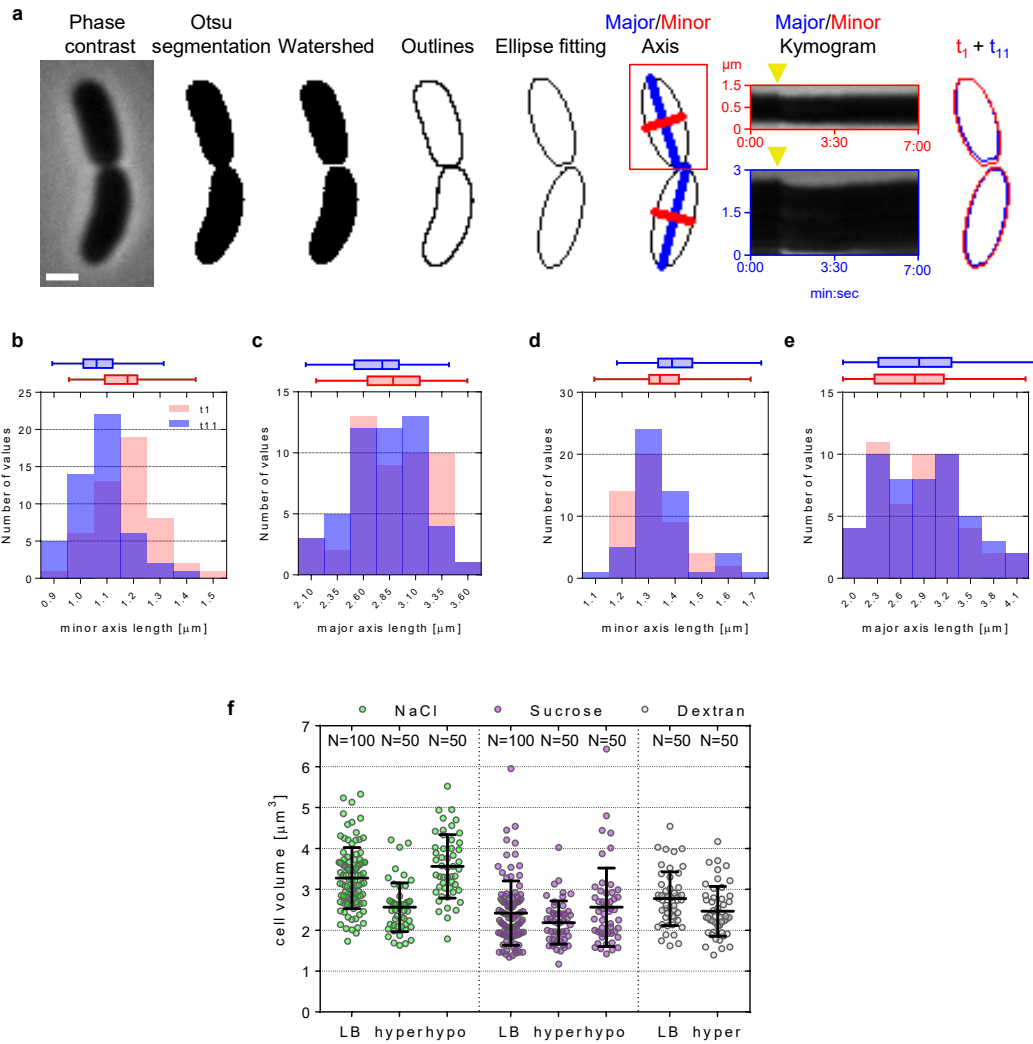
Supplementary Figure S1: Cell volume dynamics in response to osmotic shocks. Pipeline for cell volume calculation in Fiji **(a)**: Cells were segmented from phase-contrast image using Otsu algorithm (Otso 1979). Dividing cells were separated through water shedding. To segmented cells an ellipse was fitted from which the major (blue) and minor (red) axis was measured. Kymograms of minor (red) and major (blue) axis in response to hyperosmotic shock (yellow triangle) of the top cell (red square) are depicted. Overlay of ellipses from the first frame (red, t1) and the fourth frame upon hyperosmotic shock (blue, t11) are displayed. Minor **(b)** and major **(c)** axis length from 50 cells in response to hyperosmotic shock (+ 170 mM NaCl) are depicted. Minor **(d)** and major **(e)** axis length from 50 cells in response to hypoosmotic shock (- 170 mM NaCl) are depicted. Data is represented as histogram as well as whisker plots with minima and maxima; 75% of all data points lay within the box, horizontal line represents the median. **(f)** Cell volume was calculated as described in Material and Methods and was displayed from the first frame (LB) and the fourth frame upon osmotic shock (hyper, hypo respectively). Data is represented as mean ± one SD.
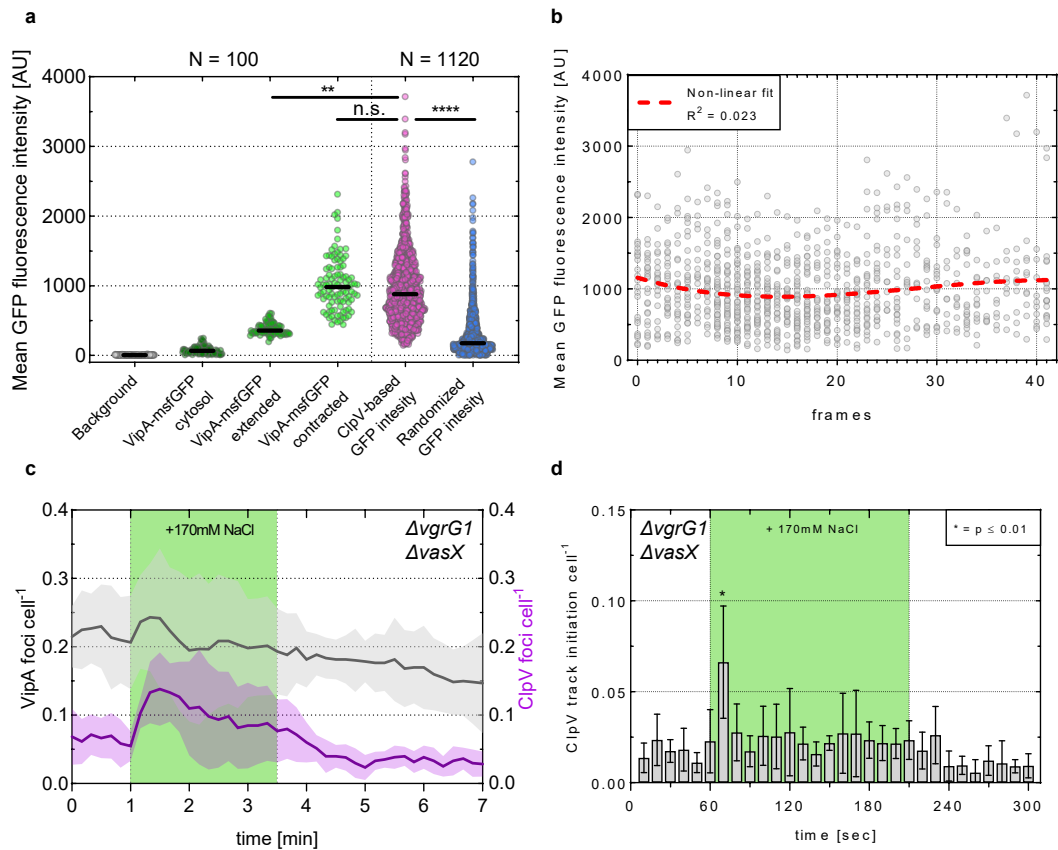
Supplementary Figure S2: Semi-automated ClpV foci detection by TrackMate identifies sheath contractions events. **(a)** Mean GFP fluorescence intensity was measured manually using an oval with 0.4 μm diameter as indicated. Contracted sheaths were identified by ClpV co-localization. X, Y and time coordinates from TrackMate identified ClpV foci were used as center of mass for generating an oval (0.4 μm diameter) at the corresponding frame and subsequent mean GFP fluorescence intensity measurement. For randomized GFP intensity measurements 'Salt and Pepper' noise generator was applied as described in material and methods. **(b)** Mean GFP fluorescence intensity distribution over time from ClpV-foci identified sheath was plotted. **(c)** T6SS dynamics in VipA-msfGFP and ClpV-mCherry2 labeled *vgrG1-vasX* double deletion mutants was monitored in response to hyperosmotic shock (green area). The number of VipA foci per cell (grey curve) as well as the number of ClpV foci per cell (purple curve) was assessed. Data is represented as mean ± one SD. **(d)** The number of new arising ClpV tracks per cell was assessed in response to hyperosmotic shock (green area) and compared to each frame. Data is presented as mean ± one SD, two-sided t-test p < 0.01, N > 1'000 cells from 3 biological replicates.
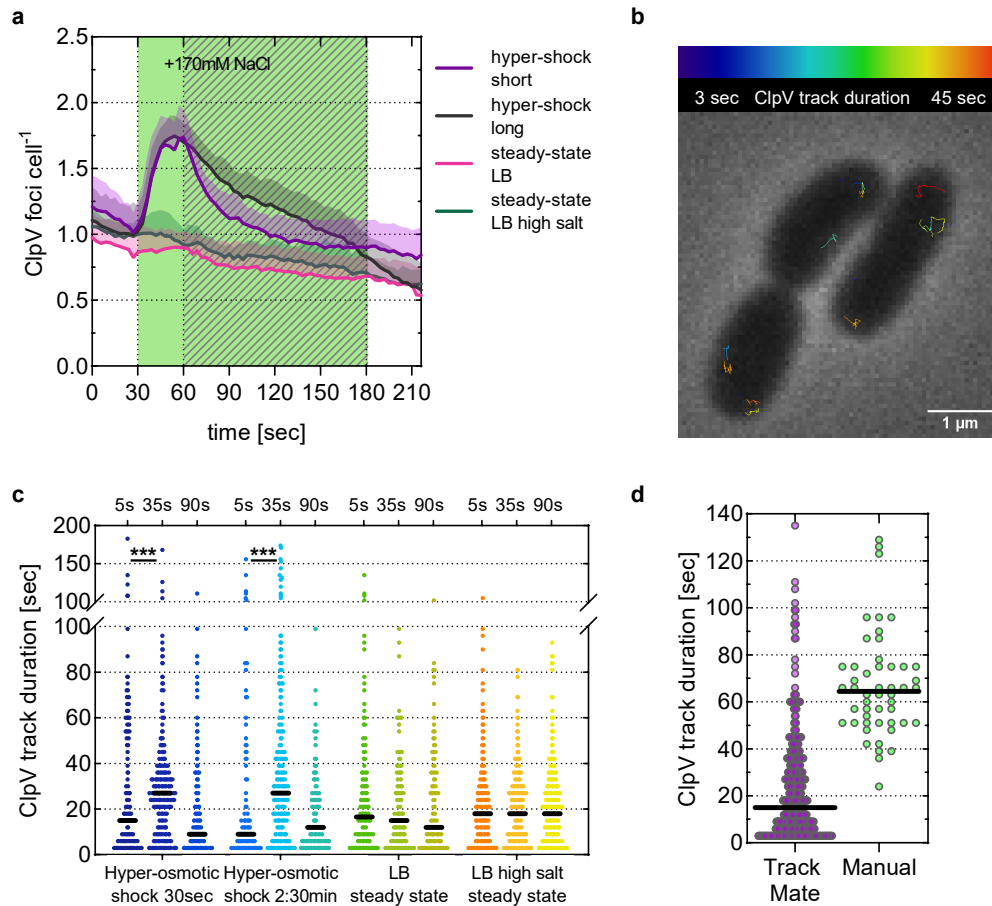
Supplementary Figure S3: Semi-automated ClpV tracking by TrackMate does not account correctly for sheath disassembly time. **(a)** T6SS contractions were monitored during 3:30min at 3s acquisition frame rate by detecting ClpV foci through TrackMate in response to short (green area) and long (green-straited area) or steady-state conditions. **(b)** Examples of ClpV tracking from steady-state LB conditions: tracks are color-coded according to duration and overlaid to phase-contrast image. **(c)** Distribution of ClpV track dynamics prior (5s), during (35s) or after (90s, except for cells exposed for 2:30min) hyperosmotic shock. Black line indicates median, Kruskal-Wallis, N = 3908, *** = p > 0.0001. **(d)** ClpV track duration was assessed manually from time the same set of time-lapse series and compared to values from TrackMate under steady-state conditions for LB.
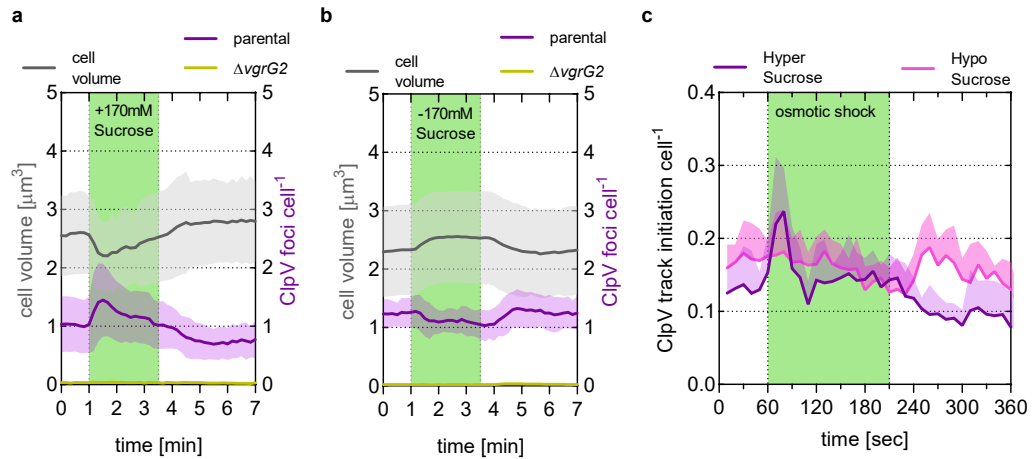
Supplementary Figure S4: T6SS dynamics in response to osmotic shocks with sucrose. T6SS dynamics were monitored by following VipA-msfGFP and ClpV-mCherry2 during 7min at 10s acquisition frame rate in wild-type as well as T6SS negative vgrG2 deletion mutant. Cells were exposed to either a hyper- **(a)** or hypoosmotic **(b)** shock. Cell volume dynamics (grey curve) from 50 cells each in response to osmotic shock (green area) was assessed by measuring difference in major and minor axis length from phase-contrast images as described in material and methods as well as Fig. S1. In addition, the number of ClpV foci per cell for indicated strains is plotted on the right Y-axis. ClpV detection was carried out in > 1'000 cells for each genotype from 3 independent biological replicates. Data is represented as mean ± one SD. **(c)** The number of new arising ClpV tracks per cell was assessed from each frame in response to osmotic shock (green area). Data is presented as mean ± one SD.
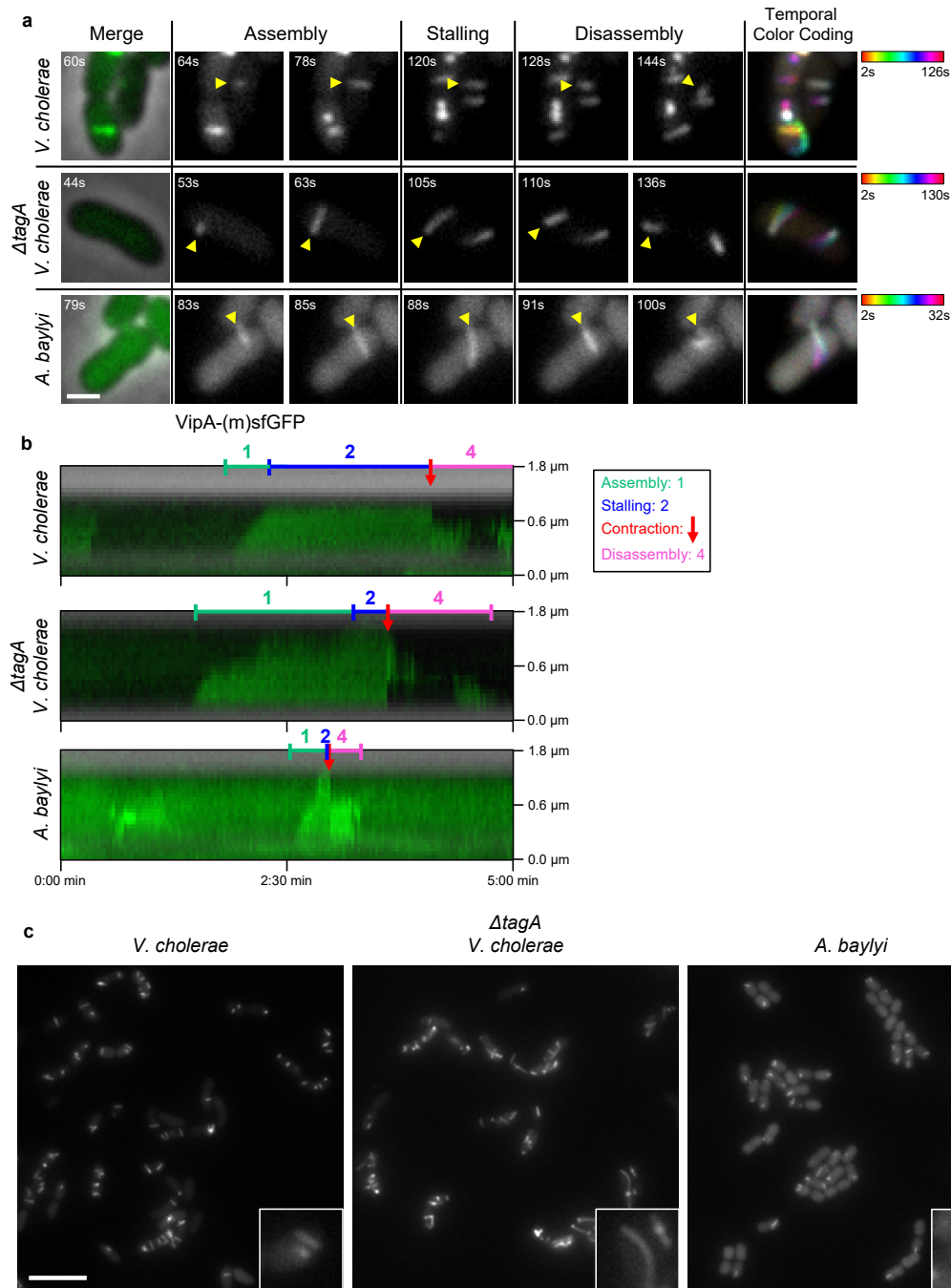
Supplementary Figure S5: Differences in sheath dynamics correlate with presence of TagA. **(a)** Sheath dynamics (assembly, stalling, disassembly) were monitored by following VipA-GFP derivates in *V. cholera*, isogenic *tagA* deletion mutant (both VipA-msfGFP) and *A. baylyi* (VipA-sfGFP) cells at 2s acquisition frame rate on 1% agarose in LB pads. Scale bar = 1 μm. Yellow arrowhead mark sheaths from which kymorgams **(b)** were generated. Respective stage of sheath dynamics is indicated. **(c)** 30x30 μm overview picture showing sheath phenotypes for indicated strains. Scale bar = 5 μm.

Table S1: Strains used in this study, related to Experimental Procedures

* = Same C-terminal clpV-mCherry construct as previously used by Basler and Mekalanos 2012, was added onto the chromosome of V. cholerae at its native locus through homologous recombination and introduced into the indicated backgrounds. All these strains were characterized previously.

Organism	Genotype	Plasmid	Relevant features	Source
V. cholerae 2740-80	lacZ, Str^r		Parental strain	(Basler et al., 2012)
	lacZ, Str^r, vipA-msfGFP, clpV-mCherry2*		C-terminal chromosomal fusion of msfGFP to VipA and mCherry2 to ClpV, respectively	This study
	lacZ, Str^r, vipA-msfGFP, clpV-mCherry2, ΔvgrG2		T6SS negative control by deletion of vgrG2 in dual color background	(Vettiger et al., 2016) this study
	lacZ, Str^r, vipA-msfGFP, clpV-mCherry2, ΔvipA	pBAD24-vipA3AA	Non-contractile sheath mutant in dual color background	(Wang et al., 2017), this study
	lacZ, Str^r, vipA-msfGFP, clpV-mCherry2, ΔvgrG1, ΔvasX		Combination of vgrG1 and vasX deletions in double color background	(Vettiger et al., 2016) this study
	lacZ, Str^r, vipA-msfGFP, clpV-mCherry2, ΔtagA		TagA deletion in vipA-msfGFP background	(Schneider et al., accepted), this study
A. baylyi ADP1	rpsL-K88R		Parental strain	(Ringel et al., 2017)
	rpsL-K88R, vipA-sfGFP, clpV-mCherry2		C-terminal chromosomal fusion of msfGFP to VipA and mCherry2 to ClpV, respectively	(Ringel et al., 2017)
E. coli SM10 λ pir	Km^r, thi-1, thr, leu, tonA, lacY, supE, recA::RP4-2-Tc::Mu, pir	pWM91/pEXG2	Allelic replacement vector used for all in-frame deletions by conjugation; sacB, Amp^r/Gent^r	
DH5α λ pir	F-, endA1, glnV44, thi-1, recA1, relA1, gyrA96 deoR, nupG, Φ80dlacZΔM15, (lacZYA-argF)U169, hsdR17(rK-mK+), λ-		Cloning strain	

APPENDIX C

Supplementary material to chapter 4

Type VI secretion system substrates are transferred and reused among sister cells

Andrea Vettiger and Marek Basler

**Supplementary Information**

Supplemental Figures
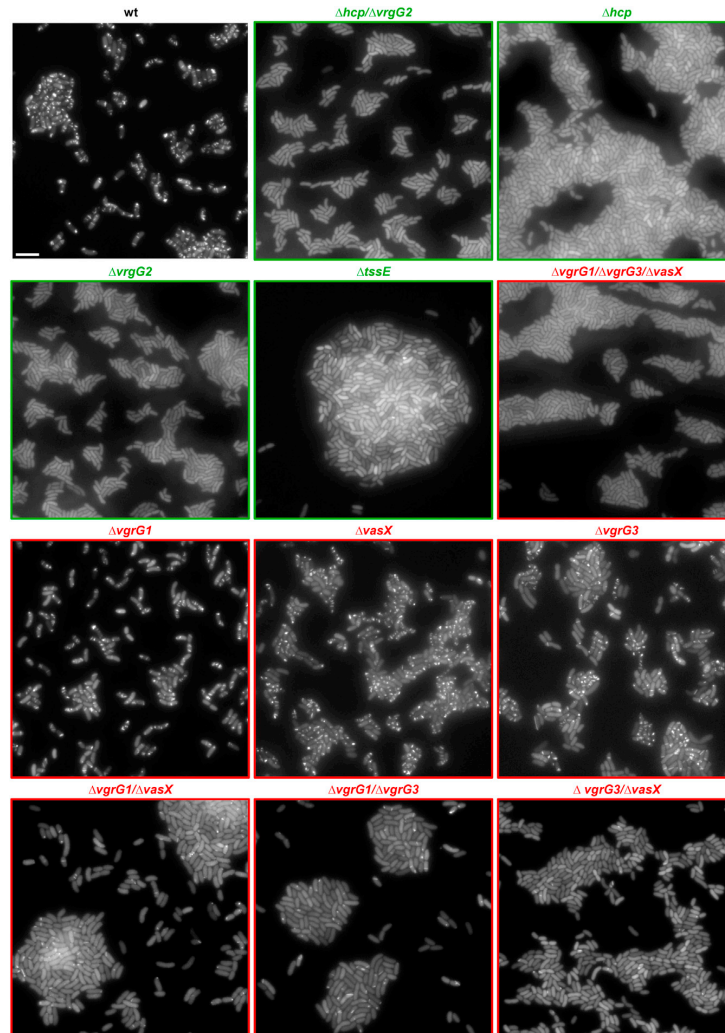
Figure S1. The Deletion of Secreted Structural Components and Effector Proteins Leads to a Complete Absence or Reduced Rate of Sheath Assembly, Related to Figures 1A and 3A

Depicted are representative 50 × 50 μm fields of GFP fluorescence channel for each indicated strain (all *vipA-msfGFP* background). Green label/frame indicates structural components. Red label/frame indicates effector proteins. Scale bar = 5 μm.
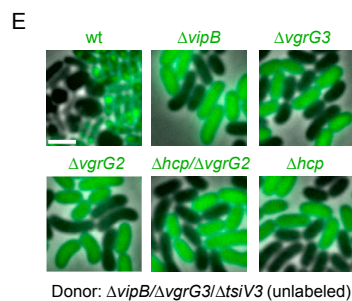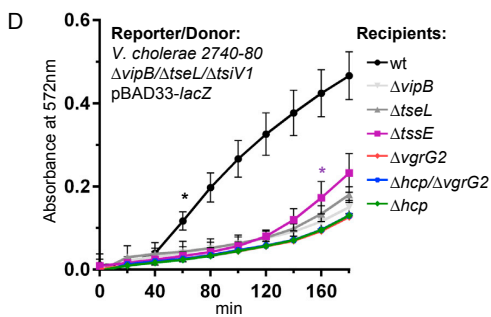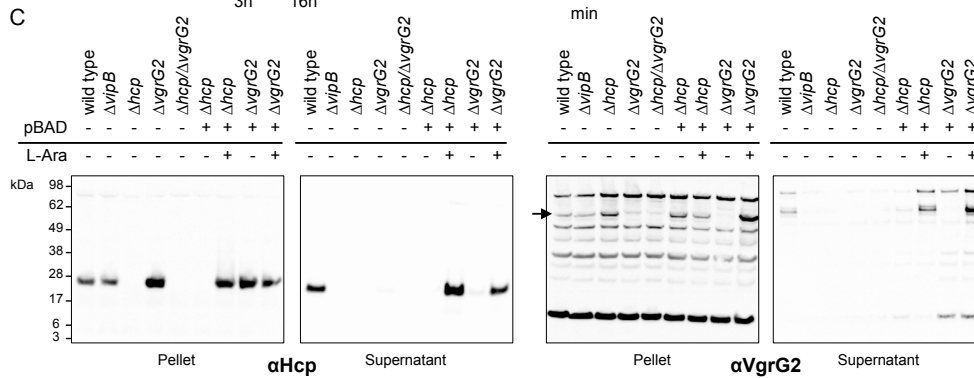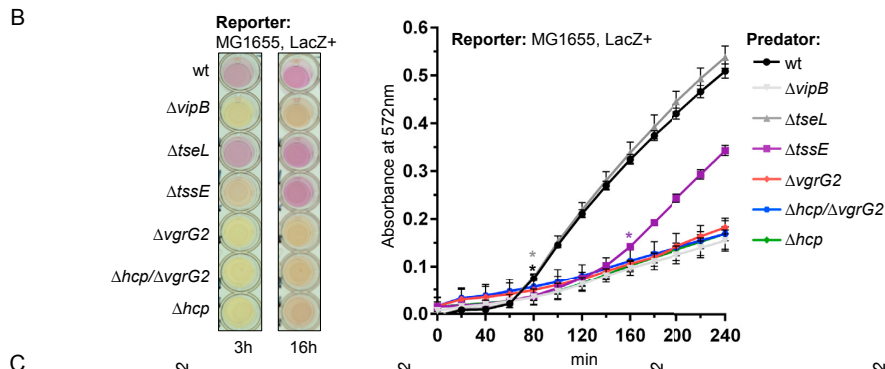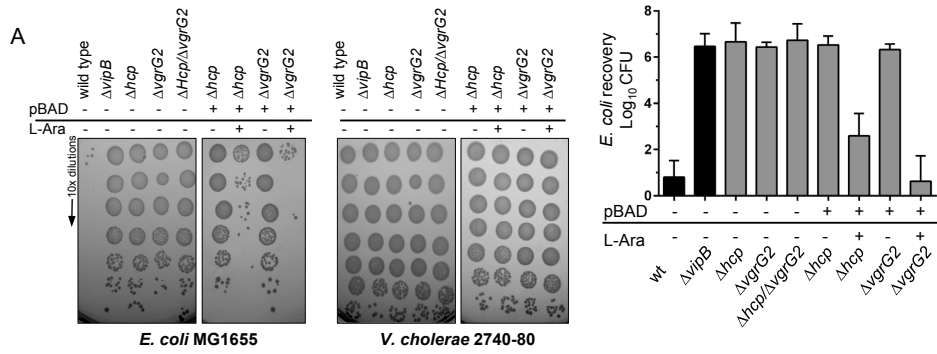
(legend on next page)

Figure S2. The Deletion of *hcp* and *vgrG2* Leads to a Complete Absence of T6SS Activity, Related to Figures 1A and 4

(A) Depicted are recovered cells after 2 hr of co-incubation on LB agar plate. Images represent examples of the quantified data in the graph on the right. Black bars represent positive (wild-type) and negative control (*ΔvipB*). The presence or absence of pBAD vectors and induction of protein expression for complementation is indicated by "+" or "-", respectively.

(B) Indicated *V. cholerae* strains were co-incubated with LacZ+ *E. coli* (reporter). A representative image of a 96-well plate is shown after 180 min and subsequent over-night co-incubation of indicated strains is shown on the left. For cell lysis quantification (right) indicated recipient strains were mixed with the donor strain and incubated for 3 h at 37°C in 96-well plate. Absorbance was measured in 20 min intervals at 572 nm. Colored asterisks mark time point from which chlorophenol red absorbance was significantly higher as compared to background absorbance (*ΔvipB* + reporter) determined by unpaired t-test.

(C) Presence of Hcp (left) and VgrG2 (right) was assessed by western blotting in pellet and cell-free supernatant fractions. Predicted molecular weight for Hcp: 18 kDa; VgrG2: 72 kDa. The presence and absence of pBAD vectors and induction of protein expression for complementation is indicated by "+" or "-", respectively, arrow indicates specific band for VgrG2.

(D) Lipase sensitive, T6SS-, lacZ+ reporter strain was co-incubated with indicated recipient strains at a ratio of 1:10 (reporter/recipient) for the detection of reporter cell lysis. Bacterial mixtures were incubated for 3 h at 37°C in 96-well plate. Absorbance was measured in 20 min intervals at 572 nm. Colored asterisks mark time point from which chlorophenol red absorbance was significantly higher as compared to background absorbance (*ΔvipB* + reporter) determined by unpaired t-test.

(E) A VgrG3 sensitive, T6SS- reporter strain was used as donor for interbacterial protein complementation. Bacterial mixtures were co-incubated on LB agarose pad under a glass cover slip for 1 h prior to screening for cell-rounding. Representative images of cells are shown and are a merge of phase contrast and GFP fluorescence channels depicting cell-rounding in VgrG3 sensitive donor cells (black label, no fluorescence) and indicated *vipA-msfGFP* background strains (green label, GFP fluorescence). Cell-rounding was assessed in 40'000 donor cells for each mixture. Scale bar = 2 μm.
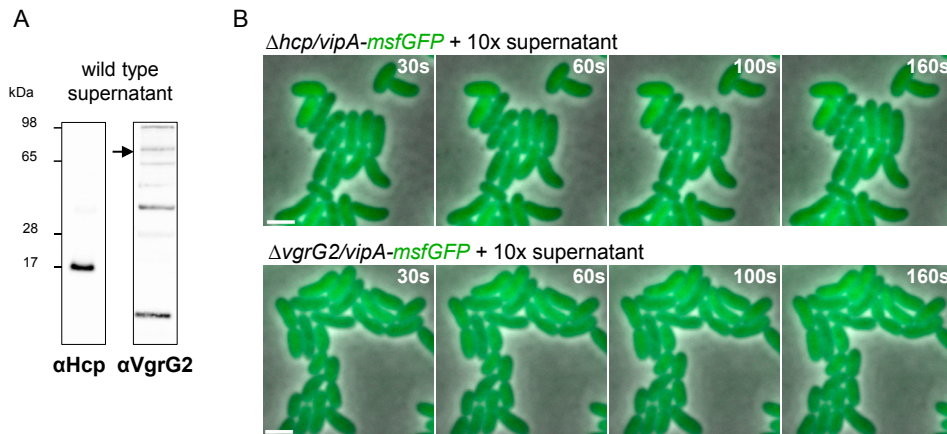
Cell

A

wild type
supernatant

kDa

98

65

28

17

αHcp αVgrG2

B

Δhcp/vipA-msfGFP + 10x supernatant

| 30s | 60s | 100s | 160s |

ΔvgrG2/vipA-msfGFP + 10x supernatant

| 30s | 60s | 100s | 160s |

Figure S3. Interbacterial Protein Complementation Relies on T6SS-Mediated Protein Translocation into Recipient Cells, Related to Figure 1
(A) Supernatant from a fresh day culture of wild-type *V. cholerae* 2740-80 was concentrated 10-fold by Amicon spin tube according to the manufacturer's recommendations. Presence of Hcp and VgrG2 (indicated by arrow) was confirmed by western blot on diluted (1x) precipitated supernatant.
(B) Indicated strains were prepared for imaging as normal but resuspended in 10x concentrated supernatant. Depicted are individual frames from a 5 min time-lapse movie and are a merge of phase contrast and GFP fluorescence channel. No T6SS activity was detected during 2 hr observation period. Scale bars = 2 μm.
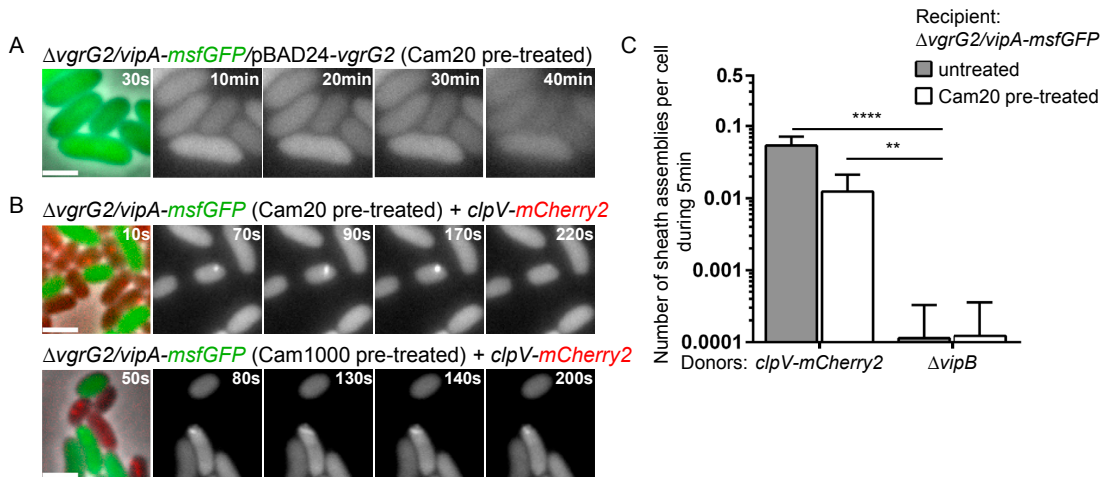
Cell

Figure S4. Interbacterial Protein Complementation Does Not Require De Novo Protein Synthesis for the Initiation of a New T6SS Assembly, Related to Figure 1

(A) VgrG2 was expressed from pBAD24 vector in *vipA-msfGFP* strains lacking *vgrG2*. Thirty minutes prior to imaging 20 µg/ml chloramphenicol was added to the cultures. Subsequently cells were spotted on a pad with 0.1% L-arabinose. The time after protein induction is indicated. Depicted are individual frames of a 60 min time-lapse movie. The first frame shows all cells and is a merge of phase contrast and GFP fluorescence channels, whereas the following 4 frames show only GFP fluorescence channel to clearly visualize sheath assembly. No sheath assembly was detected within 1 hr of imaging.

(B) *VipA-msfGFP* labeled strains lacking *vgrG2* were pretreated with chloramphenicol (20 µg/ml for 30 min – top; 1 mg/ml for 90 min – bottom) prior to mixing them with untreated donor cells for interbacterial protein complementation assay. Depicted are individual frames of a 5 min time-lapse. The first frame shows all cells and is a merge of phase contrast, GFP (chloramphenicol treated *ΔvgrG2* - T6SS- recipient) and mCherry2 (wild-type donor) fluorescence channels. The following four frames only show GFP fluorescence channel to visualize sheath dynamics. Scale bar = 2 µm.

(C) Sheath assembly was monitored in untreated and chloramphenicol pretreated (20 µg/ml for 30min) *ΔvgrG2/vipA-msfGFP* strains for 5 min immediately after co-incubation either with *clpV-mCherry2* (wild-type T6SS activity) or *ΔvipB* (T6SS-) donor cells. Total number of sheath assemblies was counted in 5'000 GFP+ cells for indicated strains. Data are represented as mean ± SD. **** = p < 0.0001; ** = p < 0.01; one-way ANOVA and Tuckey post hoc test for multiple comparison.
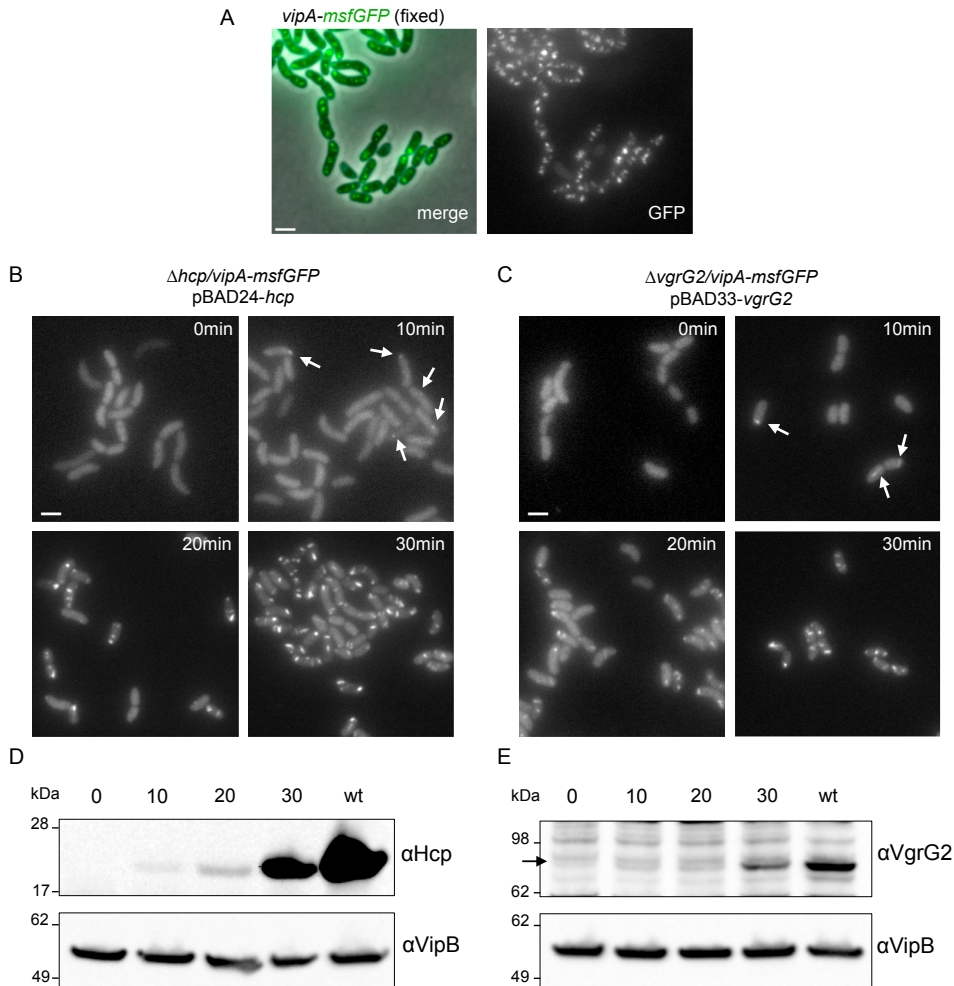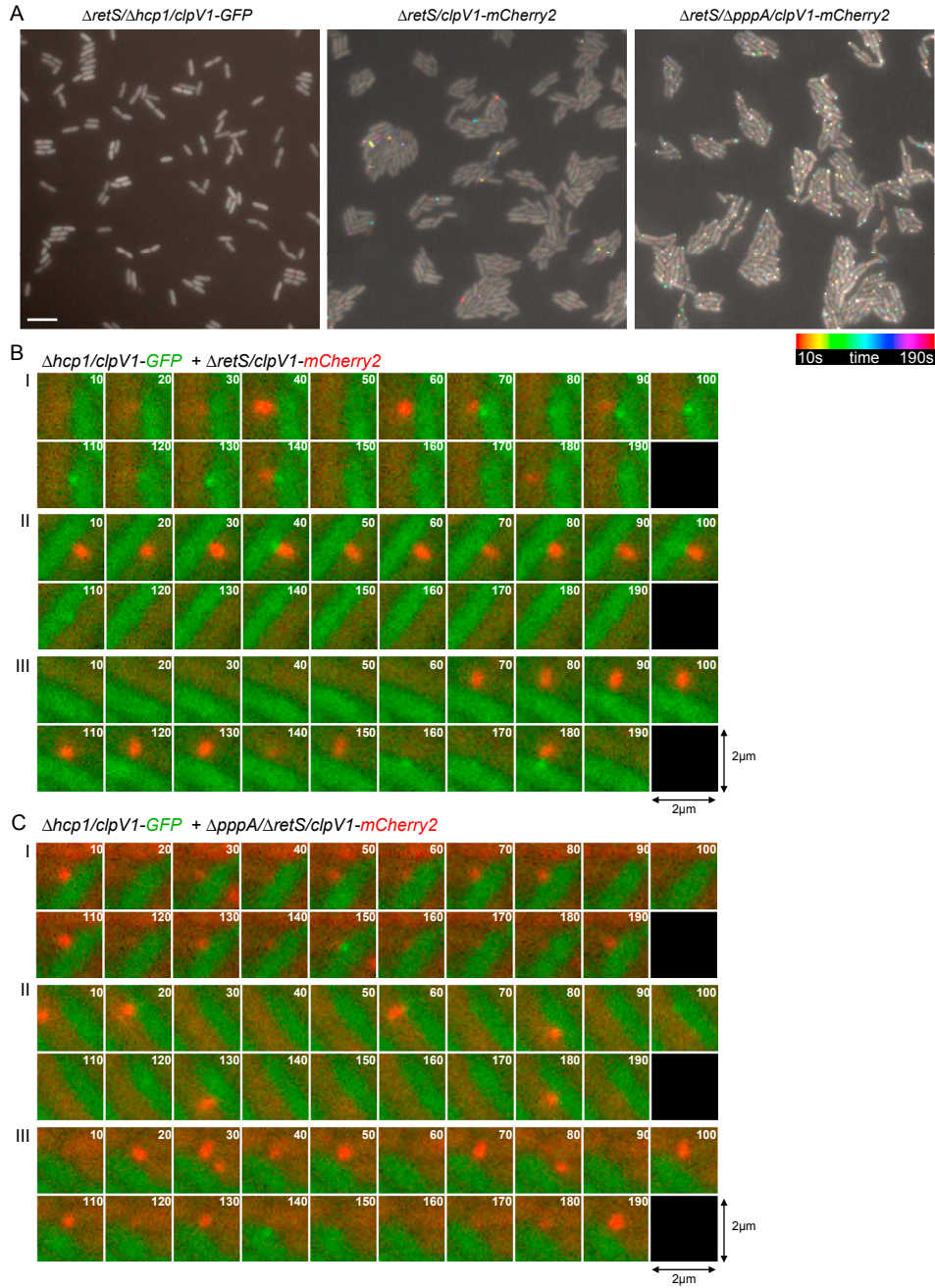
Figure S5. Protein Concentrations of VgrG2 and Hcp Correlate with the Number and Length of Sheath Assemblies, Related to Figure 2

(A) Representative image showing T6SS sheaths in wild-type *vipA-msfGFP* labeled *V. cholerae* strain. Cells were fixed by the direct addition 4% formaldehyde, 0.2% glutaraldehyde to the culture and incubated for 20 min at room temperature. Subsequently fixative was removed and cells were resuspended in PBS and stored until microscopic analysis.

(B and C) Hcp (B) or VgrG2 (C) were expressed from pBAD vectors in *vipA-msfGFP* background strains lacking *vgrG2* or *hcp1/hcp2*, respectively by the addition of 0.01% L-arabinose to the culture. The time after harvesting and fixing (as described above) a sample of to the culture is indicated. Images show representative cells in GFP fluorescence channel to visualize sheath assembly. Arrows indicate first sheath assemblies. Scale bar = 2 μm.

(D and E) Presence of Hcp (D) and VgrG2 (E) was assessed by western blotting in pellet fractions harvested and immediately boiled in SDS sample buffer at indicated time points after the addition of 0.01% L-arabinose and compared to wild-type levels. Arrow indicates specific (lower) band for VgrG2. Presence of VipB was detected and serves as a loading control.

A *ΔretS/Δhcp1/clpV1-GFP*   *ΔretS/clpV1-mCherry2*   *ΔretS/ΔpppA/clpV1-mCherry2*

10s time 190s

B *Δhcp1/clpV1-GFP + ΔretS/clpV1-mCherry2*

C *Δhcp1/clpV1-GFP + ΔpppA/ΔretS/clpV1-mCherry2*

(legend on next page)

Cell

Figure S6. *P. aeruginosa* Displays T6SS Activity upon Interbacterial Protein Complementation, Related to Figure 6

(A) Temporal color coded projections of 3 min time-lapse series of ClpV1-GFP or ClpV1-mCherry2 fluorescence signal are depicted for each indicated strain (50 × 50 μm fields). Scale bar is 5 μm. Time-color code is shown.

(B and C) Representative time-lapse series of six of ClpV1 assembly events between *pppA+* (B) and *pppA-* (C) donor (*ΔretS/clpV1-mCherry2* - T6SS+, red) and recipient (*ΔretS/Δhcp1/clpV1-GFP* - T6SS-, green) cells are depicted. All 19 frames of a 3 min time-lapse series acquired with a frame rate of 10 s are shown. Image series were corrected to reduce effects of photo-bleaching.
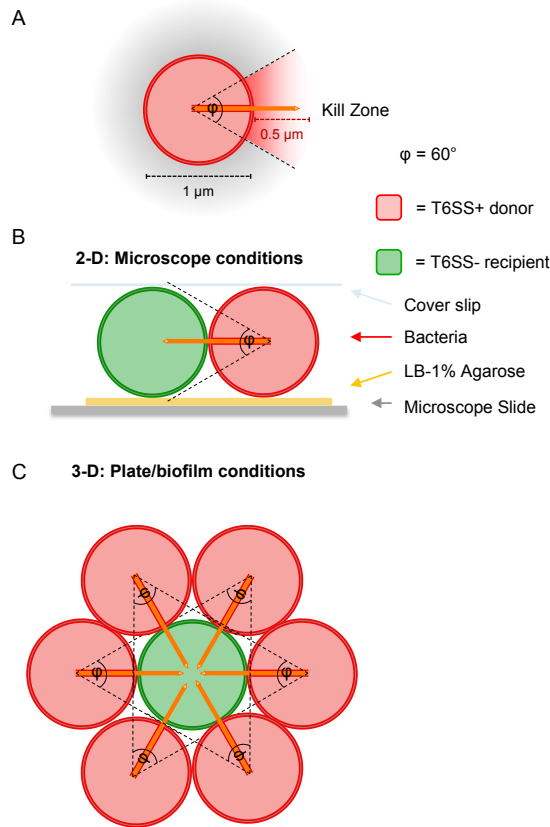
Figure S7. Theoretical Efficiency of T6SS Substrate Delivery, Related to Figure 7

(A) An average fully extended T6SS sheath reaches up to 1 μm in length and contracts to half of its initial length, thereby propelling out the inner Hcp tube and associated effectors to a maximum distance of 0.5 μm. It is reasonable to expect that cells lying within a 60° angle of a contracted sheath will be hit by secreted T6SS substrates (Red shade = potential kill zone).

(B) Since *V. cholerae* was shown to assemble its T6SS machinery at random subcellular localization, a donor has maximum one in six chance of translocating its T6SS substrate into target cells.

(C) Dense three-dimensional biofilms may provide 6 times more contact sites to sister cells than in a single layer of cells. Bacterial cells are simplified as cross-sections.

Table S1A

Organism	Genotype	Plasmid	Relevant features	Source
V. cholerae 2740-80	lacZ⁻, Str^r		Parental strain	(Basler et al., 2012)
	lacZ⁻, Str^r, ΔvipB		Deletion of vipB	(Basler et al., 2012)
	lacZ⁻, Str^r, clpV-mCherry2		C-terminal chromosomal fusion of mCherry2 to clpV	(Basler and Mekalanos, 2012)
	lacZ⁻, Str^r, vipA-msfGFP		C-terminal chromosomal fusion of msfGFP to vipA	(Kudryashev et al., 2015)
	lacZ⁻, Str^r, vipA-msfGFP, ΔvipB		Deletion of vipB in vipA-msfGFP background	(Kudryashev et al., 2015)
	lacZ⁻, Str^r, vipA-msfGFP, ΔvgrG2		Deletion of vgrG2 in vipA-msfGFP background	this study
	lacZ⁻, Str^r, vipA-msfGFP, ΔvgrG2	pBAD33-vgrG2	Complementation of vgrG2 deletion from inducible vector; added RBS, Cm^r	this study
	lacZ⁻, Str^r, vipA-msfGFP, ΔvgrG2	pBAD24-vgrG2	Complementation of vgrG2 deletion from inducible vector; Amp^r	this study
	lacZ⁻, Str^r, vipA-msfGFP, Δhcp1, Δhcp2		Deletion of both hcp variants in vipA-msfGFP background	this study
	lacZ⁻, Str^r, vipA-msfGFP, Δhcp1, Δhcp2	pBAD24-hcp2	Complementation of hcp deletion from inducible vector; Amp^r	this study
	lacZ⁻, Str^r, vipA-msfGFP, ΔvgrG2, Δhcp1, Δhcp2		Combination of vgrG2 and hcp deletions in vipA-msfGFP background	this study
	lacZ⁻, Str^r, vipA-msfGFP, ΔvgrG1, ΔvgrG2, ΔvgrG3		Complete vgrG deletion of in vipA-msfGFP background	this study
	lacZ⁻, Str^r, vipA-msfGFP, ΔvgrG1		Deletion of vgrG1 in vipA-msfGFP background	this study
	lacZ⁻, Str^r, vipA-msfGFP, ΔvgrG3		Deletion of vgrG3 in vipA-msfGFP background	this study
	lacZ⁻, Str^r, vipA-msfGFP, ΔvasX		Deletion of vasX in vipA-msfGFP background	this study
	lacZ⁻, Str^r, vipA-msfGFP, ΔvgrG1, ΔvasX		Combination of vgrG1 and vasX deletions in vipA-msfGFP background	this study
	lacZ⁻, Str^r, vipA-msfGFP, ΔvgrG1, ΔvgrG3		Combination of vgrG1and vrgG3 deletions in vipA-msfGFP background	this study
	lacZ⁻, Str^r, vipA-msfGFP, ΔvgrG3, ΔvasX		Combination of vgrG3 and vasX deletions in vipA-msfGFP background	this study
	lacZ⁻, Str^r, vipA-msfGFP, ΔvgrG1, ΔvgrG3, ΔvasX		Combination of vgrG1, vgrG3 and vasX deletions in vipA-msfGFP background	this study

Organism	Genotype	Plasmid	Relevant features	Source
V. cholerae 2740-80	lacZ-, Str^r, clpV-mCherry2, ΔvgrG1, ΔvasX		Combination of vgrG1 and vasX deletions in clpV-mCherry2 background	this study
	lacZ-, Str^r, ΔvgrG3, ΔtsiV3		Combination of vgrG3 and tsiV3 deletions mediating sensitivity to VgrG3	this study
	lacZ-, Str^r, ΔvgrG3, ΔtsiV3, ΔvipB		VgrG3 sensitive, T6SS negative reporter	this study
	lacZ-, Str^r, ΔtseL		Lipase (tseL) deletion	this study
	lacZ-, Str^r, ΔtseL, ΔtsiV1	pBAD33-lacZ	Combination of tseL and tsiV1 deletions mediating sensitivity to TseL, as well as expression of β-galactosidase from inducible vector	this study
	lacZ-, Str^r, ΔtseL, ΔtsiV1, ΔvipB	pBAD33-lacZ	TseL sensitive, T6SS negative, LacZ+ reporter	this study
	lacZ-, Str^r, ΔtssE, vipA-msfGFP		Deletion of tssE (base-plate component) in vipA-msfGFP background, control for low T6SS activity	this study
P. aeruginosa PAO1	ΔretS		Parental strain	Mougous et al., 2006
	ΔretS, clpV1-mCherry2		C-terminal chromosomal fusion of mCherry2 to clpV1	this study
	ΔretS, ΔpppA, clpV1-mCherry2		C-terminal chromosomal fusion of mCherry2 to clpV1 in pppA background	this study
	ΔretS, ΔpppA, ΔtssB1, clpV1-mCherry2		C-terminal chromosomal fusion of mCherry2 to clpV1 in tssB1 background	this study
	ΔretS, ΔtssC1		Deletion of tssC1	this study
	ΔretS, Δhcp1, clpV1-GFP		Deletion of hcp1 variant in clpV1-GFP background	this study
	ΔretS, Δhcp1, clpV1-GFP	pPSV35-hcp1	Complementation of hcp1 deletion from inducible vector; Gent^r	this study
E. coli MG1655	K-12, F-, λ-, ilvG-, rfb-50, rph-1, lacZ+	pBAD24	Used for quantitative killing and cell lysis assays, Amp^r	(Basler et al., 2012)
SM10 λ pir	Km^r, thi-1, thr, leu, tonA, lacY, supE, recA::RP4-2-Tc::Mu, pir	pWM91/pEXG2	Allelic replacement vector used for all in-frame deletions by conjugation; sacB, Amp^r/Gent^r	
DH5α λ pir	F-, endA1, glnV44, thi-1, recA1, relA1, gyrA96 deoR, nupG, Φ80dlacZΔM15, (lacZYA-argF)U169, hsdR17(rK-mK+), λ-		Cloning strain	

- 167 -

Table S1B

Plasmid Name	Peptide scar left on the chromosome after allelic exchange
pWM91-Δ*vgrG2*	MATLAYSEEAKGN*
pWM91-Δ*hcp1*	MPTPCYIRKPIEA*
pWM91-Δ*hcp2*	MPTPCYIRKPIEA*
pWM91-Δ*vgrG1*	MATLAYEWQRIIA*
pWM91-Δ*vasX*	MSNPNQAALVVGKG*
pWM91-Δ*vgrG3*	MARLQFQGLEVDIK*
pWM91-Δ*vgrG3*-Δ*tsiV3*[$]	MARLQFQGLEVDIK*MNNLLSAEDVDNS*
pWM91-Δ*tseL*-Δ*tsiV1*	MDSFNYVSDDN*
pEXG2-Δ*hcp1*	MAVDNVQA*
pEXG2-Δ*tssB1*	MGSTTSSQA*
pEXG2-Δ*tssC1*	MAELSPSAKEA*
pEXG2-*clpV1-mCherry2*[#]	-

[*] - stop codon
[$] - genes encoding the *vgrG3* and *tsiV3* scar peptides are partially overlapping similarly to the full length open reading frames
[#] - the same plasmid and cloning strategy was used as before for ClpV1-GFP fusions, except the *gfp* portion of the plasmid was replaced by *mCherry2* (Mougous *et al.*, 2006)

APPENDIX D

Supplementary material to chapter 5

The Evolution of the type VI secretion system as a lytic weapon

William P. J. Smith, Andrea Vettiger, Julius Winter, Till Ryser, Laurie E. Comstock, Marek Basler, and Kevin R. Foster

Manuscript submitted to Nature, 2019

Supplementary Information

Supplementary movie S1-6 associated with this manuscript can be found in on the attached CD under the folder, Chapter 5.

File name: Movie S1

Description: Simulated T6SS competitions at different firing rates. Representative agent-based model simulations show communities growing from a randomly-scattered 1:1 inoculum of T6SS+ attacker cells (green) and T6SS- susceptible cells (magenta). Here, monolayers of 3-D rod-shaped cells grow exponentially through elongation, dividing after doubling their initial volume, and pushing on neighboring cells during expansion. T6SS+ cells attack T6SS- cells with discrete, randomly-oriented needles, fired at average rate k_{fire}; intoxicated T6SS- cells (black) cannot divide, and lyse after a time delay $1/k_{lysis}$. From left to right, the T6SS firing rate is increased (0, 50 and 250 firings cell^{-1} h^{-1}, respectively). Simulation parameters: $N_{hits} = 1$, $c = 0.001$, $k_{lysis} = 0.8$, 8.0 h^{-1}. Screen measures ~700 x 350μm; frame rate 5 frames per second.

File name: Movie S2

Description: Simulations of microfluidic chamber competitions. Representative agent-based model simulations of T6SS+ attacker cells (green) competing with T6SS- susceptible cells (magenta) in 100 x 10μm microfluidic chambers, under conditions of fast (top, $k_{lysis} = 8.0$

h^{-1}) and slow (bottom, k_{lysis} = 0.8 h^{-1}) victim lysis. Intoxicated T6SS- cells are shown in black; initial cell positions are identical. Simulation parameters: N_{hits} = 1, c = 0.001, K_{fire} = 50 firings cell^{-1} h^{-1}. Screen measures ~115 x 58μm; frame rate 5 frames per second.

File name: Movie S3

Description: Microfluidic competition assay comparing *E. coli* survival between lytic and non-lytic *A. baylyi* single-effector strains. T6SS+ *A. baylyi* (*vipA-sfGFP*, green) were competed with T6SS-susceptible *E. coli* (*mRuby3*, magenta) cells in 1μm-deep microfluidic channels. Fast lytic *tae1* single-effector aggressor strains is displayed on the left; slow-lytic *tse2* single-effector aggressor strain is displayed on the right. Five representative time-lapse series acquired with a rate of 5min per frame are shown. GFP and mRuby3 fluorescence channels are displayed individually as grey scale images in addition to a merge of phase contrast and both fluorescence channels. Scale bar = 2μm. The video plays at a rate of 12 frames per second.

File name: Movie S4

Description: Microfluidic competition assay in presence or absence of T6SS mediated prey cell killing. Parental (left) and isogenic T6SS- (*Δhcp*, right) *A. baylyi* (*vipA-sfGFP*, green) strains were competed with T6SS-susceptible *E. coli* (*mRuby3*, magenta) cells in 1μm-deep microfluidic channels. A representative time-lapse series acquired with a rate of 5min per frame is shown. GFP and mRuby3 fluorescence channels are displayed individually as grey scale images in addition to a merge of phase contrast and both fluorescence channels. Scale bar = 2μm. The video plays at a rate of 12 frames per second.

File name: Movie S5

Description: Osmo-protective conditions prevent target cell lysis. T6SS+ *A. baylyi* attacker strain (*vipA-sfGFP*, green) armed with Tae1 was competed with T6SS-susceptible *E. coli* cells on LB 1% agarose pads containing 2 μg/mL propidium iodide (magenta). Agarose pads were left untreated (-OP, left) or supplemented with 0.4M sucrose, 8mM MgSO$_4$ (+OP, right). Ten representative 45min time-lapse series acquired with a rate of 30s per frame are shown. Field of view is 10 x 10μm and shows a merge of phase contrast and two fluorescent channels: VipA-sfGFP and propidium iodide. Scale bar = 2μm. The video plays at a rate of 12 frames per second.

File name: Movie S6

Description: Microfluidic competition experiment in presence of osmo-protective conditions. T6SS+ *A. baylyi* attacker strain (*vipA-sfGFP*, green) was competed with T6SS-susceptible *E. coli* (*mRuby3*, magenta) cells in presence of OP in 1μm-deep microfluidic channels. Five representative time-lapse series acquired with a rate of 5min per frame are shown. GFP and mRuby3 fluorescence channels are displayed individually as grey scale images in addition to a merge of phase contrast and both fluorescence channels. Scale bar = 2μm. The video plays at a rate of 12 frames per second.

Table S1: Model parameters

Category	Parameter	Symbol	Value(s)	Units	Source
Cell-based	Max. specific growth rate	k_{grow}	1.0	h^{-1}	(Rudge, Steiner, Phillips, & Haseloff, 2012)
	Pro rata T6SS cost	c	0-0.05	1 / (firings cell^{-1} h^{-1})	This study
	T6SS firing rate	k_{fire}	0-250.0	firings cell^{-1} h^{-1}	Estimated from (Ringel, Hu, & Basler, 2017)
	Lysis delay	$1 / k_{lysis}$	0.125-1.25	h	This study
	Lethal hit threshold	N_{hits}	1	-	Estimated from (Ringel, Hu, & Basler, 2017)
	Extracellular needle length	L_{needle}	0.5	µm	Estimated from (Basler et al., 2012)
	Min. needle penetration for hit	$L_{penetration}$	10	nm	Estimated from bacterial outer membrane width
	Cell radius	R	0.5	µm	Estimated from (Ringel, Hu, & Basler, 2017)
	Cell volume at birth	V_0	1.16	µm^3	(Smith et al., 2016)
	Cell division volume noise	$\eta_{division}$	9	%	(Smith et al., 2016)
	Cell division orientation noise	$\eta_{orientation}$	0.2	%	(Smith et al., 2016)
Numerical	Simulation timestep	dt	0.025	h	(Rudge, Steiner, Phillips, & Haseloff, 2012)
	Cell / needle sorting grid element size	h	10	µm	(Smith et al., 2016)
	CG absolute tolerance	ϵ_{CG}	0.001	-	(Rudge, Steiner, Phillips, & Haseloff, 2012)
	Max. contact iterations	$M_{Iter, max}$	8	-	(Rudge, Steiner, Phillips, & Haseloff, 2012)
Mechanical	Regularization weight	α	0.04 (0.1 for chambers)	-	(Smith et al., 2016)
	Growth restriction factor	$1 / \gamma$	0.002 (0.1 for chambers)	-	(Smith et al., 2016)

Table S2: Model variables

For each cell i:

Category	Variable	Symbol	Units
Genetic	Cell genotype	T6+ (green), T6- (magenta)	-
	Centroid vector	$\mathbf{c_i} = (c_x, c_y, c_z)_i$	μm
	Orientation unit vector	$\mathbf{a_i} = (a_x, a_y, a_z)_i$	-
Geometric	Segment length	L_i	μm
	Volume	$V_i = 4\pi R^3/3 + \pi L_i R^2$	μm³
	Specific growth rate	$k_{grow,i} = k_{grow}(1-c_{total,i})$	h^{-1}
	Total cost	$c_{total,i} = ck_{fire,i}$	-
T6SS	Firing rate	$k_{fire,i} = N_{firings,i}(t) / dt$	Firings cell^{-1} h^{-1}
	Firings this timestep	$N_{firings,i}(t)$	Firings
	Cumulative hits	$N_{hits,i}$	Hits

Table S3: Bacterial Strains

| Organism	Genotype	Relevant features	Source
Acinetobacter baylyi ADP1	*rpsL-K88R, vipA-sfGFP*	Parental strain, VipA labeled to sfGFP, Sm^R	This study
	rpsL-K88R, vipA-sfGFP, Δhcp	Deletion of *hcp*, T6SS negative	This study
	rpsL-K88R, vipA-sfGFP, Δtpe1, Δtse1, Δtse2, ΔtseL	Tae1(lytic) single effector strain	This study
	rpsL-K88R, vipA-sfGFP, Δtpe1, Δtae1, Δtse1, ΔtseL	Tse2 (non-lytic) single effector strain	This study
	rpsL-K88R, vipA-sfGFP, clpV-mCherry2, Δtae1	Deletion of *tae1*	(Ringel, Hu, & Basler, 2017)
Escherichia coli MG1655 Gm^R	K-12, F⁻, λ⁻, *ilvG⁻, rfb-50, rph-1, lacZ+*	Unlabeled prey strain used for propidium iodide imaging	(Basler, Ho, & Mekalanos, 2013)
	K-12, F⁻, λ⁻, *ilvG⁻, rfb-50, rph-1, lacZ+, yfgI:: Pj23119-mRuby3-FRT*	Prey strain, constitutive cytosolic mRuby3 expression	This study

SI Figures
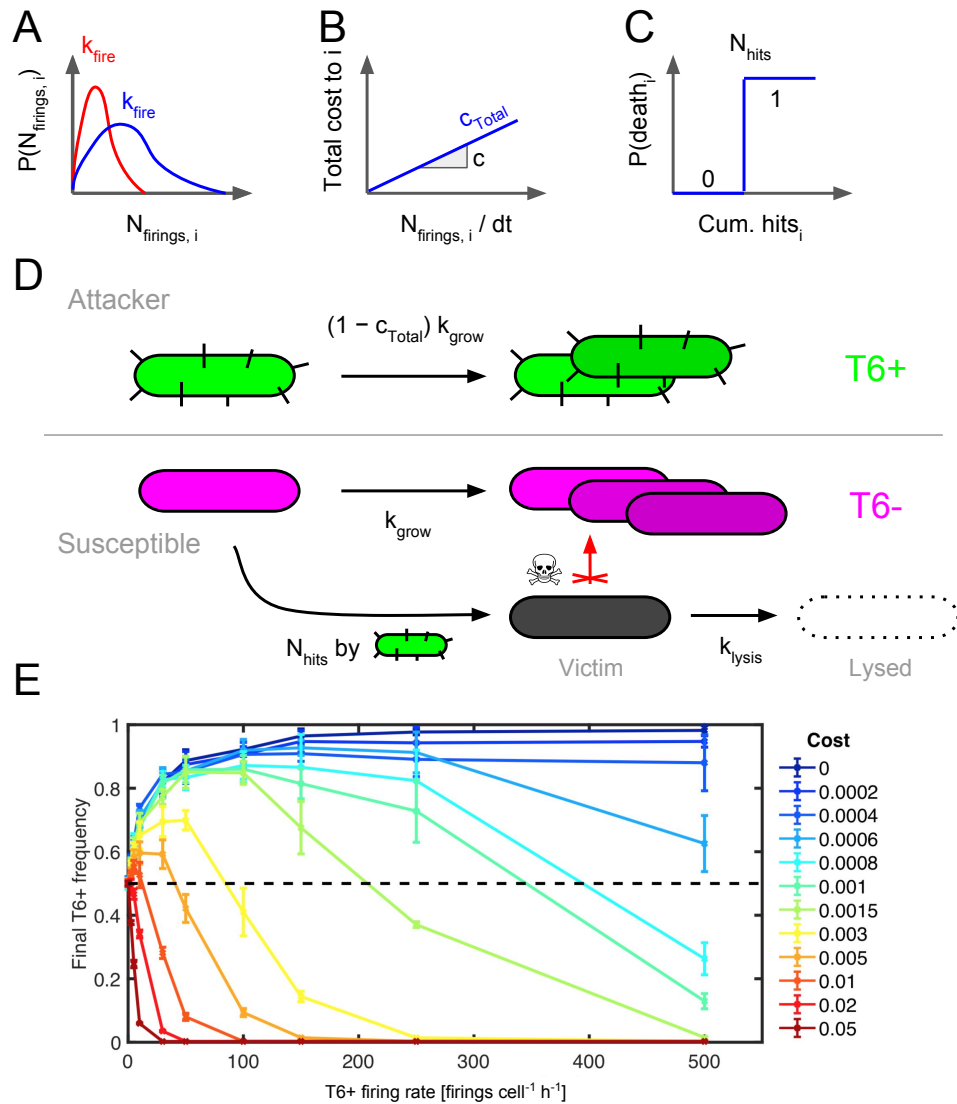
Figure S1: Agent-based modelling of T6SS firing and response. **(A)** Each simulation timestep, every T6SS+ cell fires $N_{firings,i}$, i times with $N_{firings,i}$ drawn independently from a Poisson distribution with mean k_{fire}. **(B)** Cell's growth costs are computed from values of $N_{firings,i}$; costs are assumed to scale linearly with a cell's firing rate. **(C)** Cells respond to successful translocations with a step-like dose-response curve; once a cell's cumulative translocation count reaches threshold N_{hits}, that cell dies and becomes a 'Victim' (see D). Cells of the same genotype are immune to each other's effectors. **(D)** Cartoon of cell-based processes summarizing cell-based T6SS firing and response parameters; here, k_{grow} is the maximum specific growth rate, and k_{lys} the lysis rate post-T6SS intoxication. **(E)** Initial parameter sweep showing final attacker frequencies as a function of T6SS firing rate, for various weapon cost parameters c (legend). Circles and bars denote means and standard deviations; 5 simulation replicates per case.
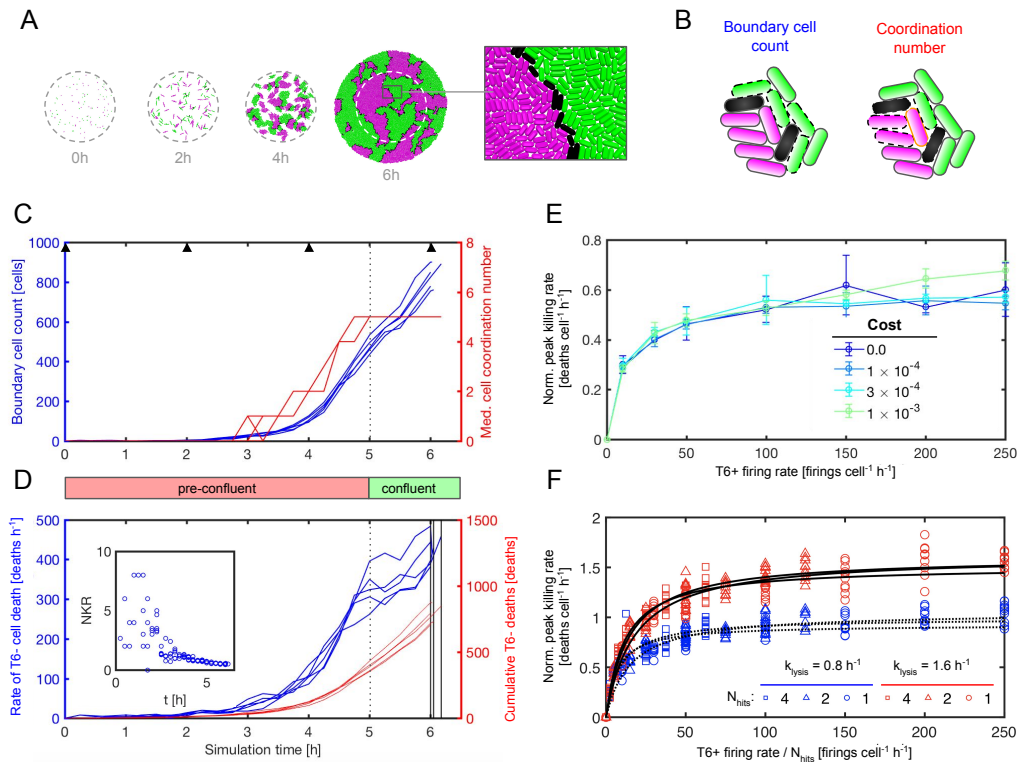
Figure S2: Quantifying T6SS kill rate per unit inter-strain boundary. **(A)** Images of T6SS competition simulations, run as in Figure 1, highlighting a section of inter-strain boundary between attacker (T6SS+, green) and susceptible (T6SS-, magenta) cell groups. **(B)** Diagrams of boundary cell classification (boundary cells shown with dashed outline) and of cell coordination number (5 neighbours of orange focal cell shown with dashed outline). **(C)** Boundary cell count traces (left axis) show number of T6+ cells in contact with non-kin cells (see B) as function of simulation time. Median cell coordination number (right axis, see B) plateaus to 5±1 cells at confluency, after ~5h growth. Black arrows correspond to the simulation snapshots shown in A. **(D)** Absolute kill rates (blue traces, left axis) are measured by counting T6-dependent cell deaths per simulation step and then numerically computing the gradient of cumulative kill count trace (red traces, right axis). The maxima of these traces (vertical black lines) are normalised by the number of boundary cells at each corresponding timepoint (see A) to give a kill rate per unit interface (inset), which converges to a constant value in confluent colonies. **(E)** Normalised peak T6- kill rates, computed as in D, plotted against T6+ firing rate k_{fire} for different weapon cost parameters c (legend). Circles and bars denote means and standard deviations, respectively. 5 simulation replicates per case. **(F)** Normalised peak T6- kill rates plotted against the ratio k_{fire} / N_{hits}, for different lysis rates k_{lysis}. Symbols denote the value of the lethal hit threshold N_{hits} used in each simulation (legend). For each of the six resulting simulation groups, we found that increasing N_{hits} was equivalent to proportionally reducing k_{fire}, such that plotting peak kill rates against the ratio k_{fire} / N_{hits} yielded the same curve for each k_{lysis} value. Black lines correspond to Monod curves, fitted for each N_{hits} value, as a test of their similarity (solid, k_{lysis} = 1.6 h-1; dashed, k_{lysis} = 0.8 h-1). 10 simulation replicates per case.
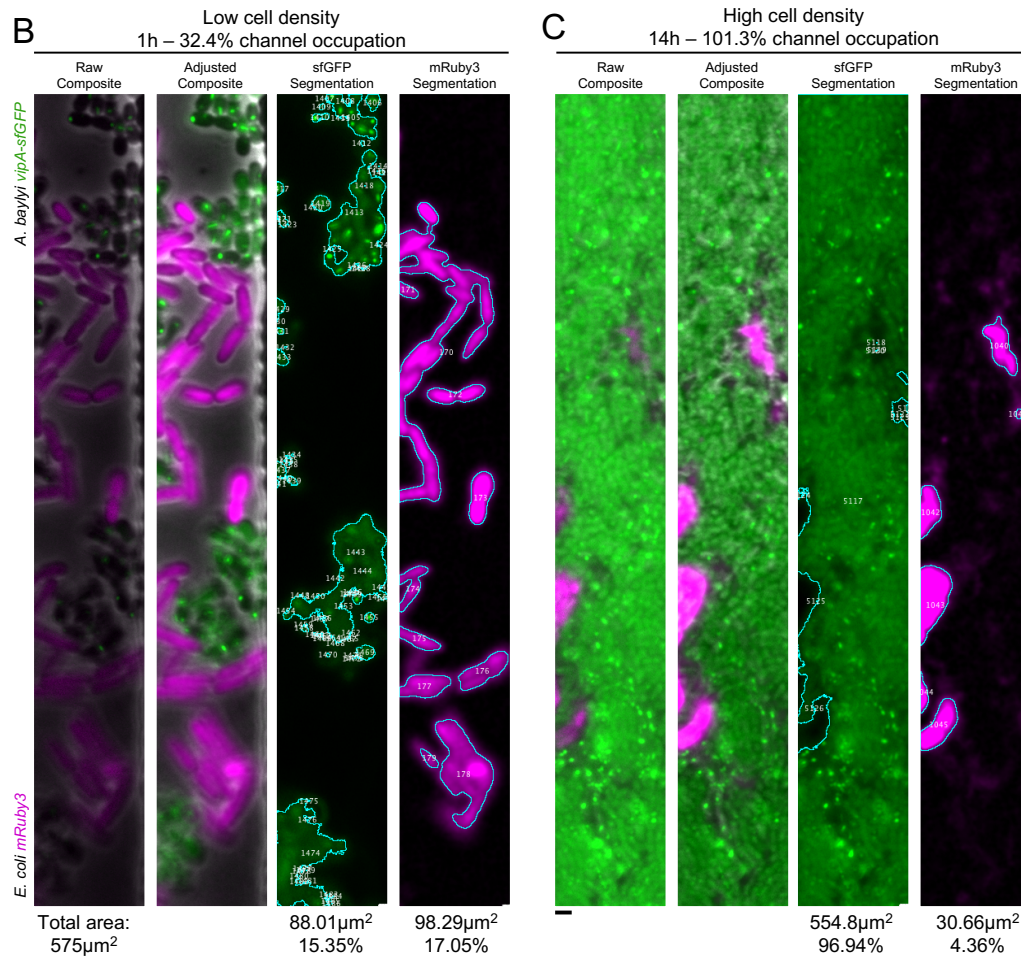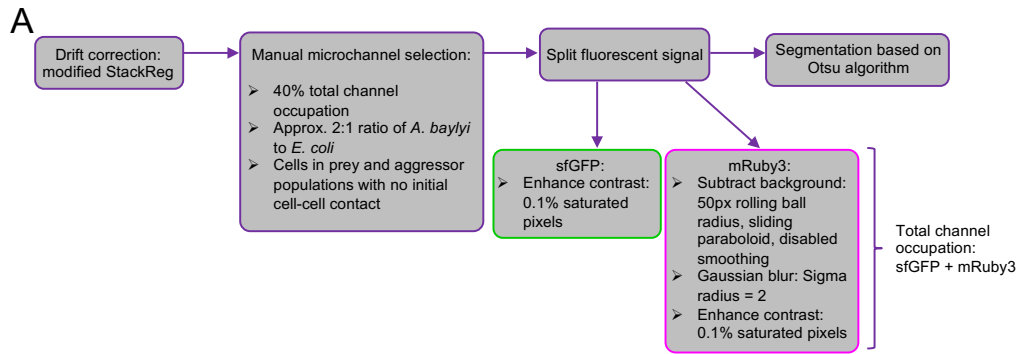
Figure S3 Automated image analysis for microfluidic experiments. Flow diagram **(A)** summarizing workflow for image post-processing and segmentation in Fiji. **(B + C)** Examples for image preprocessing (contrast enhancement, blurring and background subtraction) are shown in the adjusted composite image. GFP and mRuby3 fluorescence signal was used for segmentations (turquois outlines). Examples are provided for low **(B)** and high **(C)** chamber occupancies. Scale bar: 2µm.
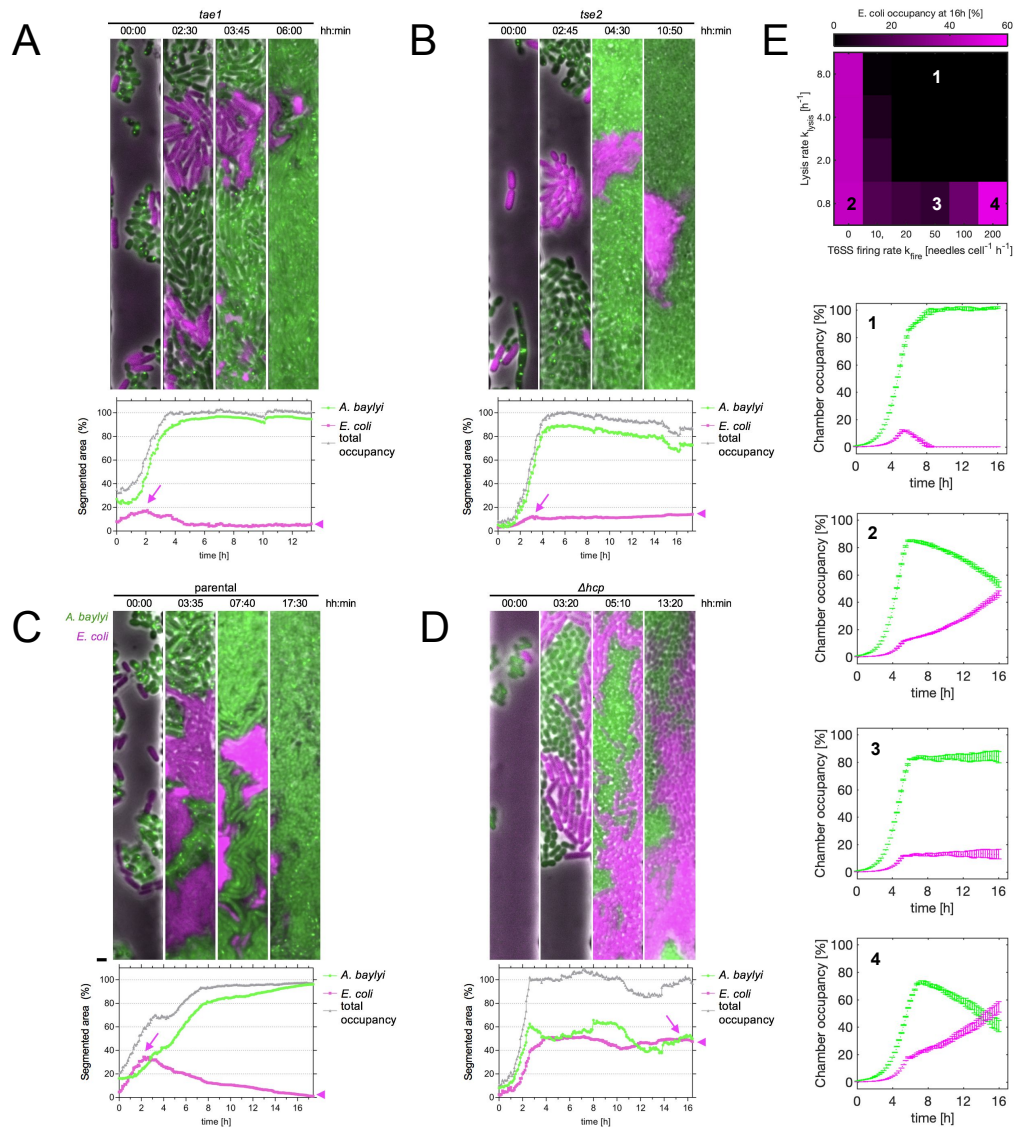
Figure S4: Microfluidic chambers: timeseries, occupancy traces and additional simulations. Fluorescence time-lapse series showing microfluidic competition experiments, between *E. coli* expressing cytosolic mRuby3 (magenta) and *A. baylyi* expressing vipA-sfGFP (green) armed with different T6SS effectors. **(A)** *A. baylyi* secreting Tae1. **(B)** *A. baylyi* secreting Tse2**. (C)** *A. baylyi* Parental strain. **(D)** Non-secreting *A. baylyi* T6SS- mutant *(Δhcp)*. Below each timeseries, the corresponding strain area occupancy plot, computed using the procedure described in Figure S3, is shown. C and D are reproduced from Figure 3, but show full channel overview. Additional time-lapse series are shown in Movies S3 (A, B) and S4 (C, D). Scale bar: 2*µ*m. **(E)** Colormap representing final (=16h) E. coli occupancy in chamber simulations, performed as in Figure 3, for different k_{fire} and k_{lysis} parameter values. Four example strain occupancy plots (1-4) are marked and shown below. Legends as in in A-D; dashed lines and bars denote occupancy means and standard deviations, respectively. 5 simulation replicates per case.
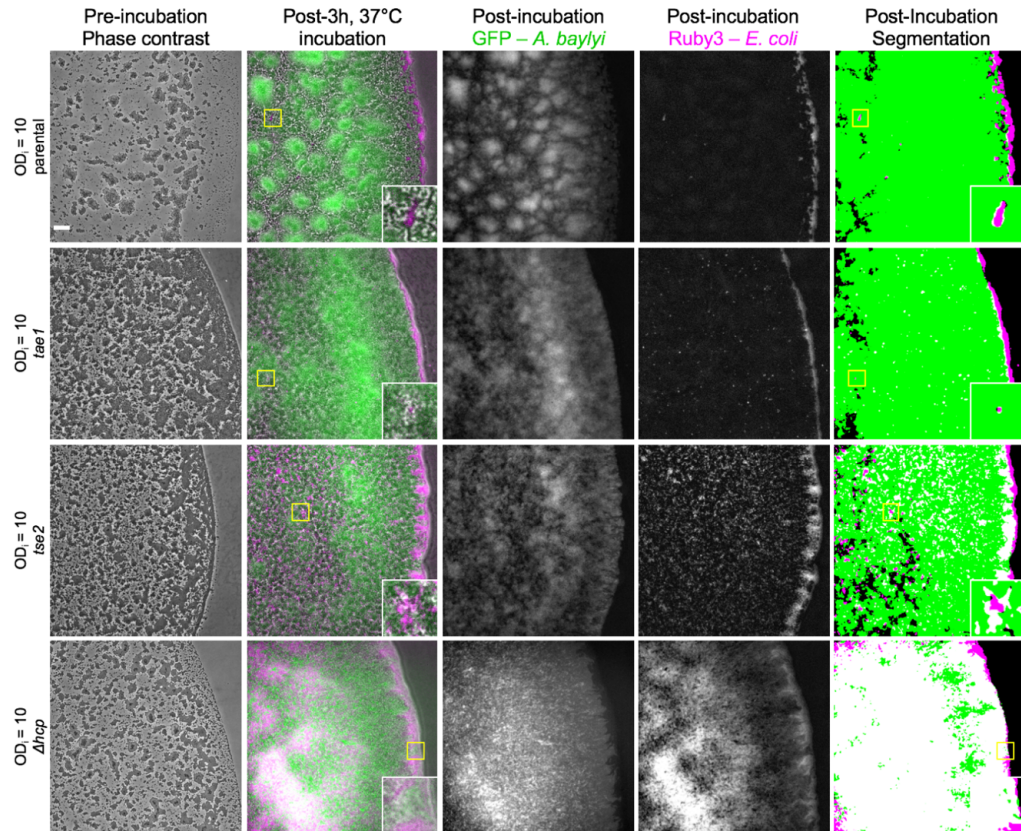
Figure S5: Fluorescence images and cell recovery for agarose competition experiments. Surface competition assays comparing performance of T6SS+ attacker *A. baylyi* (*vipA-sfGFP*, green) armed with lytic (Tae1) and non-lytic (Tse2) effectors, competing with susceptible *E. coli* (*mRuby3*, magenta). Representative phase-contrast and fluorescence micrographs show pre- and post- 3h, 37°C co-incubation distributions of *A. baylyi* and *E. coli* cells, for mixtures of parental *A. baylyi*, Tae1 and Tse2 single effector strains, and T6SS- *Δhcp* mutant. Tae1 and Tse2 are reproduced from Figure 4A for reference. Fluorescence signal for each channel was blurred and background subtracted prior to Otsu segmentation (right-most column). Based on this, the respective area occupancies of *A. baylyi* and *E. coli* within the community was quantified. White pixels indicate overlapping signals for both attacker and susceptible strain. Scale bar = 50µm; inserts depict a 50 x 50µm field of view.

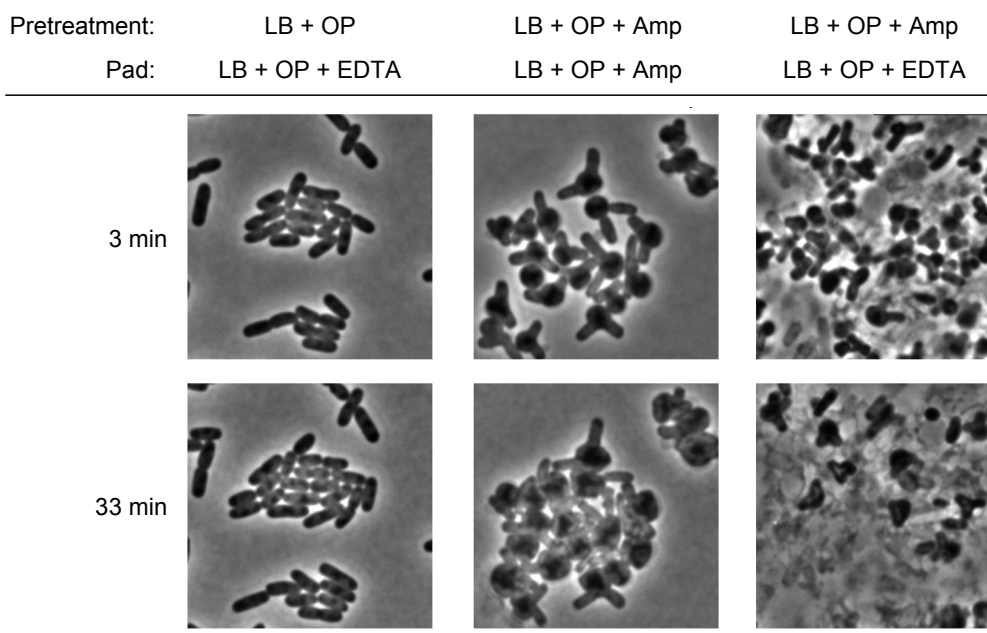| Pretreatment:	LB + OP	LB + OP + Amp	LB + OP + Amp
Pad:	LB + OP + EDTA	LB + OP + Amp	LB + OP + EDTA

Figure S6: EDTA induces lysis in wall-compromised *E. coli*, negating osmo-protection. Micrographs show *E. coli* cells following 3 min (top row) and 33 min incubation (bottom row) on agarose pads, following different pre-treatment conditions (column labels). Osmo-protectant (OP) prevents cell lysis from cell wall damage sustained from ampicillin (Amp, middle column); addition of 20mM EDTA to pad media (LB) negates osmo-protection, resulting in mass lysis (right column). Scale bar: 2μm.

SI References

Basler, M., Ho, B. T., & Mekalanos, J. J. (2013). Tit-for-Tat: Type VI Secretion System Counterattack during Bacterial Cell-Cell Interactions. Cell, 152, 884–894. http://doi.org/10.1016/j.cell.2013.01.042

Basler, M., Pilhofer, M., Henderson, G. P., Jensen, G. J., & Mekalanos, J. J. (2012). Type VI secretion requires a dynamic contractile phage tail-like structure. Nature, 483. http://doi.org/10.1038/nature10846

Ringel, P. D., Hu, D., & Basler, M. (2017). The Role of Type VI Secretion System Effectors in Target Cell Lysis and Subsequent Horizontal Gene Transfer. Cell Reports, 21(13), 3927–3940. http://doi.org/10.1016/j.celrep.2017.12.020

Rudge, T. J., Steiner, P. J., Phillips, A., & Haseloff, J. (2012). Computational Modeling of Synthetic Microbial Biofilms. ACS Synthetic Biology, 1, 345–352. http://doi.org/10.1021/sb300031n

Smith, W. P. J., Davit, Y., Osborne, J. M., Kim, W., Foster, K. R., & Pitt-Francis, J. M. (2016). Cell morphology drives spatial patterning in microbial communities. Proceedings of the National Academy of Sciences, E280–E286. http://doi.org/10.1073/pnas.1613007114

CURRICULUM VITAE

Personal Information

Name: Andrea David Vettiger

Date of Birth and Place: 04.03.1989, Basel, Switzerland

Current address: Max-Kämpf Platz 1, 4058 Basel, Switzerland

Education

02/2015 – 07/2019	PhD in Microbiology, Research Group Prof. Marek Basler, Focal Area Infection Biology, Department Biozentrum, University of Basel, *Grade: -*
09/2011 – 02/2013	MSc in Infection Biology, Research Group Prof. Gerd Pluschke, Molecular Immunology, Swiss Tropical and Public Health Institute, University of Basel, *Grade: 5.5*
09/2008 – 06/2011	BSc in Integrative Biology, University of Basel, *Grade: 5.2*
08/2003 – 06/2008	Matura, Major in Spanish Language and Literature, Gymnasium am Münsterplatz, Basel

Publications in scientific peer-review journals

Google Scholar Profile: https://scholar.google.com/citations?user=Zv-WmKkAAAAJ&hl=en

First Author:

1. **Vettiger, A.,** Winter J., Lin, L., and Basler M. (2017). Type VI secretion system sheath assembles at the end distal from the membrane anchor. Nat. Commun. 8, 16088

2. **Vettiger, A.,** and Basler, M. (2016). Type VI Secretion System Substrates Are Transferred and Reused among Sister Cells. Cell *167*, 99–110.e12.

3. **Vettiger, A.,** Scherr, N., Ruf, M.-T., Röltgen, K., and Pluschke, G. (2014). Localization of Mycobacterial Antigens by Immunofluorescence Staining of Agarose Embedded Cells. Mycobact. Dis. *4*

Contributing Author:

1. Lüönd F.; Bill R.; **Vettiger A**.; Oller H.; Pelczar P.; Christofori G. (2018). A transgenic MMTV-Flippase mouse line for molecular engineering in mammary gland and breast cancer mouse models. J Mammary Gland Biol Neoplasia.

2. Bolz, M., Bénard, A., Dreyer, A.M., Kerber, S., **Vettiger, A.**, Oehlmann, W., Singh, M., Duthie, M.S., and Pluschke, G. (2016). Vaccination with the Surface Proteins MUL_2232 and MUL_3720 of Mycobacterium ulcerans Induces Antibodies but Fails to Provide Protection against Buruli Ulcer. PLoS Negl. Trop. Dis. *10*, e0004431.

3. Dreyer, A., Röltgen, K., Dangy, J.P., Ruf, M.T., Scherr, N., Bolz, M., Tobias, N.J., Moes, C., **Vettiger, A.**, Stinear, T.P., et al. (2015). Identification of the Mycobacterium ulcerans protein MUL_3720 as a promising target for the development of a diagnostic test for Buruli ulcer. PLoS Negl. Trop. Dis. *9*, e0003477.

4. Porter, J.L., Tobias, N.J., Pidot, S.J., Falgner, S., Tuck, K.L., **Vettiger, A.**, Hong, H., Leadlay, P.F., and Stinear, T.P. (2013). The cell wall-associated mycolactone polyketide synthases are necessary but not sufficient for mycolactone biosynthesis. PloS One *8*, e70520.

5. Hall, M.D., **Vettiger, A.**, and Ebert, D. (2013). Interactions between environmental stressors: the influence of salinity on host-parasite interactions between Daphnia magna and Pasteuria ramosa. Oecologia *171*, 789–796.

Awards and honors

- 2019   EMBO long-term postdoctoral fellowship

- 2018   Poster Prize at Gordon Research Conference: Bacterial Cell Surfaces

- 2018   Get on Track: Family support grant for PhD-students with family reconciliations

- 2017   J.C.W. Shepherd PhD Student Prize

- 2015   Poster Prize at Biozentrum's PhD Retreat

- 2014   "Fellowship for Excellence" 3-year PhD fellowship from the University of Basel